UNIVERSITY OF SOUTHAMPTON

A fundamental surface study of phosphorus based antiwear films on iron

by John Vincent Thomas Heffernan

A thesis submitted to the
University of Southampton
for the degree of
Doctor of Philosophy

October 1994

UNIVERSITY OF SOUTHAMPTON

ABSTRACT

FACULTY OF SCIENCE
CHEMISTRY

Doctor of Philosophy

A FUNDAMENTAL SURFACE STUDY OF PHOSPHORUS BASED ANTIWEAR FILMS ON IRON

by John Vincent Thomas Heffernan

The interaction of PH_3 with Fe(100) at different temperatures has been studied with LEED, TPD and ellipsometry. At 160 K, PH_3 dissociates and phosphorus uptake saturates at 0.5 monolayers in a chemisorbed c(2x2) overlayer. From 300 to 445 K, phosphorus saturates in very-thin (20 Å or less), structurally disordered, optically absorbing films with optical constants (n - ik) of about (3.5 - i2.8). This is interpreted as the dissolution of phosphorus, by place exchange, into the subsurface region. From 495 to 640 K, films do not reach limiting thickness but grow with a temperature-dependent, near linear rate over several hundred Ångstroms. These films are also structurally disordered and have optical constants that typically vary from (3.32 - i2.85) to (3.37 - i2.66) depending on pressure, temperature and film thickness. These results are interpreted as showing the initiation and growth of iron phosphide where small differences in optical constants reflect compositional inhomogeneity.

The kinetics of the oxidation of Fe(100) and the affect of preadsorbed phosphorus has also been studied. Oxygen uptake on the clean surface has been followed with ellipsometry and LEED, and results are in broad agreement with previous studies. The range of uptake curves has been extended, and for first time the uptake kinetics have been correlated with LEED. Disagreement between the uptake kinetics and previous work may be explained by small compositional variations in the oxide. A saturated c(2x2)P overlayer is found to promote oxide growth.

Adsorption of PH_3 on Fe(110) has been investigated with LEED and TPD. At 160 K, PH_3 dissociates and phosphorus uptake saturates, at 0.25 monolayers, in a poorly ordered structure which on annealing forms a p(1x4) structure which can be interpreted as a surface reconstruction. At 540 K, a p(2x2) overlayer or a complex, unidentified structure precedes formation of a well-ordered p(1x4) structure. The appearance of disorder at high PH_3 may be associated with uptake beyond 0.25 monolayers. Several reconstructions are detected at high temperatures (800 to 990 K).

Then structural environment of elements in the antiwear films of ZDDP and similar oil additives has been characterised with EXAFS. Phosphorus is located in a phosphate glass structure and is insensitive to the type of additive. Zinc is intimately mixed into the glass matrix as a modifier cation. Structure about sulphur depends on the type of additive. Two sulphur environments can be distinguished, in some cases together in the same film: as an iron sulphide and as a glass forming sulphate.

To Mother

While watching
the long rains falling on this world
my heart, too, fades
with the colour
of the spring flowers.

ONO NO KOMACHI,
Japan, 9th Century A.D.
(tr. J. Hirshfield)

ACKNOWLEDGEMENTS

Thanks to John Evans and Brian Hayden, my supervisors at Southampton, and Katrina Delargy, my industrial supervisor at the Thornton Research Centre, who introduced me to ZDDP and tribology. I am grateful to SERC and Shell UK Ltd for funding this work and providing maintenance grants.

At Thornton, I would also like to thank Graham Smith, Elizabeth Shaw, especially for her help with EXAFS, and Steve for helping run the wear test machine.

Thanks to my numerous Room 15 labmates who were, in chronological order, Graham Nicholson, Drew Murray, Fred Mosselmans, Neil Williams and Gang Lu - everyone good company. Other members of the Hayden group who deserve special mention are Dave Butler, John Jones and Dave Pegg. Thanks to Nick Dartnell for help and advice with ellipsometry analysis. On the sixth floor, thanks to those who ran (or tried to run) my samples at Daresbury over the years and special thanks to Martyn Pillinger and Neil Cruise for a last-minute, crash course in EXAFS analysis.

Finally, I would like to thank my family and Kate for their love and support.

May God go with you.

ABBREVIATIONS, ACRONYMS AND SYMBOLS

Experimental

EXAFS	Extended X-ray Absorption Fine Structure
LEED	Low Energy Electron Diffraction
TPD	Temperature Programmed Desorption
L	Langmuir (unit of exposure)
ML	Monolayer (unit of coverage)
RA	Rotating Analyzer (ellipsometer)
UHV	Ultra-High Vacuum
QMS	Quadrupole Mass Spectrometry

Additives

ZDDP	zinc dialkyl dithiophosphate
DDP^-	dialkyl dithiophosphato ligand
TPP	tripropyl phosphate
DPDS	dipropyl disulphide
AW	Antiwear
EP	Extreme Pressure
FM	Friction Modifier
wt%	percentage by weight
TRC	Thornton Research Centre

Structure

BO	bridging oxygen
NBO	non-bridging oxygen
OCT	octahedral hole
TET	tetrahedral hole
TKD	tetrakaidecahedral

Other techniques

AES	Auger Electron Spectroscopy
EPMA	Electron Probe Micro Analysis
PND	Powder Neutron Diffraction
SAM	Scanning Auger Microscopy
XPS	X-ray Photoelectron Spectroscopy
XRD	X-Ray Diffraction

TPD theory

n	surface density of adsorbate
ν	frequency factor
m	order of desorption reaction
E_d	activation energy for desorption
R	molar gas constant
T	temperature
T_{max}	TPD peak temperature
n_{max}	surface density at T_{max}

LEED theory

$\mathbf{a}$, $\mathbf{b}$	real net vectors
$\mathbf{a}^*$, $\mathbf{b}^*$	reciprocal net vectors
a, b	length of $\mathbf{a}$ and $\mathbf{b}$
a^*, b^*	length of $\mathbf{a}^*$ and $\mathbf{b}^*$
γ	angle between $\mathbf{a}$ and $\mathbf{b}$
d	lattice spacing
$\mathbf{k}$	incident electron wavevector
$\mathbf{k}'$	diffracted beam wave vector
λ	de Broglie wavelength of electron
E	electron energy

Ellipsometry theory

Δ	relative phase change between two orthogonal components of reflected monochromatic light
ψ	relative amplitude change between two orthogonal components of reflected monochromatic light
θ_1	angle of incidence
θ_2	angle of reflection
θ_3	angle of refraction
n_a, n_s, n_f	refractive indices of ambient, substrate and film
n'	complex refractive index
n and k	optical constants (real and imaginary part)
ε	relative permittivity (dielectric constant)
μ	relative magnetic permeability
E	electric vector of light
E_x, E_y	orthogonal components of E
p, s	parallel and perpendicular to plane of incidence
i, r	incident and reflected
r_p, r_s	amplitude reflection coefficients for p and s components
E_r, E_i	complex amplitudes of reflected and incident E
δ	phase difference between E_r and E_i on reflection
ρ	ratio of r_p/r_s
δ_p, δ_s	phase shifts for p and s components
ϕ_B	Brewster angle
R_p, R_s	reflection coefficients for a film covered surface
β	phase delay
n_f	refractive index of film
d_f	film thickness
θ_f	complex angle of refraction in film
λ	wavelength of light in vacuum

EXAFS theory

μ	absorption coefficient
x	sample thickness
I_0, I, I_f	intensities of incident, transmitted and fluorescent light
k	photoelectron wave vector
m	mass of electron
E	incident photon energy
E_0	threshold photoelectron energy of edge
h	Planck's constant
$\hbar$	h divided by 2π
$\chi(k)$	interference function
$k^n\chi(k)$	k^n weighted interference function
$\chi(E)$	experimental EXAFS oscillations in energy-space
μ_0	absorption coefficient due to background adsorption
$A_j(k)$	amplitude in k space for each wave
N_j	number of atoms of type j
R_j	distance of j type atom from absorbing centre
$f_j(k)$	backscattering amplitude for atom j
S_j	amplitude reduction factor
$\lambda_j(k)$	inelastic mean free path of photoelectron
σ_j	Debye-Waller type parameter
σ_{vib}, σ_{stat}	vibrational and static components of σ
$\Delta_1(k)$	photoelectron phase shift due to interaction with absorbing atom
$\alpha_j(k)$	photoelectron phase shift due to interaction with backscattering atom
RDF	Radial Distribution Function
$\rho_n(r')$	modified RDF in distance (r') space
$w(k)$	window function selecting k range of transformation
R'_{min}, R'_{max}	minimum and maximum distance for Fourier transform window

EXAFS curve fitting analysis

N_s	number of shells in structural model
T_n	atom type for shell n
N_n	number of atoms in shell n
R_n	distance of shell n from absorbing atom
A_n	Debye-Waller factor for shell n
E_0	magnitude of photoelectron energy at zero wave vector
VPI	constant imaginary potential used describe photoelectron lifetime
AFAC	scaling factor used to describe of multiple excitations on centre atom
$\chi^T(k)$	theoretical EXAFS spectrum
$\chi^E(k)$	experimental EXAFS spectrum
FI	Fit Index
R	R-factor

CONTENTS

3. THEORY

4. PHOSPHORUS AND OXYGEN ON Fe(100): INVESTIGATIONS WITH ELLIPSOMETRY, LEED AND TPD SPECTROSCOPY

Notre aventure est finie. L'hiver de cette année est mort comme la tombe. Peut-être quand nous mourrons, peut-être la mort seule nous donnera la clef et la suite et la fin de cette aventure manquée.

ALAIN-FOURNIER,
Le Grand Meaulnes, 1912

1. INTRODUCTION

1.1. Motivation for this work and aims of the thesis

Lubricating oils, which are viscous mixtures of hydrocarbons, make excellent lubricants for modern machinery. However, their performance can be modified and improved by using various kinds of additives. In particular, a wide range of chemicals are added for their ability to reduce friction and wear by forming microscopic protective films on rubbing metal surfaces. It is generally accepted that these films act by separating the metal surfaces when the lubricating oil fails to give full protection. In general, the reduction in friction and wear due to the formation of surface layers is termed boundary lubrication.

An important group of chemicals used in this way are the phosphorus-based antiwear (AW) additives, which work under the comparatively mild conditions where metal-to-metal contact is infrequent. As the name suggests, their primary effect is to reduce wear. These additives, which include phosphate, phosphonate and phosphite esters, form generically similar films containing phosphorus, probably as a condensed phosphate, as will be discussed below.

Predominant among the phosphorus-based AW additives is zinc dialkyl dithiophosphate (ZDDP), which has been used extensively in automobile engine oils and other lubricant formulations. The importance of ZDDP arises primarily because, firstly, it is an excellent antioxidant, working in solution to protect the oil from degradation (ZDDP was originally added to engine oils for this property alone), and secondly, along with phosphorus, sulphur in ZDDP is also active in the formation of protective films. Sulphur-based additives, typically organic sulphides, tend to form films under the harsh conditions where metal-to-metal contact is severe. They are classed as extreme pressure (EP) additives and their chief effects are to reduce friction and prevent seizure. Because of sulphur, ZDDP can form protective films over a wider range of conditions than other phosphorus-based additives.

The protective films of phosphorus- and sulphur-based additives, and especially ZDDP, have been widely studied (as indicated by the extensive literature, reviewed in part below). However, details of the formation, composition, structure and action of antiwear and extreme pressure films remain unclear. Improved knowledge of these properties may provide the basis for the systematic development of new and better boundary lubricant additives. In the present work, two different approaches have been directed towards improving the understanding of the chemistry of phosphorus antiwear films, as described below.

Some insight into the complex chemistry of antiwear film formation might be gained from fundamental studies of the surface chemistry of suitable model compounds on iron substrates (this approach has been applied to chlorine-based EP additives, used in metal cutting and grinding processes[1]). To this end, we have investigated the chemistry of phosphorus and oxygen atoms on iron single crystal surfaces. This is far removed from the intricate chemistry of phosphorus-containing antiwear films, however, these studies seek to address the lack of general information about phosphorus and oxygen on iron surfaces and perhaps form the foundation for more directly relevant model studies in the future. Using low energy electron diffraction (LEED), temperature programmed desorption (TPD), and ellipsometry, we have investigated the interaction of phosphine (PH_3) with Fe(100) and Fe(110), representing, to our knowledge, the first time these systems have been studied (Chapters 4 and 5). The kinetics of the oxidation of Fe(100) and the effect of preadsorbed phosphorus has also been investigated with ellipsometry (Chapter 4).

The second approach used in this study is directly relevant to improving the understanding of antiwear films of ZDDP. We have used Extended X-ray Absorption Fine Structure (EXAFS) Spectroscopy to investigate the structural environments of phosphorus, sulphur and zinc in ZDDP antiwear films, prepared in wear tests (Chapter 6).

1.2. Antiwear films of zinc dialkyl dithiophosphate: Background

1.2.1. Introduction

Lubricating oils are used widely to protect the (typically ferrous) metal surfaces of bearings, gears, pistons and other components of modern machinery. The general principal of lubrication applies to lubricating oils: they reduce friction and wear (the primary purpose of lubrication) by separating sliding surfaces with a material of low shear strength. However, some degree of contact is inevitable in the normal operation of most oil lubricated systems and, consequently, the state of the surface becomes important in determine the extent of friction and wear. The protection given by surface layers, there by design or accident (as are oxide layers from atmospheric contamination, for example), is known as boundary lubrication. It is generally accepted that boundary layers protect the surfaces by preventing direct metal-to-metal contact (although other factors may be important in some systems).

The performance of lubricating oils is modified and improved by the use of various kinds of additives. Zinc dialkyl dithiophosphate (ZDDP) is an important example of a range of compounds - known as antiwear (AW) or extreme pressure (EP) additives, and often containing sulphur, phosphorus, or chlorine - that are routinely added to lubricating oils for their ability to form microscopic boundary layers on the rubbed metal surfaces of lubricated contacts.

1.2.2. Lubrication regimes

In the operation of an oil lubricated contact several lubrication regimes can be distinguished. This can be illustrated by considering a bearing where the oil shows hydrodynamic lubrication. Generally, lubricating oils work by transmitting an internal pressure that pushes the sliding surfaces apart. In hydrodynamic lubrication the pressure is generated by the flow of oil (dragged along by the moving surfaces) into a bottle-necked contact zone. In the regime of full hydrodynamic lubrication, where loads are light and sliding speeds high, the separation is complete and consequently friction is low and wear is virtually non-existent. Physical properties of the oil, especially density and viscosity, determine the range of loads and sliding speeds where the oil film provides full protection. At higher loads, the oil pressure can become so high that the metal surfaces are elastically deformed (the regime of elastohydrodynamic lubrication), but the wear rate is still very low.

As operating conditions become more severe (increasing loads, slower speeds) and the oil film becomes thinner, the surfaces eventually touch, and wear becomes a significant problem. Because all metal surfaces are to some extent microscopically uneven, contact is only made between high points (or asperities) on the surfaces, and the actual contact area is relatively small. It is widely accepted that friction is caused by the adhesion and plastic deformation of asperities ploughing across each other. Similarly, wear can arise through such mechanisms as asperity adhesion, tearing by surface protuberances, and surface fatigue. (Wear is defined as the surface damage and material loss, which if particulate is known as wear debris, at a rubbing contact. Abrasion by loose material and corrosion by the chemical environment at the contact are also categorised as wear.)

Friction and wear increase with increasing load, as more asperity contacts are made through the film. This is the regime of mixed lubrication, where both the oil film and boundary layers can give protection. If the operating conditions are pushed further, at some point, known as the initial seizure load, the oil film collapses and metal-to-metal contact is severe. At this stage, plastic deformation and high friction temperatures lead to gross seizure, extensive and irreversible wear and even welding. This is the regime of full boundary lubrication, where surface layers alone can mediate friction and wear.

1.2.3. Oil additives as boundary lubricants

The effectiveness of a boundary lubricant oil additive depends on its ability to form and maintain a protective film under the different operating conditions found at a lubricated contact. Because of fundamental difficulties in the study of lubrication systems (in particular, the closed environment of the contact and the complexity of practical situations), boundary lubricant films are often poorly characterised, and the factors that determine the formation, maintenance and effectiveness of the films are not clearly understood.

Boundary lubricant additives are usually grouped into the following classes, on the basis of their performance in wear tests (although the exact definitions vary in the literature):

1. *Friction Modifier (FM) or oiliness additives*, which are typically long-chain polar molecules (organic acids, esters and amines, for example) that reduce friction under very mild conditions by forming simple physisorbed layers;

2. *Antiwear (AW) additives*, which are typically organo-phosphorus compounds (such as phosphates, phosphites and thiophosphates) that reduce wear in the mixed lubrication regime, where the oil film is still present, by forming complex films; and,

3. *Extreme Pressure (EP) additives*, which are typically organo-sulphur and organo-chloride compounds that form protective films in the regime of full boundary lubrication, preventing seizure. EP additives allow bearings to work under conditions where they would otherwise be badly damaged or even fail.

Distinctions between the different additive classes are often hazy. For example, organo-phosphorus "AW" additives can often give some protection in the regime of boundary lubrication and are sometimes classified as EP additives.

1.2.4. Zinc dialkyl dithiophosphate (ZDDP)

ZDDP is an important boundary lubricant oil additive that, through the formation of complex protective films, has excellent wear-reducing properties, primarily in the mixed lubrication (AW) regime, but also in the full boundary lubrication (EP) regime.

ZDDPs are zinc salts of dialkyl dithiophosphoric (dialkyl phosphorodithioic) acid, with the formula $Zn[S_2P(OR)_2]_2$ where R is an alkyl group (analogues where R is an aryl group are also known, but are rarely used as oil additives). They can be regarded as complexes of zinc with the bidentate dialkyl dithiophosphato (DDP^-) ligand (fig 1.1), which binds through the sulphur atoms. The DDP^- ligand can chelate or bridge zinc atoms, the latter allowing the possibility of polymerisation. In the solid state, di-ethyl ZDDP has been shown to exist as a one dimensional polymer,[2] and di-isopropyl ZDDP as a dimer,[3] where in both cases each zinc atom is coordinated in a distorted tetrahedron to one chelating and two bridging ligands. In non-donor solutions (chloroform or toluene), both of these complexes have been found as dimers in equilibrium with monomers. In donor solvents (e.g. pyridine), the solvent molecules were found to coordinate to the zinc.[4]

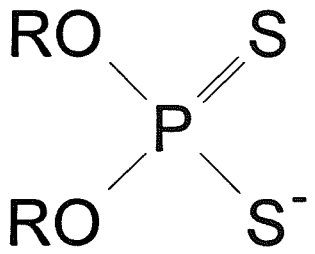

***Fig. 1.1.** The dialkyl dithiophosphato ligand.*

ZDDP can convert into a basic form, with the formula $ZnO.Zn_3[S_2P(OR)_2]_6$ (basic ZDDP is found in the commercially manufactured additive). Basic ZDDP has been shown to have a complicated structure based on a tetrahedron of zinc atoms with an oxygen atom in the centre.[5] In solution, however, it is unstable and can decompose to "neutral" ZDDP and ZnO.[4]

1.2.5. Environment of ZDDP in automobile engine oils

Some important physical and chemical factors relevant to a discussion of the antiwear behaviour of ZDDP are listed below:

1. Impurity of commercial ZDDP. Commercial engine oils contain mixtures of ZDDPs with different alkyl groups (3 to 12 carbons), and are typically only 75% pure, containing impurities such as basic ZDDP ($ZnO.Zn_3[S_2P(OR)_2]_6$) from the manufacturing process.

2. Base oil. A complex mixture of hydrocarbons, prepared from the distillation of crude oil.

3. Other oil additives. Alongside ZDDP and other boundary lubricant additives, the following additive types are usually present in commercial engine oils:

Antioxidants - various sulphur, phosphorus and nitrogen containing compounds, typically in concentrations of about 1 percent by weight (wt%), which slow the decomposition of the oil by atmospheric oxygen.

Rust inhibitors - a varied range of compounds, including amine succinates and group (II) metal sulphonates, that adsorb on ferrous surfaces to inhibit rusting.

Detergents and dispersants - compounds used in high concentration (2 to 20 wt%) to reduce formation of deposits of sludge, varnish and carbon on hot engine surfaces. Detergents include group (II) metal sulphonates, phosphonates and phenolates, while dispersants (which work better under mild operating conditions) are generally amines.

Viscosity index improvers - organic polymers, which change the temperature dependence of oil viscosity.

In wear test studies, different types of additive are often found to interact with each other, with antagonistic or synergistic effects.

4. Oil contaminants. Impurities include fuel combustion products, H_2O, oil degradation products (such as sludge and organic acids), atmospheric contaminants and soot.

5. Engine surfaces. Typically cast iron and steel. Contamination is important, especially by oxide layers.

6. High temperatures. Oil temperature can reach 200°C. Surfaces at or near the contact zone can reach temperatures of several hundred degrees celsius as frictional energy is dissipated. There are also brief and very localised flashes of extremely high temperature at asperity contacts.

7. High forces, high pressures. Powerful shear forces are found between surfaces in contact. Pressures at the surface can be of the order of 1 GPa, for example.

1.3. Literature review: Chemistry of the antiwear films of zinc dialkyl dithiophosphate

1.3.1. Basic characteristics of the antiwear film

The addition of zinc dialkyl dithiophosphate (ZDDP) to lubricating oils reduces the wear of ferrous surfaces in engines. The presence of ZDDP decreases and stabilises the wear rate[6] and increases the load carrying capacity of the oil film.[7] The reduction in wear is due to the formation of microscopic films derived from ZDDP which, it is generally believed, work by preventing direct metal-to-metal contact, although it is not clear as to what properties of the film are responsible for this. Antiwear films have been found to vary in thickness from a few nanometres[8] to a few micrometers,[9] where the film can become visible as a blue-brown discolouration.[6] The films are chemically complex, containing the elements zinc, phosphorus, sulphur and oxygen from ZDDP,[10-18] and only form on rubbed surfaces.[17,19]

1.3.2. Practical aspects of the study of antiwear films

The characterisation of antiwear films and the systematic investigation of the factors that determine their formation is difficult, if not impossible, in the complex environment of an automobile engine lubricated with a fully formulated oil. Instead, most studies have investigated antiwear films prepared in wear test rigs, which are simplified and readily controlled friction systems primarily used to measure AW/EP performance. Typically, the engine oils used in wear test studies are simple formulations of a commercially manufactured (and therefore impure) additive in base oil (other types of additive can then be added to determine their effect). Consequently, the general understanding of ZDDP antiwear films is drawn from idealised studies far removed from the complexities of the practical situation.

ZDDP is also capable of forming antiwear films on non-ferrous metal surfaces (see Buckley,[20] for example). However, this is much less relevant to the lubrication industry and consequently has rarely been studied. The chemistry of ZDDP on non-ferrous surfaces is not considered in the following discussion.

The range of techniques available to characterise antiwear films is limited because:

1. The films are very thin, and elemental concentrations of very low;

2. The films are complex and variable; and,

3. *In situ* measurements are generally impossible because the rubbing contact is closed. Consequently there is always some doubt that what is measured is present at the lubricated contact, and not some artefact.

1.3.3. Composition studies of antiwear films

The composition of antiwear films has been investigated in numerous studies, using radio-tracer,[10-12] infrared spectroscopy,[21,22] or surface analytical techniques such as Electron Probe Microanalysis (EPMA),[14] Auger Electron Spectroscopy (AES),[8,13,16,18] Scanning Auger electron Microscopy (SAM)[15] and X-ray Photoelectron Spectroscopy (XPS).[14,17,23,24] The results can be summarised by the following general points.

1. *Compositional complexity*

The relative composition Zn:P:S in the films is different to that in ZDDP and can vary considerably across the surface and in depth profiles. For example, in an XPS study of ZDDP antiwear films formed in a cam and tappet rig, Watkins[17] found that the relative composition Zn:P:S on the cam nose was 1:1.7:1.3 and on the tappet surface was 1:1.2:0.3 (the relative composition of ZDDP is 1:2:4).

2. *Phosphorus as phosphate, and sulphur as sulphide*

Some of the strongest evidence for the different film forming activities of phosphorus and sulphur from the ZDDP molecule comes from surface composition studies. Zn and P are correlated and distributed evenly across the surface while S is separate and localised, typically in regions of high wear or scoring. Along with other evidence, described below, these results have generally been taken to indicate the formation of some kind of zinc phosphate and iron sulphide, although zinc sulphide,[25] zinc phosphide,[7] iron phosphate[7] and metal sulphate[7,21] have also been postulated. XPS evidence for the oxidation states of phosphorus and sulphur is consistent with the formation of phosphate and sulphide.

3. *Dependency on operating conditions*

The relative composition of antiwear films has been found to vary considerably with experimental conditions. When wear test rigs are run under the relatively mild condition of the AW regime, Zn and P are found in high concentrations while the levels of S are

low.[14,26,27] In wear test experiments run in the extreme pressure regime, S is present in relatively high concentrations, increasing with increasing load.[8,14,18,26,27] The varying composition of ZDDP antiwear films can be explained by the separate and different abilities of sulphur and phosphorus to form antiwear films, as sulphides and phosphates, respectively. As described below, this dual action means that ZDDP can behave like other phosphorus based antiwear additives and simultaneously like other sulphur based extreme pressure additives. This combination of film forming abilities is part of the reason for the success of ZDDP in engine oils.

1.3.4. ZDDP decomposition chemistry

It is clear from numerous studies in the literature that the decomposition of ZDDP plays an important role in film formation. As will be described below, there is a wide range of phosphorus- and sulphur-containing ZDDP decomposition products many of which may be active in forming and maintaining the antiwear film.

(i). Thermal decomposition of ZDDP in oil

ZDDPs in oil solution readily decompose at temperatures typically found in use. Decomposition in solution is paralleled by the more widely studied thermal decomposition of bulk ZDDPs. On heating solid ZDDP (typically to temperatures from 60 to 150 °C) gaseous products such as alkenes, thiol (RSH, where R is an alkyl or aryl group derived from the ZDDP ester group), dialkyl sulphide R_2S and H_2S are evolved leaving a waxy-yellow solid which continues to decompose, even on cooling to room temperature.[28-30] A number of non-volatile thiophosphates and sulphides have been extracted from the solid, including $(RS)_2PS$, $(RS)_2(RO)PS$, $(RS)(RO)_2PS$, R_2S_2, $(RS)_3PO$, $(RO)_2PSSH$, $(RS)_3P$ and $(RS)_2PSOH$.[31,32] After extraction, a glassy white solid remains which has been characterised as zinc pyrophosphate[16,31] ($Zn_2P_2O_7$ *i.e.* a diphosphate formed by the condensation of two PO_4 units) or a mixture of zinc pyrophosphate and zinc orthophosphate[33] $Zn_3(PO_4)_2$ (a structure based on PO_4 monomers linked to zinc).

Thermal decomposition in oil gives a comparable range of products.[31,33,34] While volatile substances are lost, soluble end products such as $(RS)_3P$, R_2S, RSH and R_2S_2 and a solid precipitate are left in the oil. The precipitate is high in zinc and oxygen but low in sulphur, phosphorus and carbon.[34] and has been characterised as a mixture of zinc thiophosphates and condensed zinc phosphates and zinc thiophosphates.[35]

Jones and Coy[35] have proposed a mechanism for the thermal decomposition of ZDDP, using known thiophosphate chemistry, which is briefly described as follows. Decomposition is initiated by the migration of alkyl groups (R-) from O to S, which are then lost as dialkyl sulphide, thiol and dialkyl disulphide. The growth of the condensed phosphate proceeds by nucleophilic substitution reactions between phosphorus species with the displacement of RS^-. The disproportionation of the S and O atoms bound to P in ZDDP means that P-O bonds predominate in the insoluble polymer while P-S bonds are mostly found in soluble molecules. Chain growth continues until the solubility limit is reached. The insoluble precipitate is then believed to be a complex mixture of condensed phosphates species (probably containing two or three phosphorus atoms) with a low sulphur and carbon content, as illustrated in fig. 1.2.

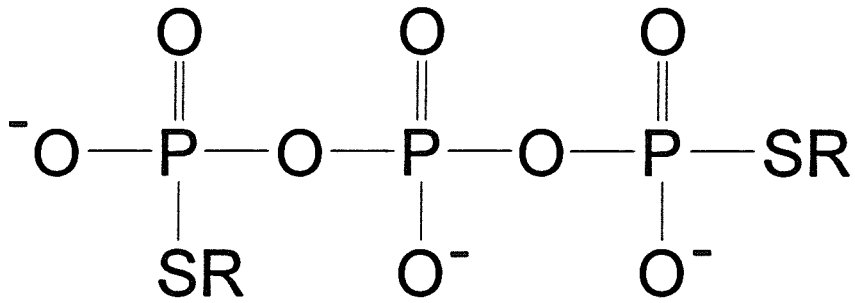

Fig. 1.2. Condensed phosphate decomposition product proposed by Jones and Coy.[35]

The thermal decomposition of ZDDP is promoted by the presence of water, a significant contaminant in engine oil.[30,36] Spedding and Watkins[31] have proposed a hydrolytic mechanism which they suggest predominates in the decomposition of ZDDP in oil. Maynard[37] has more recently proposed an alternative hydrolytic mechanism.

(ii). Oxidative decomposition of ZDDP in oil

The decomposition chemistry of ZDDP in use in automobile engines, is further complicated by the reactions of ZDDP acting as an antioxidant. ZDDP retards the autoxidation of oil (by atmospheric oxygen) and is believed to act in the following two ways, typical of antioxidant additives (see Larsen[38]):

1. As a radical scavenger - reacting with alkyl peroxy (ROO.) radicals, which propagate autoxidation. The disulphide $[(RO)_2PS_2]_2$ has been found as a product of such test-tube reactions (see Colclough and Cunneen[39]); and,

2. As a hydroperoxide decomposer - destroying ROOH, which acts as a reservoir for peroxy radicals. Numerous test-tube studies have shown that these reactions yield basic ZDDP and a disulphide $[(RO)_2PS]_2$ as end products (see for example Burn *et al.*[40]).

(iii). Decomposition of ZDDP in engines

There are comparatively few studies of the decomposition chemistry of ZDDP in use.[41-43] Basic ZDDP and $[(RO)_2PS]_2$, the products of oxidative decomposition, were detected in the used oils of wear test machines run with simple formulations of commercial ZDDP in base oil. However, with a fully formulated oil no such products were detected and a more complicated pathway was evident.[42,43] The pathways for the oxidative decomposition of ZDDP in engines were found to be complex, involving reactions with both peroxy radicals and hydroperoxide.[41] Oxidative decomposition is important in practice but it does not follow closely the pathways of test-tube oxidation studies.

1.3.5. Mechanisms of film formation

Compositional studies strongly suggest that phosphorus and sulphur from the ZDDP molecule end up in separate chemical environments. It is generally accepted that the antiwear film is composed of some kind of condensed zinc phosphate, or perhaps thiophosphate, along with iron sulphide. Numerous mechanisms of film formation have been proposed, which for convenience can be grouped into the three general classes described below. Despite the many attempts to determine the chemistry of film formation, there is no strong evidence in favour

of any particular, or general, type of mechanism. It is likely that the chemistry of film formation can radically alter with operating conditions. For example, the role of sulphur in film formation is found to be important under more severe operating conditions.

The importance of friction to film formation has not been considered in any detail for ZDDP. In general, friction is believed to promote film formation in any of a number of ways which include:

1. Generation of very high, localised temperatures;[44]

2. Exposure of fresh reactive surfaces;

3. Large sheer forces which may break bonds;[45] and,

4. Modifications of the surface electronic properties.[46]

The importance of oxygen as a necessary component in ZDDP film formation has been noted but has not been studied in any depth.[7,47,48]

(i). Adsorption of ZDDP and reaction or deposition

Several researchers have considered the adsorption of the ZDDP molecule to be the first step in film formation. The fate of the adsorbed molecule has variously been postulated as:

1. Reaction at the surface to form condensed thiophosphates;[49,50]

2. Decomposition and deposition of zinc phosphate, sulphide and oxide, which can react with the substrate under the right conditions;[8]

3. Cation exchange between zinc and iron and reaction of the iron dithiophosphate to form polymers;[48] and,

4. Reaction to form a film of metallic sulphide and oxide upon which the dissolved (thio)phosphate decomposition products of ZDDP subsequently adsorb.[51]

In an attempt to model possible film formation chemistry, numerous studies have investigated the adsorption of ZDDP in oil on ferrous surfaces (polycrystalline or powdered) using radiolabelling,[38,52-56] photometric titration,[57] flow microcalorimetry[58] and surface analysis.[17] Results are inconclusive and often contradictory, mainly because the surfaces are so poorly characterised and there is little control over the different factors that may affect the process. Most studies have shown the reversible absorption of a monolayer of ZDDP at low

temperatures (below about 60 °C)[38,52-55,57,58] which decomposes on heating. The importance of surface oxide in promoting adsorption has been indicated in adsorption studies.[56,57] Some researchers failed to detect adsorption on high purity iron surfaces.[17,58,59]

Presumably, if ZDDP adsorption is involved in film formation then it is limited to a relatively short period of time after the ZDDP is added to the lubricating system: the decomposition studies described above have shown the instability of ZDDP and the hostility of the environment towards ZDDP.

(ii). Deposition of insoluble thermal decomposition product

Compositional similarities may indicate that the antiwear film is predominantly a deposit of the insoluble condensed phosphate decomposition product of ZDDP, without reaction with the iron surface.[10,16,28,60-62] However, evidence for the expected correlation between AW performance and the thermal stability of ZDDP is contradictory.[16,29,63] In a more recent interpretation of this model, Watkins[17] has proposed that zinc polyphosphate, formed by solution decomposition, is physisorbed on the friction surface. In support of this model, Barcroft *et al.*[16] found generically similar zinc thiophosphate deposits on hot iron wires dipped in ZDDP oil solution. These deposits reacted with the substrate to form iron sulphide and some iron phosphide at high temperatures, thereby giving a possible explanation of the activity of sulphur in antiwear film formation. Deposit-like films are considered to be non-sacrificial, *i.e* the metal is not involved directly in film formation and consequently is not lost as the film is worn away (see Kapsa and Martin,[64] for example). In this case, the identity of the substrate is not crucial.[16]

(iii). Direct reaction of decomposition products with the surface

It has long been suspected that the decomposition products of ZDDP are involved in film formation by direct reaction.[38,65,66] Used oils have been shown to give good antiwear performance long after ZDDP has fully decomposed (the presence of detergent and dispersant additives was found to be important in promoting this effect, perhaps through keeping the decomposition products in solution).[67,68] Many of the thiophosphate and sulphide compounds

observed in solution during the thermal and oxidative decomposition of ZDDP have been shown[16,34,43] to give good antiwear and extreme pressure performance (although not as good as ZDDP[34]).

The involvement of sulphur-containing decomposition products, such as the alkyl sulphides or thiols, would account for the apparently independent activity of sulphur in the formation of films under the extreme pressure regimes. Several workers in recent years have tended to believe that such compounds are important in the formation of the high sulphur content films of ZDDP that form under harsh operating conditions.[8,16,17,34]

1.3.6. Structure of the antiwear film

Some indication of the structure of ZDDP antiwear films has come from a series of investigations[6,69-72] of wear debris formed in wear tests lubricated with di-isopropyl ZDDP in *n*-dodecane. The results of these studies are discussed here but also covered in more detail in Chapter 6. These studies have clearly shown the distinct chemical and structural environments of phosphorus and sulphur in the ZDDP antiwear film. Phosphorus is believed to be present as a glassy phosphate, where zinc and iron are found as counter ions, while sulphur is shown to be in a crystalline iron sulphide.

The wear particles were produced in a wear test rig operating under boundary lubrication conditions. Initial studies showed they were composed of small crystallites (5 to 10 nm across), containing sulphur, iron, zinc and oxygen, embedded in an amorphous matrix composed of zinc, phosphorus and oxygen.[6] Watkins[17] had previously hypothesised that zinc phosphate formed in the contact zone would be a low melting-point fluid glass.

Subsequently, Martin *et al.*[69] and Belin *et al.*[71] used Extended X-ray Absorption Fine Structure (EXAFS) spectroscopy to explore the local structural environment of iron and zinc in the wear particles. They concluded that both elements were coordinated to oxygen in an amorphous phase which they considered was an oxide glass where the network, or skeleton of the material, is formed by condensed phosphate chains. In the terminology of oxide glasses, phosphorus was the network "former" while zinc and iron cations were considered to be network "modifiers". Martin *et al.*[69] hypothesised that friction induced amorphisation

was a key factor in providing the antiwear protection. As will be discussed in the next section, Johnston *et al.*[73] have proposed a mechanism of action of antiwear films which is consistent with the formation of a phosphate glass.

Recently, Hallouis *et al.*[72] analyzed the crystallites embedded in the matrix, and characterised them as the iron (II) sulphide Fe_7S_8 with the hexagonal pyrrhotite structure. The sulphur-to-phosphorus ratio, which was correlated with the proportion of crystalline sulphide in the matrix, increased with increasing contact pressure. Jahanmir[18] has suggested that the hardness of such iron sulphide particles is the property responsible for the extreme pressure performance of ZDDP antiwear films.

1.3.7. ZDDP and other phosphorus-based antiwear additives

ZDDP and other phosphorus-based antiwear additives, such as phosphates $(RO)_3PO$, phosphonates $(RO)_3PO$, phosphites $(RO)_3P$ and phosphinates $R_2P(O)OH$, form protective films under the relatively mild conditions of the antiwear regime. These additives form chemically similar films based on phosphates although, as for ZDDP, exact characterisation is difficult.[73,74,75] Johnston *et al.*[73] have suggested that the phosphorus-based AW additives work in a similar way, forming thick, polymeric films which separate the moving surfaces because of their high viscosity. Evidence for these properties has come from *in situ* electrical capacitance and contact resistance measurements.[73,76,77] The films of ZDDP, for example, are found to range in thickness from 200 to 1200 nm, which is at least as thick as surface roughness.[77] Cann *et al.*[74] speculated that the films of ZDDP were a phosphate glass material based on polyphosphate chains linked by iron and zinc cations, and suggested that the antiwear films of other phosphorus-based additives would be similar.

1.3.8. ZDDP and other sulphur-based extreme pressure additives

Sulphur from ZDDP predominates in films formed at high loads or in localised areas or high wear. The different activities of sulphur and phosphorus have been clearly demonstrated by Schumacher *et al.*,[19] who compared the performance of thiophosphate, sulphide and phosphate additives in different wear tests, covering a range of operating conditions running

from the AW to the EP regime. Film formation and protection in the EP regime correlated with the presence of sulphur rich layers while good antiwear performance in the mixed lubrication regime was associated with a predominance of phosphorus. The sulphur-related EP performance of ZDDP resembles the action of other sulphur-based EP additives. It is generally accepted that additives such as polysulphides, disulphides and sulphoxides react with steel surfaces to form protective iron sulphide films under the harsh conditions of the EP regime.[78] As described above, ZDDP decomposes to give a range of sulphur containing compounds, many of which are EP active. It is possible that such compounds are active in film formation.

1.3.9. Effect of other additives on the antiwear film

In general, interactions between different additives in lubricating oils add to the complexity of lubrication systems in ways that are poorly understood (see Spikes[79]). ZDDP shows two important solution interactions with other types of additive. Succinimide dispersants have been found to reduce the antiwear and antioxidant effectiveness of ZDDP,[80,81] while alkyl benzene sulphonate and phenate detergents are also strongly antagonistic, inhibiting ZDDP decomposition in solution.[82,83,84] These interactions probably retard film formation rather than direct it. Several additive classes have also been found to interfere with antiwear film formation through interactions at the surface. The adsorption of metal carbonate detergents competes with ZDDP film formation, and calcium and magnesium from the detergent are found in the antiwear film.[17,85] Calcium napthasulphonate competitively adsorbs,[36,86] while succinimide dispersants cooperatively adsorb,[36] during ZDDP film formation.

1.4. References

1. V.S. Smentkowski, C.C. Cheng and J.T. Yates Jr, *Langmuir* 6 (1990) 147.

2. T. Ito, T. Igarashi and H. Hagihara, *Acta Cryst.* B25 (1969) 2303.

3. S.L. Lawton and G.T. Kokotailo, *Inorg. Chem.* 8 (1969) 2410.

4. P.G. Harrison and T. Kikabhai, *J. Chem. Soc. Dalton Trans.* (1987) 807.

5. A.J. Burns, R.W. Joyner, P. Meehan and K.M.A. Parker, *J. Chem. Soc., Chem. Comm.* (1986) 982.

6. J.M. Martin, J.L. Mansot, I. Berbezier and H. Dexpert, *Wear* 93 (1984) 117.

7. A. Begelinger, A.W.J. de Gee and G. Salomon, *ASLE Trans.* 23 (1980) 23.

8. I. Sieber, K. Meyer, H. Kloss and A. Schopke, *Wear* 85 (1983) 43.

9. K. Meyer, I. Sieber and H. Kloss, *Proc. Eurotrib. '81* (Warsaw, 1981) Vol. III, p180.

10. M.J. Furey, *ASLE Trans.* 2 (1959) 91.

11. E.H. Loeser, R.C. Wiquist and S.B. Twiss, *ASLE Trans.* 2 (1959) 199.

12. R.C. Wiquist and S.B. Twiss, *ASLE Trans.* 3 (1960) 40.

13. M. Phillips, M. Dewey and D. Hall, *Vacuum* 26 (1976) 451.

14. R.J. Bird, R.C. Coy and J.F. Hutton, *ASLE Trans.* 23 (1980) 121.

15. T .P. Debies and W.G. Johnston, *ASLE Trans.* 23 (1980) 121.

16. F.T. Barcroft, R.J. Bird, J.F. Hutton and D. Park, *Wear* 77 (1982) 355.

17. R.C. Watkins, *Tribology Int.* 15 (1982) 13.

18. S. Jahanmir, *J.Tribol.* 109 (1987) 577.

19. R. Schumacher, E. Gegner, A. Schmidt, H.J. Mathieu and D. Landolt, *Tribology Int.* 13 (1980) 311.

20. D.H. Buckley, *NASA Tech. Note* 1489 (1979).

21. S.A. Francis and A.H. Ellison, *J. Chem. Eng. Data* 16 (1961) 60.

22. D.L. Wooton and D.W. Hughes, *Lubr. Eng.* 43 (1987) 736.

23. B.A. Baldwin, *Lubr. Eng.* 23 (1975) 125.

24. R.J. Bird and G.D. Galvin, *Wear* 37 (1976) 143.

25. M. Antler, in the discussion of Furey.[10]

26. E.S. Forbes, K.G. Allum and H.B. Silver, *Proc. Inst. Mech. Eng.*, London 183 (1968) 35.

27. R.C. Coy and T.F.J. Quinn, *ASLE Trans.* 18 (1975) 163.

28. I.M. Feng, W.L. Perilstein and M.R. Adams, *ASLE Trans.* 6 (1963) 60.

29. C.N. Rowe and J.J. Dickert, *ASLE Trans.* 10 (1967) 85.

30. H. Luther, E. Baumgarten, K. Ul-Islam, *Erdöl and Kohle* 26 (1973) 501.

31. H. Spedding and R.C. Watkins, *Tribology Int.* 15 (1982) 9.

32. G.N. Kuz'mina, V.V. Sher, E.I. Markova and P.I. Sanin, *Neftekhimiya* 12 (1972) 112.

33. R. Molina, *ASLE Trans.* 24 (1981) 77.

34. R.C. Coy and R.B. Jones, *ASLE Trans.* 24 (1981) 77.

35. R.B. Jones and R.C. Coy, *ASLE Trans.* 24 (1981) 91.

36. F.G. Rounds, *ASLE Trans.* 18 (1975) 79.

37. I.G. Maynard, *Int. Trib. Conf.* 1987, Melbourne, (1987) 100.

38. R. Larsen, *Sci. Lubr.*, 10 (1958) 12.

39. T. Colclough and J.I. Cunneen, *J. Chem. Soc.* (1964) 4970.

40. A.J. Burn, R. Cecil and V.O. Young, *J. Inst. Petroleum* 57 (1971) 319.

41. S. Korcek, L.R. Mahoney, M.D. Johnston and W.O. Siegl, *SAE Paper* 810014, (1981).

42. R.C. Coy and R.B. Jones, *"Tribology - Key to the Efficient Engine."* I. Mech. E. Pub. (1982) 17.

43. K. Hosonuma, K. Yoshida and A. Matsunaga, *Wear* 103 (1985) 297.

44. A.D. Sarkar, *"Wear of Metals"* (Pergammon Press, Oxford, 1976).

45. J.M. Georges, *Trib. Series* Vol. 7 (1983).

46. M.F. Morizur and J. Briant, *Proc. I. Mech. Eng.*, I. Mech. Eng. Conf. 5, *"Tribology - Friction, Lubrication and Wear. 50 Years On"*, Vol. 1 (1987) 448.

47. P.A. Willermet, S.K. Kandah, W.O. Siegel and R.E. Chase, *ASLE Trans* 26 (1983) 5223.

48. K. Meyer and C. Kajdas, *Tribologie und Schmierungstechnik* 36 (1989) 71.

49. P.I. Sanin, *Neftechimija* 3 (1963) 775.

50. H. Luther, *Erdöl und Kohle* 26 (1973) 509.

51. M.F. Morizur-Jersale, J. Briant, A. Pentenero and J.J. Ehrhardt, *Proc. 4th Euro. Trib. Congr.* (Ecully, France, 1985) Vol. IV Sect. 5-4.

52. E. Baumgarten, *Erdöl und Kohle* 25 (1972) 577.

53. B. Dacre and C.H. Bovington, *ASLE Trans.* 25 (1982) 546.

54. B. Dacre and C.H. Bovington, *ASLE Trans.* 26 (1983) 333.

55. C.H. Bovington and B. Dacre, *ASLE Trans.* 27 (1984) 252.

56. K. Otto and H. Sorek, *ASME Trans., J. Tribol.* 108 (1986) 340.

57. S. Plaza, *ASLE Trans.* 30 (1987) 233.

58. W.G. Jones and M.I. Pope, *Thermochim. Acta* 130 (1988) 141.

59. F.G. Rounds, *Am. Soc. Lub. Eng. Trans.* 9 (1966) 88.

60. I.M. Feng, W.L. Perilstein and M.R. Adams, *ASLE Trans.* 7 (1964) 55.

61. N.E. Gallopoulos, *ASLE Trans.* 7 (1964) 55.

62. A.D. Brazier and J.S. Elliott, *J. Inst. Petrol.* 53 (1967) 63.

63. K.G. Allum and E.S. Forbes, *Proc. I. Mech. Eng. London, Trib. Conv.*, 183 (1968) 35.

64. Ph. Kapsa and J.M. Martin, *Tribology Int.* 15 (1982) 37.

65. E.H. Loeser, R.S. Wiquist and S.B. Twiss, *ASLE Trans.* 1 (1958) 329.

66. M.J. Furey and J.F. Kunc, *Lubr. Eng.* 14 (1958) 302.

67. M. Kawamura, K. Fujita and K. Ninomiya, *Wear* 77 (1982) 195.

68. K. Fujita, Y.E. Saki and M. Kawamura, *Wear* 89 (1983) 323.

69. J.M. Martin, G. Balossier, J.L. Mansot, I. Berbezier and M. Belin, *Wear* 107 (1986) 355.

70. J.M. Martin, M. Belin, J.L. Mansot, H. Dexpert and P. Lagarde, *ASLE Trans.* 29 (1986) 523.

71. M. Belin, J.M. Martin and J.L. Mansot, *STLE, Trib. Trans.* 32 (1989) 410.

72. M. Hallouis, M. Belin and J.M. Martin, *Lubr. Sci.* 2 (1989) 337.

73. G. Johnston, P.M.E. Cann and H.A. Spikes, *Proc. 5th Int. Colloq.* Esslingen, *"Additives for Lubricants and Operational Fluids"*, (1986) Paper 3.12.

74. P.M.E. Cann, G. Johnston and H.A. Spikes, *Proc. I. Mech. Eng.*, I. Mech. Eng. Conf.5, *"Tribology - Friction, Lubrication and Wear. 50 Years On"*, Vol. 1 (1987) 543.

75. J.M. Perez, C.S. Ku, P. Bei, B.E. Hegemann and S.M. Hsu, *Trib. Trans.* 33 (1990) 131.

76. P.M. Cann, H.A. Spikes and A. Cameron, *ASLE Trans.* 26 (1983) 48.

77. A.F. Alliston-Greiner, J.A. Greenwood and A. Cameron, *Proc. I. Mech. Eng.*, I. Mech. Eng. Conf. 5, *"Tribology - Friction, Lubrication and Wear. 50 Years On"*, vol. 1 (1987) 562.

78. C. Kajdas, *Proc. 5th Int. Colloq.* Esslingen, *"Additives for lubricants and operational fluids"*, (1986) Paper 4.6.

79. H.A. Spikes, *Lubrication Sci.* 2 (1989) 3.

80. K. Inoue and H. Watanabe, *ASLE Trans.* 26 (1983) 189.

81. F.G. Rounds, *Proc. 5th Int. Colloq.* Esslingen, *"Additives for lubricants and operational fluids"*, (1986) Paper 4.8.

82. F.G. Rounds, *ASLE Trans.* 21 (1978) 91.

83. C.J. Quilty and P. Martin Jr, *Lubr. Eng.* 25 (1969) 240.

84. C.H. Bovington and A. Hubbard, *Proc. I. Mech. Eng.*, 2nd Int. Conf. *"Combustion Engines - Reduction of Friction and Wear"*, (1989-90) 79.

85 P.H. Kapsa, J.M. Martin, C. Blanc and J.M. Georges, *J. Lubr. Tech.* 103 (1981) 486.

86. K. Inoue and H. Watanabe, *J. Jap. Petrol. Inst.* 25 (1982) 1006.

2. EXPERIMENTAL

2.1. Ultra-high vacuum (UHV) surface experiments

2.1.1. The UHV system

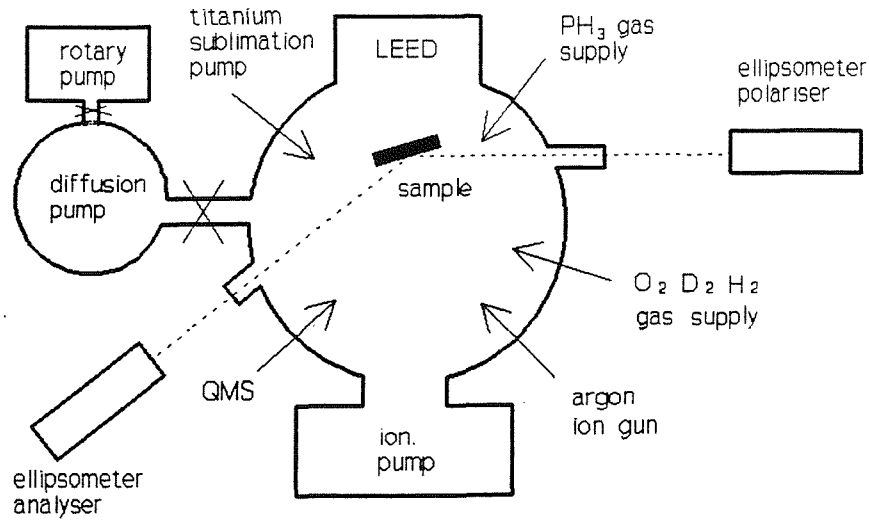

Fig. 2.1. Schematic representation of the UHV system.

The stainless steel ultra-high vacuum (UHV) chamber used in the present study of iron surface chemistry is shown schematically in fig. 2.1. The system was equipped for fixed-wavelength (λ = 623.8 nm) ellipsometry, low energy electron diffraction (LEED) and temperature programmed desorption (TPD) experiments, and for sample cleaning by Ar^+ bombardment.

2.1.2. Pumping

The chamber was pumped with an Edwards E02K diffusion pump (150 L s^{-1}) - backed by an Edwards E2M12 rotary pump - and a Varian VacIon ionisation pump (110 L s^{-1}). A foreline trap on the rotary pump and a liquid nitrogen cold trap on the diffusion pump reduced back-streaming of pump oils. After bake-out (at 160 °C, for periods of 12 to 18 hours) and outgassing, the base pressure was in the low 10^{-10} torr range. A titanium sublimation pump was used routinely, between experiments, to maintain good UHV.

2.1.3. Materials

Fe(110) and Fe(100) single crystals (99.9% purity), supplied by Metals Research Ltd, were in the form of discs, 2 mm thick, with diameters of 9 mm and 10 mm, respectively.

Oxygen, hydrogen, deuterium and argon gases (all 99.999% purity) were supplied in lecture bottles by Messer Griesheim. Phosphine (PH_3) gas, in a glass bottle, was obtained from the inorganic chemistry sub-department at the University of Southampton, and had been prepared by the combustion of phosphorus in a hydrogen atmosphere. The purity of the dosed PH_3 gas was roughly estimated as better than 97%, by quadrupole mass spectrometry.

2.1.4. Sample mounting

The iron single crystals were mounted at the base of a manipulator column, which allowed sample movement of 25 mm in the x,y and z directions, rotation in the xy plane and tilt in the xz plane. A schematic diagram of the arrangement of the sample mounting is given in fig. 2.2.

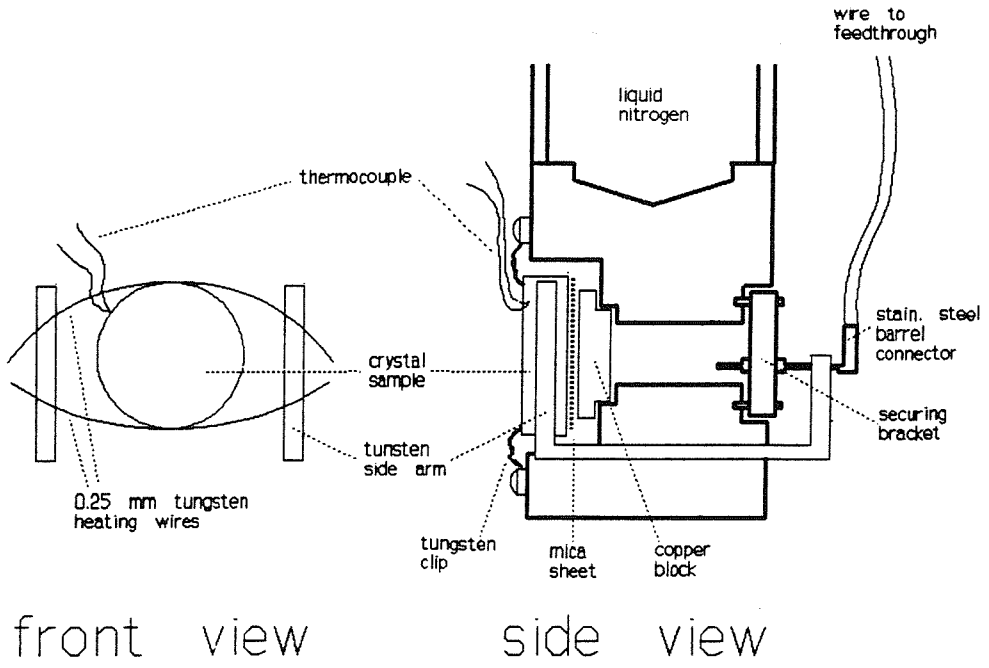

Fig. 2.2. Sample mounting.

The crystals were resistively heated. Kapton-insulated wires carried current from feedthroughs to the back of the mounting assembly. As fig. 2.2 shows, the wires were

barrel-connected to two stainless steel rods which, supported by spot-welds to insulated screws at the back of the column, bent round to lie flush with the front of the crystal. Two tungsten wires (0.25 mm in diameter) spot-welded to the top and bottom of the crystal and to the rods completed the circuit.

The samples were cooled by thermal contact with the manipulator column filled with liquid nitrogen. For good thermal conduction, the crystals were held (by insulated stainless steel pins) against a copper block set into the manipulator column, with a thin sheet of mica between to keep the samples electrically isolated. Temperatures down to 150 K were achieved routinely. Temperature was measured with a chrome-alumel thermocouple, spot-welded to the edge, and near the front, of the crystal.

2.1.5. Gas dosing

O_2, H_2 and D_2 were dosed through Vacuum Generators (VG) leak valves into the gas manifold, and on into the main chamber through a ¼" stainless steel tube that ended ~ 5 cm from the sample. Ar was admitted through a VG leak valve into the back of the saddle-field ion gun. PH_3 was dosed through a VG leak valve, ~ 30 cm from the sample.

2.1.6. Fe(110) and Fe(100) sample cleaning

Iron single crystals cannot be cleaned by flashing to high temperatures to desorb segregated impurities, because at 1183 K a phase transformation from the body centred cubic to the face centred cubic structure would shatter the crystal.[1] This limitation, together with the comparatively high levels of bulk impurities in commercially available samples, makes the preparation of clean single crystals of iron notoriously difficult. Typically, iron crystals are cleaned by cycles of annealing (to induce the segregation of contaminants) and Ar^+ sputtering (see the review by Musket *et al.*[2]). Carbon, nitrogen and sulphur are commonly observed bulk contaminants of iron. Carbon and nitrogen, with their comparatively high diffusion coefficients, quickly segregate to the surface at temperatures from 600 to 800 K, and carbon reaches a segregation equilibrium while nitrogen desorbs with a significant rate at temperatures above 770 K.[3,4] Segregation of sulphur, which has a lower diffusion coefficient,

only becomes important at temperatures above 970 K, and a segregation equilibrium is quickly reached after other surface contaminants are displaced.[5]

The various procedures used to the iron crystals in the present study were as follows:

1. *Pretreatment before mounting* - the crystals were heated in a tube furnace at 970 K under a flow of H_2 gas for several weeks to remove impurities which form volatile hydrides.[1,2,5] In particular, this was expected to reduce levels of sulphur which segregates to displace other surface contaminants at high temperatures,[5] although a carbonaceous segregation layer has been observed on a Fe(110) sample treated in this way.[6] Before mounting, the crystals were polished with diamond pastes (0.25 μm for finishing) and rinsed in acetone.

2. *Prolonged treatments in UHV* - impurity levels in the subsurface region were reduced by prolonged cycles of annealing (700-840 K) and high temperature (700-840 K) Ar^+ sputtering. An Ion Tech saddle-field ion gun with the chamber filled to an Ar pressure of about 10^{-3} torr generated Ar^+ beams with energies from 0.5 to 1 K eV. By keeping the crystal temperature well below 970 K it was hoped to prevent significant diffusion of sulphur into the sub-surface region.

3. *Oxygen treatment to reduce carbon levels* - the crystals were occasionally annealed (700 K) in O_2 (10^{-6} torr) for periods from 30 minutes to 1 hour. The carbon that segregated during this treatment was expected to desorb as CO.[1,7]

4. *Routine cleaning between experiments* - depending on the condition of the surface, the crystal was Ar^+ sputtered at 700 K for periods from 45 minutes to 5 hours and then annealed at typically 840 K for periods from 30 minutes to 1 hour.

Because the system was not equipped for compositional analysis, progress in these various cleaning procedures was checked by low energy electron diffraction (LEED) - since surface contamination often gave rise to new LEED patterns - and the thermal desorption characteristics of H_2 and D_2. The results of these experiments and particular segregation characteristics for the individual Fe(100) and Fe(110) crystals are described in Sects 4.1 and 5.1, respectively.

2.1.7. Temperature programmed desorption (TPD)

Prior to the desorption scan, the sample was moved to face the quadrupole analyzer which was enclosed by a glass shield with a small aperture (diameter = 2 mm) to restrict the angle of acceptance into the quadrupole, and thereby improve the quality of the TPD spectra. A Spectrametrics Vacscan quadrupole mass spectrometer (qms) was used to monitor the mass-to-charge ratio of the desorbate (operating on the slowest signal processing speed to reduce noise levels). During desorption scans, a computer program recorded the qms signal and the sample thermocouple voltage (amplified by an RS AD595A chip) through an analogue-to-digital interface, and converted the thermocouple voltage to temperature before saving the data to a text file (the program was calibrated by measuring thermocouple output at known temperatures). The sample was heated at a constant rate until desorption had ceased. A linear heating rate could be achieved, up to about 500 K, by maintaining a constant current through the crystal. Different heat rates were tried to find a suitable resolution for the spectra and subsequently a rate of 2.3 K s^{-1} was used. The sensitivity of the mass spectrometer, which could vary considerably over time, was estimated after each experiment by recording qms partial pressure as a function of total
(ionisation gauge) pressure for the desorbing gas.

2.1.8. Low energy electron diffraction (LEED)

LEED experiments used a Vacuum Generators 3-grid optics, with the sample grounded to prevent surface charging. The surface was usually cooled to 160 K, to reduce lattice vibration and sharpen the pattern. LEED patterns were photographed with exposure times of between 5 and 10 minutes.

2.1.9. Ellipsometry

Fig. 2.3 shows a schematic diagram of the fixed wavelength (632.8 nm) rotating-analyzer ellipsometer. The components form a polariser-sample-analyzer (PSA) arrangement, where the polariser and analyzer paths are fixed to give an angle of incidence of 70 ° at the sample. The ellipsometer had been set-up by the previous experimenter on this rig and so the

alignment of the optical paths, and the calibration of analyzer azimuth angle with respect to the plane of incidence is described elsewhere.[8]

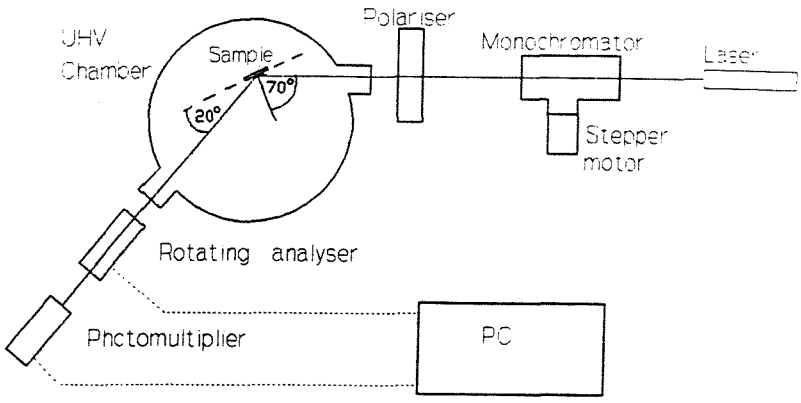

Fig. 2.3. The ellipsometer arrangement.

On the polariser side, light from a Spectra-Physics HeNe laser (632.8 nm) was linearly-polarised to an angle of 45° relative to the plane of incidence, using a rochon prism mounted in a Rudolph Research rotator. The various optical components were mounted on rails along the direction of the beam to allow optimisation of the signal. The analyzer (and the operating software) came from the Fritz-Haber Institut der Max Planck, Germany. It consists of a rotating analyzer (RA) and a photomultiplier tube (Thorn EMI QB 9973), and measures the intensity of the reflected light as a function of azimuth angle using. The ellipsometric parameters Δ and ψ were then determined by the computer from a Fourier analysis of the intensity variation.

The RA consisted of a rochon prism rotated at 25 revolutions per second by a computer-controlled synchronous motor. An electronic pulse from the RA defined the start of the revolution, and at 5° intervals the computer recorded the photomultiplier light intensity signal through an analogue-to-digital converter. Two hundred revolutions were averaged to give an acceptable signal-to-noise ratio of $\pm$ 0.05° in Δ, and $\pm$ 0.03° in ψ. Consequently, each measurement of Δ and ψ was effectively an average over a period of 8 seconds. The computer began each 8 second averaging at intervals of 16 seconds. The data acquisition time and sampling frequency, although relatively slow, were quite suitable for the rates of change in Δ and ψ found in these experiments.

Prior to experiments, the sample was stabilised at the required temperature. Measurements were made with liquid-nitrogen in the manipulator column, because surface cleanliness had to be pre-checked by low temperature LEED. As long as the column was kept topped-up, this was not found to have any significant effect on the measurement of the ellipsometric parameters at any of the temperatures used. The software produced a real time representation of the ellipse of the reflected light on the monitor screen, which helped in optimising the sample position and allowed checks for stability. Experiments were started when the values of ψ and Δ delivered by the data acquisition program were sufficiently stable. The degree of instability could vary quite considerably between experiments, and the source of the problem was not always apparent, although presumably it generally originated in tiny sample vibrations or displacements.

Experiments were typically run for periods from about 45 minutes to 1 hour, because maintaining sufficient stability over longer times became difficult. The first twenty-or-so measurements of ψ and Δ were recorded for the clean surface to check for stability and to provide a background for subtraction. The experimental gas (PH_3 or O_2) was then admitted into the chamber at pressures in the range 1×10^{-7} to 1×10^{-5} torr. Time, Δ and ψ, along with other experimental parameters were recorded by the program and written to a text file.

2.2. Extended X-ray Absorption Fine Structure (EXAFS) spectroscopy

2.2.1. Synchrotron Radiation Source at Daresbury

EXAFS measurements were made using the Synchrotron Radiation Source (SRS) at the SERC Daresbury Laboratory, Cheshire, UK. Synchrotron radiation is produced by circulating 'packets' of electrons at relativistic speeds in a magnetic field. In the SRS, electrons are accelerated by a linear particle accelerator and passed into a booster synchrotron where their energy reaches 600 MeV. They are then injected into the near-circular path of the storage ring and receive a final increase of energy to 2000 MeV. As the electrons fly around the ring a narrow cone of radiation sweeps before them, tangential to their path. The Wiggler magnet is used to modify the electron trajectory thereby extending the radiation distribution to shorter wavelengths in X-ray region. Synchrotron radiation is beamed through ports on the storage ring to various experimental stations dedicated to different techniques.

Synchrotron radiation has a number of unique properties. For EXAFS, the advantages that synchrotron radiation has over other sources of X-rays are:

1. *High intensity* - synchrotron radiation is orders of magnitude more intense than the next best source of X-rays, the rotating anode generator, reducing the time needed to record reasonable spectra from hours to minutes;

2. *A smooth, continuous and tunable spectrum* - contrasting with other sources which show emission lines; and,

3. *High collimation* - synchrotron radiation has a small angular divergence which means that an intense beam can be aimed at a small sample.

2.2.2. Experimental Stations 3.4 and 9.2 at Daresbury

X-ray absorption spectra were recorded for the K-edge of phosphorus, sulphur and zinc in antiwear films and model compounds. Phosphorus and sulphur measurements were made on the soft X-ray experimental Station 3.4 while zinc spectra were recorded on the hard X-ray Station 9.2. Edge energies and the corresponding wavelengths are shown in table 2.1.

Table 2.1. K-edges studied in this work.

K-edge	Energy (eV)	λ (Å)
P	2144	5.784
S	2472	5.016
Zn	9661	1.283

Absorption spectra of phosphorus, sulphur and zinc in antiwear films were recorded in fluorescence mode because concentrations of the absorbing atoms were very low (the films are microscopically thin). Spectra for the model phosphorus and sulphur compounds were also recorded in fluorescence mode, to avoid the problem of high background absorption which can hinder transmission measurements made in the soft X-ray region (see below). Spectra for the model compounds of zinc were recorded in transmission mode.

Essentially, the general arrangement and operation of the EXAFS spectrometer is the same for both Stations 3.4 and 9.2. The basic components of the spectrometer are shown schematically in fig. 2.4.

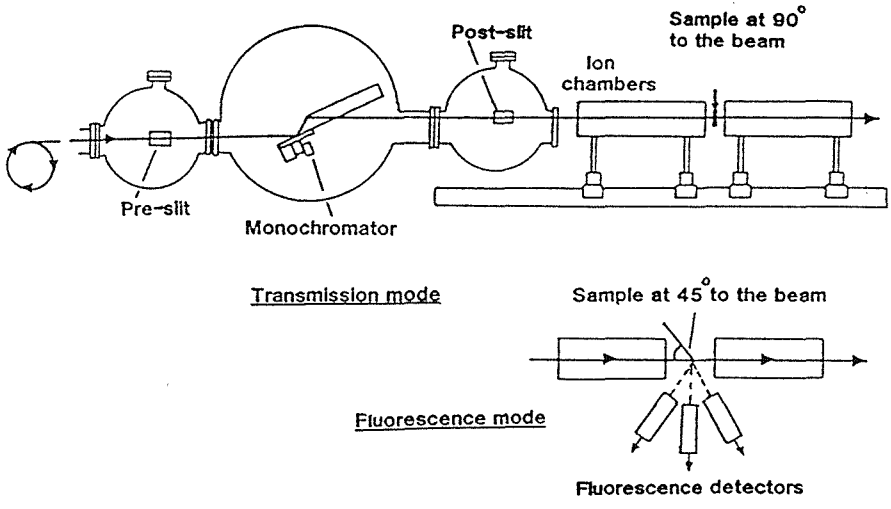

Fig. 2.4. Schematic of the components of beam lines 3.4 and 9.2.

The spectrum is scanned by an order sorting double crystal monochromator (Ge(111) on 3.4 and Si(111) on 9.2). The monochromator is operated under vacuum and so light enters and leaves through windows of beryllium on 9.2, or carbon (with its lower minimum pass energy) on 3.4. The beam from the SRS is highly collimated, with a height of about 2 mm.

The entrance slit limits beam width to between 6 and 12 mm, to prevent monochromator heating and also to make the beam size smaller than the sample. The exit slit removes light scattered by the monochromator.

On 9.2, absorption measurements are made in air with the sample and detectors mounted on an optical bench. Because air strongly absorbs soft X-rays (2 to 4 keV), measurements on 3.4 are made under vacuum. In this case, a number of samples are mounted on a manipulator column. Features of transmission and fluorescence experiments, the two techniques used in this work, are described below.

2.2.3. Monochromation

The monochromator consists of two parallel crystals (fig. 2.4), the first of which can be pivoted. The wavelength passed depends on the angle θ between the crystals and the beam according to the Bragg condition

$$n\lambda = 2d\sin\theta \qquad (2.1)$$

where d is the crystal spacing and n is an integer ($n = 1$ for the required fundamental harmonic, $n > 1$ for the undesired higher harmonics). Wavelength is scanned stepwise by rotating the crystal with a stepper motor.

Higher harmonics ($n > 1$) have to be removed because they distort the EXAFS amplitude. Each harmonic has a characteristic "rocking curve", *i.e.* dependence of the light intensity passed by the monochromator on the degree of misalignment of the two crystals. Since rocking curves for higher harmonics are narrower than that of the fundamental, it is possible by introducing a deliberate offset between the two crystals to remove most of the harmonics while still retaining 50% or more of the fundamental.

To achieve this, the orientation of the first crystal is computer-controlled through a stepper motor (for coarse adjustments) and a solenoid acting on a ferrite strip on the crystal (for fine alignment). Because the beam intensity produced by the SRS varies smoothly with energy, a servo system alters the crystal orientation to maintain constant harmonic rejection during the scan. Before the scan, the maximum intensity corresponding to the required degree of

harmonic rejection (usually 50%, but increased if the SRS beam intensity is low) is determined for the energies at the beginning end of the scan. The computer then calculates a servo reference value for each point in the scan to give the required harmonic rejection. During the scan, the servo continually adjusts the crystal offset to match the actual intensity to the reference value. Because thermal loading of the crystals causes a skewed rocking curve, the monochromator is kept to the negative side of the curve while scanning.

2.2.4. Data acquisition

(i). Transmission mode measurements

In transmission mode, absorption is measured by recording the relative attenuation of the beam on passing through the sample. As fig. 2.4 shows, the sample is placed between two ion chambers which measure the intensity of the incident and transmitted light I_0 and I. The chambers are filled with inert gas mixtures so that at the edge energy the I_0 chamber absorbs 20% of the beam, allowing most of the light through but still giving a good reference, and the I chamber absorbs 80%. The output of the chambers is enhanced by Keithley current amplifiers.

These measurements yield a relative absorbtion coefficient μ according to the equation

$$\mu = \ln\frac{I_0}{I} \qquad (2.2)$$

It is not an absolute value because it takes no account of the different transmittance of the ion chambers, variations in amplifier gain and the variability of the energy dependent spectrometer baseline. This is not a problem, however, since these effects are constant, or vary smoothly across a scan, and can be removed by background subtraction. Anyway, it is the modulation in the absorption coefficient and not the absolute value that is of interest in EXAFS.

(ii). Fluorescence mode measurements

Fluorescence measurements are generally made when the absorbing atom is present in low concentrations or the sample is highly absorbing (this is often the case for soft X-ray measurements since most elements have high absorption coefficients at high wavelengths). This is because the measured fluorescence only comes from the absorbing atom, in comparison to transmission measurements which suffer from high background absorption.

It has been shown that fluorescence intensity I_f is a direct measure of the K-shell absorption probability at a particular energy.[9] Therefore, measurement of the ratio I_f/I_0 will yield the relative absorption coefficient μ according to

$$\mu = \frac{I_f}{I_0} \tag{2.3}$$

As shown in fig. 2.4, I_f is measured using a parallel-plate gas proportional fluorescence counter placed at a 90° angle to the beam, while the sample is oriented 45° to both the beam and the fluorescence detector, to minimise detection of scattered and reflected radiation.

(v). Data collection

Data collection is computer controlled. The frequency of measurement across the scan can be varied to give high resolution or fast data collection as required. In these experiments, the absorption edge was recorded at intervals of between 0.2 and 0.5 Å. In the EXAFS region the frequency of measurements was decreased to every 1 and then 2 Å. A typical scan took about 45 minutes, and for each sample three scans were recorded for averaging. On Station 3.4, data was recorded as fluorescence yield versus photon energy. On Station 9.2, data was recorded as absorption or fluorescence yield versus monochromator angle, which was later converted to energy, using a calibration program at Southampton.

2.2.5. Sample preparation

For transmission experiments on Station 9.2, the model compounds - all solid samples - were finely ground and diluted with boron nitride so that the absorbing element was present to about 10 or 15% by weight. The powders were held between windows of cellulose adhesive tape in an aluminium sample holder about 1 mm thick. The foil sample did not require any pretreatment.

On Station 3.4, the powder samples were deposited on aluminium blocks which were mounted on to the manipulator column. To achieve this, the samples were finely ground, mixed with graphite powder (to improve electrical conductivity and reduce charging effects by the X-rays) and turned into a slurry with acetone. The slurry was then dropped on to the block so that after the solvent had evaporated a thin deposit of the powder sample was left. Foil samples were glued straight on to the aluminium blocks.

2.3. References

1. K. Yoshida and G.A. Somorjai, *Surf. Sci.* 75 (1978) 46.

2. R.G. Musket, W. McLean, C.A. Colmenares, D.M. Makowiecki and W.J. Siekhaus, *Appl. Surf. Sci.* 10 (1982) 143.

3. H.J. Grabke, W. Paulitschke, G. Tauber and H. Viefhaus, *Surf. Sci.* 63 (1977) 377.

4. H.J. Grabke, *Mat. Sci. Engineering* 42 (1980) 91.

5. M. Grunze, G. Strasser and O. Elshazly, *J. Vac. Sci. Technol.* A4 (1986) 2396.

6. V.S. Smentkowski, C.C. Cheng and J.T. Yates Jr, *Langmuir* 6 (1990) 147.

7. C.F. Brucker and T.N. Rhodin, *Surf. Sci.* 57 (1976) 523.

8. G.P. Nicholson, *Ph.D. Thesis*, University of Southampton (1991).

9. J. Jakevic, J. Kirby, M. Klein, A. Robertson, G. Brown and P. Eisenberger, *Solid State Commun.* 23 (1977) 679.

3. THEORY

3.1. Temperature programmed desorption (TPD)

3.1.1. Theory and interpretation

Temperature programmed desorption (TPD) spectroscopy provides a simple method for characterising adsorption. In the experiment, the surface is heated at a comparatively slow rate (typically from 1 to 15 K s^{-1}) so desorption is much slower than the pumping speed and therefore the pressure in the chamber is proportional to the desorption rate. The basic mathematical analysis of thermal desorption spectra has been treated by Redhead.[1]

The temperature dependence of the desorption rate of some adsorbate from a surface is given by an Arrhenius-type equation

$$-\frac{dn}{dt} = n^m \nu_m \exp(-E_d/RT) \tag{3.1}$$

where n is the surface density of adsorbate, ν is the frequency factor, m is the order of the desorption reaction, E_d is the activation energy for desorption, R is the gas constant and T is the temperature. The maximum of a desorption peak (T_{max}) corresponds to the maximum desorption rate and consequently, diagnostic expressions can be found by setting $d^2n/dt^2 = 0$ at T_{max}. For first-order reactions ($m = 1$) this gives

$$\frac{E_d}{RT_{max}^2} = \nu_1 (dt/dT) \exp(-E_d/RT_{max}) \tag{3.2}$$

and for second order reactions the expression is

$$\frac{E_d}{RT_{max}^2} = 2 n_{max} \nu_2 (dt/dT) \exp(-E_d/RT_{max}) \tag{3.3}$$

where n_{max} is the surface density at T_{max}.

For a first-order reaction, E_d can be approximated from eq. (3.2) using measured values of T_{max} and dt/dT (the inverse of the heating rate), and a guess for the value of the frequency factor ν_1 (alternatively, ν_1 is determined by repeating experiments at different heating rates). For a second-order reaction, eq. (3.3) predicts that E_d can be found from the coverage

dependency of T_{max} through a plot of $\ln(\nu_{max} T_{max}^2)$ versus $1/T_{max}$ which yields E_d/R as the slope. In practise, however, difficulties such as overlapping peaks and the coverage dependency of ν and E_d can hinder or prevent the determination of E_d.

Equations (3.2) and (3.3) suggest that the coverage dependency of T_{max} is a test for the order of the desorption reaction: for first-order reactions there is no dependency while for second-order reactions T_{max} decreases as coverage increases. However, shifts in T_{max} are also seen if ν or E_d vary with coverage, leading to false conclusions. Desorption peak shape (when it is clear and well resolved) has also been shown[1,2] to be a diagnostic for reaction order. For example, the peaks for a second-order reaction are predicted to be symmetric about T_{max}.

The area under a TPD curve is proportional to the coverage of the desorbate. The TPD area at saturation can often be calibrated from other measurements (low energy electron diffraction, for example) allowing the conversion of relative area to absolute coverage. Again, overlap with other peaks can interfere with the analysis.

3.2. Low energy electron diffraction (LEED)

3.2.1. Theory and interpretation

Through the determination of the diffraction pattern, the technique of low energy electron diffraction (LEED) readily provides information about the two-dimensional periodicity of atoms at a surface. The exact locations of the atoms can also be determined by the analysis of diffracted beam intensities, although this procedure is particularly difficult and is not considered in this section.

The surface sensitivity of LEED arises because both the elastic scattering cross-section and the probability of undergoing an energy loss mechanism are high for low energy electrons (20-200 eV). Consequently, the mean free path for inelastic scattering is short (typically about 5 Å) and elastically backscattered electrons, which contain the structural information, only emerge from the first two or three layers of a surface structure. In the experiment, a monoenergetic, collimated beam of electrons is incident normal to the surface. Backscattered electrons drift towards a fluorescent screen, passing through a grid at a potential that retards all electrons other than those which have been elastically scattered before being accelerated by a large positive potential (5 kV) onto the screen.

The LEED diffraction pattern is simply a projection of the reciprocal net of the surface which is directly and simply related to the real space surface net. The spatial relationship of the reciprocal net vectors $\mathbf{a}^*$ and $\mathbf{b}^*$ to the real net vectors $\mathbf{a}$ and $\mathbf{b}$ is given by

$$\mathbf{a}^* \perp \mathbf{b} \quad \textit{and} \quad \mathbf{b}^* \perp \mathbf{a} \tag{3.4}$$

while the lengths a^* and b^* of the reciprocal space vectors are related to the lengths a and b of the real space vectors, and the angle γ between them, by

$$a^* = \frac{1}{(a \sin\gamma)} \quad \textit{and} \quad b^* = \frac{1}{(b \sin\gamma)} \tag{3.5}$$

The Ewald sphere construction, shown in fig. 3.1, provides a useful geometric representation of the diffracted beam vectors for a given system. The construction is superimposed on an array of infinitely long reciprocal lattice rods (separated by a distance of $1/d$, where d is the

lattice spacing), which are perpendicular to the surface and pass through the points of the reciprocal net.

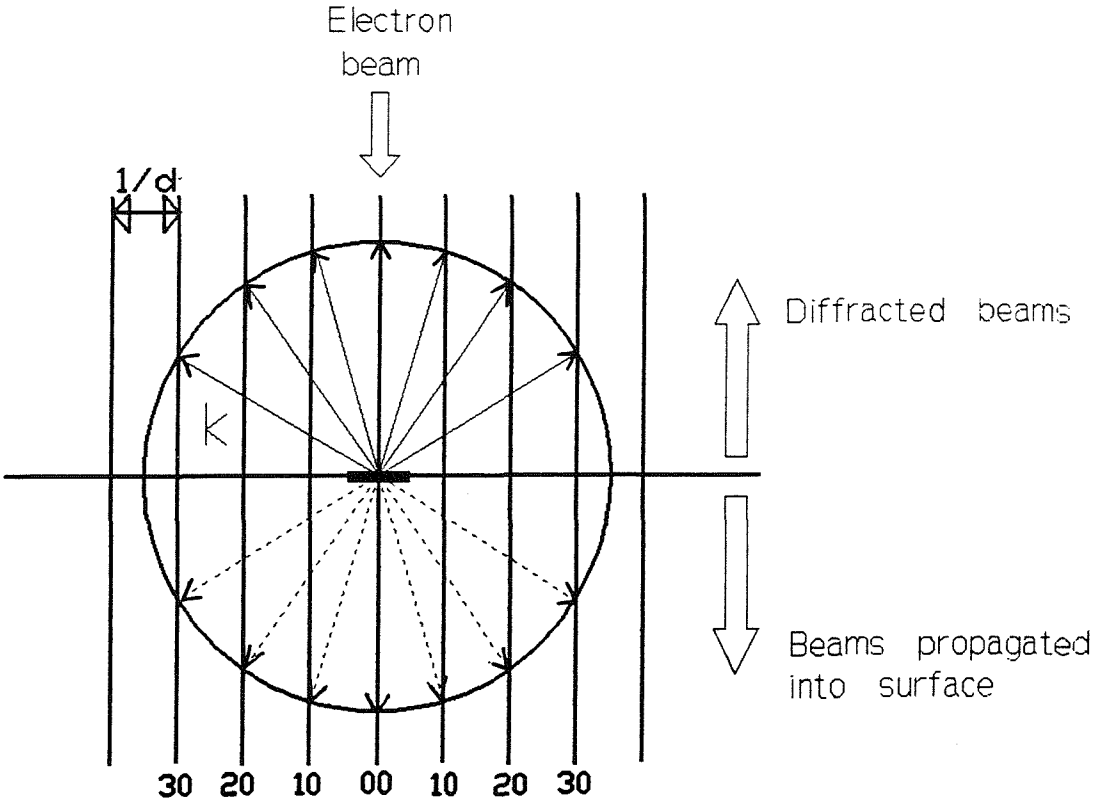

Fig. 3.1. Ewald sphere construction.

The incident electron is represented by a wavevector **k** equal in size to $1/\lambda$, where λ is the de Broglie wavelength of the electron given in Angstroms which can be determined from the electron energy E expressed in eV, according to the relationship

$$\lambda \approx \sqrt{\frac{150.4}{E}} \tag{3.6}$$

The sphere is traced out by the tip of the wavevector **k** and positioned so that the surface of the sphere touches the origin of the reciprocal net, while the angle of the radius ($1/\lambda$) relative to the lattice rods is equal to the incident angle of the electron (measured relative to the surface normal).

The centre of the sphere represents the origin of real space, and therefore the position of the sample, and a line drawn from the centre to any point where the sphere passes through a lattice rod represents a diffracted beam vector **k'**. Each lattice rod gives rise to a pair of

diffracted beams, although obviously only the backscattered beam need be considered. In a typical LEED experiment, the electron beam is incident normal to the surface and the origin of the sphere, representing the sample, lies on the 00 lattice rod. Because the hemispherical LEED screen is also centred on the sample it can be readily seen that the diffraction pattern is simply a projection of the reciprocal net with a scaling factor given by **k**. Increasing beam energy corresponds to an increase in the wave vector and therefore the radius of the sphere.

At normal incidence the diffraction pattern shows the point group symmetry of the substrate surface. Unambiguous determination of the point group symmetry of overlayer structures is frequently difficult. It is not possible to detect reduced symmetry in the arrangements of atoms relative to the surface within the unit mesh, meaning that the adsorption site cannot be determined. However, reduction in the point group symmetry of the mesh of an overlayer structure can be identified from the appearance of superposition patterns from different structural domains (a surface structure is typically broken into small and misaligned domains of perfect periodicity). When the average domain size is 100 Å or less, coherent interference between electrons scattered from adjacent domains gives rise to such effects in the diffraction pattern as spot broadening, spot splitting, and streaking. The presence of glide symmetry at the surface can be identified by characteristic missing spots.

3.3. Ellipsometry

3.3.1. Introduction

Ellipsometry, which can be defined as the measurement and analysis of changes in the state of polarisation of light due to reflection (or sometimes transmission), is a powerful technique for the study of the optical properties of surfaces and thin films. The theory and practice of ellipsometry originates in the work of Drude[3,4] and Rayleigh[5] (and others) at the end of the Nineteenth century. However, it is only during the last few decades, with the development of fast computers and automated ellipsometers, that ellipsometry has been widely applied.

A number of qualities make ellipsometry an excellent tool for the investigation of thin films, through the determination of refractive index and film thickness. At one extreme, ellipsometry is sensitive to submonolayer coverages of adsorbate[6,7] and at the other it can determine film thicknesses of the order of micrometers. Real time measurements in modern, automated ellipsometers allow the study of film growth kinetics. The technique can also be applied in many different situations because it is non-destructive and works in any optically transparent medium.

Two parameters are measured in ellipsometry: Δ, the relative change in phase, and ψ, the relative change in amplitude, between two orthogonal components of reflected monochromatic light. From these two measurements, two properties of the reflecting surface can be determined. For a clean surface the optical constants can be found. If a transparent (dielectric) film is present, then the refractive index and thickness of the film can also be determined. For an absorbing film, one parameter from three - the refractive index, extinction coefficient, or thickness - has to be known or guessed to determine the other two quantities from measurements of Δ and ψ.

The definitive text on ellipsometry is by Azzam and Bashara[8] and seminal papers in the development of theory, technique and application have been gathered together in a single book, edited by Azzam.[9]

3.3.2. Background

(i). Reflection, refraction and optical constants

With reference to fig. 3.2, the well-known laws of reflection

$$\theta_1 = \theta_2 \tag{3.7}$$

and refraction

$$n_a \sin\theta_1 = n_s \sin\theta_3 \tag{3.8}$$

define the relationship of the angles of incidence θ_1, reflection θ_2 and refraction θ_3, and the refractive indices n_a and n_s of the different media a and s (ambient and reflecting surface).

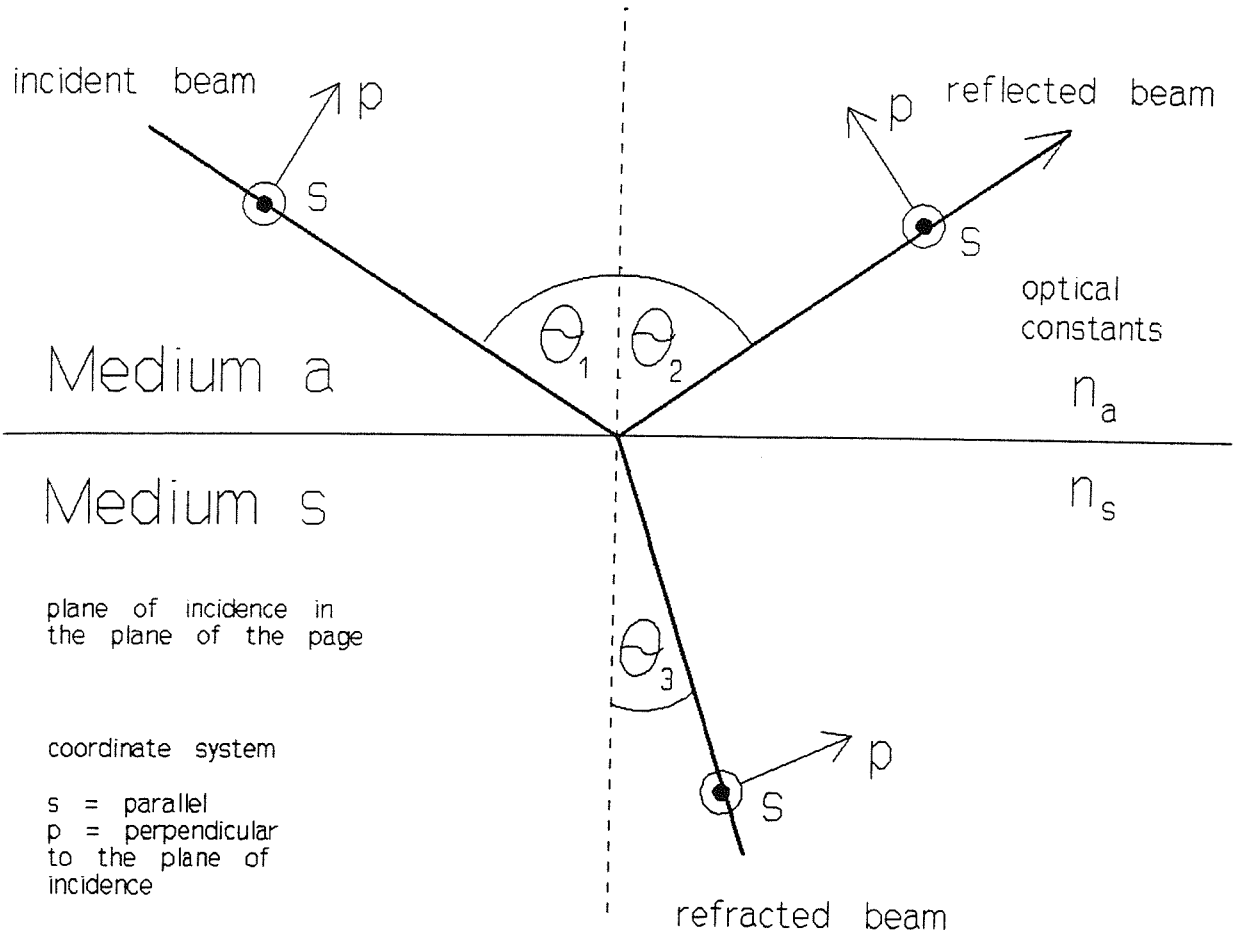

Fig. 3.2. *Geometry of reflection and refraction at a dielectric interface.*

The refractive index n' defines the optical properties of a material. In general, it is given by

$$n' = n - ik \tag{3.9}$$

where n and k are known as the optical constants. For the limiting case of a perfectly transparent medium - an ideal dielectric - the optical constant k, known as the extinction coefficient, is equal to zero. This constant describes the decay of the light's electric field, and for all materials it is finite because there are always impurities in nominally transparent media, such as glass, that will absorb light. In strongly absorbing media, such as metals, k takes comparatively large values.

(ii). Polarised light

Light waves can be described as in-phase oscillations of the mutually perpendicular electric and magnetic field strength vectors, propagated in a transverse direction. Polarisation refers to the time dependent behaviour of the (by convention) electric vector E in space. By resolving E into a pair of orthogonal components (E_x and E_y), perpendicular to the direction of propagation, the state of polarisation can be defined by the phase shift (δ) between the two components, and the ratio of the amplitudes of the two components (E_x/E_y).

Elliptical polarisation is the general state of polarised light, where the locus of E traces a helix through space (describing an ellipse when projected onto a plane perpendicular to the propagation direction). The relative amplitude E_x/E_y determines the elipticity, while the phase shift δ between the two components determines the orientation of the ellipse and the sense of rotation of E (when δ is positive, the rotation is seen as clockwise when looking into the beam, and *vice versa*). The states of linear and circular polarisation are effectively special cases of elliptical polarisation, where for linearly polarised light $\delta = 0^\circ$ or 180°, and for circularly polarised light $\delta = \pm 90^\circ$ *and* $E_x = E_y$. Unpolarised (or natural) light can be seen as elliptical vibrations where δ, E_x and E_y are continually and randomly changing.

When discussing the interactions of polarised light with surfaces, the components of the electric vector of the incident, reflected and transmitted (or refracted) light are chosen to lie parallel and perpendicular to the plane of incidence and are denoted by the subscripts p and s, respectively. The coordinate system used in this discussion is shown in fig. 3.2.

3.3.3. Basic equation of ellipsometry

The change in polarisation state on reflection is characterised by the amplitude reflection coefficients for the *p* and *s* components, r_p and r_s, respectively (they are generally different). These complex coefficients represent the ratio of the complex amplitudes of the reflected and incident electric vectors (E_r and E_i, respectively) and are given by

$$r_p = \frac{E_{rp}}{E_{ip}} \tag{3.10}$$

$$r_s = \frac{E_{rs}}{E_{is}} \tag{3.11}$$

Each coefficient can also be written in an exponential form, which separates the ratio of the real amplitudes of the reflected and incident light ($|r| = |E_r|/|E_i|$) and the phase difference on reflection (δ), as

$$r_p = |r_p| \exp(i\delta_{rp}) \tag{3.12}$$

$$r_s = |r_s| \exp(i\delta_{rs}) \tag{3.13}$$

Ellipsometry determines the ratio of these reflection coefficients for the *p* and *s* components (r_p/r_s). This complex ratio, designated ρ, is related to the measured ellipsometric angles Δ and ψ in what is often known as the basic equation of ellipsometry

$$\rho \equiv \frac{r_p}{r_s} = (\tan\psi) \exp(i\Delta) \tag{3.14}$$

Using the exponential formulations of r_p and r_s, (eqs (3.12) and (3.13)), the measurable ellipsometric angles ψ and Δ can be defined by

$$\tan\psi = \frac{|r_p|}{|r_s|} \tag{3.15}$$

$$\Delta = \delta_p - \delta_s \tag{3.16}$$

3.3.4. Reflection from clean surfaces: the Fresnel equations

Electromagnetic theory shows that the reflection coefficients r_p and r_s for a clean surface can be related to the angles of incidence (θ_1) and reflection (θ_2) and the refractive indices of the surface (n_s) and the ambient medium (n_a) by the Fresnel equations

$$r_p = \frac{(n_a\cos\theta_2 - n_s\cos\theta_1)}{(n_a\cos\theta_2 + n_s\cos\theta_1)} \tag{3.17}$$

$$r_s = \frac{(n_a\cos\theta_1 - n_s\cos\theta_2)}{(n_a\cos\theta_1 + n_s\cos\theta_2)} \tag{3.18}$$

The optical constants of a clean surface can then be found by measuring the ellipsometric ratio ρ at some angle of incidence θ_1 and using

$$n_s = n_a\tan\theta_1\left(\frac{1 - 4\rho}{(1 + \rho)^2}\sin^2\theta_1\right)^{\frac{1}{2}} \tag{3.19}$$

which is obtained by substituting the *Fresnel reflection coefficients* r_p and r_s, eqs (3.17) and (3.18), into the basic equation of ellipsometry, eq. (3.14).

Generally, the polarisation state of light is changed on reflection because the Fresnel coefficients are different for the *p* and *s* components (the exception is when the incident light is *p* or *s* plane polarised). The effect of reflection on the amplitude and phase of light, as predicted by the Fresnel equations, is illustrated in fig. 3.3. This shows the qualitative

variation of $|r_p|$ and $|r_s|$ (the ratios of the amplitudes of the reflected and incident light) and δ_p and δ_s (the phase shifts) with angle of incidence θ_1 for reflection from glass and metal - as examples of (near) transparent and strongly absorbing media, respectively - when light is incident from vacuum.

For both glass and metal, $|r_s| > |r_p|$ (meaning that the *p* component experiences a proportionally greater amplitude attenuation) at all incident angles except 0° or 90° where symmetry differences are lost. For both materials, $|r_s|$ increases with increasing θ_1, although for metals, $|r_s|$ is comparatively higher (manifesting as a higher reflectivity) at low angles of incidence. In contrast, $|r_p|$ goes through a minimum with increasing θ_1 before reaching a maximum at grazing incidence (90°). For non-absorbing glass, this minimum occurs at the Brewster angle (ϕ_B), where all of the *p* component of the incident light is refracted and none is reflected. It can be shown from eqs. (3.8) and (3.18) that when $r_p = 0$, $\tan \phi_B = (n_a/n_s)$. At a metal surface, the minimum in $|r_p|$ does not reach zero (meaning that some of the *p* component is reflected) and is found at an angle known as the pseudo-Brewster angle that depends on *k* (the extinction coefficient).

On reflection from the glass surface, $\delta_s = 180°$ for all angles of incidence, while $\delta_p = 360°$ for all incident angles up to the Brewster angle where it abruptly changes to 180°. The behaviour of the phase shifts at the surface of the metal is more complicated.

The corresponding qualitative variation of the ellipsometric parameters Δ and ψ with angle of incidence is also shown in fig. 3.3. On reflection from glass, Δ drops discontinuously (from 180° to 0°), while ψ reaches a minimum, at the Brewster angle. For metals, Δ and ψ show similar but more gradual changes at the pseudo-Brewster angle, the sharpness of the change increasing as *k* decreases.

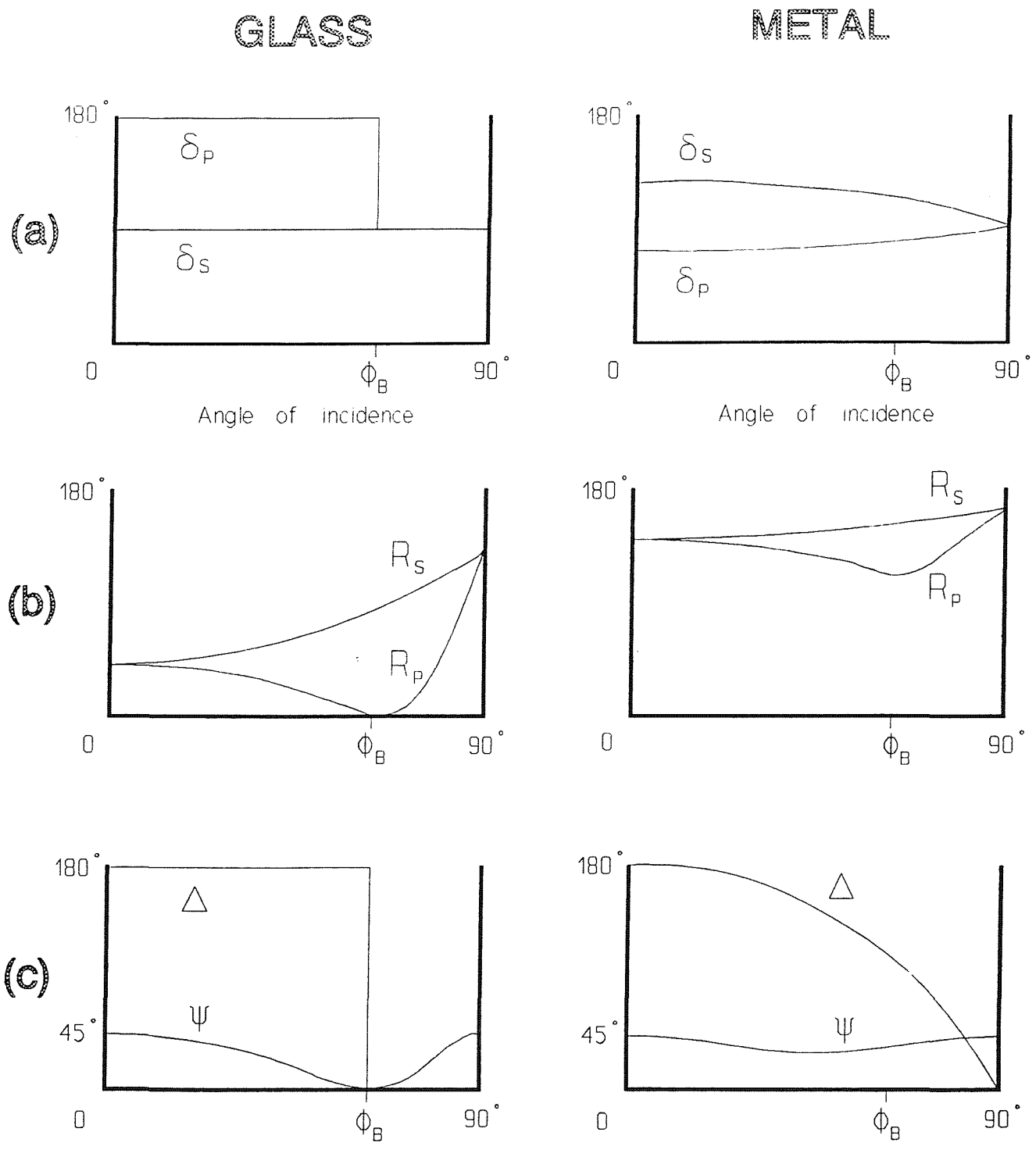

Fig. 3.3. *Reflection from clean glass and metal surfaces as a function of incident angle. (a)* $|r|$*, the real relative amplitudes. (b)* δ*, the phase shift. (c)* Δ *and* ψ*, the ellipsometric angles.*

3.3.5. Reflection from film covered surfaces: the Drude equations

The classic description of the reflection coefficients for film covered surfaces was developed by applying electromagnetic theory to an idealised model, illustrated in fig. 3.4, where the boundaries of the film are parallel and planar and the three media (ambient, film and substrate) are heterogeneous and optically isotropic.

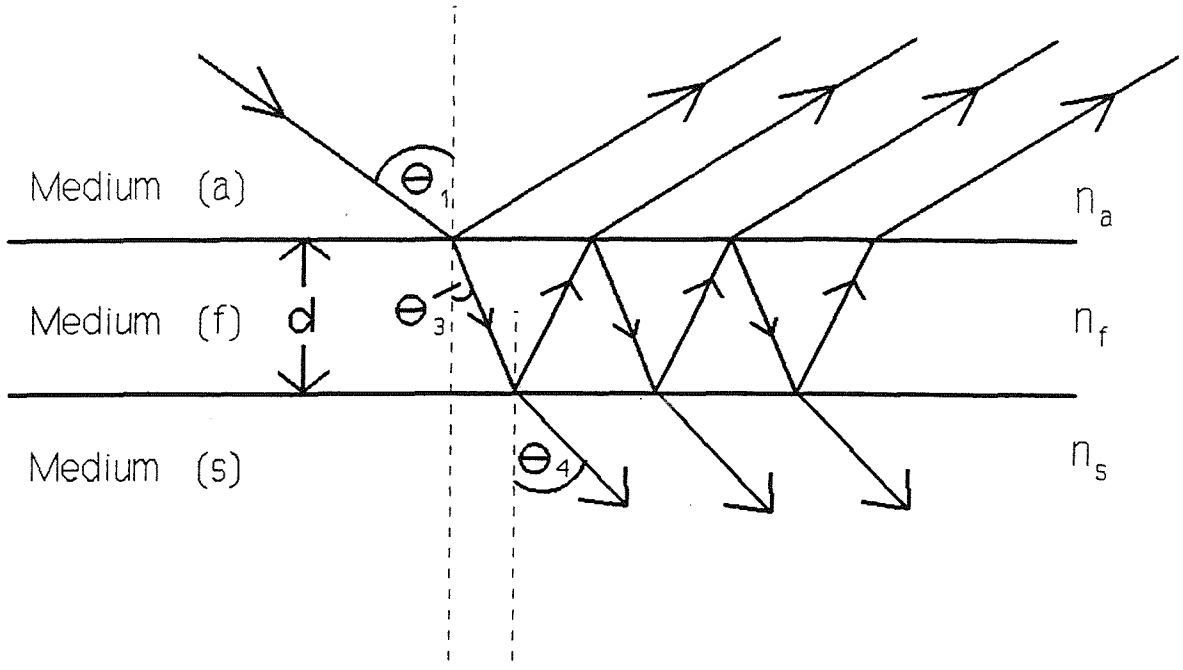

Fig. 3.4. Multiple reflections at an idealised film covered surface.

The influence of the film on the polarisation state can be described by the multiple reflections representation, where light entering the film is considered to repeatedly reflect at both boundaries of the film, with a corresponding change in Δ and ψ (in a strongly absorbing medium, the beam is quickly attenuated). Consequently, the polarisation state of the measured beam contains a fixed contribution from reflection at the top surface of the film and a complicated thickness-dependent contribution from multiple reflections within the film.

The solution is provided by the Drude equations, where the reflection coefficients R_p and R_s for a film covered surface depend on the reflection coefficients of the ambient-film and film-substrate interfaces, r_1 and r_2 respectively and the phase delay β in the following way

$$R_p = \frac{E_{rp}}{E_{ip}} = \frac{r_{1p} + r_{2p}\exp(-i\beta)}{1 + r_{1p}r_{2p}\exp(-i\beta)} \tag{3.20}$$

$$R_s = \frac{E_{rs}}{E_{is}} = \frac{r_{1s} + r_{2s}\exp(-i\beta)}{1 + r_{1s}r_{2s}\exp(-i\beta)} \tag{3.21}$$

The phase delay β for a film of refractive index n_f is given by

$$\beta = \frac{2\pi}{\lambda} d_f n_f \cos\theta_f \tag{3.22}$$

where d_f is the film thickness, θ_f the complex angle of refraction in the film, and λ the wavelength of light in vacuum.

Using the Drude model, the basic equation of ellipsometry for film covered surfaces becomes

$$\rho = \frac{(r_{1p} + r_{2p}\exp(-i\beta)(1 + r_{1s}r_{2s}\exp(-i\beta)}{(r_{1s} + r_{2s}\exp(-i\beta)(1 + r_{1p}r_{2p}\exp(-i\beta)} = (\tan\psi)\ \exp(i\Delta) \tag{3.23}$$

where expressions for r_1 and r_2 in terms of refractive indices and incident angles can be found using the Fresnel equations, eqs. (3.17) and (3.18).

In a typical ellipsometric investigation of thin film growth, the wavelength (λ), angle of incidence (θ_1) and refractive index of the ambient vacuum (n_a) are fixed and well known, while the refractive index of the substrate (n_s) can be determined by careful experiment. The variation of ρ with time is then measured during film growth so that each data point is associated with three measurements: time, Δ, and ψ. The refractive index of the film n_f (which may be complex) and the film thickness can then be found by analysis of plots of Δ versus ψ, where the time coordinate runs along the path of the curve. The Δ-ψ trajectories of dielectric films typically follow closed paths where the values repeat after an increment of 2π in the phase delay β, which is defined in eq. (3.22). Absorbing films increasingly screen the effect of the substrate as they grow so that the trajectory approaches a point characteristic of the bulk film material. The experimental Δ-ψ trajectories can then be fitted with theoretical curves, using eq. (3.23) for example, which are derived for some optical model of the system.

3.4. Extended X-ray Absorption Fine Structure (EXAFS) spectroscopy

3.4.1. Introduction

Extended X-ray Absorption Fine Structure (EXAFS) is the name given to the oscillations in X-ray absorption as a function of photon energy on the high energy side of an absorption edge, which are detected for all materials, except monatomic gases. The basic explanation of the phenomenon as arising from the modification of the final state of an ejected photoelectron has been known for over fifty years[10,11] but it was only during the 1970s that it became possible to usefully interpret the phenomenon in terms of atomic structure.[12]

In EXAFS spectroscopy the absorption spectrum is usually determined by measuring the absorption coefficient μ (or the product of μ with the sample thickness x) as a function of photon energy. The absorption coefficient is found by measuring the ratio of the intensities I_0 and I of the incident and transmitted X-ray beams, respectively, according to the equation

$$\mu x = \ln\frac{I_0}{I} \tag{3.24}$$

Interest usually centres on measurement of absorption at K-edges, which arise from the ejection of electrons from the 1s state, and L-edges, which arise from the excitation of 2s (L_I) and 2p (L_{II}, L_{III}) electrons. A typical absorption spectrum is shown in fig. 3.5.

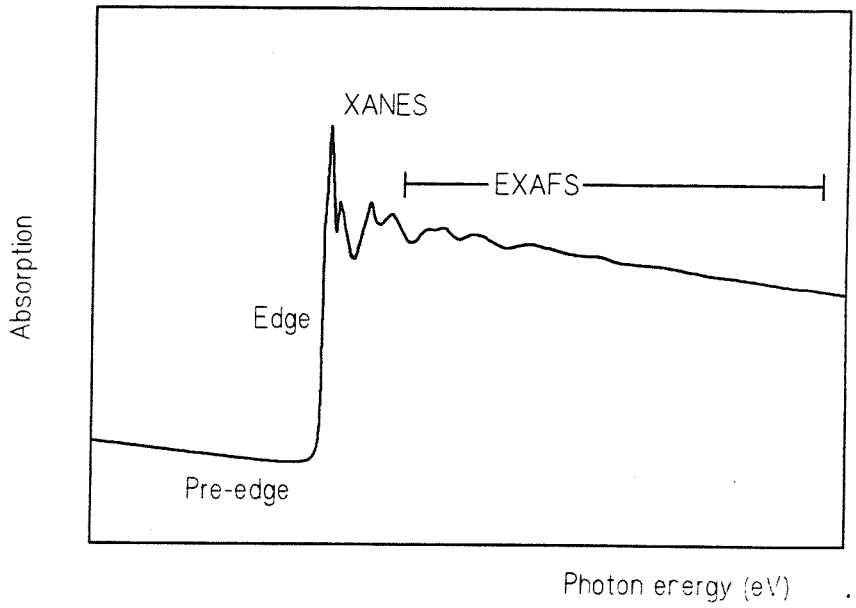

Fig. 3.5. A typical EXAFS spectrum.

The absorption edge is the large abrupt increase in μ corresponding to the ejection of a core electron from an atom. The relative position of the edge is related to the oxidation state of the atom. Fine structure at the absorption edge is associated with the excitation of the core electron into bound states (features before the edge) and complex backscattering effects (seen up to about 30 eV beyond the edge). This is known as X-ray Absorption Near Edge Structure (XANES) and contains information about site symmetry, local geometry and the type of neighbouring atoms, although analysis is difficult.

The EXAFS region typically extends from about 40 to 1000 eV above the absorption edge. Analysis of EXAFS yields a one-dimensional radial distribution curve which can be fitted with structural models to reveal the types of atom surrounding the absorbing atom, their number (with an error of about 20%) and interatomic distances (to about 1.5%) in the immediate environment, up to a distance of about 6 Å. With the availability of synchrotron radiation and improved computing power, the extraction of useful structural information from EXAFS spectra is now comparatively straightforward. Although EXAFS spectroscopy is not as accurate as other structural methods (X-ray diffraction, for example) and cannot determine the angular relationship between atoms, the ability to study structure about different elements within the same material, and the wide applicability to different systems (from liquids to surfaces) makes it a powerful tool. It has also proved singularly useful for characterising the local structure of disordered materials or biological systems.

3.4.2. Theory

The probability that an atom will absorb an X-ray photon of sufficient energy to eject a core electron depends on both the initial and final states of that electron. While the initial state corresponds to the core level within the atom, the final state, *i.e.* the ejected photoelectron, can be represented as an outgoing spherical wave, centred on the absorbing atom. The photoelectron wave vector k, in this case, is defined as

$$k = \sqrt{\frac{2m}{\hbar^2}(E - E_0)} \tag{3.25}$$

where m is the mass of the electron, E is the incident photon energy, E_0 is the threshold

energy of the edge and ħ is equal to Planck's constant h divided by 2π. The wavelength of the spherical wave is then given by

$$\lambda = \frac{2\pi}{k} \tag{3.26}$$

For isolated atoms, the absorption coefficient μ decreases smoothly with increasing energy (matter is less likely to absorb a higher energy photon). In the presence of neighbouring atoms, the outgoing photoelectron wave is backscattered, with the result that coherent interference between the outgoing and incoming (backscattered) waves modifies the final state wave function. It is this interference effect that causes EXAFS, *i.e.* the sinusoidal variation in the absorption coefficient μ on top of the atomic-like decay, as the X-ray photon energy is increased. The amplitude of the EXAFS oscillations depends on the type and bonding of the neighbouring atoms while the frequency depends on the distance of the neighbours from the absorbing atom.

This short-range order model forms the basis of the single-electron single-scattering theory of EXAFS, which provides the theory for data analysis in EXAFS spectroscopy. Theoretically, the EXAFS oscillations can be related to various factors by the interference function $\chi(k)$ which gives the variation of the relative modulation χ of the absorption coefficient with the photoelectron wave vector k. The experimental EXAFS oscillations in energy-space $\chi(E)$ can be extracted from the absorption spectrum by subtracting the smooth, atomic-like background adsorption μ_0 from the total variation of μ, and normalising the difference to μ_0

$$\chi(E) = \frac{\mu - \mu_0}{\mu_0} \tag{3.27}$$

$\chi(E)$ must be converted to give $\chi(k)$, using eq. (3.26), before it can be related to structural parameters.

The interference function $\chi(k)$ has been formulated in several ways, within the terms of the single-electron single-scattering theory.[12-17] The following basic formulation has been derived by Sayers *et al.*[12] for the excitation of an s state (K or L_I edge) in a system where the sample orientation is spherically averaged. It gives $\chi(k)$ as the summation of individual waves over

all atoms in the vicinity of the absorbing atom according to the following equation

$$\chi(k) = \sum_j A_j(k) \sin(2kR_j + 2\delta_1(k) + \alpha_j(k)) \tag{3.28}$$

where $A_j(k)$ the amplitude in k space for each wave is given by

$$A(k) = \frac{N_j S_j |f(k)| \exp[-2\sigma_j^2 k^2]\exp[-2R_j/\lambda_j(k)]}{kR_j^2} \tag{3.29}$$

For each atom of the jth type (of which there are N_j) found at a distance R_j from the absorbing atom, the EXAFS oscillations $\chi(k)$ depend on the backscattering amplitude $f_j(k)$ for the atom (a property that primarily depends on the atomic number) along with:

1. *A distance dependency for the backscattered amplitude*, given by $1/kR_j^2$;

2. *Amplitude losses due to many-body effects at the absorbing atom*, given by the amplitude reduction factor S_j;

3. *Amplitude losses due to inelastic scattering*, approximated by the factor $\exp[-2R_j/\lambda_j(k)]$ which depends on the ratio of the distance travelled ($2R_j$) to the inelastic mean free path of the electron ($\lambda_j(k)$);

4. *A smearing effect due to thermal vibration and static disorder* (the first assumed to be a harmonic vibration, the second assumed to have a Gaussian distribution), quantified by the factor $\exp[-2\sigma_j^2 k^2]$ where σ_j is a Debye-Waller type parameter which can generally be separated into two components σ_{vib} and σ_{stat} for the two effects, according to the relationship $\sigma^2 = \sigma_{vib}^2 + \sigma_{stat}^2$; and,

5. *Phase shifts experienced by the photoelectron wave.* The distance-dependent phase shift $2kR_j$ is found after the photoelectron wave has travelled from the absorbing atom to the backscattering atom (at a distance R_j) and back again. In addition there are the phase shifts $\Delta_1(k)$ and $\alpha_j(k)$ due to the interaction of the photoelectron with the potential of the absorbing atom and backscattering atoms, respectively. $\Delta_1(k)$ is experienced twice as the photoelectron wave leaves and returns to the central atom. Together these phase shifts give rise to, and determine the frequency of, the sinusoidal EXAFS oscillations.

Eq. (3.28) is developed from single-scattering theory and is widely applicable because multiple scattering processes often have no effect. This is because long path lengths are usually involved in multiple scattering processes giving rise to oscillations in k space that have high frequency (through $\sin(2kR)$) and low amplitude (through $1/R^2$) and which tend to cancel out. However, multiple scattering can become important when atoms are arranged co-linearly. In this case, the outgoing photoelectron is forward-scattered by intervening atoms, with a resultant increase in the EXAFS amplitude and a modification of the phase. This effect becomes important for absorbing atoms with bond angles to neighbours of greater than 150°.

3.4.3. EXAFS data reduction

Using the pc-based program PAXAS,[18] the following steps are taken to extract the interference function $\chi(k)$ as a function of k, from the absorption spectrum (μx versus E).

(i). Background subtraction

Glitches are removed before the background subtraction so that they do not interfere with the process. The smooth variation of the pre-edge is fitted with a polynomial curve (usually second order) which is subtracted from the total absorption. The fit curve runs through two points along the pre-edge curve and can be weighted towards the end of the spectrum so that the background-subtracted absorption slopes very slightly downwards beyond the edge. Similarly, the post-edge curve is fitted with a weighted polynomial (up to order 6) to model the smooth atomic-like absorption, which is assumed to pass through the centre of the oscillations. The background-subtracted curve is normalised against the edge jump, defined as the difference between the post-edge polynomial and baseline at the edge. The conversion of E space to k space is achieved using eq. (3.26), where E_0 is chosen as the point on the edge where the first derivative of the absorption is a maximum. To compensate for attenuation of the EXAFS amplitude at high values of k, $\chi(k)$ is multiplied by k^3 (or some other power n) to give in general the weighted interference function $k^n\chi(k)$. Of course this leads to increased noise. The oscillations in a good $\chi(k)$ curve, suitable for extracting structural information, are characterised as smooth and equally divided.

(ii). Fourier transformation and Fourier filtering

The Fourier transformation of $k^n\chi(k)$ in k-space gives a modified radial distribution function (RDF) $\rho_n(r')$ in distance (r') space

$$\rho_n(r') = \frac{1}{\sqrt{2\pi}} \int_{k_{max}}^{k_{min}} w(k)\ k^n\ \chi(k)\ \exp(i2kr')\ dk \qquad (3.30)$$

where $w(k)$ is a window function which selects the k range to be transformed. The curve of $\rho_n(r')$ gives some indication of the radial distances of atoms from the absorbing centre, but because the phase terms are part of the sine wave argument in eq. (3.28), the peaks in $\rho_n(r')$ are shifted from the true distance by a value of about 0.2 to 0.5 Å, which depends upon the elements involved, the choice of E_0 and the weighting scheme used in the data reduction. Poor background subtraction can result in spurious RDF peaks below 1 Å, which may interfere with data analysis.

Fourier filtering provides a method of simplifying the EXAFS spectrum to make theoretical curve fitting easier. The range of interest in the distance space of the Fourier transform of the $k^n\chi(k)$ spectrum is selected as a smooth window defined by values R'_{min} and R'_{max}. The data in the window is then back-transformed into k space for analysis or refinement. It is especially useful for isolating the EXAFS contribution from a particular shell, which can then be analyzed separately. In general, Fourier filtering provides a way to eliminate noise and residual background. After back-transforming the real peaks, PAXAS can go through an iterative refinement of the parameters used in the post-edge subtraction to minimise the percentage difference between the experimental EXAFS and the back transform.

3.4.4. EXAFS curve fitting analysis

k^3 weighted EXAFS data were analyzed using the EXCURV92[19] program on the Daresbury mainframe. EXCURV92 extracts structural information by comparing experimental data with theoretical spectra calculated for some structural model that can be refined to optimise the agreement. The theoretical spectra are calculated using a modified version of curved wave theory.[20,21]

(i). Phase shifts

Phase shifts are calculated using *ab initio* methods within the EXCURV92 program. They are found by calculating the photoelectron wave function for a particular atomic environment represented by a muffin tin model. In the present work, the atomic potentials for the central (excited) atom and its (non-excited) neighbours were calculated using $X\alpha$ potentials. The resulting phase shifts were verified by fitting model compounds of known structure so that the EXAFS derived interatomic distances and coordination numbers agree with literature values to within $\pm 1.5\%$ and $\pm 20\%$, respectively.

(ii). Parameters

The important parameters used in constructing theoretical models are as follows:

N_s The number of shells in the structural model - each shell consists of a number of identical backscattering atoms at a similar distance;

T_n The atom type for shell n - this defines the phase shifts to be used;

N_n The number of atoms in shell n;

R_n The distance of shell n from the absorbing atom;

A_n The Debye-Waller factor for shell n - defined as $2\sigma^2$, where σ is the root mean square variation in the distance R_n, it should be between 0.003 and 0.03 $Å^2$;

E_0 The magnitude of the photoelectron energy at zero wave vector - it is treated as a variable to correct the E_0 value used for data reduction in the PAXAS program;

VPI The constant imaginary potential used in curved wave theory to describe the lifetime of the photoelectron - it is chemically dependent, and typical values range from -5 to -1 eV; and,

AFAC An energy-independent scaling factor used to describe the reduction in EXAFS amplitude that results from effects of multiple excitations on the centre atom. Once derived for a particular edge, it is kept constant (it is chemically insensitive). Typically, it has values from 0.6 to 0.9.

Initially, these parameters are varied manually with some appropriate structural model in mind to achieve a rough fit of the experimental EXAFS. Parameters are then selected for iteration in a least-squares refinement procedure to improve the fit between theory and

experiment. N_n can be varied but it is often known in advance. *AFAC* is established for a particular atom type, and *VPI* is determined in the initial stages of the analysis so that they can be treated as constants. Typically E_0, R_n and A_n are iterated together.

(iii). Measuring the fit

The difference between the model spectrum $\chi^T(k)$ and the experimental spectrum $\chi^E(k)$ during iteration is constantly monitored until it reaches a minimum whereupon the process is terminated. This difference is characterised by the Fit Index (FI)

$$\mathrm{FI} = \sum_i [k_i^3 \{\chi_i^T(k) - \chi_i^E(k)\}]^2 \qquad (3.31)$$

which is the weighted sum, across all the i points in the spectrum, of the square of the difference between the theoretical and experimental EXAFS.

The Fit Index is not comparable between data sets because it depends on the energy range, number of data points and the magnitude of the EXAFS. To allow comparisons of the quality of fit, the R-factor is also calculated

$$\mathrm{R\text{-}}\textit{factor} = \sum_i [|\chi_i^E(k) - \chi_i^T(k)| / \sigma_i] \times 100\% \qquad (3.32)$$

In this case, the difference between the theoretical and experimental spectra is scaled against the magnitude of the EXAFS.

The quality of the fit is also measured by a reduced χ^2 function

$$\chi^2 = \frac{[\mathrm{FI} \times \mathrm{NIND}]}{[(\mathrm{NIND} - \mathrm{NPARS}) \times \mathrm{N}]} \qquad (3.34)$$

where NIND is the number of independent data points (set by the program it approximately equals $2\Delta k \Delta R/\pi$ where Δk and ΔR are the widths in k and R space, respectively, used in the data analysis) and NPARS is the number of variables refined for the system (NPARS is set by the user and should not exceed NIND).

(iv). Correlated parameters

The parameters that are normally refined separate into two highly correlated sets: those determining the amplitude (N_n, A_n, *VPI*) and those determining phase (E_0, R_n). Refining highly correlated variables together can result in false minima in the FI and so care must be taken. However, E_0 should always be included when interatomic distances are refined. Significant correlations can be found both within and between the two sets as well as between different scattering terms.

EXCURV92 can produce a table of correlation coefficients (ranging from -1 to 1). If the modulus of the coefficient is greater than 0.8 then the correlation is generally too high and confidence in the fit is limited. In this case EXCURV92 can plot contour maps of the FI as a function of the two parameters to check that the refinement has not fallen into a false local minimum. For well-defined parameters the minimum is deep and spherical while for correlated variables, the minimum is shallow and elongated.

(v). Precision of the structural data

When the minimum in the FI is reached, the program returns the final values of the refined parameters along with their statistical deviations. These errors indicate how well-defined a shell is, but they only represent the random error in an EXAFS experiment and not the various systematic errors that can occur in data acquisition and analysis. For Debye-Waller parameters ($2\sigma^2$) statistical error should be less than about $\pm 10\%$, while for interatomic distances it should be less than about ± 0.01 Å.

Realistic estimates for the true error in EXAFS derived structural parameters are, assuming good data, valid phase shifts and well-defined shells, $\pm 1.5\%$ for interatomic distances and $\pm 20\%$ for coordination numbers, where the large error arises because of the inevitable correlations between the various parameters which determine the EXAFS intensity.

Generally, for similar sized backscatterers, the contribution of different shells to the EXAFS can only be resolved if there is a difference of greater than 0.10 Å between their R_n values. If not, then their fitting parameters will be too highly correlated and resolution is not possible

and, in this case, the shells must be considered as one. When the backscatterers are of similar size, then the extracted interatomic distance is less likely to be an exact average of the separate shells.

(vi). Fourier analysis

EXCURV92 can generate Fourier transforms of the experimental and theoretical EXAFS corrected for phase shifts so that the peaks are more representative of the true interatomic distances. Fourier filtration of the data is also possible, to remove noise or to allow curve fitting with simpler models containing fewer distances. For example, shells can be isolated and analyzed if they are well separated. To avoid distortions at the boundaries of the spectrum, the Fourier filtered EXAFS must be truncated at the low and high extremes of k before analysis.

3.5. References

1. P.A. Redhead, *Vacuum* 12 (1962) 203.

2. R.J. Madix, *Cat. Rev., Sci. Eng.* 15 (1977) 293.

3. P. Drude, *Ann. Physik Chemie* 39 (1880) 481.

4. P. Drude, *Ann. Physik Chemie* 36 (1889) 532 and 865.

5. Lord Raleigh, *Phil. Mag.* 33 (1982) 1.

6. G.A. Bootsma and F. Meyer, *Surf. Sci.* 14 (1969) 52.

7. F.H.P.M. Habraken, O.L.J. Gijzeman and G.A. Bootsma, *Surf. Sci.* 96 (1980) 482.

8. R.M.A. Azzam and N.M. Bashara, *"Ellipsometry and Polarised Light"*, (North Holland, Amsterdam, 1977).

9. R.M.A. Azzam (Editor), *"Selected Papers on Ellipsometry"*, (Society of photo-optical instrumentation engineers, Washington, 1991).

10. R. de L Kronig, *Zeit. fur Physik*, 70 (1931) 317.

11. R. de L Kronig, *Zeit. fur Physik*, 75 (1932) 468.

12. D.E. Sayers, E.A. Stern and F.W. Lytle, *Phys. Rev. Lett.* 27 (1971) 1204.

13. E.A. Stern, *Phys. Rev. B* 10 (1974) 3027.

14. E.A. Stern, D.E. Sayers and F.W. Lytle, *Phys. Rev. B* 11 (1975) 4836.

15. C.A. Ashley and S. Doniach, *Phys. Rev. B* 11 (1975) 1279.

16. P.A. Lee and J.B. Pendry, *Phys. Rev. B* 11 (1975) 2795.

17. P.A. Lee, B.K. Teo and A.L. Simons, *J. Am. Chem. Soc.* 99 (1977) 3856.

18. N. Binsted, *"Program for the Analysis of X-ray Absorption Spectra"* University of Southampton (1988).

19. N. Binsted, J.W. Campbell, S.J. Gurman and P.C. Stephenson, EXCURV92 (1992).

20. S.J. Gurman, N. Binsted and I. Ross, *J. Phys. C.* 17 (1984) 143.

21. S.J. Gurman, N. Binsted and I. Ross, *J. Phys. C.* 19 (1986) 1845.

4. PHOSPHORUS AND OXYGEN ON Fe(100): INVESTIGATIONS WITH ELLIPSOMETRY, LEED AND TPD SPECTROSCOPY

4.1. Characterisation of clean Fe(100)

The clean surface of Fe(100), prepared by cycles of Ar^+ sputtering and annealing (described in Sect. 2.1.7), was characterised by low energy electron diffraction (LEED) and the temperature programmed desorption (TPD) spectra of D_2.

4.1.1. Characterisation by LEED

Iron has a body centred cubic structure (the α-Fe or ferrite phase) at temperatures up to 1180 K, thereafter transforming to a face centred cubic (β-Fe or austenite) structure.[1] LEED studies[2-5] have shown that the clean surface of Fe(100) is effectively unreconstructed, although there is a small contraction in the first interlayer spacing of about 1.4 % compared to the bulk.[5] As fig. 4.1 shows, the (100) surface - the second most densely packed after (110) - possesses a square Bravais net described by a square unit mesh of length 2.86 Å (the equivalent bulk value is given[6] as 2.8665 Å).

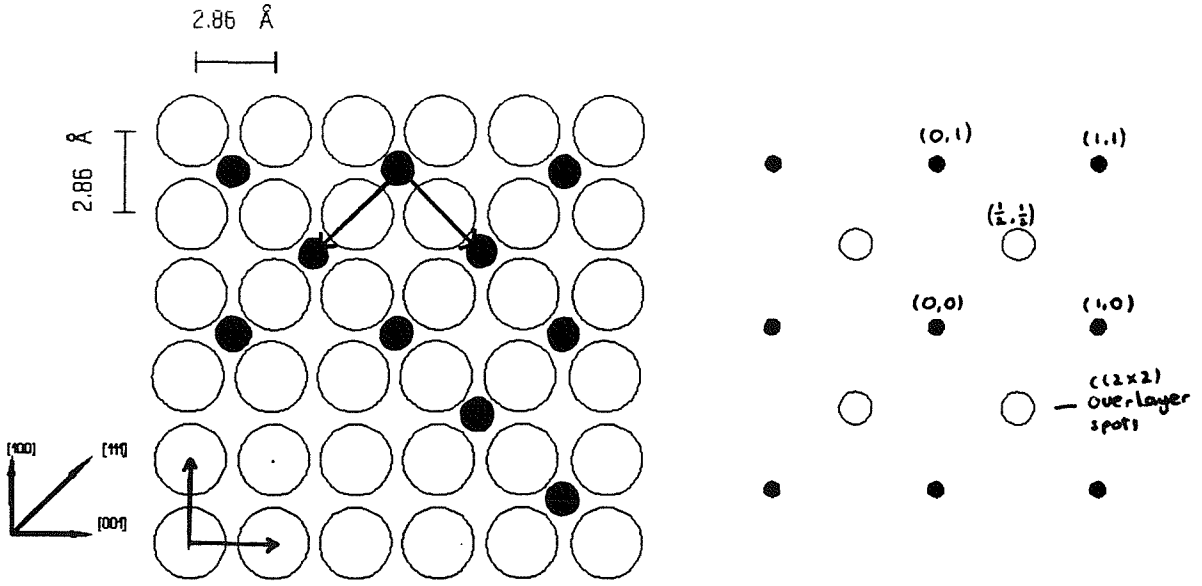

Fig. 4.1. Structure model of the clean Fe(100) surface, including one possible arrangement of the commonly observed c(2x2) overlayer, and LEED pattern (schematic) of Fe(100)-c(2x2).

In the absence of any technique to measure surface composition, LEED was used in the present work to check the surface cleanliness of Fe(100). This is justified by the general

observation that contaminant atoms such as carbon, nitrogen, oxygen and sulphur all form a $(\sqrt{2} \times \sqrt{2})R45^\circ$ overlayer, as denoted by the Wood notation,[7] at low coverages (saturating at 0.5 monolayers).[3,8-13] This structure is more conveniently and more usually described as c(2x2) with respect to a centred unit mesh, as indicated in fig. 4.1. Auger electron spectroscopy measurements have indicated that a c(2x2) pattern is not visible for surface contamination of less than 1% of a monolayer of carbon, oxygen and nitrogen,[14] but can be seen for carbon and nitrogen at concentrations as low as 4% and 9% of a monolayer, respectively,[3] which approaches acceptable levels for a "clean" surface. Because carbon[8] and oxygen (see below) have also been found to give p(1x1) patterns at concentrations of 1 or 2 monolayers, the surface in the present work was also characterised by the adsorption/desorption behaviour of D_2.

In this study, observation of a sharp p(1x1) pattern on a background of low intensity was taken to indicate a clean, well-ordered Fe(100) surface. Extra spots in a c(2x2) pattern (shown schematically in fig. 4.1) were often seen during sample cleaning, although the contaminants could not be identified. Carbon, nitrogen and oxygen were all possibilities, although sulphur was unlikely to be present as the sample was generally kept below temperatures at which sulphur segregates with an appreciable rate.[11]

4.1.2. Characterisation by thermal desorption of D_2

The clean surface of Fe(100) was characterised by a set of reproducible and well-behaved D_2 temperature programmed desorption (TPD) spectra. D_2 was chosen over H_2 for its superior signal-to-noise. Typical spectra, after exposures of between 0.3 and 2000 L at 160 K, are shown in fig. 4.2. No significant changes in the LEED were detected during these experiments.

At all exposures studied, the D_2 spectra show two peaks which are labelled[15] β_1 and β_2. The high temperature β_2 peak, seen at about 440 K for the lowest exposure of 0.03 L, shifts to lower temperature with increasing exposure indicating second-order desorption kinetics. The β_1 peak is centred at about 270 K after an exposure of 0.03 L and does not show a significant temperature shift with increasing exposure, apparently indicating first-order desorption kinetics, although it can be assigned to a recombinative desorption reaction, as will be

discussed below. At all exposures, considerably more D_2 desorbs in the β_1 peak. Features that are apparent in the line shape of the β_1 peaks in fig. 4.2 were not reproducible and probably arise from uneven sample heating or from desorption from the side of the crystal. The TPD spectra approach saturation after exposures of about 200 L. It is likely that the β_2 peak saturates at lower exposures, although overlap with the β_1 peak makes it difficult to see. Spectra were not analyzed to determine desorption energies primarily because peak overlap meant that peak temperatures could not be measured with accuracy.

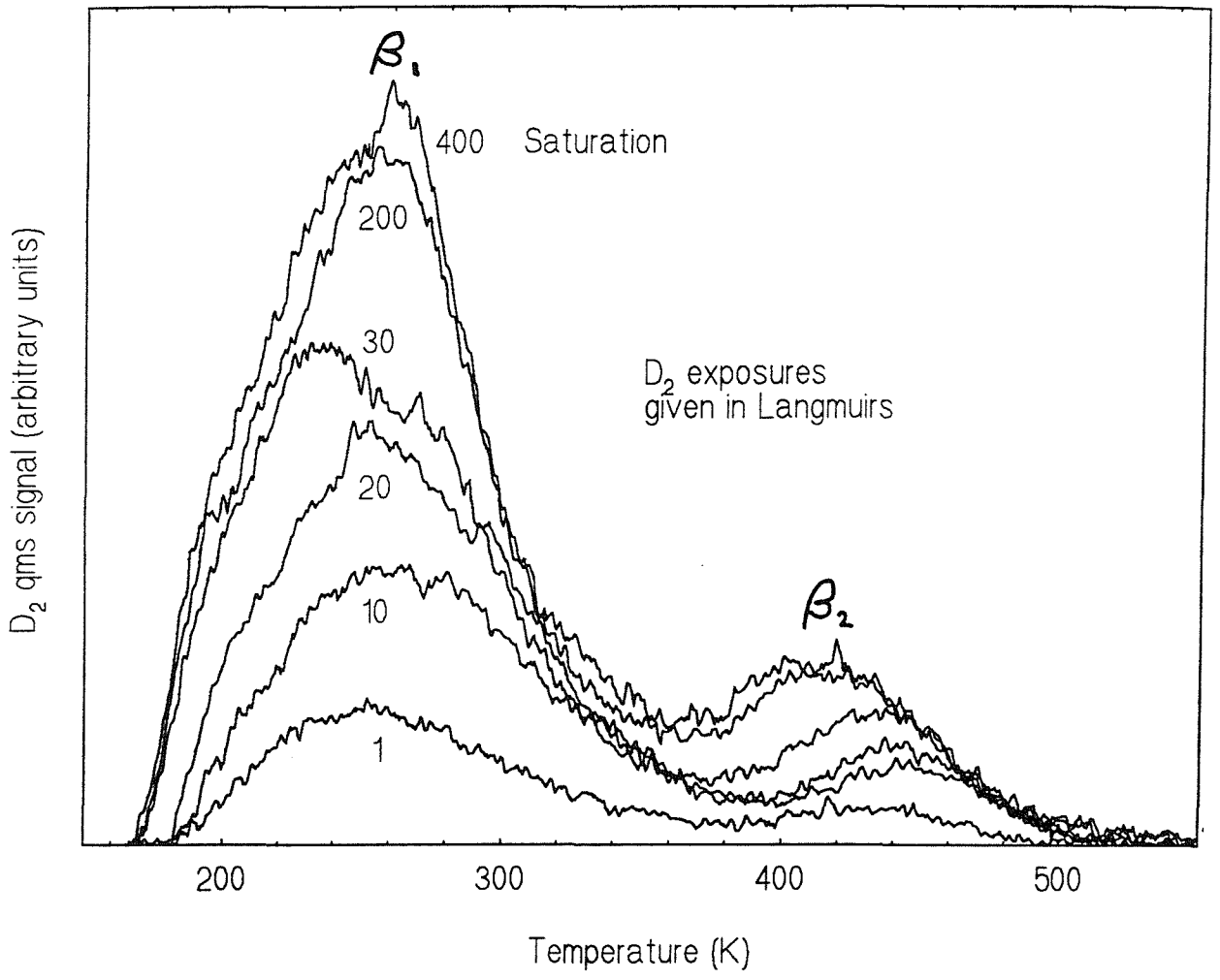

Fig. 4.2. *TPD spectra for recombinative desorption of D_2 from Fe(100) at 160 K, as a function of D_2 exposure. Heating rate 2.3 K s^{-1}.*

To the best of our knowledge, TPD spectra of D_2 on Fe(100) have not been reported previously. However, the results in fig. 4.2 are in good qualitative agreement with TPD studies of H_2 on Fe(100).[15-17] Hydrogen is known[15] to completely dissociate on Fe(100) at temperatures down to 140 K. Bozso *et al.*[15] have assigned the β_2 peak (which saturates first)

to a second-order recombinative desorption reaction, and the β_1 peak to a recombinative desorption process influenced by adatom-adatom repulsion. They assigned the β_1 peak by analogy with results for H_2 on Fe(110) where a similar peak corresponded with the formation of ordered hydrogen overlayers as indicated by LEED, although they found no evidence of such structures on Fe(100).

With a calibration for saturation uptake, a curve of deuterium coverage versus D_2 exposure can be obtained from the relative areas of the D_2/Fe(100) TPD spectra determined in the present work. In studies of H_2 on Fe(100), Benziger and Madix[16] reported a saturation coverage (θ_{sat}) of 0.46 monolayers (ML) at 250 K, but were not explicit as to how they determined this value. Berger and Rendulic,[17] in a molecular beam study, provided a much more reliable estimate of $\theta_{sat} = 1.1 \pm 0.1$ ML at 300 K. Consequently, the coverage versus exposure curve given in fig. 4.3 has been plotted by assuming that $\theta_{sat} = 1$ ML at 170 K. The error in coverage is at worst $\pm$ 5%, arising from uncertainty in the position of the base line during measurement of TPD curve area.

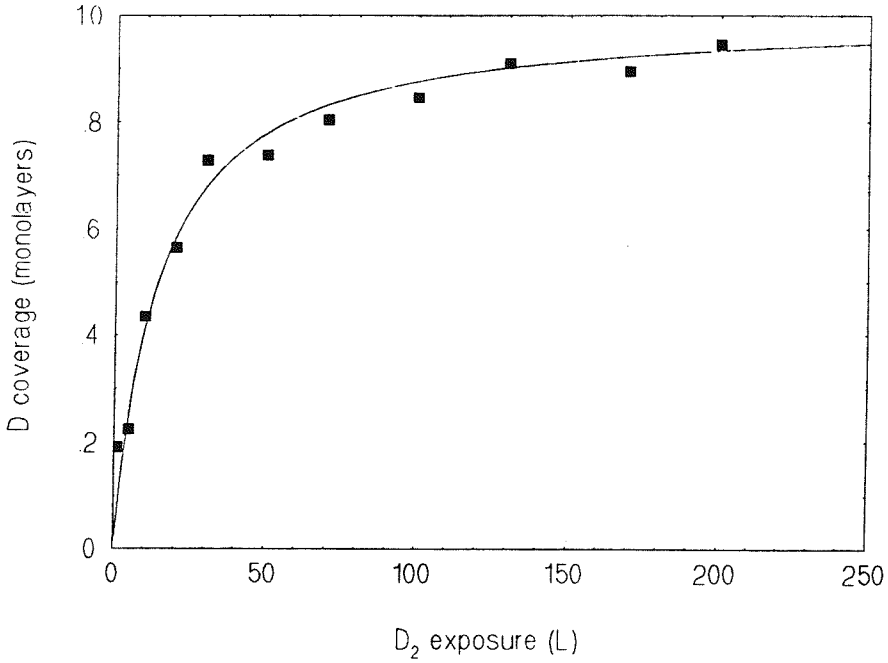

Fig. 4.3. Deuterium coverage as a function of D_2 exposure for adsorption at 160 K. Theoretical curve (solid line) given by eq. (4.1) where $S_0 = 0.07$.

A theoretical fit to the experimental data in fig. 4.3 was found by following the example of Benziger and Madix.[16] For a Langmuir-type dissociative adsorption, the sticking coefficient

S_θ varies with coverage θ as $S_\theta = S_0(1 - \theta)^2$. S_θ is also (approximately) equal to the rate of change of coverage (in monolayers) with exposure L (in Langmuirs). Equating these two expressions for S_θ and solving gives

$$\theta = \frac{S_0}{S_0 + (1/L)} \qquad (4.1)$$

A reasonable fit is obtained with an initial sticking coefficient of $S_0 = 0.07$. For H_2 on Fe(100), Benziger and Madix[16] determined S_0 to be 0.03 in uptake experiments at 250 K while Berger and Rendulic[17] measured S_0 as 0.0015 in molecular beam measurements at 300 K. The method used to determine S_0 in the present work requires too many assumptions and approximations for the value to be considered accurate. However, the good fit to theory does indicate that a simple dissociative adsorption model for D_2 on Fe(100) is valid, at least at higher coverages, as was also found for the adsorption of hydrogen[15] and deuterium[18] on Fe(110) (a recent study[19] suggests that the dependence is more likely somewhere between $(1 - \theta)$ and $(1 - \theta)^2$).

The reproducibility of the data and the good fit to theory indicates that the D_2 adsorption/desorption behaviour described above is characteristic of the clean Fe(100) surface. Deviations from this behaviour were presumed to indicate surface contamination or poor surface ordering. Typically, anomalous spectra showed less D_2 desorption than expected for a particular exposure. Occasionally, the amount of desorption was typical of the exposure used but the higher temperature β_2 peak was much smaller than expected. Although no systematic study of the deviations was made, these observations can be compared with TPD spectra, presented below in fig 4.6, of D_2 dosed onto different coverages of ordered phosphorus overlayers, where similar behaviour was detected.

In practice, D_2 TPD experiments were used in this work to check surface cleanliness during routine sample preparation. LEED observations were made as a final check before beginning PH_3 experiments.

4.2. Phosphorus on iron: Interaction of phosphine (PH_3) with Fe(100) at 160-730 K

4.2.1. Introduction

An understanding of the behaviour of phosphorus and oxygen atoms on iron surfaces may provide an insight into aspects of the chemistry of the protective films formed by phosphorus-containing oil additives in automobile engines. There are comparatively few fundamental studies of phosphorus on iron, and these are concerned almost exclusively with segregation.[13,20-22] To increase knowledge of the surface chemistry of phosphorus on iron, we have investigated the interaction of phosphine (PH_3) with Fe(100), believed to be the first time that this system has been studied, using ellipsometry, low energy electron diffraction and thermal desorption spectroscopy.

(i). Literature review: Adsorption of PH_3 on transition metals

The surface chemistry of PH_3, and its analogues, on transition metals is largely unexplored. To the best of our knowledge, the only published work on the surface chemistry of PH_3 on iron is that of Hedge and White[23] who made a study of adsorption on a polycrystalline surface at 100 K. Using TPD and Auger Electron Spectroscopy they found that PH_3 adsorbed both molecularly and dissociatively at 100 K, the dissociation being irreversible. Other workers[24] studied the molecular adsorption of a related molecule PF_3 on Fe(110) at 200 K using photoelectron spectroscopy and showed that the chemisorption bond resembled bonding in a Fe-PF_3 complex. PH_3 adsorption has also been studied on other transition metal surfaces including Rh(100),[25] Pt(111),[26] Ni(100)[27] and Ag(111).[28] These investigations were conducted at low temperature (100 K or less), and in all cases molecular adsorption was detected.

(ii). Literature review: Segregation of phosphorus to iron single crystal surfaces

Some indication of the chemistry of phosphorus atoms on iron single crystal surfaces is given by two recent studies of phosphorus segregation. In an electron spectroscopic study of high temperature (about 600 K) segregation at a Fe(100) surface, Egbert and Panzner[13] showed the presence of chemisorbed phosphorus at the surface and a different phosphorus species,

with a bonding state like P in Fe_3P, in the subsurface. The concentration of the phosphide-like phase depended on the levels of phosphorus in the bulk. Similarly, Arabczyk *et al.*[29] observed the formation of an iron phosphide phase (Fe_xP) when phosphorus segregated to a Fe(111) surface at temperatures of 670 K and above, but they also a detected a phase identified as clusters of phosphorus, segregated on top of the phosphide.

(iii). Structure of iron phosphides

As a preliminary to the discussion section, the structures of iron phosphides are now briefly introduced. As the survey by Corbridge[30] shows, in general the structures of metal phosphides are complex. Typically, metal-rich phosphides contain predominantly metal-phosphorus bonds which can probably be classified as metallic in character while phosphorus-rich phosphides tend to have metal-phosphorus bonds of covalent character along with covalent phosphorus-phosphorus linkages.

The coordination sites and bonding of phosphorus atoms in the five known stoichiometric iron phosphides (Fe_3P, Fe_2P, FeP, FeP_2 and FeP_4) are now briefly described. In Fe_3P, each phosphorus atom is surrounded by nine iron atoms in a tetrakaidecahedral (TKD) arrangement and the Fe-P bonding has metallic character.[31] Phosphorus is located in a similar ninefold TKD arrangement in Fe_2P, although there is evidence that some of the Fe-P bonds are covalent in character.[32] In FeP, phosphorus atoms are found in a distorted trigonal prismatic coordination with iron. P-P separations in FeP are short but longer than normal covalent bonds.[33] In FeP_2 and FeP_4, phosphorus is coordinated to a tetrahedron of iron and phosphorus atoms, and in both phosphides the Fe-P and P-P bonding is considered to be covalent.[34,35]

4.2.2. Results

The interaction of PH_3 with Fe(100), at sample temperatures from 160 to 730 K and pressures of 1×10^{-6} or 1×10^{-5} torr PH_3, was investigated with fixed wavelength ellipsometry (λ = 632.8 nm, angle of incidence = 70°), LEED and thermal desorption spectroscopy.

(i). LEED and TPD study of adsorption at 160 K

H_2 was the only desorbent detected in thermal desorption experiments, indicating that PH_3 is completely and irreversibly dissociated at 160 K. TPD results showed that PH_3 uptake saturates after exposures of about 40 L. Adsorption at 160 K was characterised by good c(2x2) LEED patterns, observed for exposures down to at least 10 L. The pattern became sharper and clearer (fig. 4.4) on desorbing H_2 in TPD experiments, where the sample temperature typically reached 550 K, indicating improved structural ordering. The LEED pattern was unchanged after annealing at high temperatures (800-900 K) for periods of up to 1½ hours.

(a) (b)

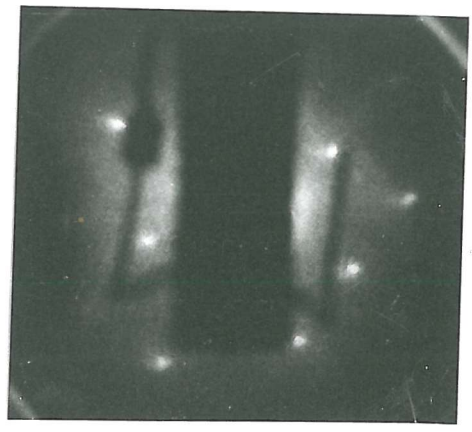

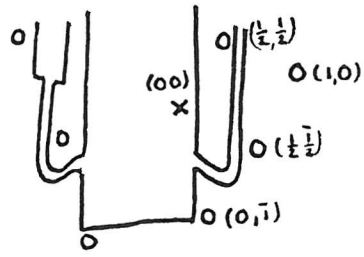

Fig. 4.4. *(a) LEED pattern of the c(2x2) surface (E = 110 eV) with (b) diagrammatic representation showing positions of first-order Fe(100) spots and half-order c(2x2) spots due to phosphorus overlayer.*

The c(2x2) structure, both before and after hydrogen desorption, can be interpreted in a straightforward way as an overlayer of chemisorbed phosphorus atoms on unreconstructed Fe(100), reaching saturation coverage at 0.5 monolayers.

Fig. 4.5 shows a series of TPD spectra for the desorption of H_2 from dissociated PH_3, at different exposures.

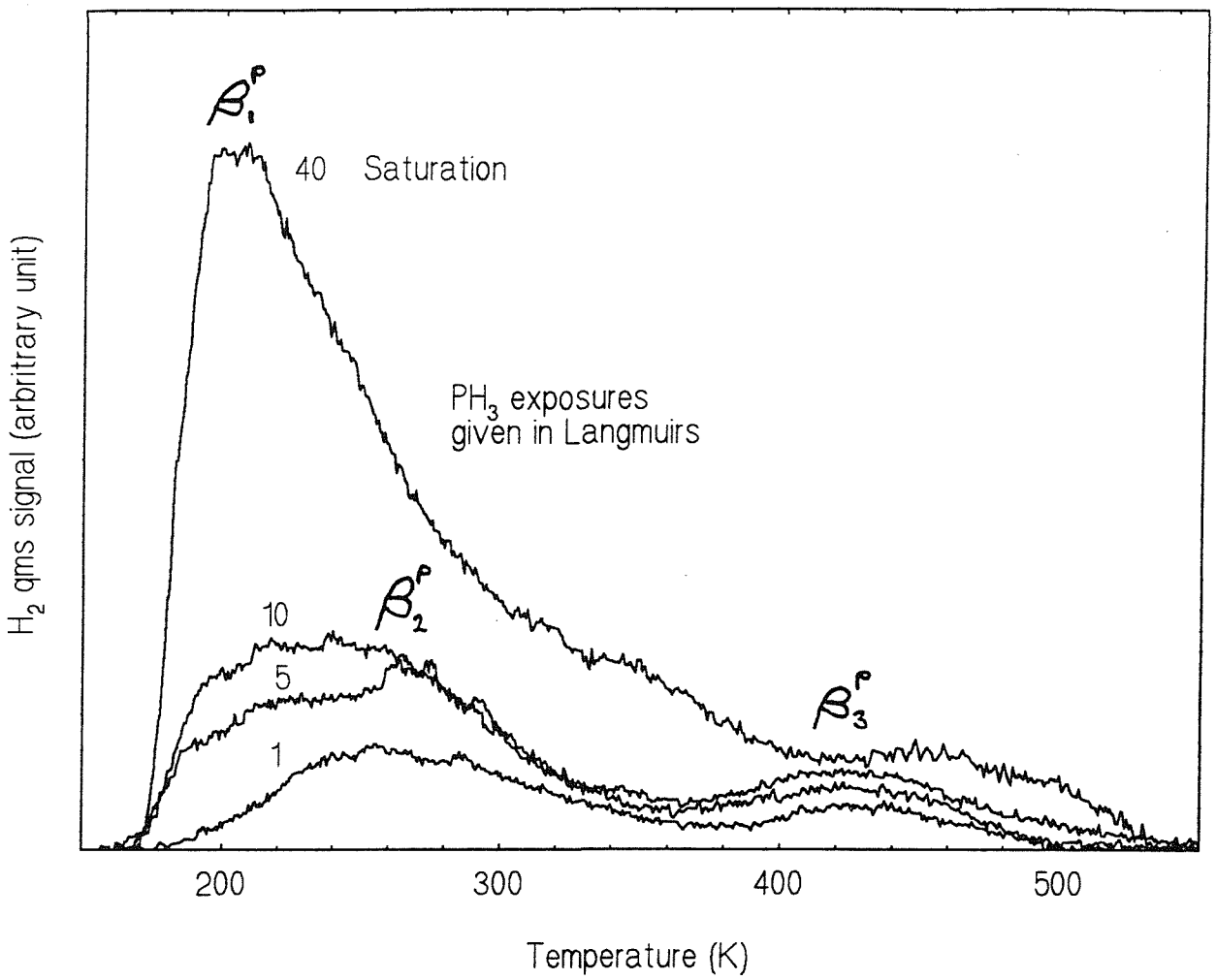

Fig. 4.5. *TPD spectra for the recombinative desorption of H_2 from dissociated PH_3 on Fe(100) at 160 K, as a function of PH_3 exposure. Heating rate 2.3 K s^{-1}.*

These spectra suffered from an erratic background, originating from outgassing at the sample mount (probably from the cracking of PH_3 by the tungsten heating wires). This was not a problem in experiments with other systems described in this work (including PH_3 on the Fe(110) surface), where the background typically decayed away smoothly after desorption from the crystal had ceased. In contrast, the background in PH_3/Fe(100) experiments was

irregular, unpredictable, and showed spurious features which often appeared in the temperature region of interest. Unambiguous background subtraction was difficult at low PH_3 exposure and impossible at high exposure (20 L and above).

Three peaks, assigned as β_1^P, β_2^P, and β_3^P with increasing temperature, can be identified in the development of the spectra. After a PH_3 exposure of 1 L, hydrogen desorbs in two features; the β_2^P peak, centred at about 260 K, and the smaller β_3^P peak, centred at about 440 K. This desorption curve is very similar to TPD spectra for low coverages of D_2 on Fe(100), reported above. The β_2^P and β_3^P peaks in fig. 4.5 correspond to the β_1 and β_2 peaks of D_2 in fig. 4.2, without showing any significant temperature shift. Apparently, very low coverages of phosphorus have no effect on coadsorbed hydrogen. By analogy with interpretation made for H_2 on clean Fe(100),[15] the β_2^P and β_3^P peaks can be assigned to recombinative desorption reactions, where the high temperature β_2^P peak obeys simple second-order desorption kinetics and the low temperature β_3^P peak arises from repulsive lateral interactions among hydrogen adatoms. Consistent with this interpretation, the β_3^P peak shows a shift to lower temperature on increasing the PH_3 exposure from 1 to 10 L.

Coadsorbed phosphorus does strongly influence the hydrogen desorption kinetics at higher coverages. This effect is dominant at saturation uptake (about 40 L PH_3), where most, if not all, of the H_2 desorbs in the low temperature β_1^P peak, centred at about 220 K. At saturation, this feature is shifted to lower temperature by as much as 40 K, compared to the saturated β_1 peak for D_2 on the clean surface. After PH_3 exposures of 5 and 10 L, the β_1^P feature can apparently be observed emerging as a low temperature shoulder on the β_2^P peak. The β_1^P peak is a characteristic of high phosphorus coverages and can reasonably be assigned to a recombinative desorption of hydrogen where the binding energy is reduced by repulsive lateral interactions between adsorbed hydrogen and phosphorus atoms.

Alongside the β_1^P peak, other features in the saturation curve (40 L) are, very likely, artifacts from sample mount outgassing, because they could not be reproduced in numerous repeated experiments. For example, it is doubtful that the feature at 340 K comes from desorption from the crystal surface. The saturation curve in fig. 4.6, is included to show the appearance of the low temperature feature. Although a background subtraction has been attempted, uncertainty in the position and shape of the background curve means that the error in the area due to H_2 from the surface may perhaps be as much as $\pm$ 30%. Consequently, it was not

possible to derive an uptake versus exposure curve from TPD area data.

The blocking effect of phosphorus in the c(2x2) overlayer was briefly studied by investigating the adsorption/desorption characteristics of postdosed D_2. Prior to experiments, the hydrogen from PH_3 was desorbed by quickly heating to 500 K (at similar rate used for TPD experiments). D_2 was postdosed at 160 K in an exposure of 200 L (1 x 10^{-6} torr). Fig. 4.6 shows the desorption spectra of postdosed D_2 as a function of the exposure of predosed PH_3. The spectra show two peaks, assigned as β_1^D and β_2^D, with increasing temperature.

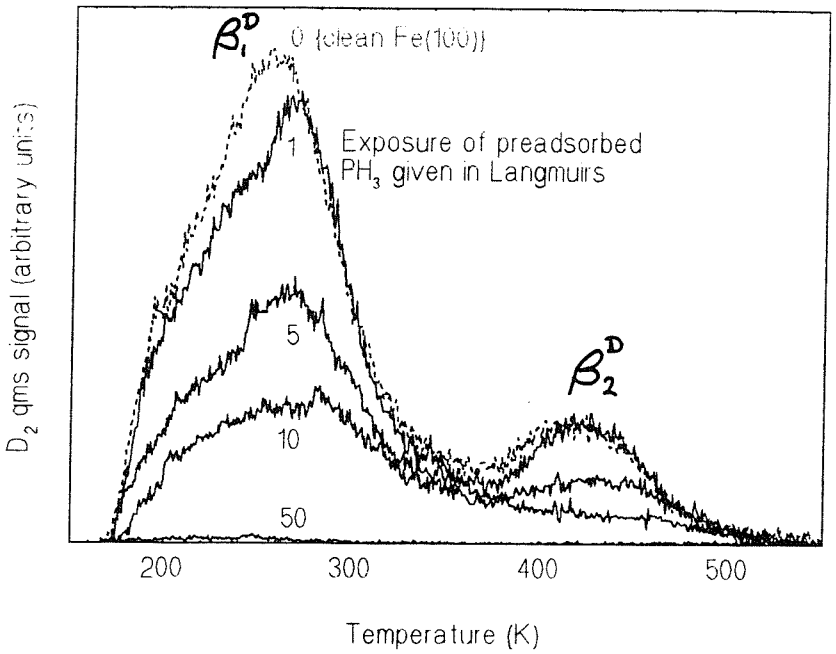

Fig. 4.6. TPD spectra for recombinative desorption of D_2 from different coverages of c(2x2)P-Fe(100) at 160 K, as a function of D_2 exposure. TPD spectrum of 200 L D_2 on clean Fe(100) included for comparison. Heating rate 2.3 K s^{-1}.

D_2 uptake is reduced as the exposure of the preadsorbed PH_3 increases. As fig. 4.6 shows, this effect is apparent after an exposure of 1 L PH_3. After a PH_3 exposure of about 50 L, which corresponds to saturation uptake, D_2 postadsorption is completely inhibited. At saturation, the half monolayer c(2x2)P structure clearly blocks all sites for D_2 adsorption (and does not provide any new ones).

After a PH_3 exposure of 1 L, the positions of the two peaks, β_1^D at about 260 K and β_2^D at 420 K, are effectively identical to the β_1 and β_2 peaks of D_2, at comparable uptake, on the clean surface (structure in the β_1^D peak is believed to be an experimental artefact as similar spurious line shapes were occasionally detected for D_2 on the clean surface). The low

coverage of phosphorus associated with the 1 L PH_3 exposure does not appear to have a effect on the desorption kinetics of D_2.

On increasing the PH_3 exposure to 10 L, the low temperature β_1^D peak does not shift but it may broaden slightly, compared to D_2 desorption curves at comparable uptake from the clean surface. It is possible that the broadening corresponds to the emergence of the low temperature β_1^P feature as a shoulder to the β_2^P peak in the spectra of H_2 from dissociated PH_3 (fig. 4.5), in which case it is an effect of coadsorbed phosphorus. The higher temperature β_2^D peak shifts to higher temperature on increasing the PH_3 exposure, as expected for lower D_2 uptake. However, after an exposure of 10 L the feature has effectively disappeared (as noted in Sect. 4.1.3, similar behaviour was detected when using D_2 TPDs to check for contamination).

The corresponding peak on the clean surface (β_2) is assigned to a simple recombinative desorption reaction.[15] After the initial 10 L PH_3 exposure, desorbing H_2 showed a similar feature (β_3^P in fig. 4.5) indicating that some of the hydrogen was located at sites uninfluenced by coadsorbed phosphorus. This suggests that there were regions of the surface that were effectively clean. After H_2 desorption, where the surface reaches 500 K, it appears that these regions have become blocked to the adsorption of postdosed D_2 since the corresponding β_2^D peak has disappeared. This may indicate that during PH_3 adsorption at 170 K, phosphorus coalesces into islands, with regions of clean-like surface in between. On annealing, phosphorus becomes mobile and spreads out from the islands to adsorb at sites in the clean-like region, thereby blocking further adsorption.

(ii). Changes in Δ and ψ versus time

Changes in the ellipsometric parameters Δ and ψ during the interaction of PH_3 with Fe(100) were measured relative to the values of the clean surface, and designated $\delta\Delta_P$ and $\delta\psi_P$. Fig. 4.7 shows $\delta\Delta_P$ and $\delta\psi_P$ as a function of time during experiments at a PH_3 pressure of 1×10^{-6} torr and sample temperatures in the range 350-730 K.

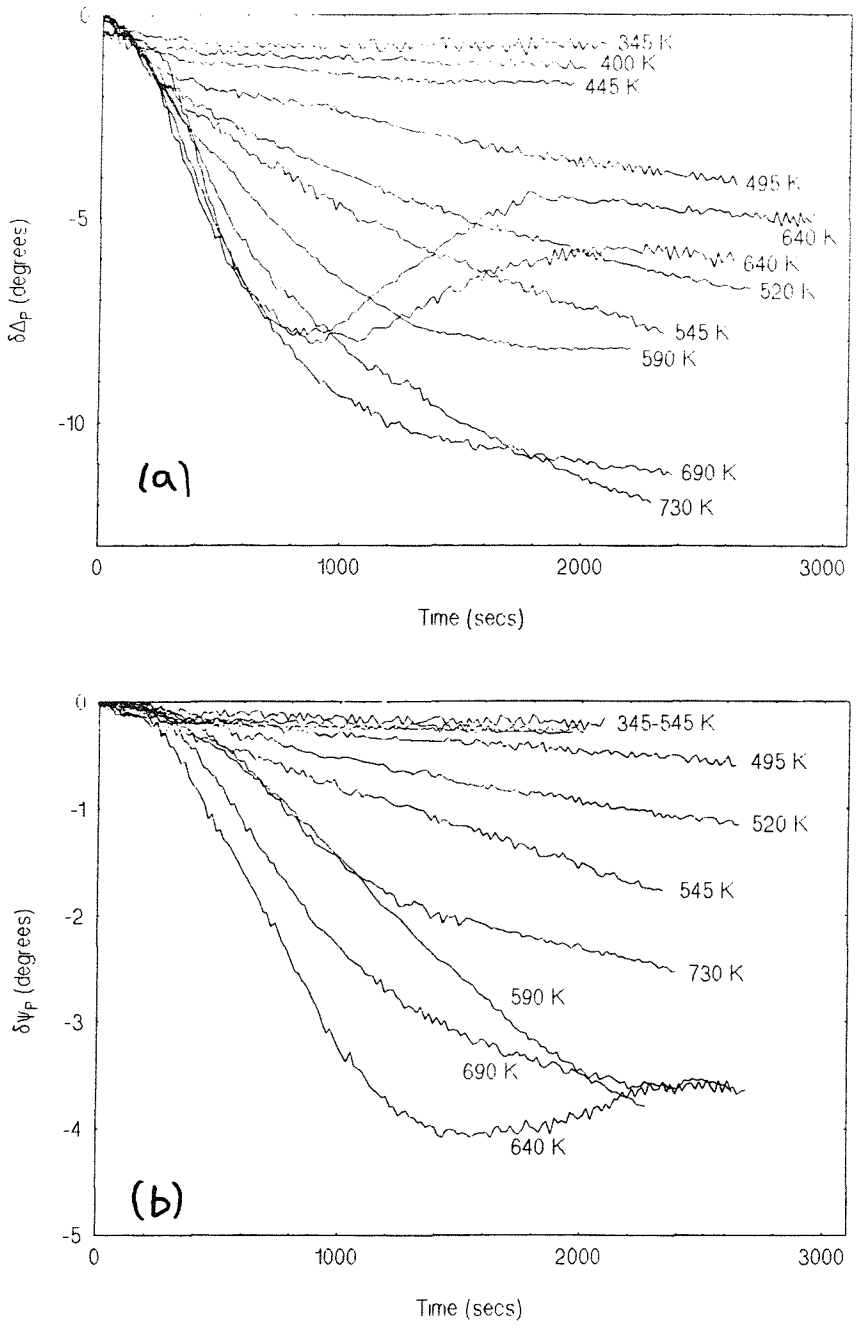

Fig. 4.7. *(a) $\delta\Delta_P$ and (b) $\delta\psi_P$ versus time for interaction of PH_3 at 1 x 10^{-6} torr with Fe(100) at 345-730 K.*

Fig. 4.8 shows $\delta\Delta_P$ and $\delta\psi_P$ as a function of time during experiments at a PH_3 pressure of 1 x 10^{-5} torr and temperatures from 520 to 640 K. Results of experiments at 160 and 300 K, where the changes in Δ and ψ are very small, are presented separately.

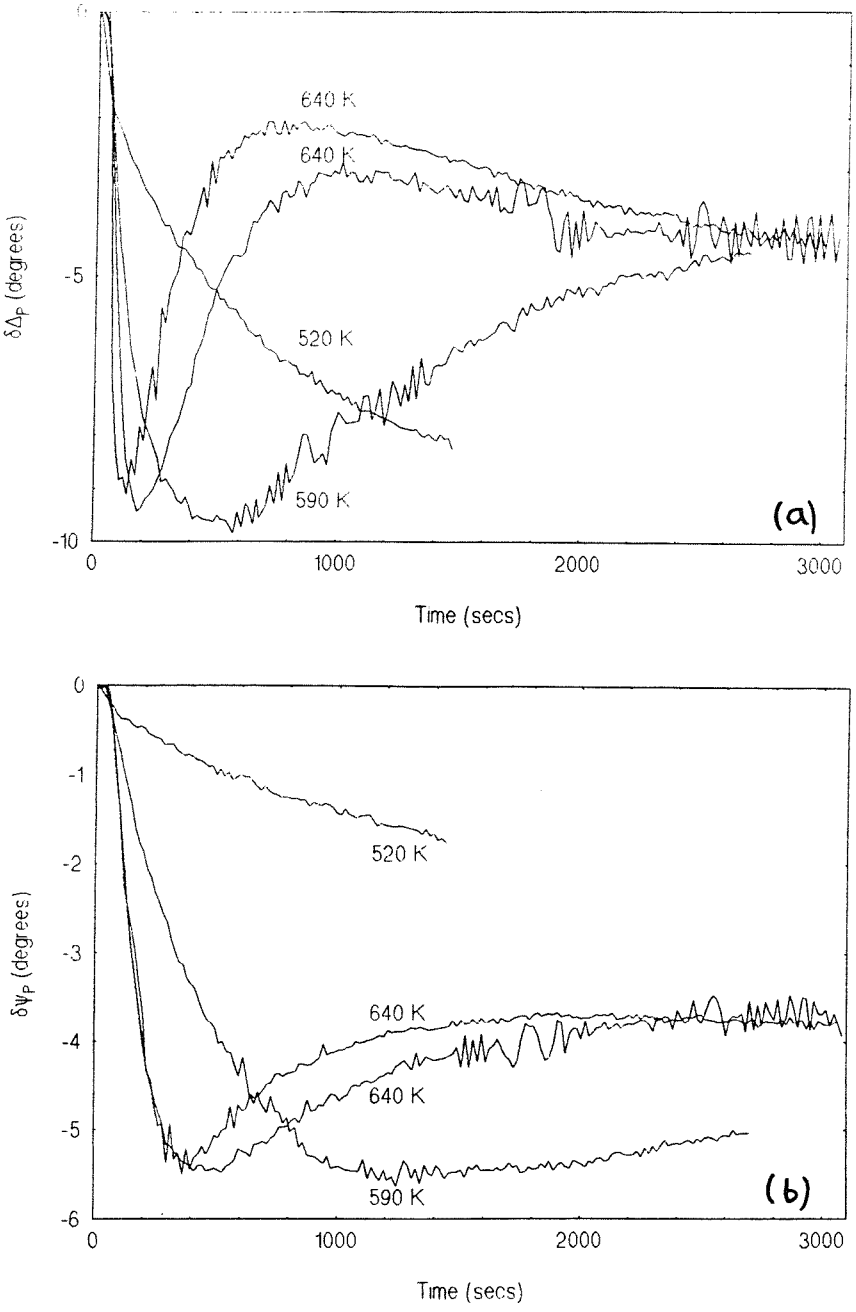

Fig. 4.8. (a) $\delta\Delta_P$ and (b) $\delta\psi_P$ versus time for interaction of PH_3 at 1 x 10^{-5} torr with Fe(100) at T = 520-640 K.

For curves recorded at temperatures up to 545 K, the time scale in these graphs represents the duration of exposure, and zero on the time axis marks the start of the dose. However, this is not the case for curves recorded at 590 K and above since, after starting the dose, there was a large temperature-dependent delay before significant changes in the ellipsometric parameters were observed (this is most clear for Δ, as shown in fig. 4.9). To simplify the graphs, the delayed $\delta\Delta_P$ curves and the corresponding $\delta\psi_P$ data in figs. 4.7 and 4.8 have been

shifted so that in the initial stages the delayed $\delta\Delta_P$ curves coincide with the lower temperature results. Zero on the time scale of these graphs effectively marks the beginning of changes in the ellipsometric parameters that are related to bulk film growth, so that the initiation of the film is ignored.

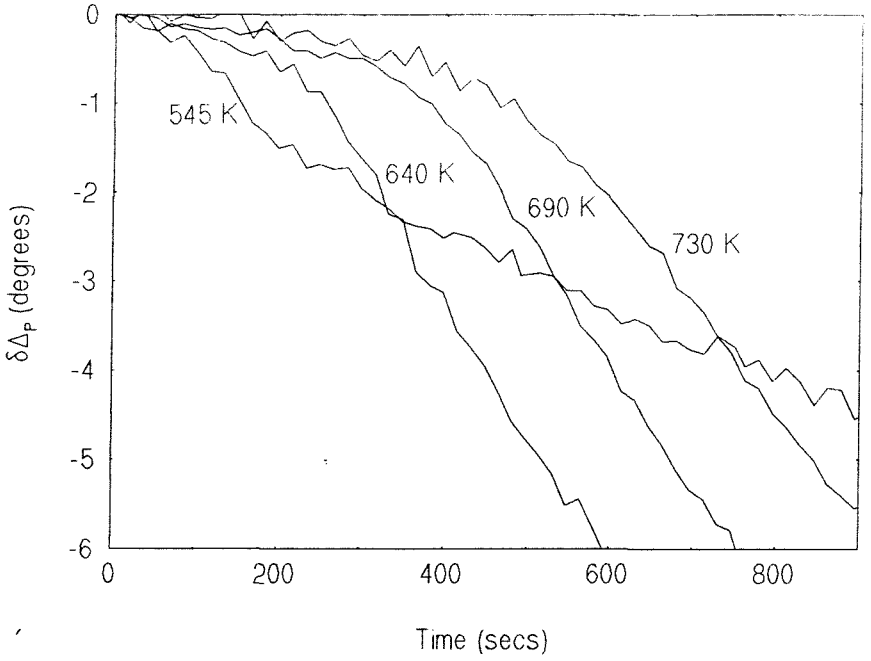

Fig. 4.9. $\delta\Delta_P$ *versus time showing delay in onset of changes in* Δ *at high temperatures and pressure of 1 x* 10^{-6} *torr.*

During experiments at 160 and 300 K, the small changes in Δ and ψ arising from film growth are comparable in size to signal noise and to background instability. In general, measured values of the ellipsometric parameters were slightly unstable over short periods of time (on top of changes due to film growth), probably because of instability in the sample position (Δ could wander by as much as 0.3° and ψ by as 0.1°). Consequently, it was not possible to reproduce the time dependency of changes in Δ and ψ during film growth at 160 and 300 K. Fig. 4.10 presents five measurements of $\delta\Delta_P$ and $\delta\psi_P$ at 160 K while fig. 4.11 shows $\delta\Delta_P$ and $\delta\psi_P$ recorded in three experiments at 300 K.

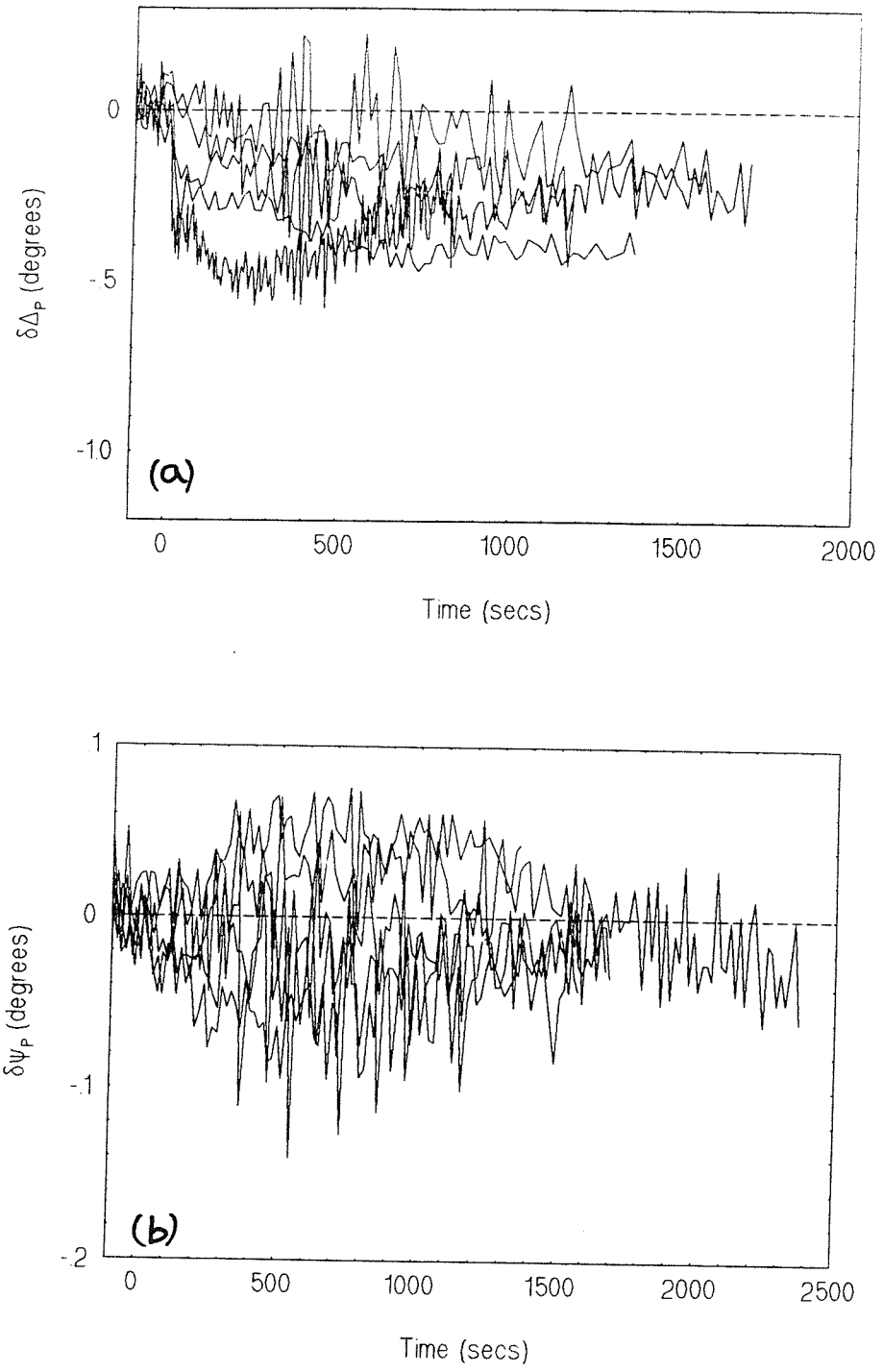

Fig. 4.10. *(a) $\delta\Delta_P$ and (b) $\delta\psi_P$ versus time for interaction of PH_3 at 1 x 10^{-6} torr with Fe(100) at 160 K.*

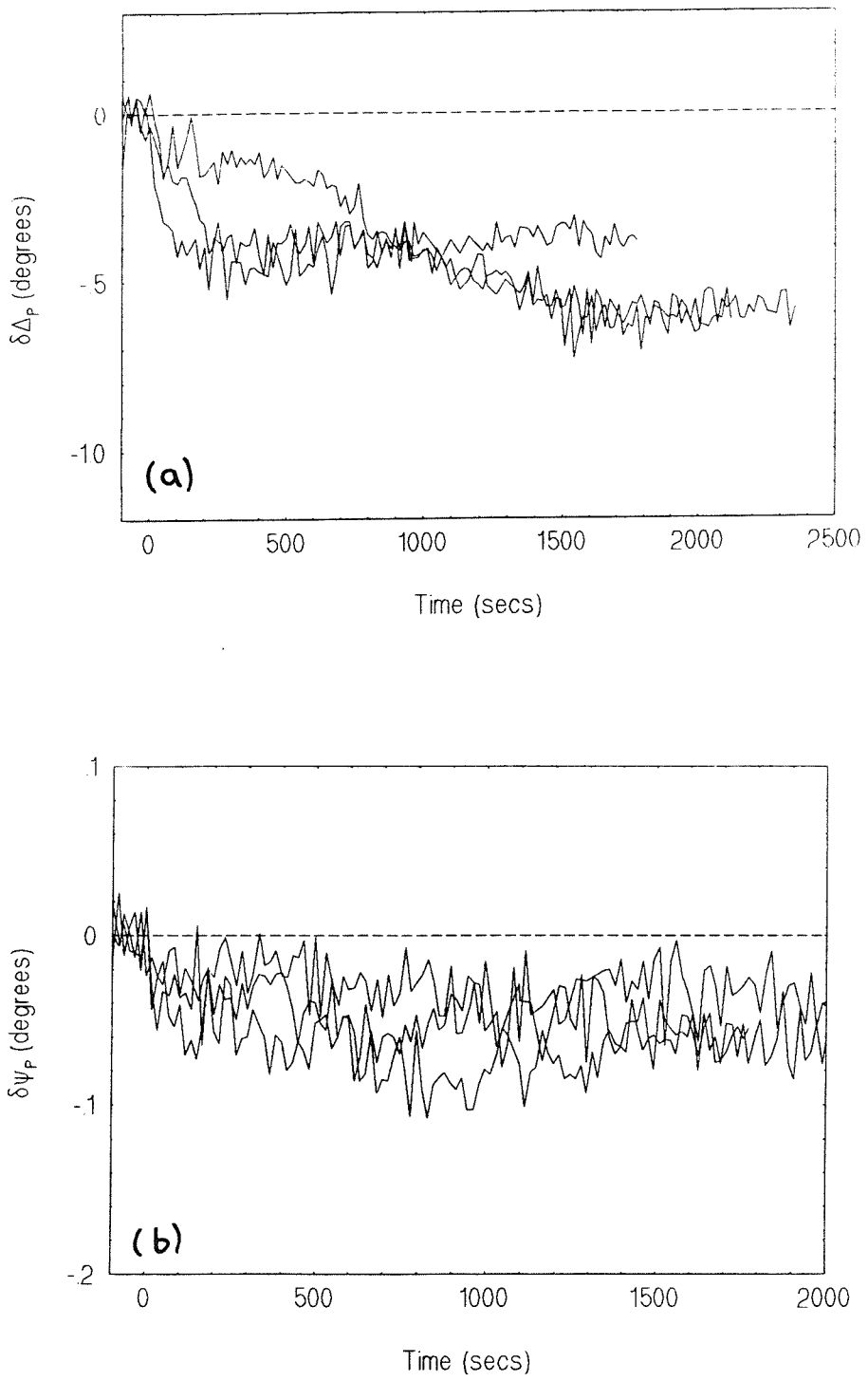

Fig. 4.11. *(a) $\delta\Delta_P$ and (b) $\delta\psi_P$ versus time for interaction of PH_3 at 1 x 10^{-6} torr with Fe(100) at 300 K.*

The TPD results in fig. 4.5 indicate that PH_3 uptake at 160 K saturates after an exposure of about 40 L. Consistently, in three of the measurements in fig. 4.10, Δ quickly decreases and reaches a steady state value within the first 100 L exposure (the much slower decrease of Δ in the other two measurements, where broadly similar steady state values are eventually reached, can be explained by background instability). The steady state magnitude of $\delta\Delta_P$ at 160 K is estimated from all the data to be $0.28 \pm 0.15^\circ$. This rather approximate value can be associated with the formation of 0.5 monolayers of chemisorbed phosphorus atoms. It is not possible to detect any significant change in ψ at 160 K (ψ is typically much less sensitive to submonolayer coverage compared to Δ[36]).

During film growth at 300 K, both Δ and ψ appear to decrease and then quickly level off. The steady state magnitudes of $\delta\Delta_P$ and $\delta\psi_P$ are estimated to be $0.49 \pm 0.1^\circ$ and $0.05 \pm 0.02^\circ$, respectively. These values are larger than those seen in experiments at 160 K suggesting that the phosphorus uptake at 300 K is greater than 0.5 monolayers.

(iii). Analysis of Δ-ψ plots

The ellipsometric results presented above are given as the relative quantities $\delta\Delta_P$ and $\delta\psi_P$ because the measured angles Δ and ψ are believed to carry significant systematic errors from a number of sources.[37] Single zone measurements were made in this study, which means that the data has to be corrected primarily for the influence of optical imperfections in both the ellipsometer components and the vacuum chamber windows.[38] The data was also likely to suffer from azimuth errors. The ellipsometer software had a procedure to refine the calibration of analyzer and polariser azimuths with respect to the plane of incidence (using the method of Aspnes[39,40]). However, it was not possible to do this because there was no operating manual and the program code was difficult to decipher (in part, because it was written in German).

Analytical plots of Δ versus ψ were obtained by calibrating $\delta\Delta_P$ and $\delta\psi_P$ using absolute angles for the clean surface derived from the optical constants of Fe(100) reported by Vink *et al.*[41] They determined the refractive index of Fe(100) at a wavelength of 632.8 nm to be $(n - ik) = (3.5 - i3.7)$, in good agreement with an earlier evaluation of (3.5 - i3.9) at 640.0 nm.[42] This room temperature calibration can be used for all temperatures studied (up to

730 K) since we did not detect any temperature dependency in the ellipsometric parameters, and therefore optical constants, of the clean surface. Because the optical constants of the clean surface are reported to one decimal place, the uncertainty in the ellipsometric angles derived for these values is about 1° in Δ and 0.3° in ψ.

The well-developed Δ-ψ trajectories of the experiments at temperatures of 590 and 640 K and pressures of 1 x 10^{-6} and 1 x 10^{-5} torr PH_3 (fig. 4.12) are characteristic of the growth of an absorbing film. For an absorbing film, the effect of the substrate is increasingly obscured, as the film thickens, by the absorption of light in the film. Consequently, the trajectory tends towards a single point which effectively represents the limit of detection of the ellipsometer. When the film grows beyond the probe depth of the light (in the following discussion this is termed the opaque thickness) the Δ-ψ curve reaches an end point, characteristic of the film, alone, without any contribution from the substrate.

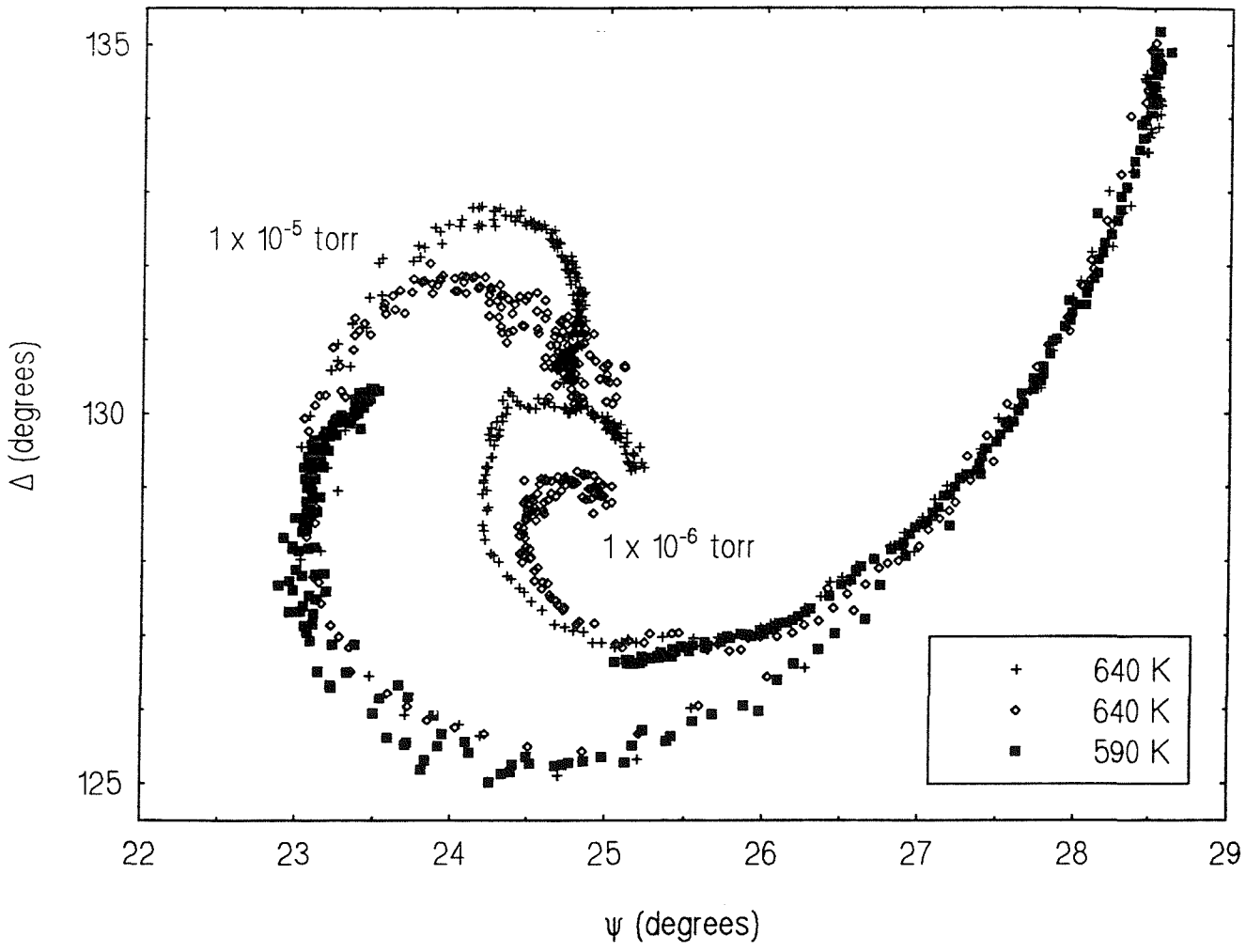

Fig. 4.12. Experimental Δ-ψ trajectories for interaction of PH_3 at 1 x 10^{-6} or 1 x 10^{-5} torr with Fe(100) at 590-640 K.

At either of the two PH_3 pressures, the 640 K trajectories (fig. 4.12) are reproducible along much of their length but diverge slightly in the later stages of film growth, indicating that the optical properties of the thicker films depend on other, unknown, factors. The trajectories are also strongly affected by PH_3 pressure. At a given temperature (590 or 640 K), the trajectories for the two different PH_3 pressures quickly separate and widely deviate before converging on the same region of the Δ-ψ plane in the later stages of film growth.

As fig. 4.7 shows, both Δ and ψ have reached, or are very close to, a steady state by the end of experiments at 640 K and 1 x 10^{-6} torr. This indicates that the films have grown to opaque thickness, and the Δ-ψ trajectories have reached an end point characteristic of the film, alone. The end points at $(\Delta,\psi) = (128.9^\circ, 24.9^\circ)$ and $(129.3^\circ, 25.2^\circ)$ correspond to the refractive indices (3.28 - i2.89) and (3.29 - i2.94), respectively. Similarly, fig. 4.8 indicates that steady state Δ-ψ values are reached by the end of the experiments at the same temperature but lower pressure (1 x 10^{-5} torr). For these trajectories, the refractive indices derived from the end points $(130.3^\circ, 25.0^\circ)$ and $(130.6^\circ, 24.7^\circ)$ are (3.37 - 2.92) and (3.39 - i2.88). On increasing pressure from 1 x 10^{-6} to 1 x 10^{-5} torr, the value of n at opaque thickness increases, but k remains effectively unchanged. The optical constants of the films at opaque thickness are fairly close to the values of the clean Fe(100) surface.

Experimental Δ-ψ trajectories were fitted with theoretical curves computed from the classical Drude equations. These curves are derived for an ideal model system where the film is plane-parallel, optically isotropic and homogeneous. In the following discussion, the optical constants (n and k) derived from theoretical fits are reported to two decimal places, reflecting the accuracy of the fit and allowing trends to be seen. However, the uncertainty in the calibration of the ellipsometric angles, as described above, means that the best fit n and k values cannot be known with an accuracy of better than one decimal place.

When used in theoretical models, the optical constants at opaque thickness fail to describe the 640 K trajectories. As fig. 4.13 shows, at 1 x 10^{-6} torr the theoretical curve is initially very close to the experimental trajectory but deviates in the later stages, while at 1 x 10^{-5} torr, the theoretical curve never runs close to the experimental data.

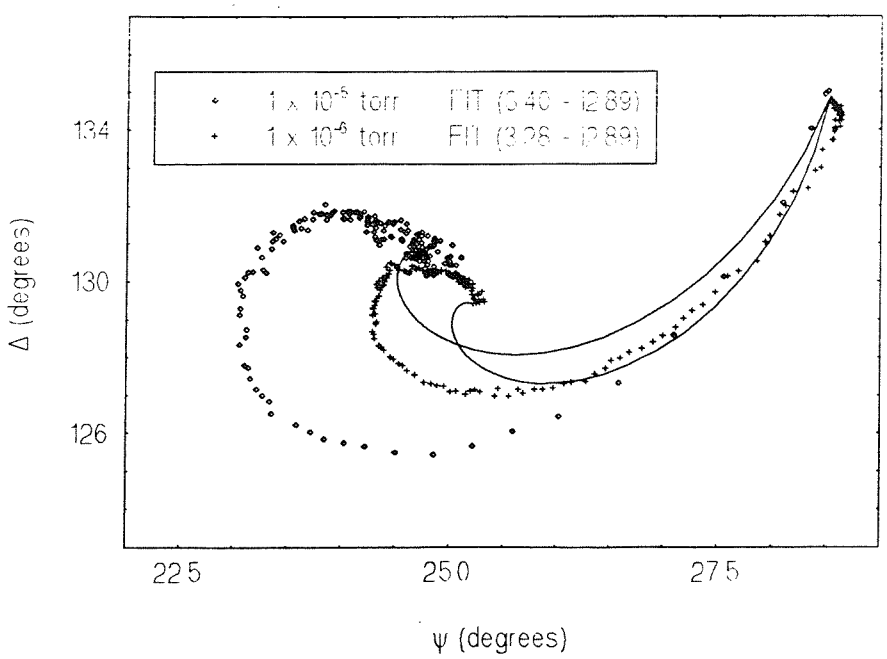

Fig. 4.13. *Two 640 K experimental trajectories comparing theoretical trajectories using optical constants at opaque thickness. Theoretical curves shown to 1000 Å.*

This indicates that the optical properties of the films change with thickness. Because there was no independent way to determine, or even guess, thickness at any stage in film growth, there could be no unambiguous determination of n and k at any point along the trajectories. Instead, it was assumed that the optical constants would be invariant in the initial stages of growth, and attempts were made to find theoretical fits. By systematically varying the model optical constants, which were initially given the values at opaque thickness, agreement with the early stages of the trajectory could be maximised. This method relies on there being significant differences between trajectories with similar optical constants.

As fig. 4.14 shows, ambiguity in a fit increases as the length of the trajectory to be fitted decreases. For example, with a fixed value of n, trajectories at slightly different k values initially follow the same path. The curves in fig. 4.14 show that it is possible to distinguish between optical constants which differ in the first decimal place. We believe that if the trajectories are long enough then it is possible to distinguish between optical constants to the second decimal place.

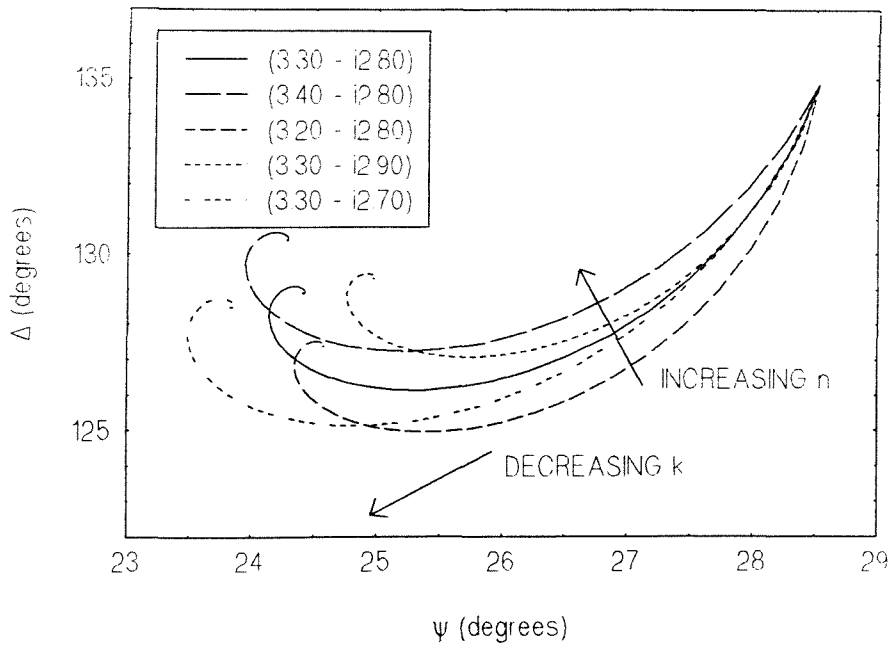

Fig. 4.14. Effect of varying n and k on theoretical Δ-ψ trajectories. Curves shown for growth to 1000 Å.

A large part of the 640 K trajectories can be fitted with a constant refractive index model (shown in fig. 4.15), for growth up to a predicted thickness of about 450 Å.

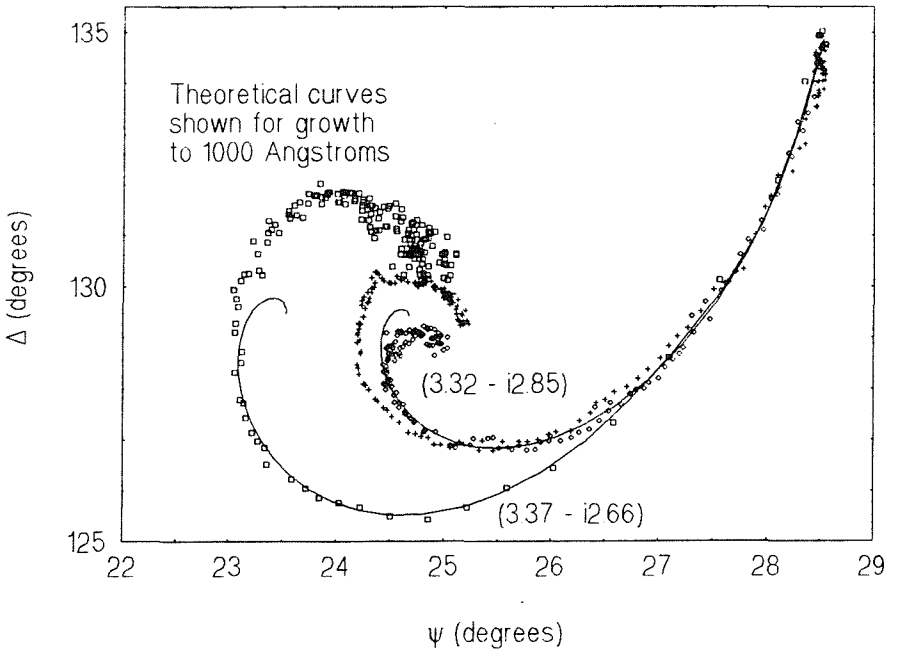

Fig. 4.15. Theoretical fits (solid lines) to experimental Δ-ψ trajectories for interaction of PH_3 at 1 x 10^{-6} or 1 x 10^{-5} torr with Fe(100) at 640 K.

Confidence in the validity of the fit is high because the theoretical curves describe a large part of the curvature of the experimental trajectories. For both experimental trajectories at

1 x 10^{-6} torr, the model fit yields a refractive index of (3.32 - i2.85) for the initial stages of film growth, compared to the values of (3.28 - i2.89) and (3.29 - i2.94) for the film at opaque thickness. Similarly at 1 x 10^{-5} torr, theory predicts a refractive index of (3.37 - i2.66) in the early stages, compared to (3.37 - i2.92) and (3.39 - i2.88) at opaque thickness. The variation of the optical constants as the film grows may be explained by subtle changes in film composition or, perhaps, surface roughness.

The trajectories of experiments at temperatures in the range 490 to 590 K (fig. 4.16) follow similar, but less advanced, paths to those for growth at 640 K.

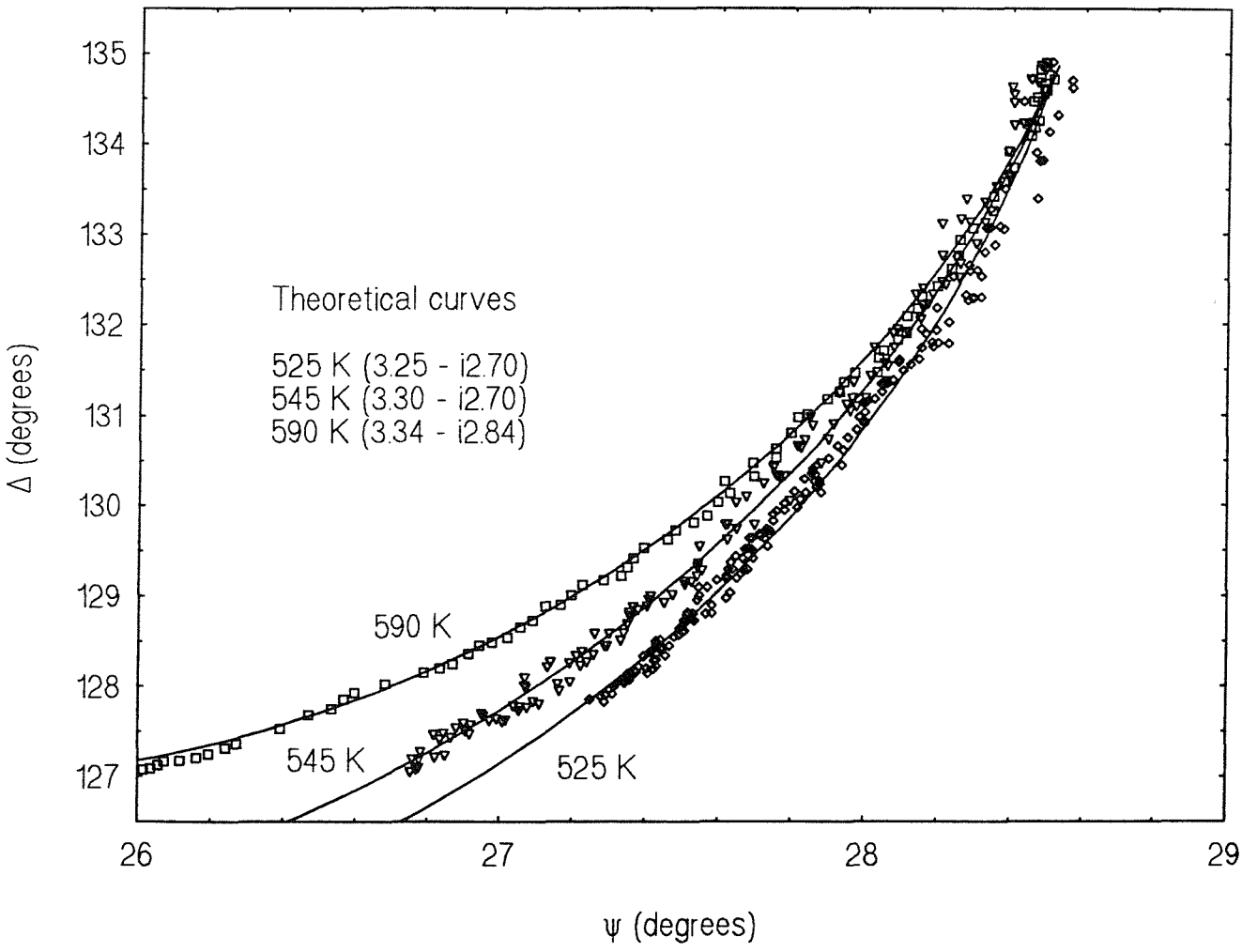

Fig. 4.16. *Experimental Δ-ψ trajectories and theoretical fits (solid lines) for interaction of PH_3 at 1 x 10^{-6} torr with Fe(100) at 525-590 K.*

Consequently, it can be assumed that the optical constants at these temperatures are similar to those found for the 640 K curves. To find fits, the model optical constants were set to

values found for the 640 K data and then systematically varied. Theoretical fits are shown in fig. 4.16 for growth at 525, 545 and 590 K, and 1 x 10^{-6} torr PH_3. The curve for 490 K, which is not shown, can be fit with the theoretical curve for growth at 525 K. Optical constants derived from these fits are (3.25 - i2.70) at 490 and 525 K, (3.30 - i2.70) at 545 K and (3.34 - i2.84) at 590 K. Similarly, fits to trajectories for growth at 1 x 10^{-5} torr (not shown) yield optical constants of (3.38 - i2.35) at 545 K and (3.36 - i2.65) at 590 K. At a given pressure, the small temperature-dependent differences in the optical constants, reflected in the slight divergences of the experimental trajectories, are too significant to be explained by the uncertainties arising from the calibration of the $\delta\Delta_P$ and $\delta\psi_P$ measurements.

At temperatures of 445 K and below, $\delta\psi_P$ is of comparable size to the small instability in the measurement of ψ (which was described above), and individual trajectories are unstable over time. However, as fig. 4.17 shows, when taken together the trajectories broadly coincide and describe a path similar to trajectories of higher temperature growth.

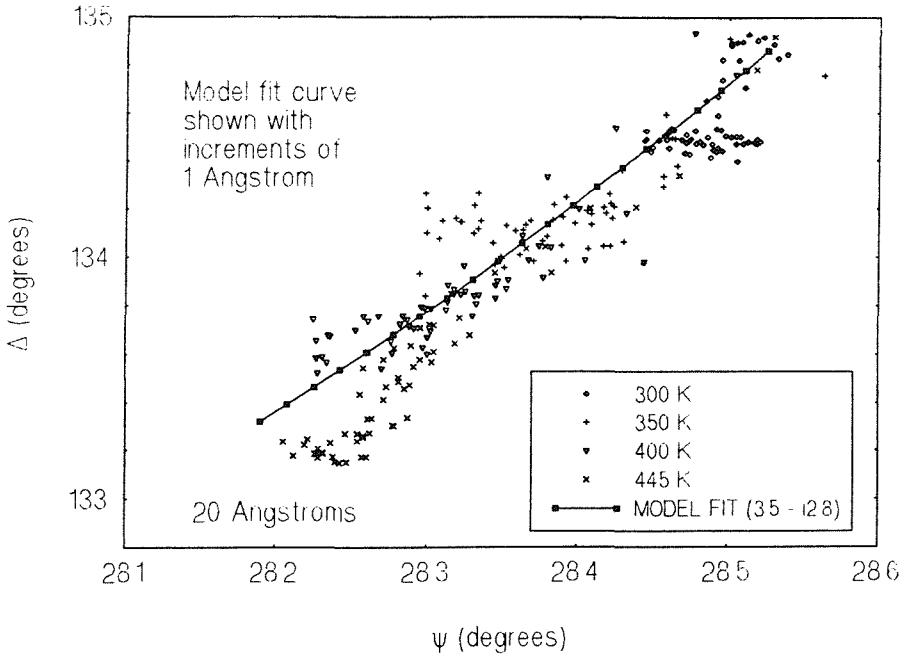

Fig. 4.17. *Experimental Δ-ψ trajectories and theoretical fit (solid line) for interaction of PH_3 at 1 x 10^{-6} torr with Fe(100) at 300-445 K.*

It would be very difficult to justify a particular k value for this data because, as fig. 4.14 indicates, trajectories with distinct k values can follow very similar paths in the early stages of film growth. However, if it is assumed that the films at these temperatures have a refractive index (in particular k) similar to that at the higher temperature then an approximate fit can be made (although not to the 160 K result where $\delta\psi_P$ is irreproducible). In this way,

the data can be fit with an optical constant of (3.5 - i2.8).

The trajectories observed during film growth at 690 and 730 K, and a pressure of 1 x 10^{-6} torr PH_3 (fig. 4.18), do not approach a steady state within the timescale of the experiments, in contrast to the results at 640 K (a curve at this temperature is included for comparison). It is not possible to find a reasonable and unambiguous fit to these data and it is likely that the refractive index of the film changes during film growth.

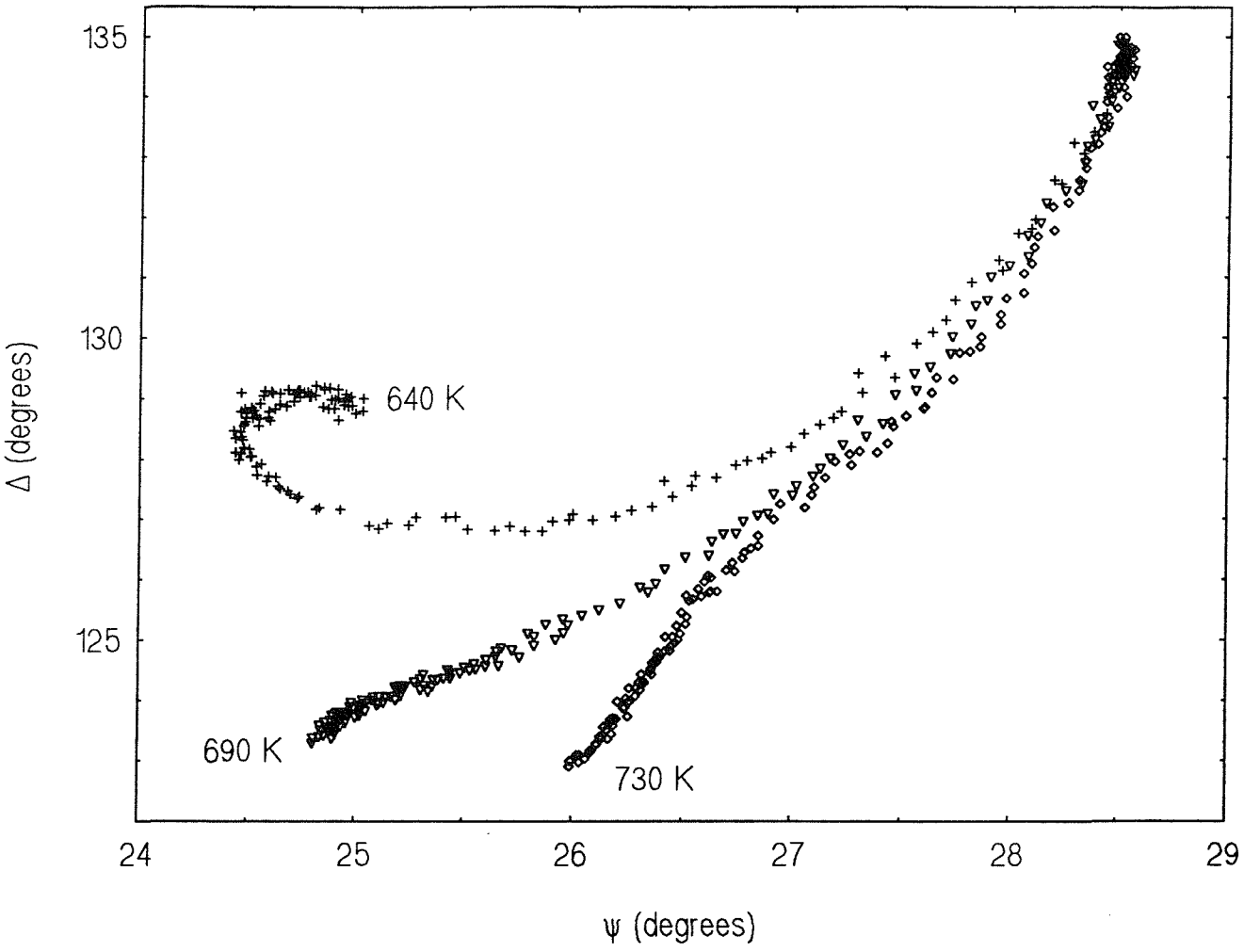

Fig. 4.18. *Experimental Δ-ψ trajectories for interaction of PH_3 at 1 x 10^{-6} torr with Fe(100) at 690-730 K.*

The method of curve fitting analysis can be summarised as follows. At 640 K, optical constants can be obtained for films grown to opaque thickness. These values do not provide fits but do justify values obtained by systematically varying *n* and *k*. A large part of the high temperature trajectories can be successfully described, and consequently the fits are

considered accurate and unambiguous. Trajectories at lower temperatures are shorter and so ambiguity is increased. However, fits are justified because it is assumed that the optical properties of films at all temperatures studied are reasonably similar.

Optical constants determined from the theoretical best fits are listed in Table 4.1. Error in both n and k, arising from uncertainty in the theoretical fits, is estimated to be $\pm$ 0.01 for the results recorded at 590 and 640 K, increasing to $\pm$ 0.06 or more at lower temperatures (as the fits become more ambiguous). As discussed above, uncertainty in k is probably higher than for n. However, it should be restated that error arising in the calibration of the angles means that the optical constants are probably only accurate to one decimal place.

Table 4.1. *Temperature and pressure dependent optical constants derived from curve fitting analysis and from steady state Δ-ψ values. Two interpretations shown for the 300-445 K data (see text).*

Temperature (K)	Pressure (torr)	(n - ik) from curve fitting	(n - ik) from steady state Δ-ψ	Fig.no.
640	1 x 10^{-6}	(3.32 - i2.85)	(3.28 - i2.89)	4.14
"	"	(3.32 - i2.85)	(3.29 - i2.94)	"
590	"	(3.34 - i2.84)		"
545	"	(3.30 - i2.70)		4.15
520	"	(3.25 - i2.70)		"
495	"	(3.25 - i2.70)		-
300-445	"	(3.5 - i2.8)		4.16
640	1 x 10^{-5}	(3.37 - i2.66)	(3.37 - i2.92)	4.14
"	"	(3.37 - i2.66)	(3.39 - i2.88)	"
590	"	(3.36 - i2.65)		"
545	"	(3.38 - i2.35)		"

During film growth at 1 x 10^{-6} torr PH_3, the optical constants are broadly similar across the temperature range 490 to 640 K, although both n and k appear to increase slightly as the sample temperature increases. Below 445 K, the experimental trajectory suffers from a wandering ψ value and because of the shortness of the trajectory, the quality of the fit is poor. Consequently, the noticeable difference of optical constants for low temperature data may well be meaningless. Comparing optical constants derived from model fits and Δ-ψ end points, it appears that, at 640 K, n decreases slightly while k increases more significantly with increasing thickness.

At 1 x 10^{-5} torr, n is slightly smaller and k is considerably larger when compared to the optical constants for film growth at comparable temperatures but lower pressure. At 640 K, n is effectively unchanged while k shows a large increase with increasing thickness.

These results are consistent with the growth of generically similar films, at least at high temperatures (495 K and above). The temperature and pressure dependency may be explained by variations in film composition or microstructure (surface roughness, for example).

(iv). Kinetics of film growth

Where theoretical model curves fit experimental Δ-ψ trajectories, it is possible to estimate film thickness and determine the kinetics of film growth (because each Δ-ψ point is recorded at a known time).

Fig. 4.19 shows thickness as a function of time during film formation at temperatures from 495 to 640 K, and a pressure of 1 x 10^{-6} PH_3 torr. As will be discussed below, the onset of fast film growth at 590 and 640 K was delayed and so, for clarity, the curves at these temperatures have been shifted to coincide with lower temperature data. In this way, the slow initiation stage is ignored and the time scale in fig. 4.19 reflects the growth kinetics of the bulk film.

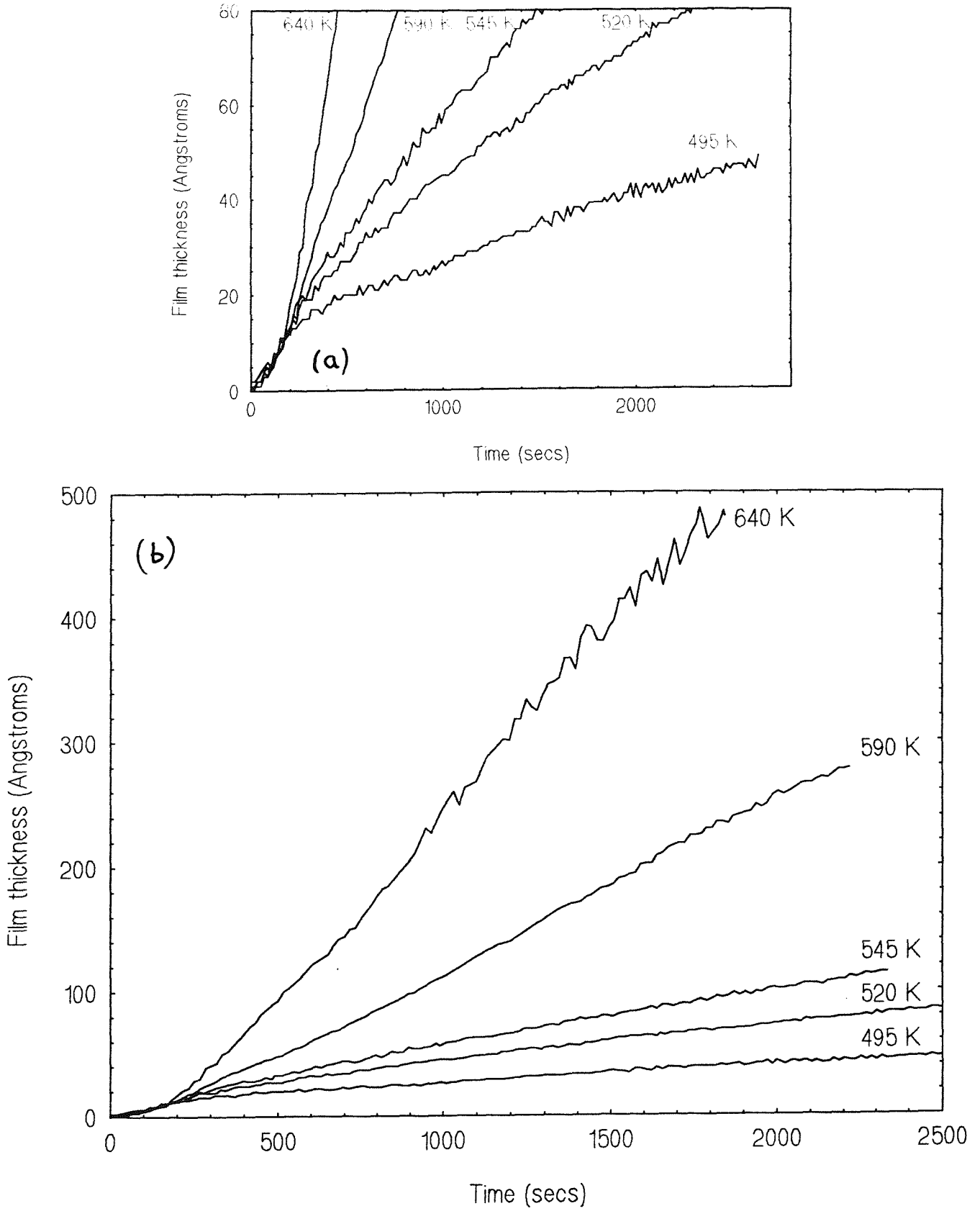

Fig. 4.19. *(a) Initial fast stage and (b) later stages of film growth for interaction of PH_3 at 1 x 10^{-6} torr with Fe(100) at 495-640 K.*

Two stages can be distinguished in the growth curve at these temperatures. There appears to be an initially fast stage (see fig. 4.19(*a*)), with a rate independent of temperature, which corresponds to the formation of the first few layers of the film (about 20 Å). This is clearest for growth at 495 K, where the contrast with the slower growth of the thicker film is strong (at higher temperatures the growth rates of the initial stage and of the thicker film become comparable). It may be that a different process controls the rate of film formation in the initial stage of growth. In the second stage, the growth rate at a given thickness increases quickly with increasing temperature. In strong contrast to the results for oxidation on Fe(100) reported below (Sect.4.3.3), there is little tendency towards a limiting thickness at any of the temperatures in the range 495-640 K. The curve cannot adequately be described by a simple growth law (parabolic, logarithmic, cubic, or linear, for example).

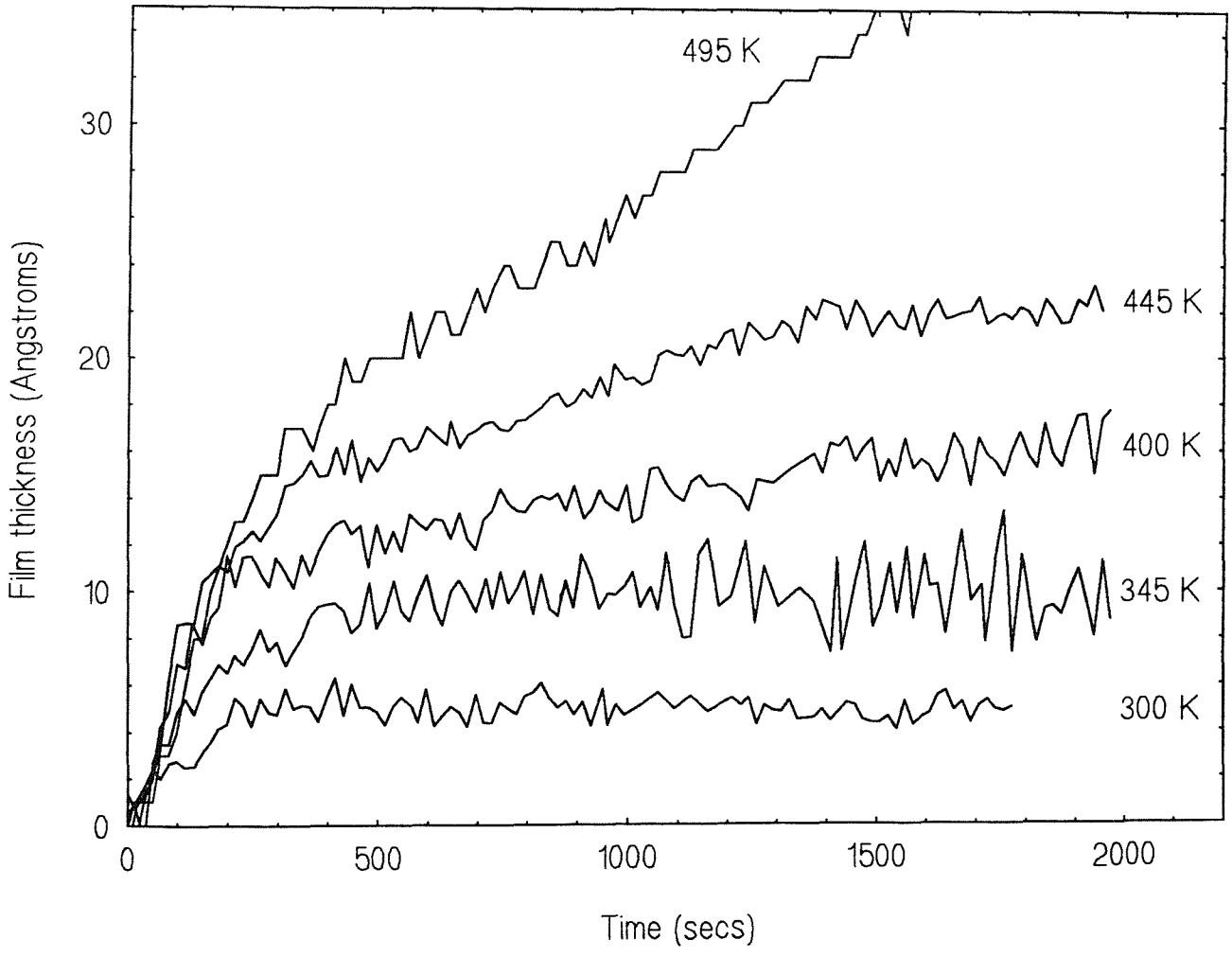

Fig. 4.20. *Film thickness versus time, PH_3 at 1 x 10^{-6} torr with Fe(100) at 300-495 K.*

The theoretical fit to the results at temperatures from 300 to 445 K (1 x 10^{-6} torr PH_3) is poor ($\delta\psi_P$ is too small and the trajectories are too short). In this case, growth rate curves can be derived more successfully if it is assumed that the magnitude of $\delta\Delta_P$ is proportional to thickness, as can be shown to a first approximation in macroscopic theory. A calibration is then provided by using the model fit to calculate the thickness at the end of the experiments. The resulting curve is shown in fig. 4.20, with the curve for 495 K (taken from fig. 4.19) included for comparison. The 300 K growth curve in fig. 4.20 is derived from the best (least erratic) $\delta\Delta_P$ result, while the results at 160 K are too poor to use.

In strong contrast to results at higher temperatures, these curves quickly reach limiting thickness. At 300 K, the model fit predicts a film thickness of atom dimensions. Repeated experiments have indicated that the growth rate at 445 K is independent of pressure. The rate of uptake in the early stages of the low temperature interaction is comparable to the rate of the fast initial stage of film growth at higher temperatures, perhaps indicating a common mechanism.

The effect of pressure on film growth is shown in fig. 4.21. The rate of film growth at a given thickness increases with increasing pressure (at least over the first few hundred Angstroms), although the form of the pressure dependency has not been determined. This indicates that the growth rate is controlled by processes at the surface of the film, at least for the lower pressure.

In contrast to the low pressure results, the growth curves recorded at 1 x 10^{-5} torr PH_3 (fig. 4.21) show a clear tendency towards limiting thickness. The curve for film growth at 520 K obeys a simple parabolic rate law, indicating that the growth rate is limited by charge or mass transport processes across the film.[43] It is not possible to describe the other curves in fig. 4.21 with a simple rate law.

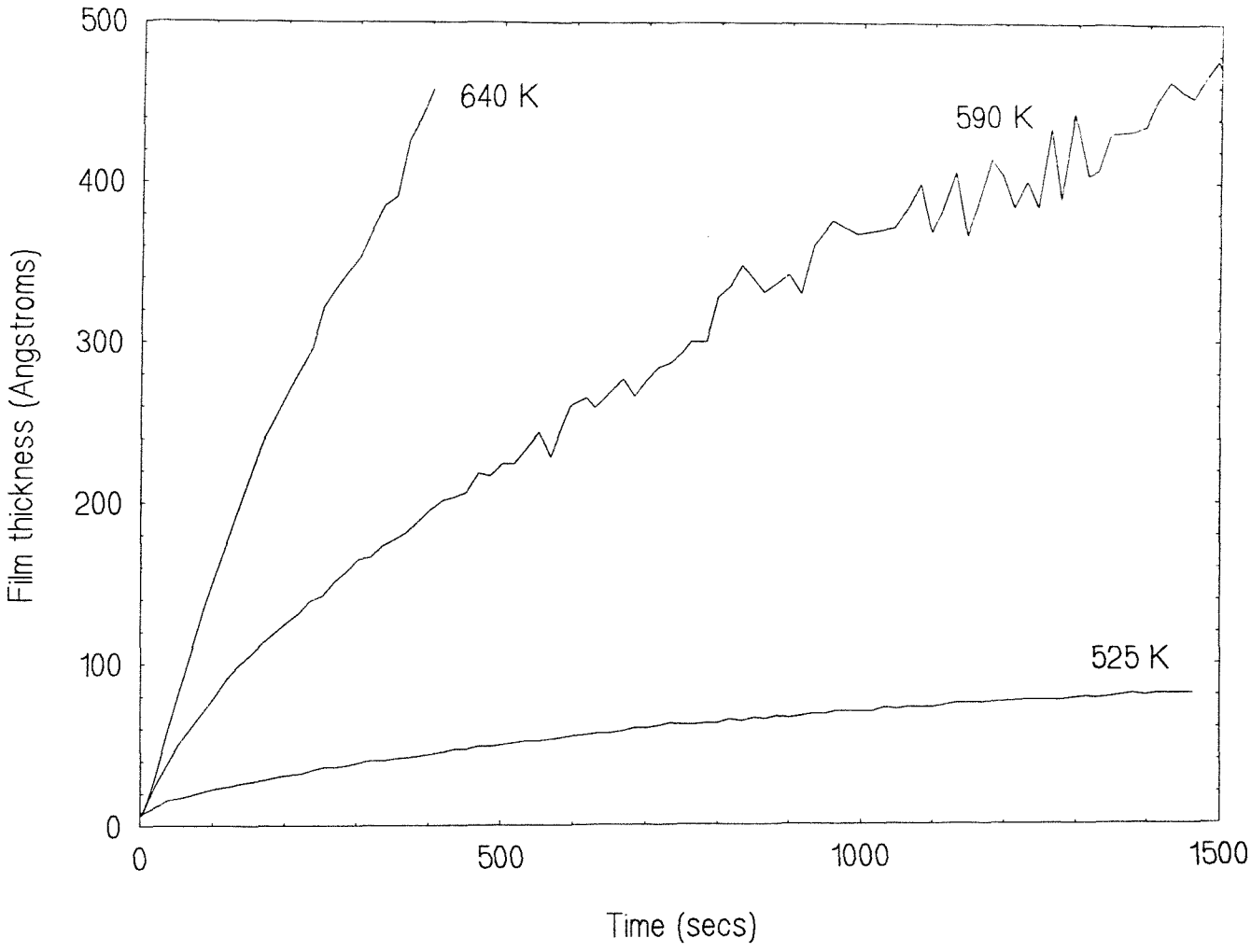

Fig. 4.21. *Film thickness versus time for interaction of PH_3 at 1 x 10^{-5} torr with Fe(100) at 520-640 K.*

As the ellipsometric results presented above (fig. 4.9) suggest, the onset of rapid growth at high temperatures (590 K and above) is delayed. Fig. 4.22 illustrates this delay, in a more informative way, where the ellipsometry results for growth at 1 x 10^{-6} torr PH_3 are converted into film thickness (this was only possible for growth at 590 and 640 K). It can be seen that at 640 K there is a period of slow growth over the first 10 Å, before the rate takes off, which is not observed at lower temperatures. At a given temperature, the delay shortens when PH_3 pressure is increased to 1 x 10^{-5} torr. Segregation of bulk impurities, interfering with PH_3 adsorption and film formation, can be discounted as an explanation because no such phenomenon is seen during oxide growth on Fe(100) at comparable temperatures (see Sect. 4.3.2).

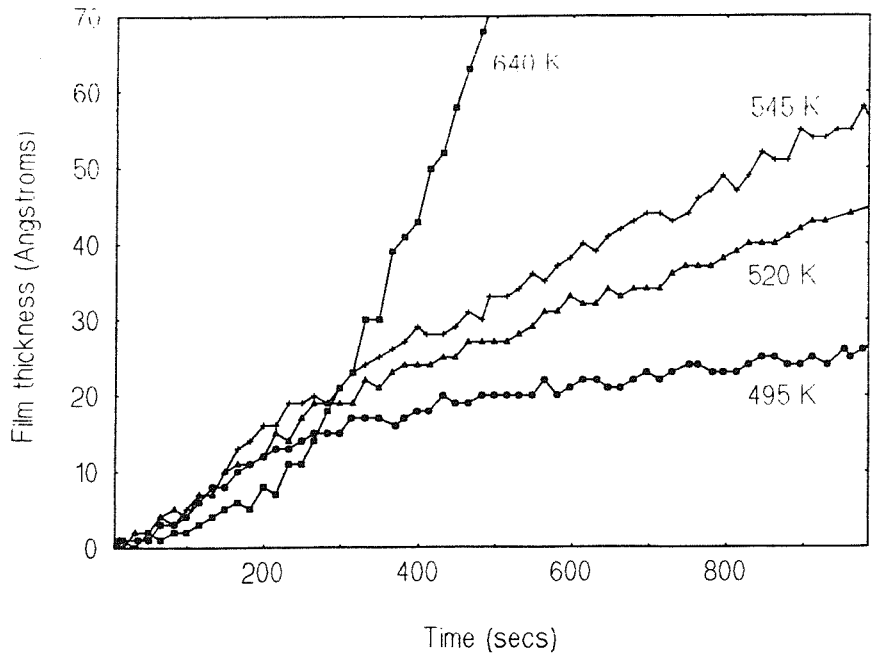

Fig. 4.22. Delay in film growth at high temperatures.

(v). LEED studies

All LEED observations were made after cooling the surface to 160 K, to improve pattern quality. Results of LEED experiments following adsorption at 160 K are described above.

Films grown during ellipsometric experiments at temperatures of 300 K and above showed no LEED features on a background of high intensity, indicating long range structural disorder in the surface layer of the film.

The effect of heating on these disordered films was investigated in LEED experiments. No phosphorus desorption was detected by the quadrupole mass spectrometer during annealing. Disordered films grown during experiments at temperatures in the range 300 to 445 K, which are estimated by ellipsometry to be no thicker than 20 Å, reconstructed to a c(2x2) structure after annealing for a few minutes at 780 K or above. Longer periods of annealing at slightly lower temperatures (715 and 755 K) did not induce ordering. In a study of the effect of preadsorbed phosphorus on the oxidation kinetics of Fe(100), reported in Sect. 4.4, a reconstructed surface obtained by annealing a disordered film grown at 445 K was found to behave like a chemisorption c(2x2)P overlayer (0.5 ML), formed by adsorption at 160 K. This suggests that the reconstructed c(2x2) structure is not simply a rearrangement in the top

layer of the film. Instead, the thin disordered films appear to have been reduced in thickness, probably through diffusion into the bulk, to leave a half monolayer of phosphorus on the surface. In contrast, the disordered films formed during experiments at 495 K and above, which are greater than 50 Å in thickness, could not be ordered by annealing at temperatures as high as 850 K and for periods up to hours.

4.2.3. Discussion

The results described above can be separated into three distinct temperature regions where, it is proposed, different processes predominate.

(i). Chemisorption at 160 K

Results of experiments at 160 K can be explained as a straightforward dissociative chemisorption process. The absence of PH_3 desorption and the TPD evidence of H_2 recombination reactions indicate that PH_3 completely and irreversibly dissociates into phosphorus and hydrogen atoms. Uptake continues until phosphorus saturates (at 0.5 monolayers) in a c(2x2)P overlayer, a widely reported chemisorption structure in low temperature adsorption studies on Fe(100). Segregated phosphorus on the Fe(100) surface has also been reported to saturate in a c(2x2) structure.[13] A structural model for a c(2x2) overlayer has already been given in fig. 4.1, where the adatoms are shown tentatively located in the fourfold symmetric hollow sites. Experiments with postdosed D_2 suggest that phosphorus may initially form into islands of c(2x2) structure during adsorption at 170 K. The desorption spectra of H_2 from dissociated PH_3 clearly show the effect of coadsorbed phosphorus. At saturation uptake, most hydrogen desorbs in a low temperature feature, the β_1^P peak, which does not correspond to any desorption feature for the clean surface. The β_1^P peak probably arises from recombination reactions where hydrogen binding energy is strongly reduced by repulsive lateral interactions with phosphorus.

In ellipsometric measurements, formation of the saturated c(2x2)P chemisorption layer can be associated with a decrease in Δ of $0.28 \pm 0.15°$.

(ii). Saturated uptake at 300-445 K

At low temperatures (300-445 K), phosphorus uptake begins immediately and rapidly approaches saturation in a structurally disordered layer. Although optical properties are difficult to determine unambiguously at these temperatures, it appears that the films are optically absorbing and have optical constants similar to those found at higher temperatures.

At room temperature and above hydrogen desorbs immediately and does not interfere with the film formation process.

The phase diagram for the Fe-P system is given in fig. 4.23. It can be seen that at very low concentrations (less than 1%) phosphorus is dissolved in the α-Fe phase for temperatures up to about 1200 K.

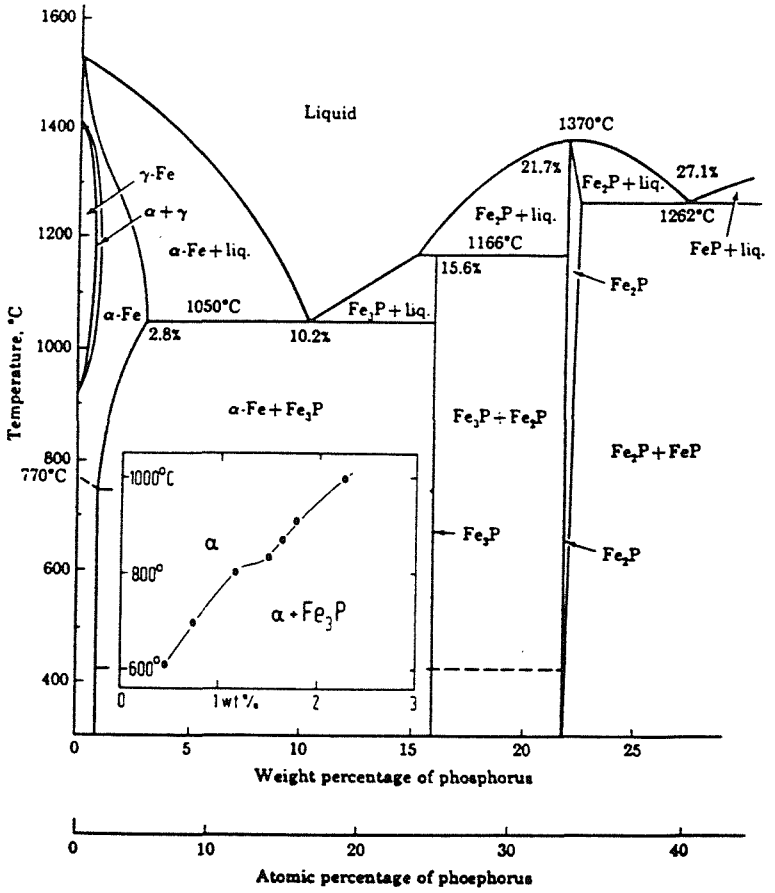

Fig. 4.23. Phase diagram of iron-phosphorus alloys.[44]

This suggests that, because of the small concentrations involved, phosphorus adsorbed at the surface may dissolve into the bulk as a solid solution, if there is sufficient energy to drive the process. We propose that the saturated films detected in ellipsometric experiments at temperatures in the range 300 to 445 K correspond to the dissolution of phosphorus into the subsurface. The following model is proposed to explain the experimental observations. At temperatures from 300 to 445 K, diffusion through the bulk is slow so that the phosphorus does not disperse into the substrate. Instead, phosphorus dissolves into the top few layers of the subsurface region, driven by a small decrease in surface free energy. The penetration depth increases slightly with temperature. Because of similarities in atomic radius,

phosphorus penetrates the substrate lattice by substitution with iron atoms,[1] a process which may cause the disordering detected in LEED. When phosphorus can penetrate no further, and the subsurface volume has become saturated, subsequent PH_3 uptake is blocked by structural changes at the surface. The optical properties of the phosphorus enriched subsurface are similar to those of the clean substrate because phosphorus does not profoundly effect the electrical and therefore optical properties of the iron. On annealing the films to 800 K, diffusion through the bulk begins at an appreciable rate and phosphorus in the subsurface region is quickly dispersed into the bulk. Phosphorus is surface active, however, and a half monolayer remains held at the surface in a c(2x2) overlayer on a substrate that has reordered into the p(1x1) structure. A similar overlayer is detected on annealing Fe(100) crystals doped with phosphorus at concentrations in the α-Fe solid solution range.[13]

As fig. 4.24 shows, the low temperature uptake curves can apparently be fitted with a logarithmic rate equation of the form

$$\textit{Thickness} = K \ln(Bt) \tag{4.2}$$

where K is a rate constant. The initial part of the 495 K curve can also be fitted with a logarithmic rate equation, which may indicate a common mechanism, as will be discussed below.

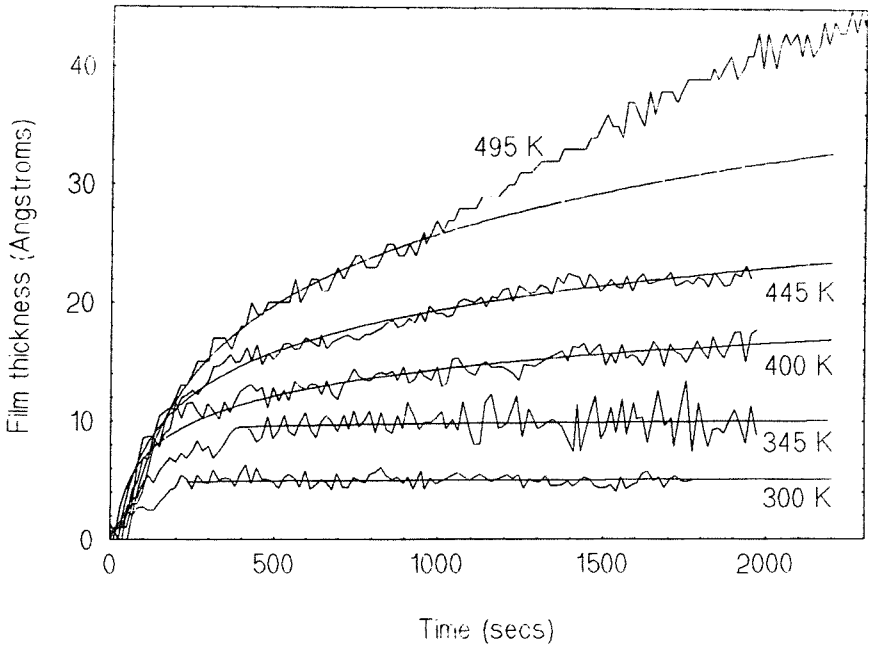

Fig. 4.24. Logarithmic fit to film growth kinetics at temperatures in the range 300-495 K.

An Arrhenius plot of K, given in fig. 4.25, yields an activation energy of 29.7 kJ mol^{-1}. This value can be associated with the process of dissolution into the subsurface region, which is arguably a place exchange mechanism of phosphorus with iron.

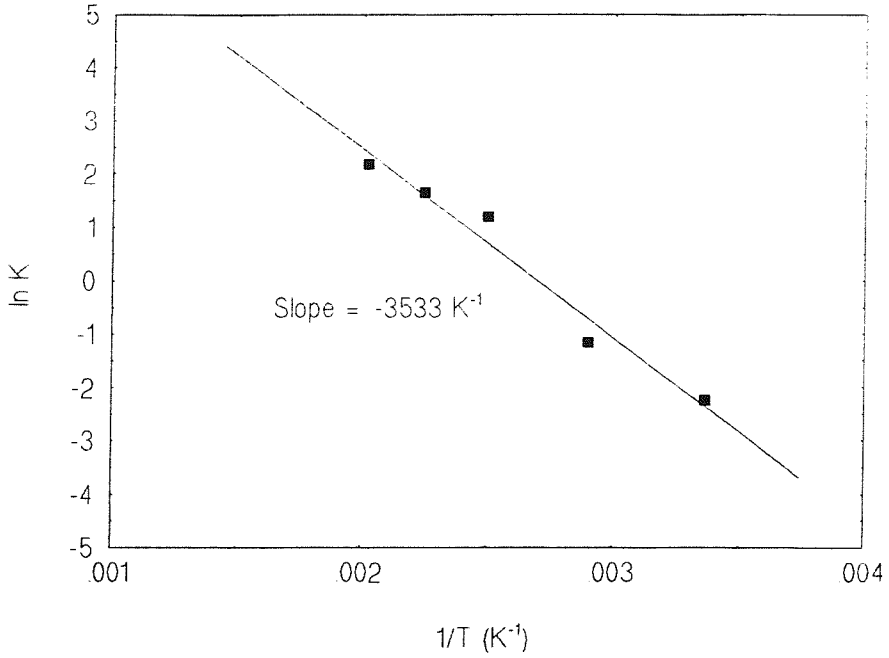

Fig. 4.25. *Arrhenius plot of logarithmic rate constant (K) for phosphorus film growth curves at T = 300-495 K.*

(iii). Rapid growth at temperatures of 495 K and above

At temperatures from 495 to 545 K, the growth kinetics can be interpreted as a two stage mechanism. The first stage shows similar kinetics to those seen during uptake at lower temperatures, suggesting that phosphorus initially dissolves into the subsurface region, substituting for iron atoms. In contrast with growth at lower temperatures, phosphorus uptake at 495 K and above does not saturate but continues in the second stage with a slower, near-linear rate.

We propose that growth in the second stage corresponds to the formation of iron phosphide. The following model is suggested to account for the experimental observations. At 495 K sufficient energy is available for the initiation of iron phosphide formation to proceed at a significant rate. Phosphorus atoms are held in the subsurface region because diffusion into the bulk is still comparatively difficult. The concentration of phosphorus near the surface then becomes sufficiently high that phosphide can be formed.

At 590 and 640 K, the onset of fast film growth is delayed. As fig. 4.21 shows, growth over the first 10 Å is much slower at 640 K compared to 545 K and below. It is suggested that at 590 K phosphorus diffusion into the bulk becomes facile. The phosphorus is quickly dispersed into the bulk so that no significant ellipsometric changes can be detected. This process competes with the initiation stage of iron phosphide growth, which consequently is slower than at lower temperatures. Eventually, however, the first layer of phosphide is formed and growth takes off at a rate determined by processes in the iron phosphide phase.

Known stoichiometric forms of iron phosphide are (in order of increasing phosphorus content) Fe_3P, Fe_2P, FeP, FeP_2 and FeP_4. To our knowledge, the optical constants of these compounds have not been reported in the literature, however, all of them are good electrical conductors and are therefore optically absorbing. The phosphorus rich phosphides FeP_2 and FeP_4 are semiconducting,[45,46] while the iron rich phosphides Fe_3P, Fe_2P and FeP tend to have metallic properties.[30] The comparatively small differences between the optical constants of the films and those of the Fe(100) surface implies that the phosphide is iron rich, *i.e.* a "metallic" phosphide such as Fe_3P or Fe_2P. There is no evidence of charge transfer between iron and phosphorus in metallic iron phosphides,[13] and the bonding between the atoms can be considered to be metallic.[29]

The initiation process for the formation of a metallic iron phosphide may well involve a rearrangement of iron about phosphorus to the ninefold tetrakaidecahedral (TKD) configuration found in bulk Fe_3P or Fe_2P.[31,32]

The P-H bonds in PH_3 are expected to homolyse, leaving uncharged phosphorus on the surface. Consequently, the growth kinetics are expected - and are found - to contrast with those for the oxidation of Fe(100), where growth is strongly rate-limited by field-controlled cation diffusion (see Sect. 4.3). Iron phosphide probably grows *into* the iron substrate, in contrast to iron oxide where the opposite is found, by the diffusion of phosphorus from the surface to the interface of the phosphide and the iron substrate. A diffusion process involving uncharged phosphorus would account for the observed parabolic rate law, seen for growth at 525 K and 1 x 10^{-5} torr (fig. 4.21).

Presumably, the reconstruction to the phosphide phase prevents phosphorus from simply dissolving away into the film. Compared to iron, the phosphide must offer a greater

resistance to phosphorus diffusion, so that phosphorus is not dispersed but can participate in phosphide growth.

The slower, near-linear growth rates observed at the lower pressure, 1 x 10^{-6} torr, may be explained if the rate of supply of phosphorus to the iron phosphide surface (*i.e.* the PH_3 collision rate) is slower than the rate of diffusion of phosphorus into the substrate, so that it becomes rate limiting.

Growth at 690 and 730 K probably involves the formation of iron phosphide. It might be expected that, as for growth at 640 K, these films have reached opaque thickness. The failure to reach a steady state point in the Δ-ψ trajectory may indicate that the optical properties of the film within the probe depth of light change with time.

(iv). Variable optical constants

The optical constants of the iron phosphide films - derived from model fits and the values of Δ-ψ at opaque thickness - vary slightly with temperature, pressure and thickness, probably because of corresponding changes in film composition. The iron phosphide layers may well be inhomogeneous, containing regions of bulk iron or dissolved phosphorus, perhaps. The variations of the optical constants might then be explained by changes in the relative composition of the different phases.

Another possible explanation, especially in thicker films, is the effects of differences in microstructure, which could include surface roughness, dislocations, or voids. A porous or cracked film could also account for the near-linear growth rate, seen at pressures of 1 x 10^{-6} torr PH_3, through a mechanism where the defects expose clean iron surfaces for reaction with PH_3 or superficial phosphorus.

4.3. Oxygen on iron: Interaction of O_2 with Fe(100) at 160-750 K

4.3.1. Introduction

In this section, results of an ellipsometric and LEED investigation into the kinetics and structural chemistry of the oxidation of Fe(100) are presented. The effect of preadsorbed phosphorus on the kinetics has also been studied (the results are described in Section 4.4) to see if any aspects of the protectiveness of phosphorus in antiwear/anticorrosion films can be modelled. The present investigation of O_2 on Fe(100), to some extent, repeats the work of Leibbrandt *et al.*,[47] but also extends the adsorption temperature range studied and perhaps more importantly correlates kinetic measurements with LEED results. Previous research on the oxidation of Fe(100) is summarised below, after the structures of bulk iron oxides are briefly described.

(i). Structure of iron oxides

Four oxides are observed during the oxidation of iron in air, namely: α-Fe_2O_3, FeO and the two "spinels" γ-Fe_2O_3 and Fe_3O_4. Their crystal structures are based on close-packed arrays of oxygen ions (O^{2-}) where iron cations occupy tetrahedral or octahedral interstitial sites (holes). The thermodynamically most stable phase α-Fe_2O_3 (which has the corundum structure, based on a hexagonally close-packed array of oxygen) has never been connected with oxide growth on Fe(100), although it is seen during the oxidation of Fe(110),[48] and is not described here in any detail. The other three compounds, all of which are possibly related to the oxide grown on Fe(100), are based on a cubic close-packed (ccp) array of oxygen ions (with one octahedral and two tetrahedral holes for each ion). The lattice parameter of the oxygen ccp lattice increases linearly with iron content across the range of composition of these oxides.[49]

The monoxide FeO ideally has the rock salt (NaCl) structure, where Fe^{2+} ions occupy all of the octahedral holes, but always shows a cation deficiency that can vary from 5 to 15 atomic%. The lattice parameter varies linearly with composition, for example in $Fe_{0.94}O$ a = 4.3010 Å while in $Fe_{0.91}O$ a = 4.2816 Å.[50]

The mixed oxide Fe_3O_4 has the inverse spinel structure, with a lattice parameter of 8.3967 Å.[51] The valence structure is $(Fe^{3+})_{TET}(Fe^{3+}Fe^{2+})_{OCT}(O^{2-})_4$, where half of the Fe^{3+} ions and all of the Fe^{2+} ions are found in the octahedral holes (OCT), and the other half of the Fe^{3+} ions occupy the tetrahedral holes (TET). In this structure, the distance corresponding to the lattice parameter of FeO (which is effectively the lattice parameter of the fcc unit cell of the oxygen lattice) is 4.20 Å. Fe_3O_4 transforms into FeO on heating in air, at temperatures above 843 K.[52]

The metastable phase γ-Fe_2O_3 has a disordered spinel structure, where Fe^{3+} ions are distributed randomly among the tetrahedral and octahedral holes, with a slightly smaller lattice parameter, compared to Fe_3O_4, of 8.33 Å.[53] γ-Fe_2O_3 is formed from Fe_3O_4 with moderate annealing in air.

(ii). Literature review: the oxidation of Fe(100)

The interaction of oxygen with Fe(100) has been studied widely with a variety of surface techniques, mainly at room temperature and low pressure (typically in the 10^{-8} to 10^{-6} torr range). It is generally accepted that the interaction begins with a fast process involving dissociative chemisorption and rearrangement to form a surface oxide, and is then followed by the slow growth of a three-dimensional oxide (approaching a limiting thickness of a few Ångstroms, at room temperature). However, much of the detail of this complicated process remains unknown, or is controversial.

Oxidation is preceded by the dissociative chemisorption of O_2, as indicated by electronic structure studies.[10,14,54,56] During the chemisorption stage at room temperature, the sticking coefficient *S* (determined from AES and PES uptake measurements[10,14,54-57]) is initially high, probably close to unity on the clean surface, but decreases rapidly with exposure to a minimum at about 20% of the initial value. Several LEED studies[10,14,58,59] found that chemisorbed oxygen formed a c(2x2)O overlayer during adsorption at room temperature, which at saturation (0.5 monolayers) could be linked[10,14] with the minimum in *S* (quantitative AES gave a consistent coverage[10]). However, other groups[3,8,56,57,60] have failed to observe the c(2x2)O pattern - even with careful experiment[57] - for reasons unknown. Simmons and Dwyer[10] have proposed that chemisorption involves molecular oxygen as a mobile precursor,

although there has been no evidence of such a species until recently.[55]

With increasing uptake at room temperature, oxygen forms a p(1x1)O structure.[3,5,10,14,46,54,56,58-62] The p(1x1) LEED pattern was observed, after c(2x2)O spots (if present) had faded. The uptake range for this structure correlated with the upswing in *S* beyond the minimum,[10,14,54] although Legg *et al.*[57] suggested that saturation of the p(1x1)O structure at monolayer (and not the c(2x2)O structure) corresponds to the minimum in *S*. All studies agree that the p(1x1)O pattern disappears with increasing oxygen uptake and most have indicated that the surface of the room temperature oxide at saturation is disordered. The coverage range of the p(1x1)O structure has been estimated by quantitative AES[8,10] to be from 0.5 to 2 ML, although van Zoest *et al.*[62] claimed that the adsorbed oxygen was disordered at 1 ML.

The p(1x1)O structure has the same cubic symmetry as, and similar dimensions to, the basal plane of bulk FeO. A LEED analysis of one monolayer of the p(1x1)O structure, by Legg *et al.*,[57] determined that oxygen atoms sink into the four-fold hollow sites (theoretically, the lowest energy configuration[61]) causing an outward relaxation of the top layer of Fe atoms and an increase in the first interlayer spacing of 7.5% compared to the bulk. This distortion does indeed tend towards the structure of the (100) surface of FeO (a NaCl type lattice) but without any significant change in dimensions towards the larger unit mesh expected for bulk FeO. The lattice parameter of bulk FeO varies with composition (the monoxide is always found to be cation deficient), but typical values are[50] 4.3010 Å for $Fe_{0.94}O$ and 4.2816 Å for $Fe_{0.91}O$. The corresponding distance in the p(1x1)O-Fe(100) structure is 4.04 Å. Correlated changes in the electronic structure have also indicated the formation of an oxide.[10,14,54] It appears that the low coverage p(1x1)O structure is best described as a surface oxide.

The characterisation of the limiting thickness oxide at room temperature is controversial. As noted above, nearly all structural studies reported no further changes in the LEED after the p(1x1) pattern had disappeared, indicating that the top layer is disordered. Leygraf and Ekelund,[3] however, saw the emergence of poor cubic patterns at high exposure, which they attributed to a spinel type oxide of lattice parameter $a = 8.4 \pm 0.1$ Å. The two stoichiometric phases Fe_3O_4 and γ-Fe_2O_3 have the spinel structure and similar lattice parameters of 8.3967 Å[51] and 8.33 Å,[53] respectively. The electron energy loss spectroscopy (EELS) study of Sakisaka *et al.*,[54] also indicated the formation of a spinel, characterised as

γ-Fe_2O_3, but the structure was disordered, as indicated by LEED. However, Leibbrandt *et al.*,[63] combining high energy ion scattering (HEIS) and ellipsometric measurements, deduced the formation of the monoxide $Fe_{0.95\pm0.07}O$. The PES measurements of Brucker and Rhodin[14] also suggested the formation of FeO. The thickness of the room temperature oxide at saturation has been variously estimated as: either 10 Å[63] or 15 Å[64] by ellipsometry, 15 Å by depth profiling[60] and 20 Å by reflection high energy electron diffraction (RHEED).[8] Oxygen uptake at saturation has been estimated at about 4 monolayers, by nuclear reaction analysis.[47,63]

A few studies have reported observations for the oxidation of Fe(100) at temperatures other than 298 K. In a study of O_2 adsorption at 103 K, Lu *et al.*[55] found that after dissociation oxygen saturates in a disordered phase at a coverage of greater than 1 monolayer. Their high resolution electron energy loss spectroscopy (HREELS) results indicate that oxygen initially occupies the four-fold hollow sites, but also fills the bridging and perhaps on-top sites as coverage increases. In a RHEED study of oxidation at 420 K, Sewell *et al.*[8] found a sequence of diffraction patterns. With increasing exposure, they observed the formation of a p(1x1)O structure at one monolayer, followed by the growth of what they termed a face centred cubic (fcc) oxide with a lattice parameter of about 4.10 Å (they did not consider it to be FeO), and finally a spinel type oxide of lattice parameter 8.34 $\pm$ 0.06 Å. Leygraf and Ekelund,[3] in a LEED study of oxidation at 400 K, also reported a similar sequence of structures culminating with a spinel. Leibbrandt *et al.*,[47] however, characterised an oxide grown at 470 K as the monoxide $Fe_{0.95\pm0.07}O$.

Electron spectroscopy and ellipsometry have proved to be complementary techniques in the measurement of the oxidation kinetics of Fe(100). While the sensitivity of AES and PES is best-suited for measurement of the early stages of the interaction, the much larger probe depth of ellipsometry allows the study of bulk-like oxide growth (it has been shown that AES fails to describe the full uptake curve at room temperature[60]). Several workers have reported room temperature measurements.[60,63,64] In one of these studies, Leibbrandt *et al.*[63] have found a linear relationship between the ellipsometric parameter Δ and oxygen uptake. Their recently reported ellipsometric results[47] for oxidation at temperatures from 300 to 570 K (discussed in more detail in Sect. 4.3.3) emphasise the contrast between the vigorous growth over the first few hundred Langmuirs and the comparatively negligible growth at higher exposure. Uptake saturates during oxidation at 420 K and below, but not at higher temperatures.

The kinetics of the early stages of the oxidation of Fe(100) has been modelled by Simmons and Dwyer.[10] They propose that islands of two-dimensional FeO nucleate and grow, with molecular oxygen acting as a mobile precursor state, until they coalesce. The O_2 precursor then saturates over the top in a liquid-like layer - which would account for the diffuse LEED pattern - and the rate of further uptake is determined by processes in the three-dimensional oxide. Leibbrandt *et al.*[47] have modelled the kinetics of the later stages of oxide growth, at different temperatures, using the "coupled currents" oxidation theory of Fromhold and Cook[65-67] (see Sect. 4.3.3).

The effect of annealing on the oxide layers has been investigated in some detail. The disordered, room temperature oxide is consistently reported to reconstruct, at temperatures from 470 to 1023 K, to give cubic diffraction patterns of the same symmetry and comparable dimensions to the substrate.[3,10,56-58,60] In the most obvious interpretation these patterns have been attributed to FeO, grown with the FeO(100) plane parallel to the substrate surface, and the FeO[010] and Fe[110] directions running together.[3,10,54,58] Sakisaka *et al.*,[54] who had characterised the disordered oxide as γ-Fe_2O_3, saw changes in electronic structure consistent with reconstruction to FeO. Leygraf and Ekelund[3] reported lattice parameters ranging from 4.04 to 4.34 Å with increasing O_2 exposure, which they interpreted as intermediate stages on the way to the formation of bulk FeO.

However, recent results have prompted a different interpretation of the observed structural chemistry. The depth-profiled low energy ion scattering (LEIS) experiments of Vink *et al.*[60] indicated that an annealed (640 K) room temperature oxide, which showed a cubic LEED pattern, consisted of a thin oxygen-rich layer on top of a different incorporated oxide phase, about 50 Å thick. They concluded that the top layer was a monolayer of oxygen, and labelled the structure p(1x1)O. In support, a LEIS structural analysis by van Zoest *et al.*[62] suggested that the structure of the p(1x1)O layer on top of the incorporated oxide was identical to the structure of a monolayer of oxygen on the Fe(100) surface (their structural determination of the oxygen monolayer agreed with the LEED analysis of Legg *et al.*[57]). In the low temperature study of Lu *et al.*,[55] thin saturation layers of oxygen grown at 103 K were also found to reconstruct to a p(1x1)O structure. Their results indicated that the oxygen coverage had reduced to monolayer through diffusion into the bulk.

Simmons and Dwyer[10] reported another coverage dependent LEED pattern on annealing a disordered room temperature oxide at 470 K, which they attributed to the two orientations of the (111) plane of FeO. Lu *et al.*[55] also observed this pattern when annealing a 103 K saturated oxygen layer at temperatures in the range 573 to 723 K. They proposed that this structure is an unstable intermediate in the transition between disorder and the p(1x1)O structure.

From this literature survey it can be seen that many aspects of the interaction of O_2 with Fe(100) remain unclear. Further studies are necessary for a clearer understanding of the processes involved. A general conclusion appears to be that Fe(100) promotes the growth of an epitaxial array of cubic close-packed oxygen ions where iron occupancy of the interstitial sites varies, in a way that is not clearly understood, so that composition can range from close to FeO to that of a spinel (Fe_2O_3 or Fe_3O_4). The details of the early stages of the interaction, the reasons for the varying composition and structure of the saturated room temperature oxide and the effect of annealing remain controversial. There is also a lack of information for oxide growth at different temperatures.

(iii). Fromhold-Cook theory of oxidation

Numerous theories have sought to explain the oxidation of metals and the kinetics of oxide growth by considering the various mass and charge transport processes that can occur as an oxide grows (see the reviews by Lawless[42] and Smeltzer and Young,[68] for example). Mechanisms of mass transport include the diffusion of interstitial ions or vacancies while quantum mechanical tunnelling and thermionic emission are examples of electron transport processes important in thin (50-500 Å) and very thin (5-50 Å) oxide films. An important theoretical consideration is the effect on ion and electron transport - and therefore oxidation rate - of surface-charge and space-charge electric fields, which develop with asymmetric distributions of charged defects during growth.

Fromhold and Cook have developed a general theory of oxidation, covering all scales of film thickness (from atomic to macroscopic), where different rate equations are obtained by considering various possible combinations of charge and mass transport processes (a detailed treatment is given in two monographs by Fromhold[69,70]). In formulating the rate equations,

they use a *coupled currents* approach where the condition of equal but opposite electronic and ionic currents is used to obtain an evaluation of the electric field as a function of other boundary conditions. The equations can only be solved by numerical analysis.

This approach has been used to study the growth of very thin oxide films (up to a few tens of Angstroms thick), where tunnelling and thermionic emission are expected to be the dominant modes of electron transport. Fromhold and Cook's description of the early stages of oxidation is essentially an extension of earlier theories due to Mott,[71,72] and Cabrera and Mott,[72] which appear as limiting cases in the general theory. Mott was first to propose that electron tunnelling[71] and thermionic emission, coupled with electric field enhanced ion diffusion,[72] were possible rate controlling processes. These ideas were developed in the theory of Cabrera and Mott[73] which holds that electrons from the metal can readily cross the oxide to ionise oxygen on the surface so that the electrochemical potential of electrons at both interfaces of the oxide is in equilibrium. The resulting potential creates a homogeneous, surface-charge electric field promoting the diffusion of metal cations across the oxide, which is assumed to be rate limiting. Exact solutions to the equations are impossible, but by approximation the theory predicts an inverse logarithmic rate law

$$\frac{1}{X} = A - B\ln(t) \tag{4.3}$$

where X is the oxide thickness at time t, and A and B are constants.

Calculations of the Fromhold and Cook theory for growth controlled by electron tunnelling and ion diffusion[67,69] indicate that initially electron current equilibrium is achieved so that the rate is limited by ionic diffusion, giving a rate equation of the same form predicted by the Cabrera and Mott theory (inverse logarithmic, eq. (4.3)). There then follows a sharp transition at a thickness of about 20-30 Å where, because of current attenuation, electron tunnelling becomes rate limiting. At this stage, the rate is predicted to obey a direct logarithmic law

$$X = A\ln(Bt) \tag{4.4}$$

in agreement with the Mott model,[71] so that in the absence of any other electron transport mechanism growth is effectively halted.

For growth at temperatures where thermionic emission is also possible, the theory predicts that initially electron tunnelling predominates, but only over a limited thickness range (about 30-50 Å at room temperature) before the current is attenuated completely. In thicker films thermionic emission becomes the only possible electron transport mechanism and allows the continuation of growth beyond the limit set by electron tunnelling. Calculations for growth controlled by thermionic emission and ion diffusion[67,69] predict an inverse logarithmic (eq. (4.3)) or parabolic rate law

$$X^2 = At + B \tag{4.5}$$

when ion diffusion is rate limiting (at high temperatures, when ion mobility is low, or where the energy barrier to electron emission is small). When the thermionic emission current is rate controlling (lower temperatures, highly mobile ions, or large energy barrier to emission) the rate is adequately described by a Schottky emission equation.[65]

4.3.2. Results

The interaction of O_2 with Fe(100), at sample temperatures from 160 to 610 K and O_2 pressures of between 1 x 10^{-7} and 1 x 10^{-6} torr, was investigated with fixed wavelength ellipsometry (λ = 632.8 nm, angle of incidence = 70°) and LEED.

(i). Changes in Δ and ψ versus time

Fig. 4.26 shows the development of the ellipsometric parameters $\delta\Delta_o$ and $\delta\psi_o$ (Δ and ψ measured relative to the values of the clean surface) during experiments at an O_2 pressure of 1 x 10^{-6} torr and sample temperatures in the range 160-470 K. For clarity, the large changes in $\delta\Delta_o$ and $\delta\psi_o$ during film growth at 610 K are shown, separately, in fig. 4.27.

In contrast to the experiments with PH_3 (Sect. 4.2.2) the change in Δ and ψ is effectively immediate at all temperatures and, consequently, zero on the timescale marks the start of the dose. Changes in Δ during experiments with O_2 are much larger, and more easily measured, than those found with PH_3 at comparable temperatures and over similar timescales (figs. 4.10 and 4.11).

Both Δ and ψ decrease when the surface is exposed to O_2. At all temperatures studied (160-610 K), the rate of decrease of Δ is initially very rapid but then quickly decelerates. For temperatures up to 420 K, $\delta\Delta_o$ apparently reaches a steady state value within the timescale of experiments (about 40 minutes). The size of the steady state value ($|\delta\Delta_o|$), and the time taken to reach it, increases with increasing temperature. As will be discussed in the next section, these results are qualitatively similar to data published by Leibbrandt *et al.*[47] (for temperatures in the range 300 to 570 K), but there are some significant quantitative differences. The steady state value of $\delta\Delta_o$ at room temperature is found to be 3.4 $\pm$ 0.1° in the present work. This agrees with the value of 3.5 $\pm$ 0.1° reported by Leibbrandt *et al.*[63] and also Vink *et al.*[60] (who only reported data for this temperature). However, as will be discussed below, Leibbrandt *et al.*[47] reported steady state values of $|\delta\Delta_o|$ at higher temperatures that are significantly larger than those found in the present work.

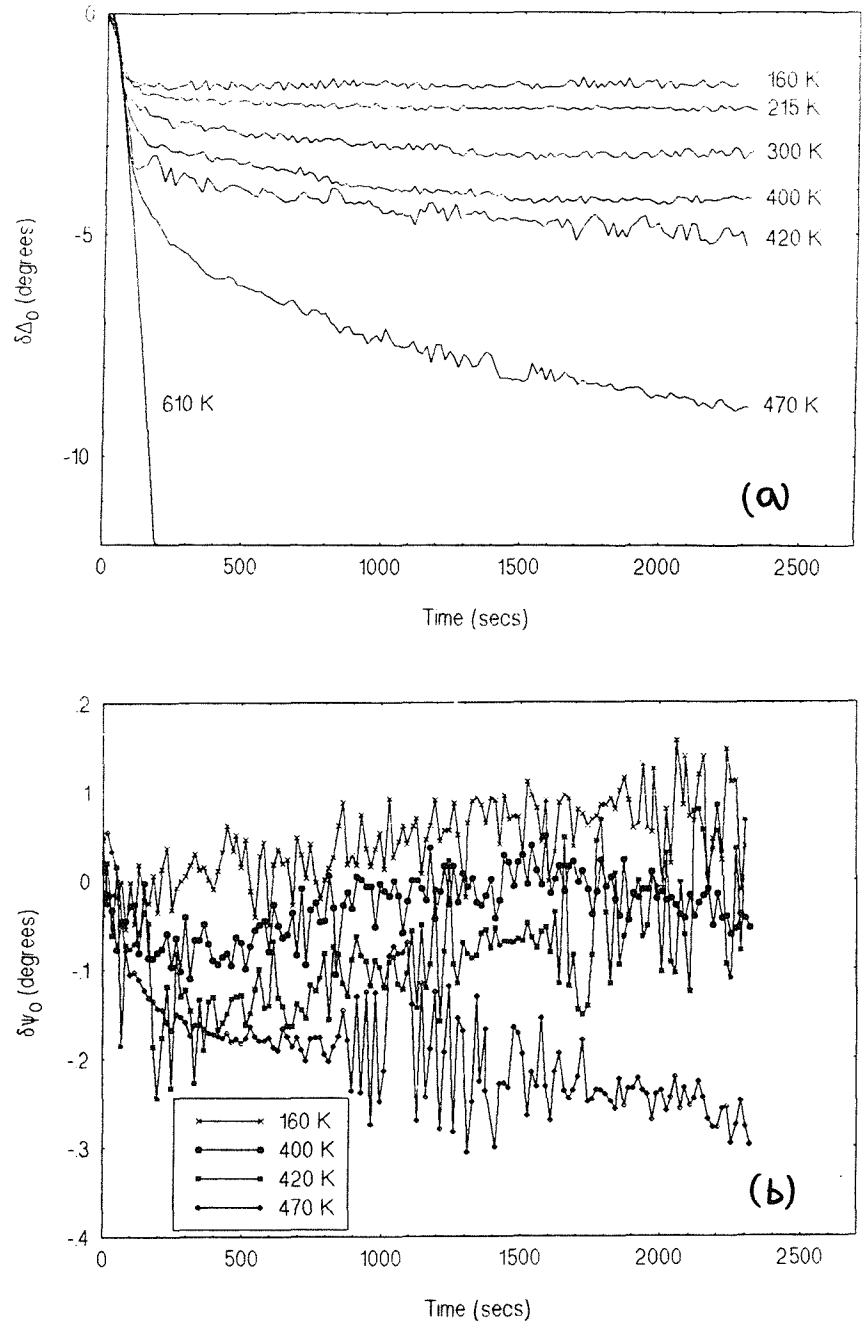

Fig. 4.26. *(a) $\delta\Delta_o$ and (b) $\delta\psi_o$ versus time for interaction of O_2 at 1 x 10^{-6} torr with Fe(100) at 160-470 K.*

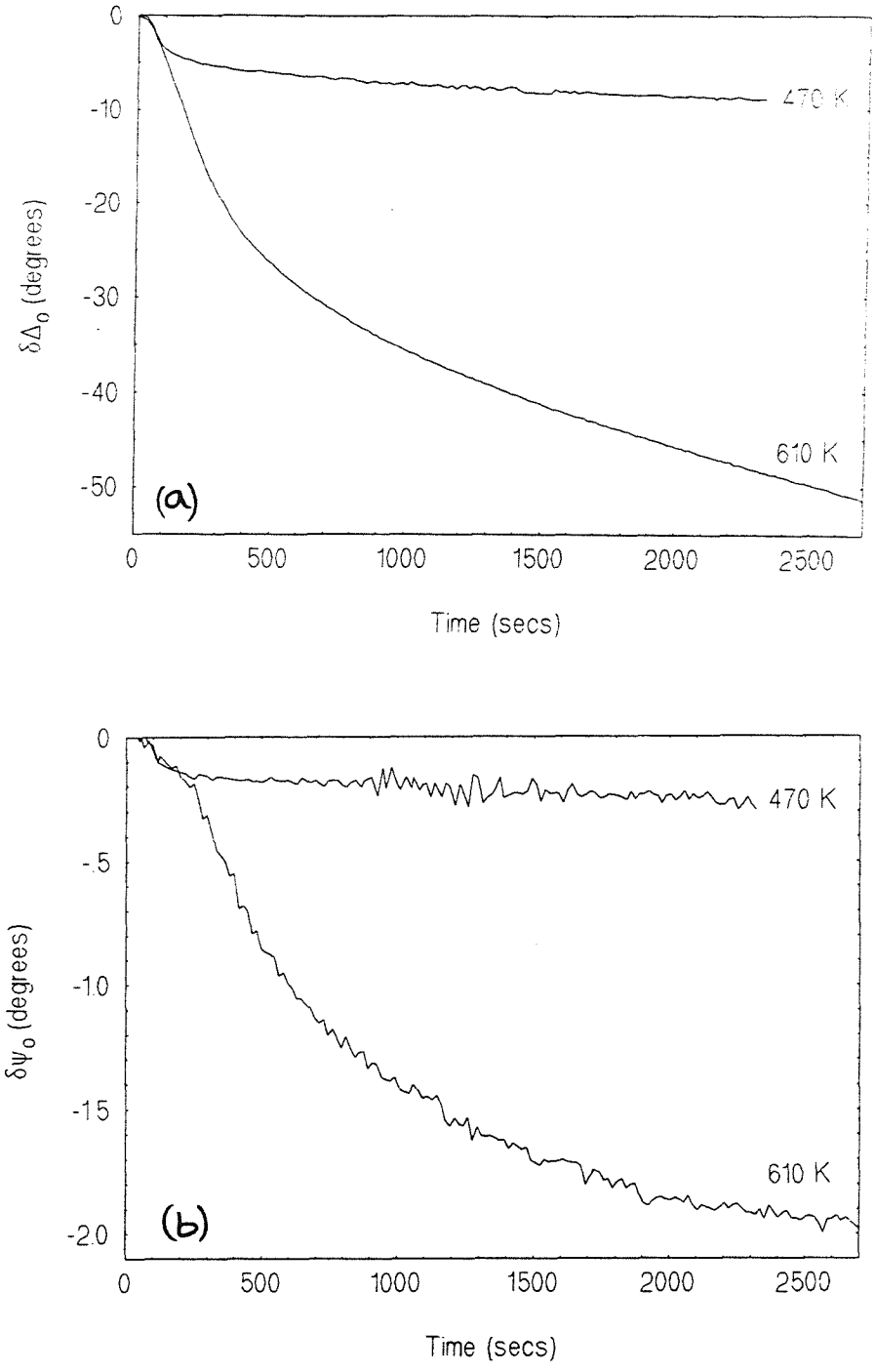

Fig. 4.27. *(a) $\delta\Delta_o$ and (b) $\delta\psi_o$ versus time for interaction of O_2 at 1 x 10^{-6} torr with Fe(100) at 610 K, compared to 470 K.*

The corresponding changes in ψ during experiments with O_2 are comparable in size to those found for PH_3. Once again, the time dependency of $\delta\psi_0$ is difficult to detect behind the unstable background. At 470 and 610 K, an initially fast decrease in $\delta\psi_0$ is followed by much slower changes over longer periods of time. At lower temperatures, an initially fast drop in ψ over the first 100 seconds can be recognised but $\delta\psi_0$ tends to vary over time in a way that is not reproducible. It is expected that ψ has reached a steady state value in these low temperature experiments, as for Δ. Of the results not included in fig. 4.26 (for clarity), the $\delta\psi_0$ curve at 215 K was completely erratic while the curve for 300 K was comparable to that for 400 K.

Fig. 4.28 shows that O_2 pressure, in the range 1 x 10^{-7} to 1 x 10^{-6} torr, affects the time dependency of $\delta\Delta_0$ during room temperature experiments. In particular, pressure has a strong effect on the fast decrease in Δ when the surface is first exposed to O_2.

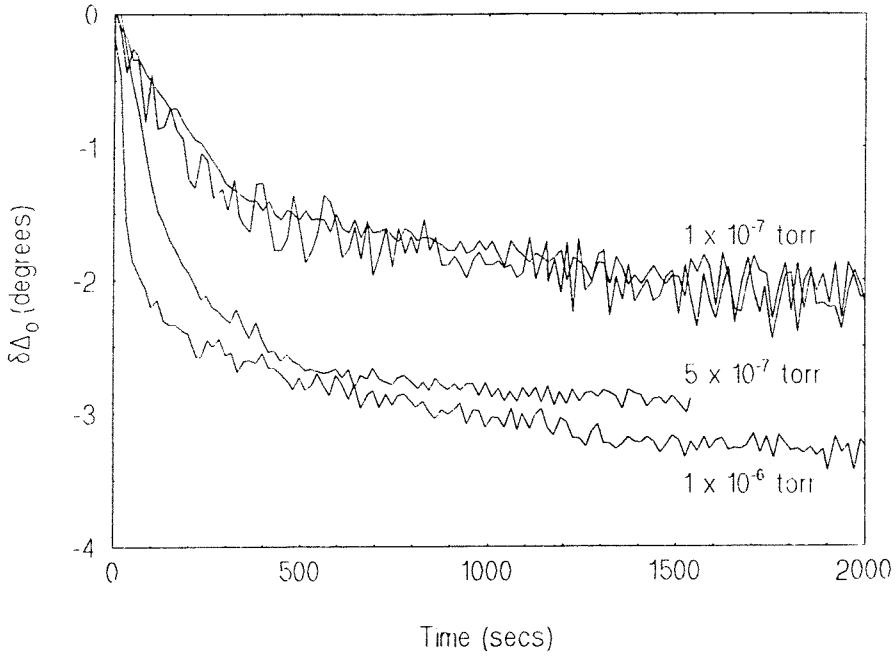

Fig. 4.28. Pressure dependency of change in $\delta\Delta_0$ with time at 300 K.

Leibbrandt *et al.*[47,63] have shown that $\delta\Delta_0$ is directly related to oxygen uptake. As will be discussed below, the steady state values of $\delta\Delta_0$ at temperatures of 300 K and above (and perhaps at lower temperatures, too) are associated with the formation of iron oxides grown to limiting thickness.

(ii). Analysis of Δ-ψ plots

The relative measurements $\delta\Delta_0$ and $\delta\psi_0$ have been calibrated to give Δ-ψ plots, by deriving absolute values for Δ and ψ from the literature (for details see the PH_3/Fe(100) results in Sect. 4.2.2). The trajectory for the experiment at 610 K shown in fig. 4.29 is well-developed, but in contrast to the results for PH_3 there is no indication of a tendency towards a steady state region of the Δ-ψ plane within the time scale of the experiment.

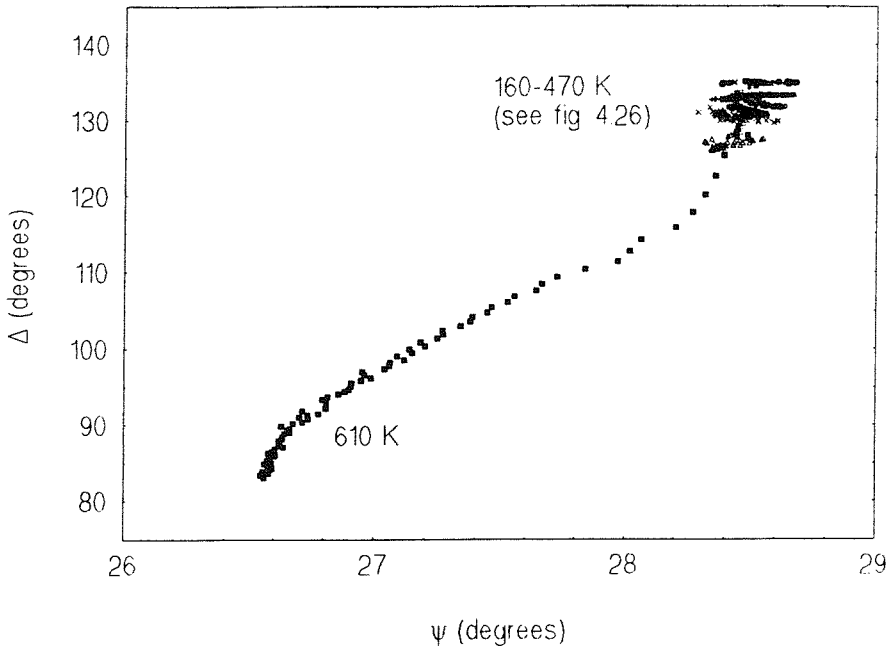

Fig. 4.29. *Experimental Δ-ψ trajectory interaction of O_2 1 x 10^{-6} torr with Fe(100) at 610 K.*

The trajectories for experiments at temperatures from 160 to 470 K are shown in detail in fig. 4.30, along with the initial part of the 610 K curve. If the scatter in ψ is ignored then the trajectories at all temperatures studied follow the same path, which is clearest for the 610 K result. The scatter in ψ (about ± 1.5° either side of the 610 K trajectory) is related to instability in the measured signal, rather than changes in optical properties as can be seen by the comparable size of scatter for the clean surface. It is not clear why these experiments suffered from a comparably large background instability.

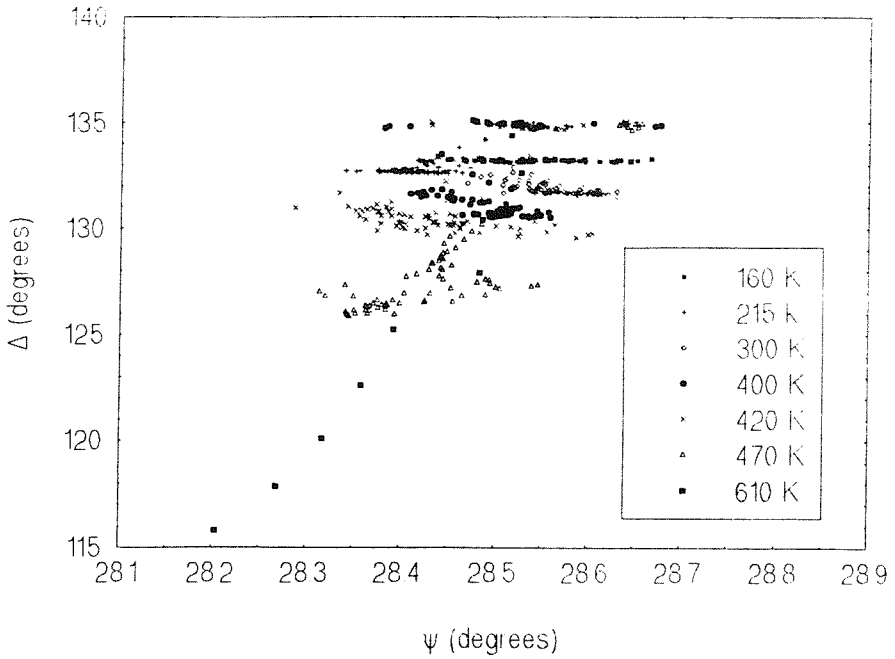

Fig. 4.30. *Experimental Δ-ψ trajectory for interaction of O_2 at 1 x 10^{-6} torr with Fe(100) at 160-470 K.*

The literature (reviewed in Sect. 4.3.1) clearly shows that iron oxides are formed when O_2 interacts with Fe(100) at temperatures of 300 K and above (this assertion cannot be made for lower temperatures where there is a lack of published experimental data). The scatter in ψ hinders interpretation, but the collinearity of the trajectories in fig. 4.29 suggests that optically similar iron oxides have grown at temperatures in the range 160-470 K, and in the initial stages, at least, of growth at 610 K. At lower temperatures (160-420 K) the oxides have grown to a limiting thickness and the trajectories have terminated.

We were unsuccessful in attempts to model the experimental Δ-ψ trajectories using the Drude equations. Iron oxides are optically absorbing (they are semiconducting), and so, to find a fit it was necessary to know, or have some idea of, one or more of the three film parameters *n*, *k* and thickness. Because the experimental trajectories did not tend towards a steady state Δ-ψ point, there was no indication of the optical constants of the film (as there was for PH_3 on Fe(100)), and we were unable to find optical constants for iron oxides in the literature. Trial and error did not reveal any reasonable fit to any part of the data. As will be discussed below, film thickness could be estimated at the end of experiments at temperatures from 300 to 470 K. However, attempts to find a fit using the estimated thicknesses and their associated Δ and ψ values failed to produce reasonable fits (presumably because of errors in Δ, ψ, and the estimated thickness). Leibbrandt *et al.*[47] did not publish changes in ψ, nor report any analysis of the optical properties of oxides grown.

That the Δ-ψ trajectory for oxidation at 610 K curve did not reach a steady state probably indicates that the film did not grow beyond the probe depth of the light. Alternatively, the optical properties of the oxide, sampled by the probe depth, may have changed during growth. Consistent with this, phase transitions between various iron oxides have been found during the oxidation of Fe(110)[48] and the oxidation of iron in air (see work reviewed by Atkinson[74]).

(iii). LEED studies

All LEED observations were made after cooling the surface to 160 K, to improve the quality of the patterns. During oxidation at 300 K, the surface gave a p(1x1) pattern which became weaker with increasing O_2 exposure until, after about 70 L, no features could be observed. The limiting thickness oxide grown during ellipsometry experiments at 300 K also showed no LEED features on a background of high intensity, indicating complete long range structural disorder. These observations are in good agreement with the literature[3,8,10,14,57-60] (see discussion). A similar transition to disorder was detected during adsorption at 160 K, where all LEED features disappeared after exposures of about 5 L (comparing well with results reported[55] for adsorption at 103 K). Saturated phases formed after ellipsometric experiments at 215 and 400 K also showed diffuse LEED patterns. Apparently, the surface layer of films formed during the interaction of O_2 with Fe(100) at temperatures from 160 to 400 K is disordered on the long range scale.

In contrast, new features in a cubic LEED pattern (fig. 4.31) were observed after oxidation (during ellipsometric experiments) at 420, 470 and 610 K. The pattern was faint at 420 K and sharper at the higher temperatures. This pattern has been reported by Leygraf and Ekelund[3] after oxidation at 400 K, and by Sewell *et al.*[8] after oxidation at 420 K. Following their interpretations, the pattern can be attributed to the formation of a spinel-type oxide.

The thermal stability of the disordered surface and the spinel-like structure was also investigated in LEED experiments. No oxygen desorption was detected by the quadrupole mass spectrometer during annealing. The disordered room temperature oxide reconstructed to give a well-ordered (sharp LEED spots on a low intensity background) p(1x1) structure after annealing at temperatures from 750 to 800 K for a few minutes. The disordered phase

formed at 160 K also showed a p(1x1) LEED pattern after annealing at 550 K for 10 minutes. These observations are in accordance with the literature.[3,10,55,57,58,60]

The spinels were stable to short, high temperature anneals (2 or 3 minutes at 700 K), but after longer periods they reconstructed to a p(1x1)O structure. Similar observations were made by Leygraf and Ekelund.[3]

(a) (b)

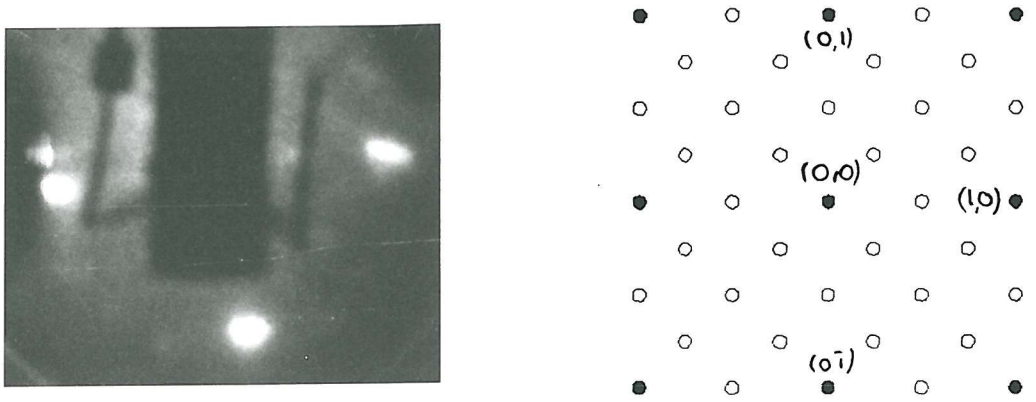

Fig. 4.31. (a) LEED pattern of spinel iron oxide (E = 62 eV) with (b) schematic representation of positions of iron oxide spots (open circles) compared to first-order Fe(100) spots (filled circles).

4.3.3. Discussion

Leibbrandt *et al.*[47] have published results of a similar ellipsometric study of the temperature dependence of the oxidation of Fe(100), but at a wavelength of 554 nm. They have reported the variation of $\delta\Delta_o$ (but not $\delta\psi_o$) at sample temperatures from 300 to 575 K. Although there is broad qualitative agreement between their results and the curves determined in the present work (figs. 4.22 and 4.23), the quantitative match is poor. Leibbrandt *et al.*[47,63] have shown that the size of $\delta\Delta_o$ ($|\delta\Delta_o|$) is directly proportional to oxygen uptake, at least up to $|\delta\Delta_o| = 20°$. Consequently, differences between the two sets of results imply that the oxidation kinetics in the two studies are dissimilar.

(i). Structural chemistry

The LEED observations described above are in good agreement with the literature,[3,8,10,14,55,57-60] although we did not observe the occasionally-reported c(2x2)O chemisorption structure,[10,14,58,59] nor the room temperature spinel reported by Leygraf and Ekelund.[3] Following conclusions in the literature, it can be assumed that the p(1x1) pattern observed in the later stages of the interaction at 300 K is associated with the development of the first layer of oxide. The absence of LEED features for the saturated oxide at room temperature has been explained by the formation of a disordered layer of chemisorbed oxygen on top of the oxide.[10] The same conclusion can be made for the saturated surfaces at 160 and 215 K. The p(1x1) pattern observed on annealing the disordered room temperature surface has often been attributed[3,10,54,58] to the formation of the monoxide FeO, although recently it has been interpreted as showing the formation of an ordered monolayer of chemisorbed oxygen atoms on top of an oxide phase.[60] As noted above, the pattern observed during oxidation at temperatures of 400 K and above can be attributed to the formation of a spinel-type oxide.[8]

(ii). $\delta\Delta_o$ as a measure of oxygen uptake

Measuring oxygen uptake with nuclear reaction analysis (NRA), Leibbrandt *et al.*[47] found a linear relationship between $|\delta\Delta_o|$ and oxygen uptake for coverages up to at least

30 x 10^{15} O atoms cm^{-2} (equivalent to 24 ML). Their $\delta\Delta_O$ measurements were then calibrated using a proportionality constant (not stated) of about 0.69° *per* 1 x 10^{15} O atoms cm^{-2}. Errors associated with the calibration and the measurement of $\delta\Delta_O$ gave rise to an uncertainty of about 8% in the coverages determined from their data. Linear relationships between $|\delta\Delta_O|$ and oxygen coverage have also been determined in studies of chemisorption on Cu and Ag surfaces in the (sub)monolayer range, and there are several microscopic theories to explain the dependency (see the review by Habraken *et al.*[75]). The macroscopic theory of the Drude equations can be shown to predict a linear relationship, to a first approximation, between $\delta\Delta$ and thickness for the first few layers of growth of an optically absorbing film.

Leibbrandt *et al.*[63] have also shown that the same quantitative relationship between $|\delta\Delta_O|$ and oxygen uptake is found during the initial growth of NiO on Ni(111), and FeO or α-Fe_2O_3 (which has the corundum structure) on Fe(110), for coverages up to at least 10 x 10^{15} O atoms cm^{-2} (8 ML). Clearly, $\delta\Delta_O$ is insensitive to small differences in the composition and structures of substrates and their oxides.

It is expected that the direct proportionality between $\delta\Delta_O$ and oxygen uptake holds for the ellipsometric results determined in the present work (at least up to 470 K). However, there might be some doubt that the proportionality constant applies, because ellipsometric measurements in the two studies were made at different wavelengths (554 nm in their work compared to 632.8 nm in the present study). It can be shown that in theory Δ is more sensitive to changes in the thickness of an absorbing film at 554 nm compared to 632.8 nm. This implies that the proportionality constant for 632.8 nm should be smaller than that derived for 554 nm. However, as noted in the previous section, there is no significant difference in the room temperature measurement of $\delta\Delta_O$ at saturation as determined in the present study or by Vink *et al.*,[60] both measured at 632.8 nm, compared to that reported by Leibrandt *et al.*[47] at 554 nm. This indicates that any difference in the sensitivity at the two wavelengths is small enough, at least in the initial stages of growth, to be ignored. Therefore, in the present study $\delta\Delta_O$ has been calibrated (0.69° *per* 1 x 10^{15} O atoms cm^{-2}) to give the oxygen uptake curves described in the next section.

(iii). Oxygen uptake curves

Fig. 4.32 shows oxygen uptake during experiments at temperatures from 160 to 470 K. The curve for growth at 610 K is not included in fig. 4.32, because it is doubtful that the linear relationship ($|\delta\Delta_O|$ *versus* uptake) holds across the large change in Δ observed at that temperature.

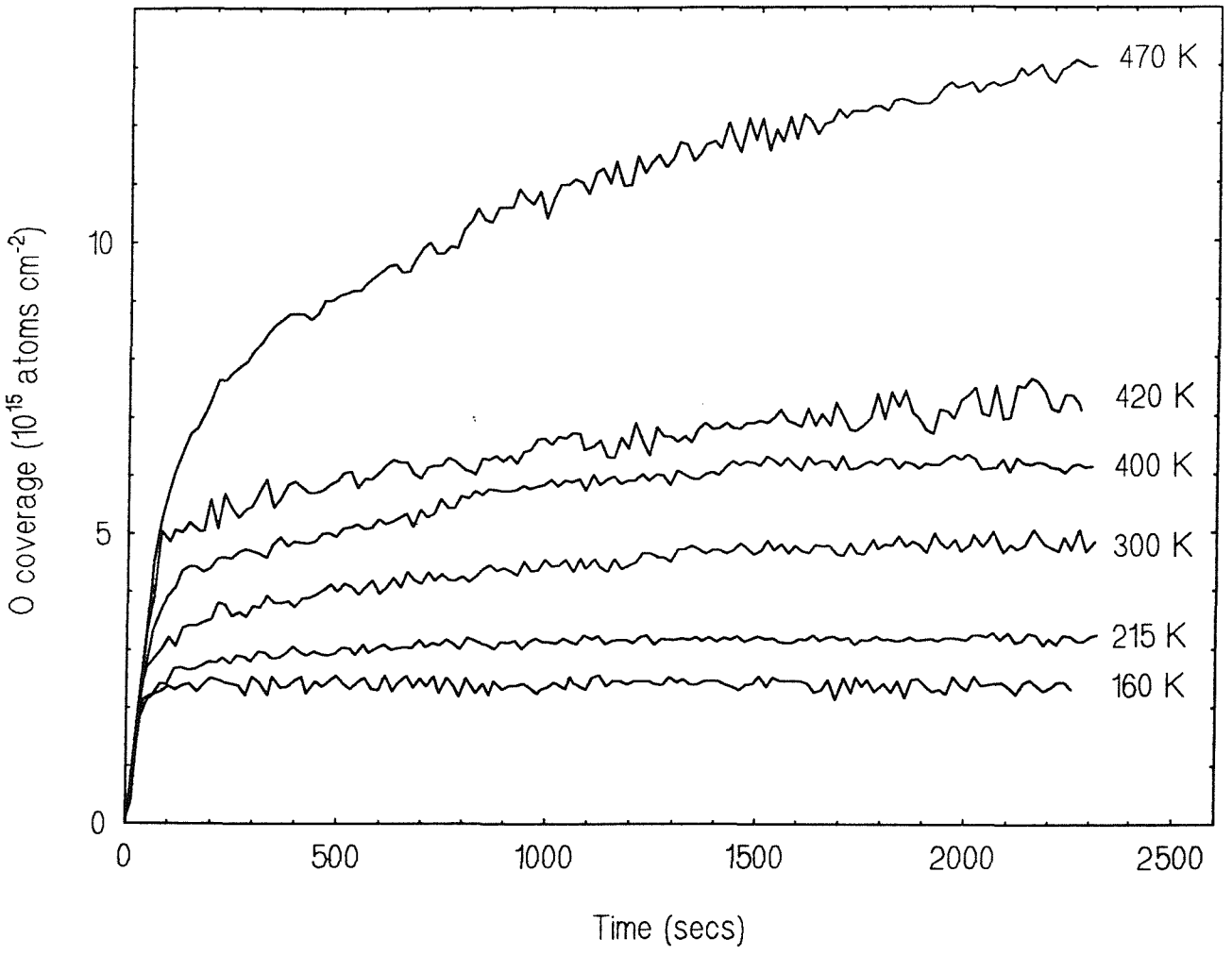

Fig. 4.32. *Oxygen uptake versus exposure of O_2 at 1 x 10^{-6} torr on Fe(100) at 160-470 K.*

The curves are characterised by two stages. In the first stage, on exposing the surface to O_2, the rate of oxygen uptake is rapid, approximately linear and similar at all temperatures studied. In the second stage, the rapid uptake is quickly checked and further uptake proceeds at a much slower rate. For temperatures up to 420 K, uptake tends to saturate within the timescale of the experiments (about 40 minutes) as is most clearly seen at 160 K. The

saturation uptake, and the time taken to reach it, increases with increasing temperature. The uptake kinetics at 470 and 610 K are similar but distinct in that the rate of uptake in the later stages of growth is considerably faster and there is no strong tendency towards a limiting uptake.

These curves can be compared with the results of Leibbrandt *et al.*,[47] remembering that their results have been derived in the same way. As will be discussed below, the results in the two studies are qualitatively similar, but there are some significant quantitative differences.

In agreement with Leibbrandt *et al.*,[47] we find that oxygen uptake at room temperature saturates at $4.9 \pm 0.4 \times 10^{15}$ O atoms cm^{-2} (equivalent to 4.0 ± 0.3 ML). We also find that oxygen uptake at 215 and 160 K saturates at $3.2 \pm 0.4 \times 10^{15}$ O atoms cm^{-2} (2.6 ± 0.3 ML) and $2.4 \pm 0.4 \times 10^{15}$ O atoms cm^{-2} (2.0 ± 0.3 ML), respectively (Leibbrandt *et al.*[47] did not record curves below room temperature).

Unambiguous estimation of film thickness from this uptake data is not possible, because it is unclear, from either our results or the literature, as to what structural form the oxygen takes. It is quite possible, for example, that a layer of chemisorbed oxygen exists on top of the oxide, which may account for the absence of LEED features after oxidation at room temperature.[10] Nevertheless, Leibbrandt *et al.*[46] have obtained a limiting thickness for room temperature growth of about 10 Å by, assuming that bulk-like FeO has formed. The thickness of the room temperature oxide at saturation has previously been estimated as 15 Å, by both ellipsometry[64] (an early study) and depth-profiled chemical analysis.[60]

The uptake measurements at 160 and 215 K can be compared with the results of Lu *et al.*[55] in their study of adsorption at 103 K. They found that dissociated oxygen saturates in a disordered phase at a coverage (not determined) of greater than 1 monolayer. Initially the oxygen adsorbed in the four-fold hollow sites, but at higher coverage also occupied bridging and, perhaps, on-top sites. There is not sufficient evidence to determine how this low temperature oxygen uptake relates to oxide growth at room temperature, but, since uptake at 160 and 215 K has passed beyond 2 monolayers, it might be expected that the first layer of an oxide has formed.

In agreement with Leibbrandt *et al.*,[47] our results indicate that oxygen uptake tends to saturate at temperatures up to about 420 K, although the limiting values differ in the two studies. We find that uptake saturates at 6.13 ± 0.4 x 10^{15} O atoms cm^{-2} at 400 K, and 7.33 ± 0.4 x 10^{15} O atoms cm^{-2} at 420 K. Leibbrandt *et al.*,[47] however, reported much larger values at comparable temperatures: 8.0 x 10^{15} O atoms cm^{-2} at 370 K, and 10.5 x 10^{15} O atoms cm^{-2} at 420 K. At temperatures of 400 K and above, our LEED experiments indicate that a spinel has formed, with a bulk-like lattice parameter (*a*) of about 8.3 ± 0.1 Å (similarly, Sewell *et al.*[8] observed a spinel of a = 8.34 ± 0.06 Å at 420 K). Assuming that the spinel is bulk-like, the saturation coverage at 400 K corresponds to the formation of 5.4 ± 0.4 layers of cubic close-packed (ccp) oxide ions which, with the dimensions found in bulk γ-Fe_2O_3 or Fe_3O_4, would be about 14.8 Å thick. Similarly, the uptake at the end of experiments at 420 K corresponds to the formation of 6.4 ± 0.4 layers of ccp oxide ions, or a bulk-like spinel approximately 17.7 Å thick.

At 470 K, where again LEED experiments show the formation of a spinel, the rate of oxygen uptake in the second stage of growth is noticeably faster than at lower temperatures and does not tend towards saturation within the timescale of the experiment. Correspondingly, Leibbrandt *et al.*[47] noted that there were apparently two temperature regimes: up to 420 K, growth tended to saturate after the initial rapid phase, while at 450 K and above growth took off with a fast temperature-dependent rate. Leibbrandt *et al.*[47] have reported only a small part of the uptake curve at 470 K, however, it is clear that the growth rate is much faster in their study (their uptake passes 10 x 10^{15} O atoms cm^{-2} after about 75 seconds at 7.5 X 10^{-7} torr compared to about 800 seconds at 1 x 10^{-6} torr in the present work).

The differences between the two sets of uptake curves can be summarised as follows:

1. Saturation uptake at temperatures of 400 K and above is smaller, and the growth rate at 470 K is slower, in the present work.

2. Steady state uptake values are reached more quickly in the present work. Changes in the initial stage are much faster in the present work (in the results of Leibbrandt *et al.*[47] the uptake curves at different temperatures are resolvable and the rate of uptake is found to increase slightly with temperature). If the supply of oxygen to the surface is rate controlling in the initial stages of the process then the difference between the two studies might be explained by the higher O_2 pressure of 1 x 10^{-6} torr used in the present study, compared to 5 x 10^{-7} torr used by Leibbrandt *et al.*[47]. Such an effect is apparent in the observations of

room temperature uptake as a function of O_2 pressure described in the next section (see fig. 4.35).

3. The relative differences in saturation uptake and growth rate among the different temperature curves *within each data set* do not compare at all well between the two studies.

As noted above, the two sets of data were recorded at different wavelengths (554 nm in their work, 632.8 nm in the present study). If the optical constants of clean Fe(100) or the oxide or both vary significantly between the two wavelengths (they do for polycrystalline iron[76]) then some difference between the ellipsometric measurements might be expected. However, it would still be difficult to explain why the relative differences among the curves at the various temperatures are so disparate in the two studies.

(iv). Oxidation kinetics

Leibbrandt *et al.*[47] have compared their oxygen uptake kinetics with the coupled-currents theory of Fromhold and Cook[69] (see Sect. 4.3.1). The curves have been fitted with a theoretical rate equation, derived by Fromhold and Cook,[65] where the rate limiting step is considered to be a Schottky emission of electrons from the metal substrate into the conduction band of the oxide (Schottky emission is the thermionic emission of electrons over a potential energy barrier reduced by the combined effects of an image potential and the electric field associated with the concentration gradient of cations across the oxide). Leibbrandt *et al.*[47] established experimentally that three conditions necessary for the theory to apply are met for the oxidation of Fe(100), namely: that the oxide thickens homogeneously, that cations are the mobile species in oxide formation and that only one type of oxide (they identified it as nonstoichiometric FeO) is involved in the temperature range considered (300-550 K). Consequently they were able to conclude that O_2/Fe(100) was a model system for testing the Fromhold and Cook theory of coupled currents (in a recent paper[77] they have also applied the theory to the oxidation of Fe(110)).

Leibbrandt *et al.*[47] found that the theoretical rate equation successfully described uptake curves at 450 and 470 K, although not over the first 20 Å of growth. The theory is believed to fail below this threshold thickness because tunnelling becomes the dominant electron transport mechanism, and, anyway, electron transport in the initial stages of growth is

expected to be so fast that iron transport or O_2 supply becomes rate limiting. At 570 K, the observed uptake rate was much slower than theory and so Leibbrandt *et al.*[47] proposed that either diffusion of iron through the oxide or the supply of O_2 from the gas phase was rate limiting (they favoured the latter). At 300 and 370 K, the uptake curves could not be fitted with the theoretical rate equation and so they concluded that thermionic emission was negligible and therefore electron tunnelling controlled the rate.

The growth kinetics determined in the present study (fig. 4.32) can be discussed with respect to these conclusions. Leibbrandt *et al.*[47] have shown that thermionic emission is negligible at temperatures up to 370 K, and only becomes important at higher temperatures for thicknesses of greater than 20 Å (1 x 10^{15} O atoms cm^{-2}). In the present work, tunnelling is obviously expected to be the only electron transport mechanism for the oxides grown at temperatures from 160 to 300 K. At 400 and 420 K, the measured oxygen uptakes and speculative thickness calculations (14.8 and 17.7 Å, respectively, as described in the previous sections) are such that tunnelling must be considered the most important, and perhaps only, electron transport mechanism.

According to the theory of Fromhold and Cook,[66,69] under these conditions the growth rate should initially obey an inverse-logarithmic law (eq. (4.3)), where the rate is controlled by ion diffusion, followed by a direct-logarithmic law (eq. (4.4)) in the later stages, where electron tunnelling becomes rate limiting.

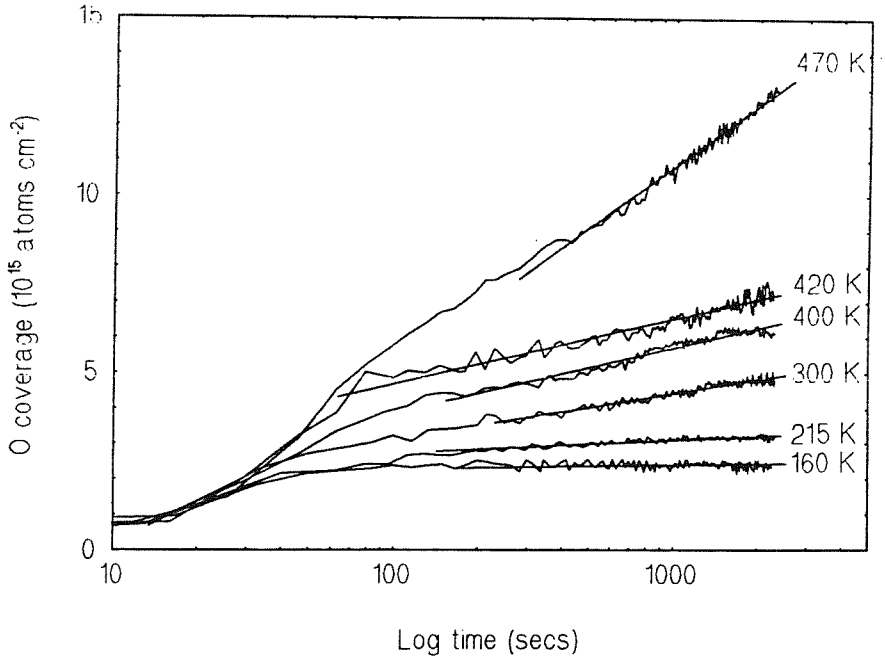

***Fig. 4.33.** Oxygen uptake versus logarithm of time, showing best fit curves.*

As fig. 4.33 shows, the uptake curves in fig. 4.32 do appear to obey a direct-logarithmic law in the later stages (a similar observation was also made by Yolken and Kruger[64] for room temperature growth). It should be noted, however, that a number of alternative theories predict a direct logarithmic law in the very-thin film region.[42]

The curves in fig. 4.33 can be fitted over two orders of magnitude with a simple, direct-logarithmic rate equation of the form

$$O \text{ coverage} = K \ln(Bt) \tag{4.6}$$

where K is a rate constant. An Arrhenius plot of K is given in fig. 4.34.

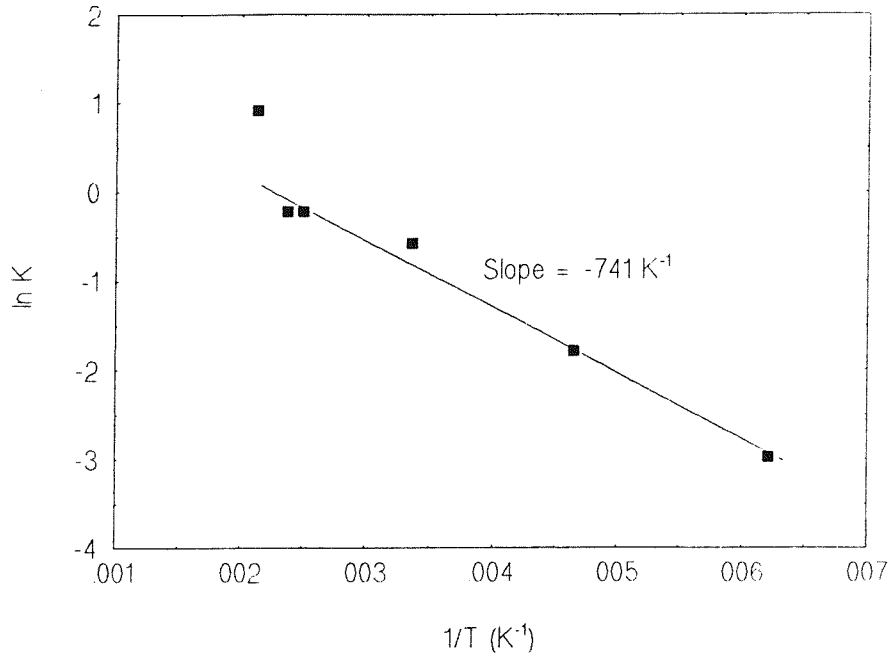

Fig. 4.34. Arrhenius plot of the direct logarithmic rate constant (K) for the oxygen uptake curves 160-470 K.

In the graph, data points for temperatures from 160 to 420 K can be fitted by a linear curve, indicating a common activation energy E_{act} (slope of curve = - E_{act}/R, where R is the molar gas constant), but the data point for 470 K is distinct (a difference that cannot be explained by poor fit or background instability). This may well be related to the transition in electron transport mechanism from electron tunnelling to thermionic emission, which Leibbrandt *et al.*[47] believed to occur at between 420 and 470 K. For this reason the 470 K data point has been ignored and points up to 420 K have been fitted (least-squares) to yield an activation energy of 6.2 $\pm$ 5 kJ mol^{-1}. This very small value is consistent with a process controlled by electron tunnelling. It can be compared with the value of 24.2 $\pm$ 4 kJ mol^{-1}

reported[78] for low temperature oxide growth on Ni(110), where electron tunnelling is also believed to be rate controlling. Leibbrandt *et al.*[47] did not report an activation energy for their results and it is not possible to extract a value from their published data.

The effect of O_2 pressure, in the range 1 x 10^{-7} to 1 x 10^{-6} torr, on oxygen uptake at room temperature is shown in fig. 4.35 (derived from the $\delta\Delta_O$ measurements in fig 4.24).

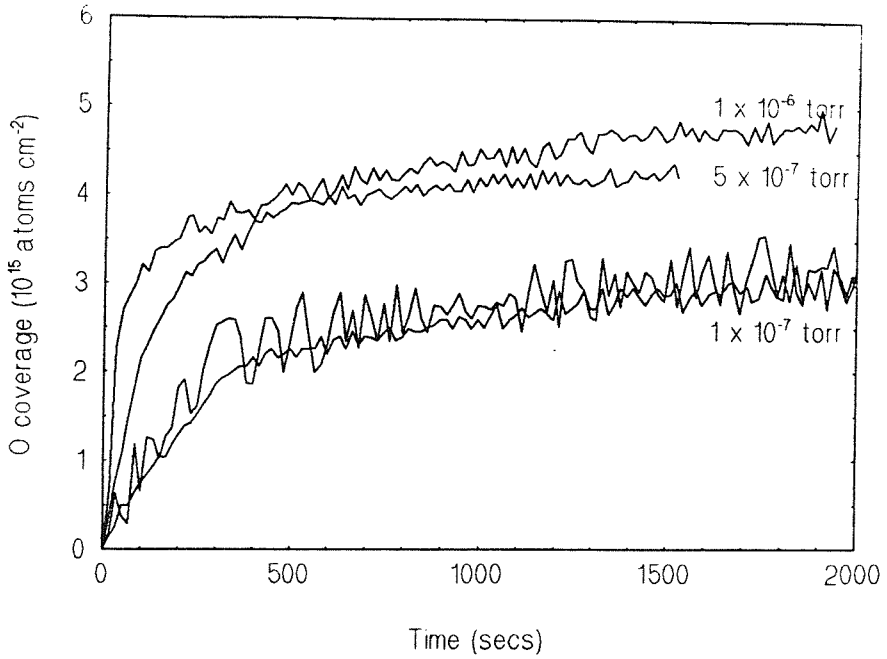

Fig. 4.35. *Oxygen uptake as a function of pressure (1 x 10^{-7} to 1 x 10^{-6} torr) on Fe(100) at 300 K.*

Increasing O_2 pressure has a strong effect on the rate of the fast initial stage and also lowers the threshold oxygen coverage at which the slow, second stage begins. The rate of uptake in the initial stages of growth at 300 K has been reported[8,10] to vary linearly with O_2 pressure, and the initial growth rates observed in the present work are consistent with this. According to Fromhold,[69] electron tunnelling is facile in the initial stages of oxide growth so that the supply of reacting particles is expected to be rate controlling. The pressure dependency in fig. 4.35 indicates that O_2 collision rate determines the growth rate, through the supply of oxide ions for reaction. The curves also show that pressure affects the slow growth phase, which in theory should be controlled by the electron tunnelling current. A possible explanation is that a decreased oxide uptake at lower pressure reduces the size of the electric field which promotes the diffusion of iron cations through the oxide. Presumably, growth at an O_2 pressure of 1 x 10^{-7} torr would continue until the film reaches the saturation uptake seen at higher pressures, which is determined by the "reach" of the tunnelling current.

It appears that oxide growth rate at temperatures up to 420 K is controlled by electron tunnelling. Saturation uptake is therefore determined by the thickness at which the tunnelling current, which is quickly attenuated, tends towards zero. As expected from the theory of Fromhold and Cook, limiting thickness increases with increasing temperature.

This interpretation is in good general agreement with the analysis of Leibbrandt *et al.*[47] However, they have reported higher saturation uptakes at 400 and 420 K, and a faster growth rate at 470 K. It is not obvious why the kinetics determined in the two studies should be so disparate. As discussed above, it is unlikely to be related to the different wavelengths used in the two studies. A pressure effect, like that described above, can also be discounted since, in reverse of the tendency seen in fig. 4.35, Leibbrandt *et al.*[47] use a slightly lower O_2 pressure but see larger and faster oxygen uptakes. However, a possible explanation could be differences in the cleanliness or structural order of the Fe(100) surfaces, in the two studies.

We can also speculate that differences in oxide composition may account for the dissimilarities in the kinetics data of the two studies. As described above (Sect. 4.3.1), conflicting observations in the literature may suggest that the composition and structure of oxides grown at room temperature and above can vary from FeO to γ-Fe_2O_3 or Fe_3O_4. In our experiments, LEED results indicated that a spinel (γ-Fe_2O_3 or Fe_3O_4) was formed at temperatures of 400 K and above, in agreement with previous structural studies.[3,8] Leibbrandt *et al.*,[47,63] however, determined the composition of oxides formed at 300 and 470 K to be a non-stoichiometric monoxide $Fe_{0.95\pm0.07}O$, although they noted that XPS measurements indicated the presence of the Fe^{III} oxidation state as well as Fe^{II}.

The metal-to-oxide work function is an important chemically-dependent variable of the Fromhold and Cook theory that is predicted to determine oxide growth kinetics in the regimes of both electron tunnelling and thermionic emission. It is equal to the work function of the iron substrate minus the difference in energy between the edge of the oxide conduction band and the vacuum level. It represents the barrier over which electrons from the metal have to climb, or penetrate, to enter the oxide.

Numerical results presented by Fromhold[69] show that when the kinetics are controlled by thermionic emission, the growth rate quickly decreases with increasing metal-to-oxide work function, because the fraction of electrons with enough energy to climb the barrier decreases

as the barrier height increases. For oxide growth where electron tunnelling is rate limiting, the theory predicts that again the growth rate in the later stages decreases with increasing work function, because tunnelling through the barrier is hindered by an increased barrier height. Therefore, if the metal-to-oxide work function of a spinel-type oxide (γ-Fe_2O_3 or Fe_3O_4) is greater than that of FeO, the difference between our growth kinetics and those reported by Leibbrandt *et al.*[47] is readily explained. However, the data to confirm or deny this suggestion is not available.

4.4. Oxygen and phosphorus on iron: Interaction of O_2 with phosphorus covered Fe(100)

4.4.1. Introduction

In this section, we report some ellipsometric measurements of the effect of preadsorbed phosphorus on the oxidation kinetics of Fe(100). We have investigated the interaction of O_2 with (1). c(2x2)P overlayers at temperatures in the range 300-640 K, and (2). thin phosphorus films, characterised as dissolved phosphorus or iron phosphide, at room temperature. In the only comparable study, Arabczyk *et al.*[22] have studied the room temperature adsorption of O_2 on segregated phosphorus at a Fe(111) surface, using AES and XPS. For submonolayer phosphorus coverages, they proposed a model for adsorption where oxygen displaces phosphorus atoms into lower layers, with the formation of phosphorus clusters and Fe-O bonding. After adsorption on a surface characterised as a layer of Fe_xP covered with phosphorus clusters, they detected an oxidised state of phosphorus by AES (probably induced by beam effects, they suggest). On heating, XPS measurements indicated the formation of a Fe-P-O species at 420 K, which decomposed at 700 K.

4.4.2. Results: Oxygen uptake on c(2x2)P-Fe(100) at 300-640 K

The interaction of O_2 with c(2x2)P-Fe(100), at sample temperatures from 300 to 640 K and an O_2 pressure of 1×10^{-6} torr, was investigated with fixed wavelength ellipsometry (λ = 632.8 nm, angle of incidence = 70°) and LEED.

(i). Preparation of the c(2x2)P surface

The c(2x2)P surface was prepared, as described above (Sect. 4.2.2), by either of the two following ways:

1. By adsorbing PH_3 to saturation at 160 K and then desorbing all of the H_2 by quickly heating to about 500 K; or,

2. By annealing very-thin (less than 20 Å), saturated phosphorus films, formed during PH_3 exposures at 300-445 K.

In the experiments described below, we have found that at a given temperature there is no significant difference in the ellipsometric results during film growth on c(2x2)P structures prepared by either method *1* or *2*. For example, the two curves for room temperature adsorption given in fig. 4.36 were measured for oxygen uptake on c(2x2)P structures prepared by either PH_3 adsorption at 160 K or annealing a film of about 18 Å thick. It is believed that the c(2x2)P structure formed at 160 K is a simple saturated overlayer of phosphorus atoms (0.5 ML) on unreconstructed Fe(100). The same conclusion can then be made for the c(2x2)P structure formed by the second method. It appears that during annealing at temperatures of about 780 K these very-thin films have been reduced in thickness to leave a half monolayer of phosphorus on the surface (in Sect. 4.2.3, it is argued that these films are phosphorus dissolved in the subsurface region). In the results presented below, therefore, the method of preparation of the c(2x2)P structure is not considered.

The c(2x2)P LEED pattern is not significantly changed after hour long periods of high temperature annealing (700-800 K), which probably indicates that the structure is sufficiently stable to last throughout these experiments.

(ii). Changes in Δ and ψ versus time

Fig. 4.36 shows the development of the relative ellipsometric parameters $\delta\Delta_o$ and $\delta\psi_o$ during oxygen uptake on the c(2x2)P-Fe(100) surface at sample temperatures in the range 160-470 K. For clarity, the large changes in $\delta\Delta_o$ and $\delta\psi_o$ during film growth at 640 K are shown separately in fig. 4.37. As found for oxygen uptake on the clean surface, the change in Δ and ψ is effectively immediate at all temperatures, and, consequently, zero on the timescale marks the start of the dose. Δ decreases when the surface is exposed to O_2. As with oxygen uptake on clean Fe(100), the rate of decrease of Δ is initially rapid but then quickly decelerates. For temperatures up to 420 K, $\delta\Delta_o$ reaches a steady state within the timescale of experiments (about 40 minutes). The size of the steady state, and the time taken to reach it, increase with increasing temperature. At 300 K, the steady state value of $\delta\Delta_o$ ($3.4 \pm 0.1^\circ$) is identical to that found for oxygen uptake on the clean surface at the same temperature. At higher temperatures, however, a larger decrease in Δ is detected on the c(2x2)P surface, when compared to the clean surface (fig. 4.26).

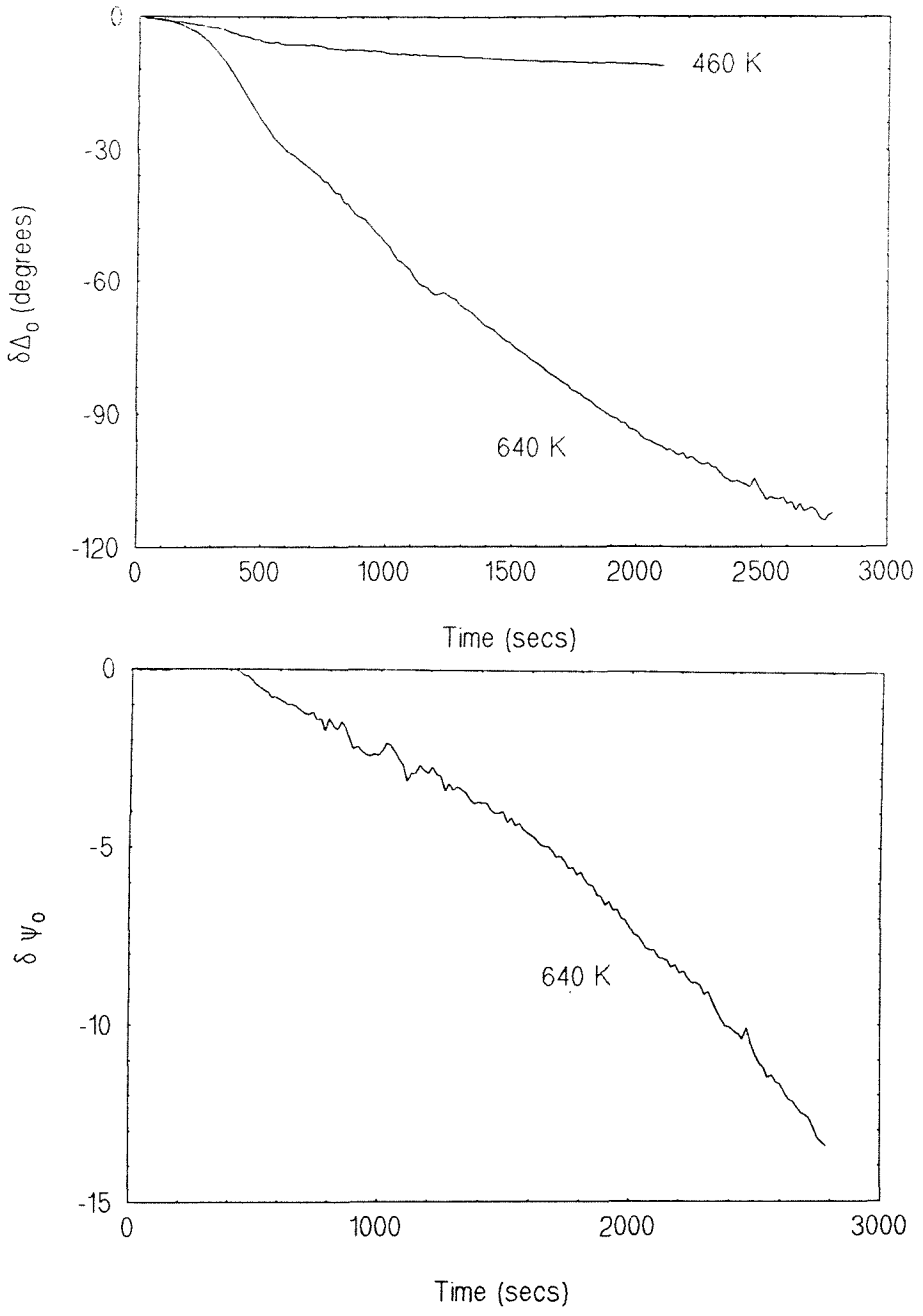

Fig. 4.37. (a) $\delta\Delta_0$ and (b) $\delta\psi_0$ versus time for interaction of O_2 at 1 x 10^{-6} torr with c(2x2)P-Fe(100) at 640 K.

(iii). Analysis of Δ-ψ plots

Fig. 4.38 shows the Δ-ψ trajectory during film growth at 640 K. The relative measurements $\delta\Delta_0$ and $\delta\psi_0$ are calibrated to give Δ and ψ by taking literature values for Δ and ψ of the clean surface (see Sect. 4.2.2). The effect of the c(2x2)P overlayer on the ellipsometric

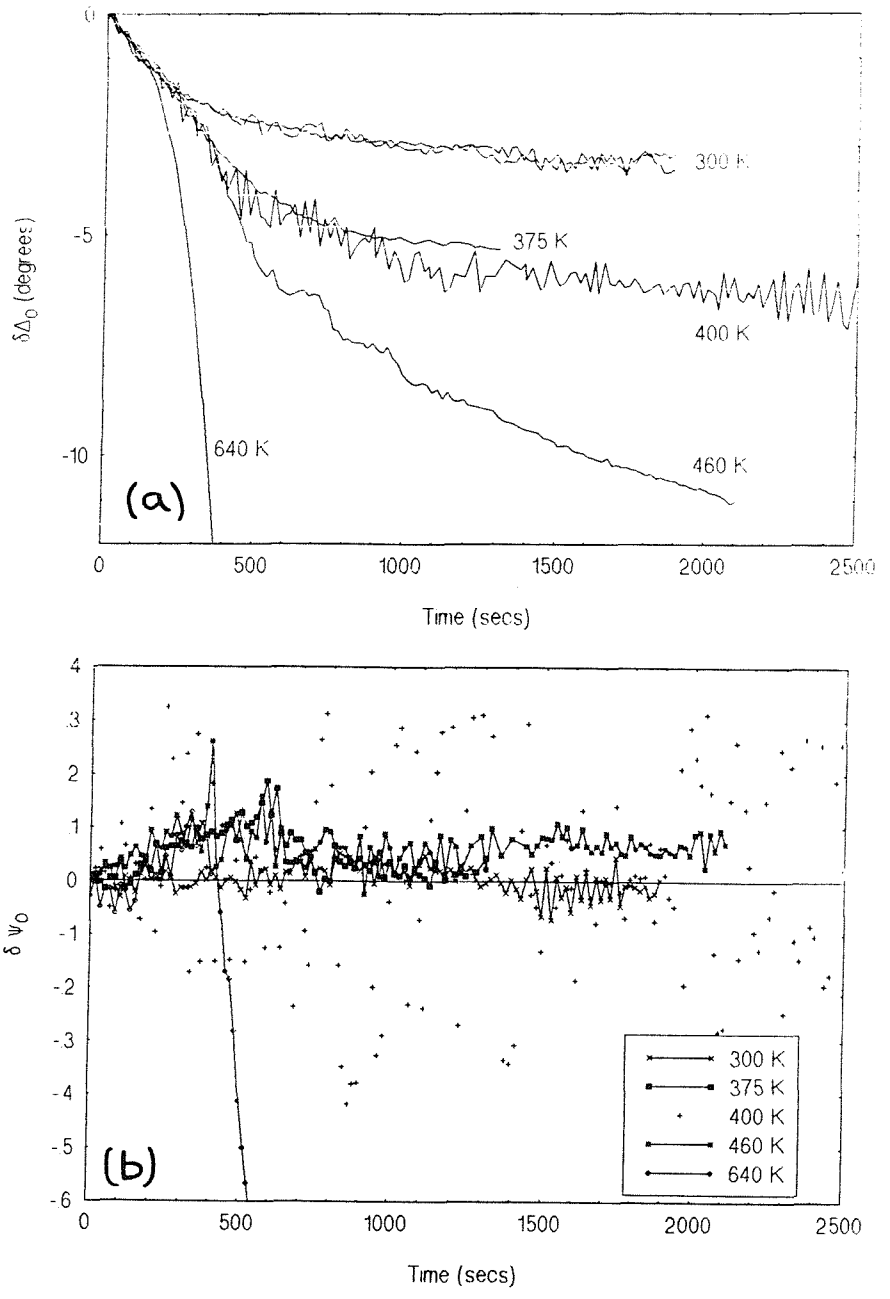

Fig. 4.36. *(a) $\delta\Delta_o$ and (b) $\delta\psi_o$ versus time for interaction of O_2 at 1 x 10^{-6} torr with c(2x2)P-Fe(100) at 300-470 K.*

There is no measurable change in ψ at temperatures from 300 to 460 K. At 640 K, however, a large decrease in ψ is observed after a period of a few hundred seconds where no sizeable change is detected. The rate of decrease of ψ is much faster than that found for oxidation of the clean surface at a comparable temperature.

parameters is tiny and can be ignored ($\delta\Delta_p$ for saturation of the overlayer at 160 K is about 0.28° while $\delta\psi_p$ cannot be measured).

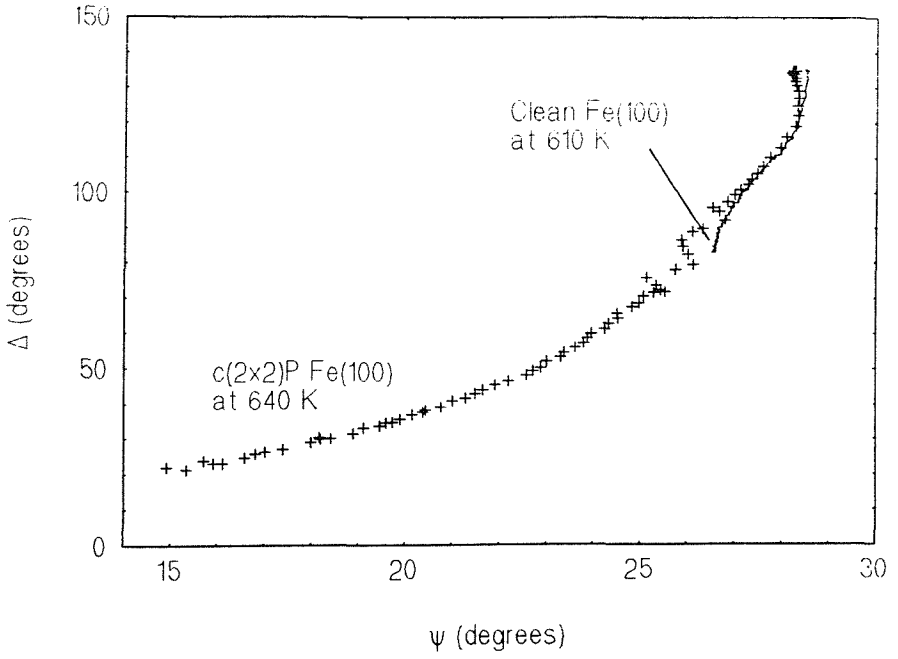

Fig. 4.38. Experimental Δ-ψ trajectory for interaction of O_2 at 1 x 10^{-6} torr with c(2x2)P-Fe(100) at 640 K (points marked with crosses). Trajectory for oxidation of the clean Fe(100) surface at 610 K included for comparison (solid line).

Although the trajectory is comparatively well-developed, there is no indication of a tendency towards a steady state region of the Δ-ψ plane (at least after 40 minutes). The curve closely follows that for the oxidation of Fe(100) at 610 K (also given in fig. 4.38), although, as described below, there are some significant differences. This is good evidence that an optically similar iron oxide has formed on top of the c(2x2)P overlayer. The trajectory for growth on the phosphorus overlayer at 640 K is much more advanced than for the clean surface at 610 K. Since they were recorded over similar lengths of time, it appears that oxide formation is much faster in the presence of a half monolayer of phosphorus. Further evidence for this remarkable conclusion is given below, for growth at lower temperatures.

The trajectories of experiments at temperatures from 160 to 470 K are shown in detail in fig. 4.39, along with the initial part of the 640 K curve (and, for comparison, the 640 K trajectory for growth on a clean surface).

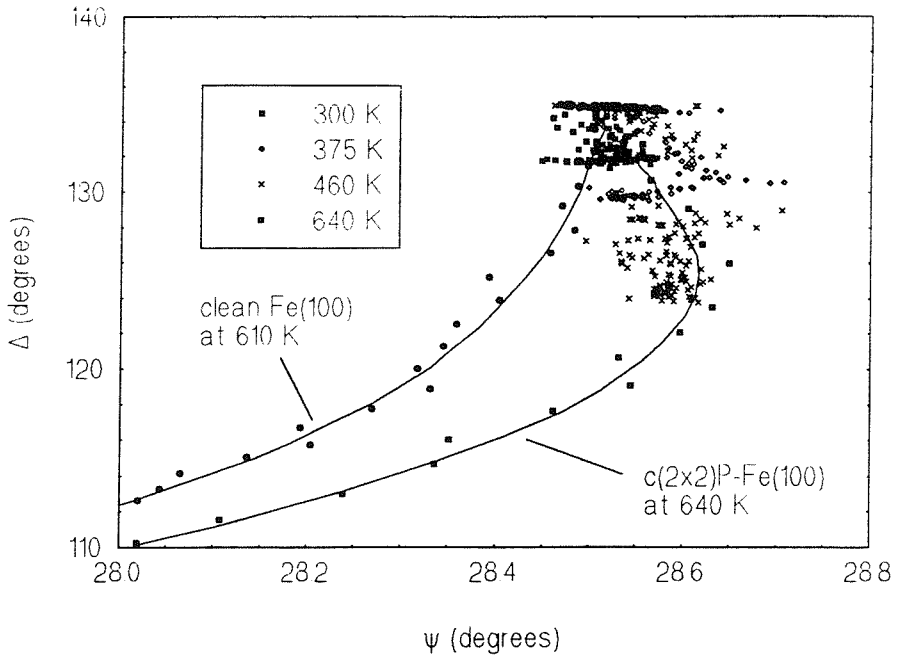

Fig. 4.39. Experimental Δ-ψ trajectory for interaction of O_2 at 1 x 10^{-6} torr with c(2x2)P-Fe(100) at 300-460 K (see key for symbol used for each data set) with initial part of trajectories for growth on c(2x2)P at 610 K and clean Fe(100) at 640 K - shown by solid line (approximate best fit) and associated points - included for comparison.

Despite the scatter in ψ (which, as described above, was also a problem in experiments of the oxidation of the clean surface), it is clear that curves for growth at temperatures from 300 to 460 K, follow the higher temperature (640 K) trajectory. It appears that optically similar iron oxides are grown, on the phosphorus layer, in the temperature range 300 to 600 K. At lower temperatures (300-400 K) the oxides have grown to a limiting thickness (as indicated by the $\delta\Delta_o$ curves reaching a steady state in fig. 4.36) and the trajectories have terminated.

Although the well developed high temperature trajectories for growth on the c(2x2)P overlayer and the clean surface are similar, there are some significant differences. In particular, the initial parts of the trajectories in the two cases follow distinct pathways, as shown in fig. 4.39. The difference between the two pathways is small, compared with uncertainty in the measurement of ψ, but is clearly visible when the different temperature results are considered together (contrast fig. 4.39 with similar results for the clean surface, given in fig. 4.30). Since the low levels of phosphorus appear to have a negligible effect on the ellipsometric properties of the clean surface, it is likely that the small differences between the trajectories of the clean and c(2x2)P surfaces are explained by the effect of phosphorus

on the optical properties of the oxide layers. As will be discussed below, this may be related to slight compositional changes induced by phosphorus.

As with the results of oxidation on the clean surface, we were unsuccessful in attempts to model the experimental Δ-ψ trajectories using the Drude equations. Although it was well-advanced, the 610 K trajectory did not tend towards a steady state Δ-ψ point and so there was no indication of the optical constants of the film (as there was for PH_3 on Fe(100)). Trial and error did not reveal any reasonable fit to any part of the data. Film thickness could be guessed at the end of low temperature experiments (300-400 K). However, attempts to extract n and k values, from Δ and ψ at known thickness, failed to produce reasonable fits. It is possible that the optical constants of the oxide films vary with thickness.

(iv). LEED studies

After ellipsometric experiments, the films showed featureless, high intensity LEED patterns indicating structural disorder on the long range scale. Ordering could not be induced by annealing for periods of from 10 minutes to 2 hours at temperatures up to 800 K.

4.4.3. Results: Oxygen uptake on phosphorus films at 300 K

Results of a preliminary investigation into oxygen uptake on thin phosphorus films at room temperature are briefly described in this section. The interaction of O_2 (1 x 10^{-6} torr) with film covered surfaces at room temperature was investigated with fixed wavelength ellipsometry (λ = 632.8 nm, angle of incidence = 70°) and LEED.

(i). Characterisation of the phosphorus films

Phosphorus films were prepared by the interaction of PH_3, and were characterised by ellipsometry as described in Sect. 4.2.2. The saturated film labelled as 9 Å thick in fig. 4.40 was formed after PH_3 exposures at 345 K, and has been interpreted, in Sect 4.2.3, as layers of phosphorus dissolved in the subsurface region. The films labelled as 48 Å or thicker were formed during exposures at 495 K and above. They are believed to be iron phosphide layers which in some cases have grown beyond opaque thickness, to many hundreds of Ångstroms.

(ii). Ellipsometric results

Changes in Δ were too small to be measurable and consequently are not reported here. Oxygen uptake was characterised by measurement of $\delta\Delta_O$, the change in Δ relative to Δ of the surface before it is exposed to O_2, as shown in fig. 4.40. For convenience, $\delta\Delta_O$ is shown positive in fig. 4.40 so that the results can be considered as oxygen uptake curves in the discussion. To this end, a possible coverage calibration is given on the axis on the right (as will be discussed below).

The curve of $\delta\Delta_O$ for room temperature oxygen uptake on clean Fe(100) is also included in fig. 4.40 (dashed line) and it can be seen that in all cases, $\delta\Delta_O$ is reduced by the presence of phosphorus. When the phosphorus film is 48 Å or thicker (up to several hundreds of Angstroms thick), which is believed to be an iron phosphide, the change in Δ is small and apparently independent of film thickness.

The oxygen layers formed in these experiments were disordered as indicated by LEED.

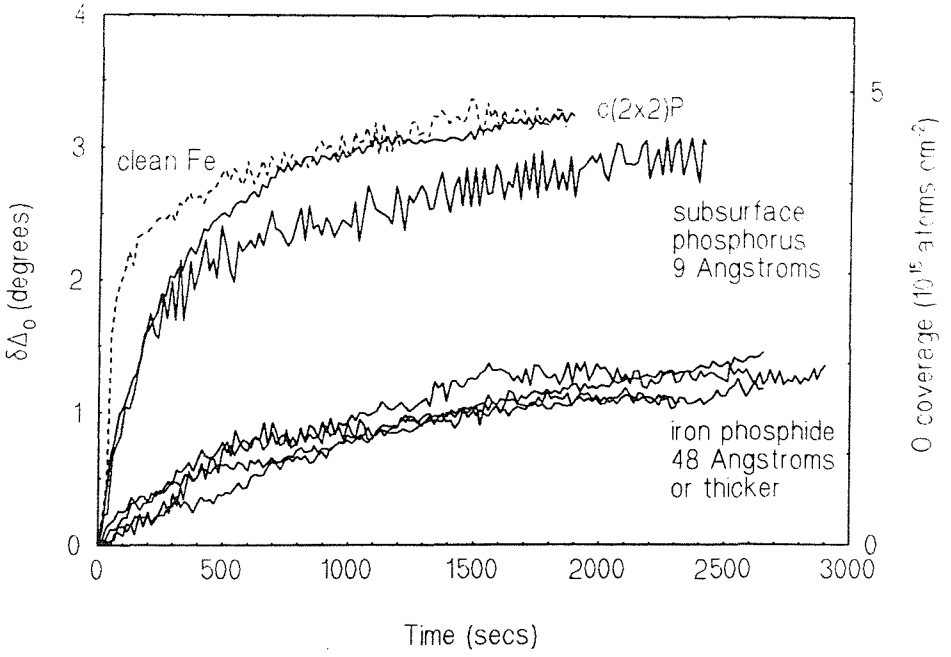

Fig. 4.40. *$\delta\Delta_0$ versus time interaction of O_2 at 1 x 10^{-6} torr with phosphorus films of different thickness at 300-460 K.*

4.4.4. Discussion

(i). Oxygen uptake kinetics on c(2x2)P-Fe(100)

The presence of a saturated c(2x2) phosphorus overlayer on the Fe(100) surface clearly does not prevent film growth when the surface is exposed to O_2 at temperatures in the range 300 to 640 K. The Δ-ψ trajectories during film growth on the c(2x2)P surface (figs. 4.38 and 4.39) are very similar to those found during oxidation of clean Fe(100), as described above (Sect. 4.3.2). This strongly indicates that for much of the film growth, at least, iron oxide is formed on the c(2x2)P surface. Quantitative analysis of the Δ-ψ plots has proved impossible so conclusions are limited. However, the differences between the well-developed Δ-ψ trajectories for high temperature film growth on the clean and c(2x2)P surfaces (fig. 4.38) are so small that they probably only represent slight compositional or microstructural dissimilarities in the two films.

The Δ-ψ trajectories of the clean and phosphorus covered surfaces show a small but significant divergence in the early stages of their development. As fig. 4.39 shows, the trajectories are farthest apart when the 460 K experiment has terminated. However, as the 640 K curve indicates, the c(2x2)P trajectory bends back towards the path of the clean surface. Film thickness at the bend in the c(2x2)P trajectory can be estimated from the oxygen uptake at termination of the 460 K experiment (16×10^{15} atoms cm^{-2}, fig. 4.41). For example, assuming that FeO has grown, this coverage corresponds to a thickness of about 49 Å.

Presumably, phosphorus accounts for the deviation of Δ-ψ trajectories in the early stage of film growth. It is not possible to say what the effect may be. Arabczyk *et al.*[22] found that oxygen and segregated phosphorus on Fe(111) reacted to form a Fe-P-O species at high temperatures (about 700 K). The deviation may indicate that reaction between phosphorus and oxygen has occurred. However, the temperatures in the present study are much lower (the deviation is apparently significant down to at least 370 K). It may be that phosphorus induces small structural or compositional changes in the oxide, which account for the early divergence. The results presented above are fairly consistent with the idea that iron oxide is formed on the c(2x2)P surface. The following discussion is presented from that viewpoint.

As discussed above (Sect. 4.3), Leibbrandt *et al.*[47,63] have shown that the size of $\delta\Delta_O$ ($|\delta\Delta_O|$) is directly proportional to oxygen uptake during the formation of very-thin oxides on iron single crystal surfaces. If an oxide has formed on the c(2x2)P surface then a linear relationship between $|\delta\Delta_O|$ and oxygen uptake is expected. The calibration used for uptake on the clean surface can reasonably be applied to the c(2x2)P data, since Leibbrandt *et al.*[47,63] have shown that the relationship is fairly insensitive to composition (the effect of phosphorus, therefore, can be considered negligible).

In this way, fig. 4.41 shows oxygen uptake as a function of time for the c(2x2)P surface exposed to O_2 (1 x 10^{-6} torr) at different temperatures. Uptake curves for oxygen on clean Fe(100), at the same pressures and comparable temperatures, are also included.

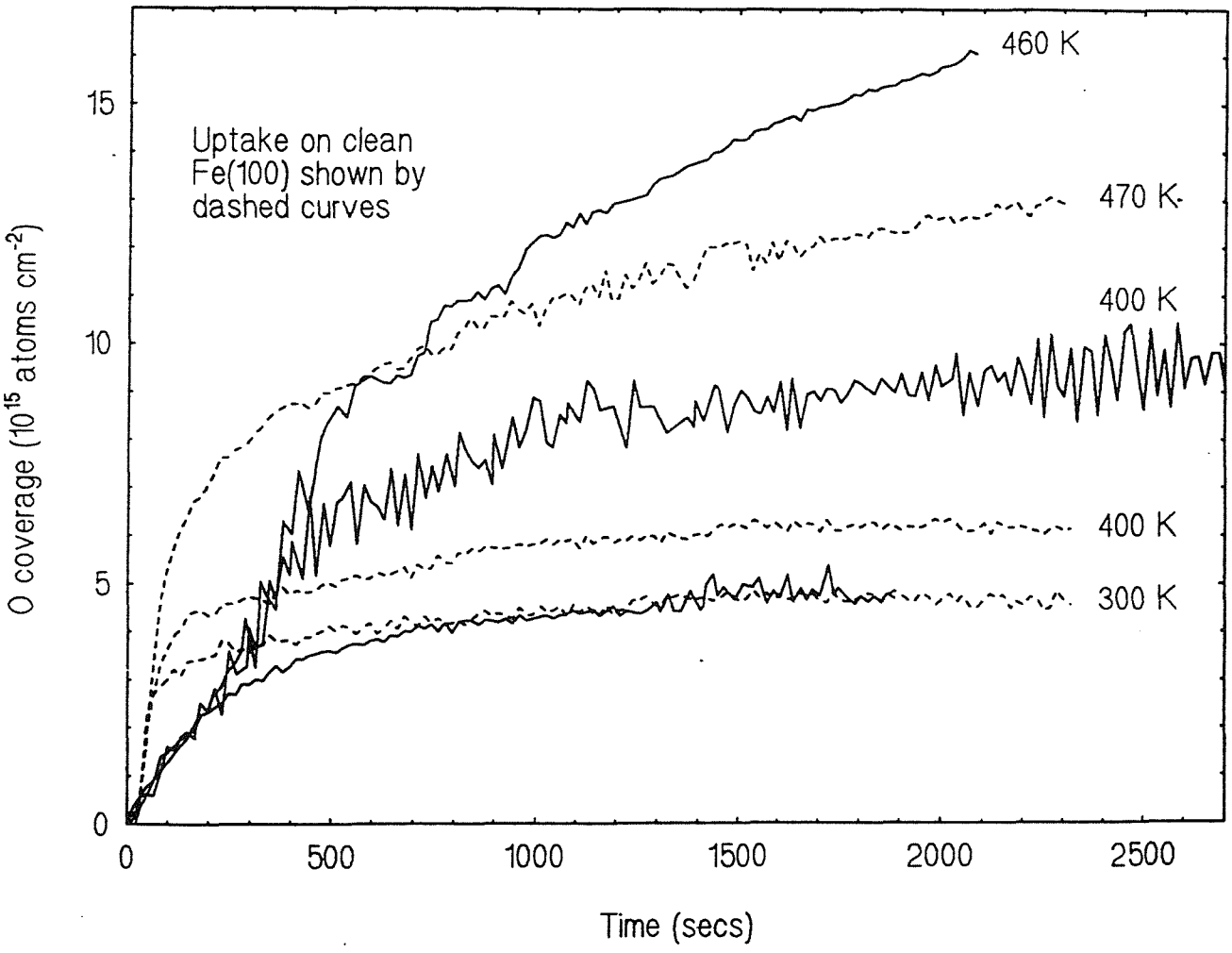

Fig. 4.41. *Oxygen uptake versus time for interaction of O_2 at 1 x 10^{-6} torr with c(2x2)P-Fe(100) at 160-460 K. Curves for interaction of O_2 with Fe(100) under identical conditions shown with dotted lines.*

Assuming that iron oxide has grown on the phosphorus covered surface, it appears from fig. 4.41 that the presence of phosphorus in a saturated c(2x2)P overlayer promotes iron oxide growth on Fe(100) at high temperatures.

As found for the oxidation of the clean surface, the uptake curves are characterised by two stages. In the first stage, on exposing the surface to O_2, the rate of oxygen uptake is rapid, approximately linear and similar at all temperatures studied. In the second stage, the rapid uptake levels off, at a logarithmic rate, reaching saturation at temperatures between 300 and 400 K. The saturation uptake, and the time taken to reach it, increases with increasing temperature. The close similarity of the uptake kinetics on the c(2x2) and clean surfaces is further evidence that iron oxide (and not some Fe-P-O reaction product) has formed on the c(2x2)P surface.

According to the theory of Fromhold and Cook,[69] electron transport is initially so facile that oxide growth rate is, at first, limited by the supply of reactants. Leibbrandt *et al.*[47] have established that the initial fast stage of oxygen uptake on clean Fe(100) is limited by mass transport. As fig. 4.41 shows, the comparable stage on the c(2x2)P surface is much slower, indicating that oxygen uptake is initially more difficult on the phosphorus saturated surface.

For the first layer of film growth, a lower sticking coefficient for O_2 on the phosphorus covered surface would explain the slower uptake. Arabczyk *et al.*[22] have proposed a model for the low temperature interaction of O_2 with a segregated p(1x1)P overlayer on Fe(111) where adsorbed oxygen atoms deposit on sites of phosphorus defects and displace the atoms into the substrate. If the c(2x2)P layer is displaced by oxygen, then it might be expected that the growth rate will change (presumably increase) when the first layer of the oxide film has formed. No such effect is observed, although this may well be beyond the resolution of the ellipsometric measurement (both in Δ and in time).

It seems likely that, rather than remaining on top of the growing oxide, phosphorus stays at the substrate-oxide interface, or is displaced into the bulk. This might be expected from the accepted mechanism of iron oxide growth, where iron cations pass from the substrate into the oxide.[47] There is no evidence of phosphorus retarding growth in the second stage (indeed, as will be discussed below, the opposite is found). This indicates that phosphorus is not located on top of the growing oxide.

A layer of phosphorus located at the film-substrate interface or in the subsurface region could conceivably interfere with the diffusion of iron cations into the oxide thereby slowing the rate of growth in the early stages, compared to the clean surface.

At 300 K, the saturation uptake is effectively identical to that found on the clean surface at the same temperature. Since it has been shown that electron tunnelling current controls the growth rate and limiting thickness of an oxide formed on clean Fe(100) at room temperature, it appears that this process is not affected by a half-monolayer of phosphorus atoms at, or near, the surface.

Remarkably, as fig. 4.41 shows, phosphorus appears to promote high temperature (> 370 K) oxide growth compared to the clean surface. At 400 K, oxygen uptake tends towards saturation coverage on both the clean and c(2x2)P surfaces, but more oxygen uptake is found in the presence of phosphorus. At 460 K, there is no tendency to saturation on either surface within the timescale of the reaction, but in the presence of phosphorus, the growth rate in the later stages is faster at a given thickness. According to Leibbrandt *et al.*,[47] the rate of oxidation of Fe(100) at temperatures from 450 to 470 K is controlled, in the latter stages, by thermionic emission, while at 400 K the rate is also partially determined by electron tunnelling. It might be expected that oxide growth on the c(2x2)P surface at 460 K is controlled by thermionic emission, while growth at 400 K is controlled by electron tunnelling.

The enhanced oxide growth rate on the c(2x2)P surface might be explained, in theoretical terms, if phosphorus at the substrate-oxide interface lowers the metal-to-oxide work function. As discussed above (Sect. 4.3.3), this parameter effectively represents the potential energy barrier over which electrons must cross to enter the oxide from the metal. Theoretically, a decrease in the metal-to-oxide work function leads to a larger limiting thickness when the growth rate is controlled by tunnelling, or faster growth in the later stages when the rate is determined by thermionic emission.[69] However, this suggestion does not explain why the limiting thickness at room temperature is unaffected by the presence of phosphorus.

Another interesting suggestion is that different iron oxide phases are formed on the clean and phosphorus covered surface. This possibility was considered, in Sect. 4.3, to explain why the oxide kinetics on the clean surface were different to those previously reported by

Leibbrandt *et al.*[47] The oxides in the two studies had been characterised, respectively, as a spinel or a non-stoichiometric FeO. It was then suggested that small compositional and structural differences in the growing oxides could account for the different growth rates.

Remarkably, the ($\delta\Delta_O$ curves and therefore) oxygen uptake kinetics determined for the oxidation of the c(2x2)P surface are quantitatively very similar to the results of Leibbrandt *et al.*[47] For example, on the phosphorus covered surface at 400 K, oxygen uptake tends to saturate at an oxygen uptake of about 9.5 $\pm$ 0.4 x 10^{15} atoms cm^{-2} (fig. 4.39) which is much higher than saturation uptake determined, in the present work, on the clean surface at 400 K at 6.1 $\pm$ 0.4 x 10^{15} atoms cm^{-2} but compares well with the value at 420 K of 10.5 $\pm$ 0.4 x 10^{15} atoms cm^{-2} found by Leibbrandt *et al.*[47] If, as we have tentatively suggested, the different oxidation kinetics of clean Fe(100) in the two studies can be explained by the growth of different iron oxide phases, then it follows that different oxide phases are formed on the clean and phosphorus covered surface. The characterisations made in the two clean surface studies would suggest that although a spinel is formed on the clean surface, non-stoichiometric FeO is formed on the phosphorus covered surface. Consistent with this interpretation, we did not observe a spinel LEED pattern for the oxide films grown on the c(2x2)P surface at 400 or 460 K (the surface was disordered).

(ii). Oxygen uptake on phosphorus films at 300 K

In fig. 4.38, ellipsometric measurements have been calibrated to give oxygen uptake, as in the previous section, by assuming that $|\delta\Delta_O|$ is proportional to oxygen coverage and that the proportionality constant used for the oxidation of the clean surface applies in this case. The curve for oxygen uptake on the clean surface at 300 K is also included in fig. 4.38, for comparison. As discussed in Sect. 4.3, oxygen uptake on clean Fe(100) saturates as the oxide reaches a limiting thickness determined by the attenuation of the electron tunnelling current.[69] It has already been shown that oxide grows on the half monolayer of phosphorus, which does not appear to affect saturation thickness, although it does slow the initiation stages.

Fig. 4.38 shows a curve for uptake on a film formed after PH_3 exposures at 345 K, which has been characterised in Sect. 4.2 as phosphorus dissolved into the subsurface region to 9 Å deep. Kinetic similarities indicate that iron oxide grows on this surface. The rate of uptake

in the early stages is identical to that found on the c(2x2)P overlayer. On the clean surface it can be shown by theory[69] and experiment[47] that the rate of the analogous fast stage is controlled by mass transport. Fig. 4.38 suggests that for thin phosphorus films the rate-limiting mass transport process does not depend on the concentration of phosphorus in the subsurface, which may indicate that the process is controlled by surface reactions. The saturation uptake on the 9 Å film is reduced slightly, indicating that the barrier to electron tunnelling at the surface has increased.

The other curves presented in fig. 4.38 are for growth on films ranging in thickness from 48 Å to several hundred Ångstroms (opaque thickness for the ellipsometer) which, it is proposed, are iron phosphide. Oxygen uptake on these films is comparatively slow and tends towards a low saturation uptake of about 2 x 10^{15} atoms cm^{-2}. It is possible that iron oxide could grow on a metallic iron phosphide, in which case this saturation uptake reflects the growth of the first one or two layers (perhaps more resembling an oxide initiation stage). If this is the case, then the reduced saturation uptake is explained by a much greater barrier to electron tunnelling at the iron phosphide surface.

4.5. Conclusions

(i). PH_3 on Fe(100)

The interaction of PH_3 with Fe(100) has been studied with ellipsometry, LEED and TPD spectroscopy. This work represents the first time that this system has been investigated. Results indicate that three different types of phosphorus-containing film are formed, depending on temperature.

At 160 K, PH_3 completely dissociates and phosphorus saturates (at 0.5 monolayers) in a chemisorbed c(2x2) structure. Postdosing experiments with D_2 suggest that phosphorus may initially form up into c(2x2) islands. Desorption spectra of H_2 from dissociated PH_3 show two peaks, both of which can be assigned to recombinative desorption reactions influenced by strongly repulsive lateral interactions between coadsorbed hydrogen and phosphorus atoms.

Between 300 and 445 K, phosphorus uptake quickly saturates with an apparently logarithmic rate of uptake in structurally disordered, optically absorbing films of a few Ångstroms thick. Results are explained by a process involving dissolution into the subsurface region. Delays in film formation at higher temperatures indicate that diffusion into the bulk only becomes important at about 590 K or above. Between 300 and 445 K, bulk diffusion is slow so that phosphorus dissolves in the top few layers of substrate, perhaps by substitution with iron. On annealing to 800 K, diffusion becomes rapid and most phosphorus quickly dissolves into the bulk, leaving a half monolayer c(2x2) overlayer on the surface.

At temperatures from 495 to 545 K, kinetic similarities with lower temperature data indicate that phosphorus also initially dissolves into the subsurface region. However, whereas uptake saturates at temperatures up to 445 K, at 495 K and above growth continues with a slower, near-linear rate, in a process which we have assigned to iron phosphide formation. The optical constants indicate that the phosphide is iron rich (perhaps Fe_3P or Fe_2P).

It is proposed that the initiation of iron phosphide growth involves localised reconstructions of iron about dissolved phosphorus atoms, to form nine-fold coordination sites, which are believed to be the most stable arrangements in iron phosphides.[30] This process requires a sufficiently high phosphorus concentration, as well as high temperatures (about 495 K).

Between 495 and 545 K, phosphorus is held in the subsurface and iron phosphide initiation is quick. At 590 K and above, however, diffusion into the bulk competes with the initiation process and the onset of iron phosphide growth is delayed.

When the first layer has formed, continued growth of iron phosphide becomes comparatively easy. The kinetics of iron phosphide formation indicates that the growth mechanism involves diffusion of uncharged phosphorus atoms (the uptake curve obeys a parabolic rate law at higher pressure). Again, it is speculated that phosphide grows by the localised reconstruction of iron atoms about phosphorus. Resistance to diffusion is high in the phosphide, compared to iron, so that phosphorus atoms remain around long enough to induce localised reconstructions and thereby maintain phosphide growth.

The optical constants of the iron phosphide films (derived from model fits and Δ-ψ values at opaque thickness) vary slightly with temperature, pressure and thickness. These effects can be explained by subtle changes in chemical composition in the probe depth of the light. For example, an inhomogeneous phosphide film, which contains region of bulk iron or even phosphorus solid solution, might account for these observations.

(ii). O_2 on Fe(100)

The oxidation of Fe(100) has been studied with ellipsometry and LEED. The ellipsometric experiments, to some extent, repeat work carried out by Leibbrandt *et al.*[47] However, we have increased the temperature range studied and also correlated data with structural information from LEED. Interestingly, substantial differences in kinetics and uptake measurements have been found between the two studies.

Using a calibration provided by Leibbrandt *et al.*,[47,62] ellipsometric measurements have been converted to oxygen coverage. The uptake curves are characterised by two stages: an initial rapid uptake where rate is controlled by mass transport (through the supply of O_2 to the surface or effect of adsorbed oxide on cation transport) and a much slower, logarithmic growth stage where rate is limited by electron transport. At temperatures up to 420 K, the oxide tends to saturate, indicating that electron tunnelling predominates. At 470 and 610 K there is no strong tendency towards limiting thickness, a difference which can be explained

by a transition to thermionic emission as the predominant electron transport mechanism. Oxides grown at 400 K and above are characterised as a spinel by LEED.

Possible explanations for the discrepancy between the results in the present work and the data of Leibbrandt *et al.*[47] include the different wavelengths used (affecting interpretation of the ellipsometric results) or pressure effects or the condition of the surface (both affecting the uptake kinetics). There is also some evidence that compositionally and structurally different iron oxides have grown in the two studies, which could account for the dissimilarities in the kinetics results.

(iii). O_2 on phosphorus covered Fe(100)

Oxygen uptake on phosphorus covered Fe(100) has been studied with ellipsometry and LEED, and ellipsometric measurements have been converted to oxygen uptake.

On the c(2x2)P surface, results have been interpreted as showing the growth of iron oxide. The oxidation kinetics on this and the clean surface are broadly similar. The uptake curves are characterised by an initially fast stage limited by mass transport, and a second much slower stage limited by electron transport, which quickly saturates at temperatures up to 400 K. Growth in the initial stage is slower on the phosphorus covered surface, indicating that phosphorus interferes with mass transport processes. Remarkably, growth in the second stage is considerably faster on the phosphorus covered surface.

This may indicate that phosphorus interferes with electron transport processes. It is also suggested that the different kinetics observed on the clean and phosphorus covered surface may indicate that different oxide phases are grown.

4.6. Future work

XPS could be used to distinguish between the three proposed films formed during the interaction of PH_3 with Fe(100). The effect of pressure on film growth kinetics needs to be more clearly defined.

The possibility of the growth of different oxide phases on the clean and phosphorus covered surfaces should be investigated. XPS could be applied to distinguish between the growth of FeO (Fe^{II}) and spinels (Fe^{II} and Fe^{III}).

There is still much to learn about oxygen uptake on phosphorus films. It would be interesting to investigate high temperature oxidation on thin phosphorus films.

4.7. References

1. W. Hume-Rothery, *"The Structures of Alloys of Iron"*, (Pergammon Press, Oxford, 1966).

2. S. Kato and H. Kobayashi, *Surf. Sci.* 27 (1971) 625.

3. C. Leygraf and S. Ekelund, *Surf. Sci.* 40 (1973) 609.

4. R. Feder, *Phys. Stat. Solidi* 58 (1973) K137.

5. K.O. Legg, F. Jona, D.W. Jepsen and P. Marcus, *J. Phys. C* 10 (1977) 937.

6. R.W.G. Wyckoff, *"Crystal Structures"*, 2nd Ed. (Interscience, New York, 1963).

7. E.A. Wood, *J. Appl. Phys.* 35 (1964) 1306.

8. P.B. Sewell, D.F. Mitchell and M. Cohen, *Surf. Sci.* 33 (1972) 535.

9. J. Benziger and R.J. Madix, *Surf. Sci.* 94 (1980) 119.

10. G.W. Simmons and D.J. Dwyer, *Surf. Sci.* 48 (1975) 373.

11. H.J. Grabke, W. Paulitschke, G. Tauber and H. Viefhaus, *Surf. Sci.* 63 (1977) 377.

12. H.J. Grabke, *Mat. Sci. Engineering* 42 (1980) 91.

13. B. Egbert and G. Panzner, *Surf. Sci.* 118 (1982) 345.

14. C.F. Brucker and T.N. Rhodin, *Surf. Sci.* 57 (1976) 523.

15. F. Bozso, G. Ertl and M. Weiss, *Appl. Surf. Sci.* 1 (1977) 103.

16. J. Benziger and R.J. Madix, *Surf. Sci.* 94 (1980) 119.

17. H.F. Berger and K.D. Rendulic, *Surf. Sci.* 251/252 (1991) 882.

18. E.A. Kurz and J.B. Hudson, *Surf. Sci.* 195 (1988) 31.

19. A. Hodgson, A. Wight, G. Worthy, D. Butler and B.E. Hayden, *Faraday Dicuss.* 96 (1994) 161.

20. C.A. Shell and J.C. Riviere, *Surf. Sci.* 40 (1973) 149.

21. H. Viefhaus, R. Möller, H. Erhart and H.J. Grabke, *Scr. Metall.* 17 (1983) 165.

22. W. Arabczyk, T. Baumann, F. Storbeck, H.-J. Müssig and A. Meisel, *Surf. Sci.* 189/190 (1987) 190.

23. R.I. Hedge and J.M. White, *J. Phys. Chem.* 90 (1986) 2159.

24. G. Ertl, J. Küppers, F. Nitschke and M. Weiss, *Chem. Phys. Lett.* 52 (1977) 309.

25. R.I. Hedge, J. Tobin and J.M. White, *J. Vac. Sci. Technol.* A3 (1985) 339.

26. G.E. Mitchell, M.A. Henderson and J.M. White, *Surf. Sci.* 191 (1987) 425.

27. M. KIiskinova and D.W. Goodman, *Surf. Sci.* 108 (1981) 64.

28. X.-L. Zhou and J.M. White, *Surf. Sci.* 221 (1989) 534.

29. W. Arabczyk, H.-J. Müssig and F. Storbeck, *Surf. Sci.* 251/252 (1991) 804.

30. D.E.C. Corbridge, *Topics in Phosphorus Chem.* 3 (1966) 527.

31. S. Rundqvist, *Acta Chem. Scand.* 16 (1962) 1.

32. H. Fujii, S. Komura, T. Takeda, T. Okamoto, Y. Ito and J. Akimitsu, *J. Phys. Soc. Japan* 46 (1979) 1616.

33. S. Rundqvist, *Acta Chem. Scand.* 16 (1962) 287.

34. E. Dahl, *Acta Chem. Scand.* 23 (1969) 2677.

35. W. Jeitschko and D.J. Braun, *Acta Cryst.* B34 (1978) 3196.

36. G.A. Bootsma and F. Meyer, *Surf. Sci.* 14 (1969) 52.

37. R.M.A. Azzam and N.M. Bashara, *"Ellipsometry and Polarised Light"*, (North Holland, Amsterdam, 1977).

38. J.M.M. de Nijs and A. van Silfhout, *J. Opt. Soc. Am.* 5 (1988) 773.

39. D.E. Aspnes, *J. Opt. Soc. Am.* 64 (1974) 812.

40. D.E. Aspnes and A.A. Studna, *Appl. Opt.* 14 (1975) 220.

41. T.J. Vink, O.L.J. Gijzeman and J.W. Geus, *Surf. Sci.* 150 (1985) 14.

42. H.T. Yolken and J. Kniger, *J. Opt. Chem. Soc. Am.* 55 (1965) 842.

43. K.R. Lawless, *Rep. Prog. Phys.* 37 (1974) 231.

44. J.R. van Waser, *"Phosphorus and its Compounds"*, (New York, 1958).

45. S. Fiechter, H. Tributsch, M. Evain and R. Brec, *Mat. Res. Bull.* 22 (1987) 543.

46. G. Boda, B. Strenström, V. Sagredo, O. Beckman, B. Carlsson and S. Rundqvist, *Phys. Scripta* 4 (1971) 132.

47. G.W.R. Leibbrandt, G. Hoogers and F.H.P.M. Habraken, *Phys. Rev. Letts.* 68 (1992) 1947.

48. V.S. Smentkowski and J.T. Yates, *Surf. Sci.* 232 (1990) 113.

49. H.J. Goldschmidt, *J. Iron Steel Inst. (London)* 146 (1942) 157.

50. A.F. Wells, *"Structural Inorganic Chemistry"*, 2nd Ed. (Oxford University Press, 1950).

51. S. Weissmann, B. Post, M.E. Melrose, H.F. McMurdie, M.C. Morris and W.F. McClune, Eds, *"Selected Powder Diffraction Data for Metals and Alloys"*, JCPDS International Centre for Diffraction Data, 1st Ed., (Pennsylvania, 1978).

52. F. Koch and J.B. Cohen, *Acta Cryst.* B25 (1969) 275.

53. Von R. Schrader and G. Büttner, *Z. Anorg. Allgem. Chemie* 320 (1963) 205.

54. Y. Sakisaka, T. Miyano and M. Onchi, *Phys. Rev. B* 30 (1984) 6849.

55. J.P. Lu, M.R. Albert, S.L. Bernasek and D.J. Dwyer, *Surf. Sci.* 215 (1989) 348.

56. T. Horiguchi and S. Nakanishi, *Japan J. Appl. Phys.* Suppl. 2, Pt.2 (1974) 89.

57. K.O. Legg, F. Jona, D.W. Jepsen and P.M. Marcus, *Phys. Rev. B* 16 (1977) 5271.

58. A.J. Pignoccio and G.E. Pellisier, *J. Electrochem. Soc.* 112 (1965) 1188.

59. C.R. Brundle, *IBM J. Res. Develop.* 22 (1978) 235.

60. T.J. Vink, J.M. Der Kinderen, O.L.J. Gijzeman, J.W. Geus and J.M. van Zoest, *Surf. Sci.* 26 (1986) 357.

61 H. Huang and J. Hermanson, *Phys. Rev. B* 32 (1985) 6312.

62. J.M. van Zoest, J.M. Fluit, T.J. Vink and B.A. van Hassel, *Surf. Sci.* 182 (1987) 179.

63. G.W.R. Leibbrandt, S. Deckers, M. Wiegel and F.H.P.M. Habraken, *Surf. Sci. Letts.* 244 (1991) L101.

64. H.T. Yolken and J. Kruger, *J. Electrochem. Soc.* 114 (1967) 796.

65. A.T. Fromhold, Jr. and E.L. Cook, *Phys. Rev. Lett.* 17 (1966) 1212.

66. A.T. Fromhold, Jr. and E.L. Cook, *Phys. Rev.* 158 (1967) 600.

67. A.T. Fromhold, Jr. and E.L. Cook, *Phys. Rev.* 163 (1967) 650.

68. W.W. Smeltzer and D.J. Young, *Prog. Solid State Chem.* 10 (1975) 17.

69. A.T. Fromhold, Jr., *"Theory of Metal Oxidation - Volume 1, Fundamentals"*, in the series Defects in Crystalline Solids, Vol. 9 (North-Holland, 1976, Amsterdam).

70. A.T. Fromhold, Jr., *"Theory of Metal Oxidation - Volume 2, Space Charge"*, in the series Defects in Crystalline Solids, Vol. 12 (North-Holland, 1980, Amsterdam).

71. N.F. Mott, *Trans. Faraday Soc.* 35 (1939) 1175.

72. N.F. Mott, *Trans. Faraday Soc.* 36 (1940) 472.

73. N. Cabrera and N.F. Mott, *Rep. Prog. Phys.* 12 (1949) 163.

74. A. Atkinson, *Rev. Mod. Phys.* 57 (1985) 437.

75. F.H.P.M. Habraken, O.L.J. Gijzeman and G.A. Bootsma, *Surf. Sci.* 96 (1980) 482.

76. J.H. Weaver, E. Colavita, D.W. Lynch and R. Rosei, *Phys. Rev. B* 19 (1979) 3850.

77. G.W.R. Leibbrandt, L.H. Spiekman and F.H.P.M. Habraken, *Surf. Sci.* 287/288 (1993) 245.

78. D.F. Mitchell, P.B. Sewell and M. Cohen, *Surf. Sci.* 69 (1977) 310.

5. PHOSPHORUS ON Fe(100): THE ADSORPTION OF PHOSPHINE (PH_3) STUDIED WITH LEED AND TPD SPECTROSCOPY

5.1. Characterisation of clean Fe(110)

After preparation by cycles of Ar^+ bombarding and annealing (described in Sect. 2.1.7), the clean surface of Fe(110) was characterised by low energy electron diffraction (LEED) and the temperature programmed desorption (TPD) spectra of H_2.

5.1.1. Characterisation by LEED

The clean surface of Fe(110) has been found to be unreconstructed,[1-5] although there is a small expansion (0.5%) in the first interplanar spacing.[5] The arrangement of atoms in the (110) surface (the most densely packed plane in a bcc metal) has the superficial appearance of a hexagonal structure, but possesses a centred rectangular Bravais net described by a centred unit mesh of length a = 2.86 Å and b = 4.04 Å (fig. 5.1). However, a primitive unit mesh is used to index the Fe(110) LEED pattern, shown schematically in fig. 5.1, to avoid the problem of spurious "missing" spots. The same primitive mesh will be used in the denotation of overlayers reported in this study.

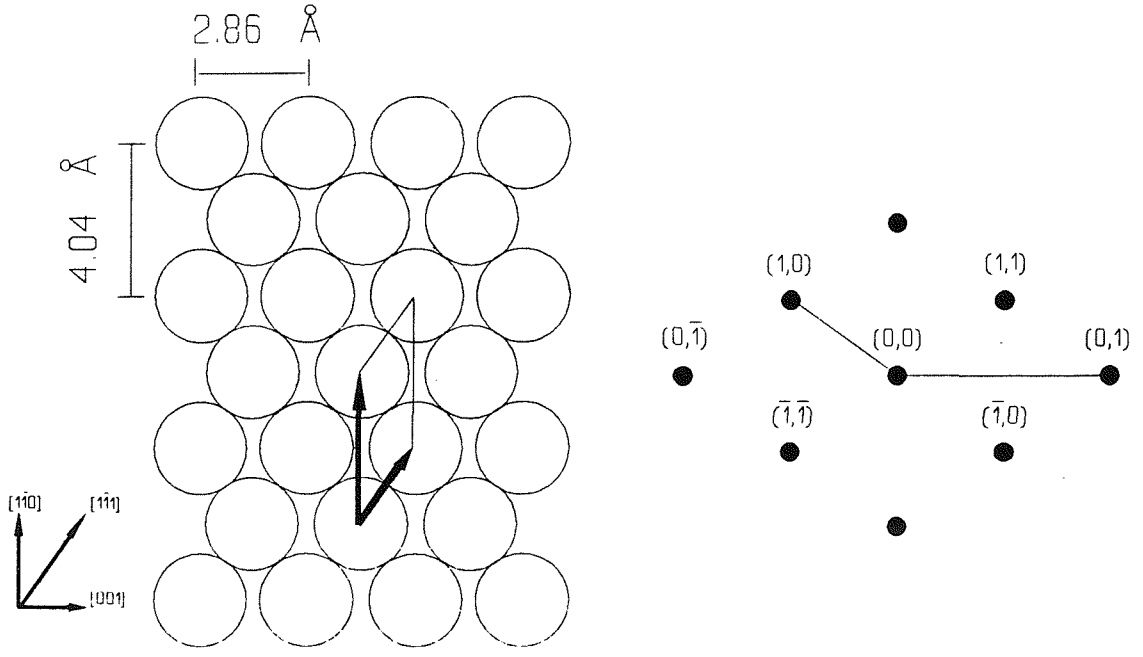

Fig. 5.1. (a) Structural model of Fe(110) surface and (b) schematic representation of LEED pattern of the Fe(110) surface, showing first order spots. Vectors of the real space and corresponding reciprocal space unit meshes also shown.

In the absence of any technique to measure surface composition, LEED was used in the present work to check the surface cleanliness of Fe(110). We were helped in this by the rich variety of structures formed by atoms on Fe(110), which often made it possible to identify the contaminant and gain some idea of its coverage. The LEED patterns reported in the literature for some expected contaminant atoms are now briefly described. The Wood notation[6] is generally used to describe structures on Fe(110), although it leads to some confusion and ambiguity through the possibility of three different basis vectors (fig. 5.2).

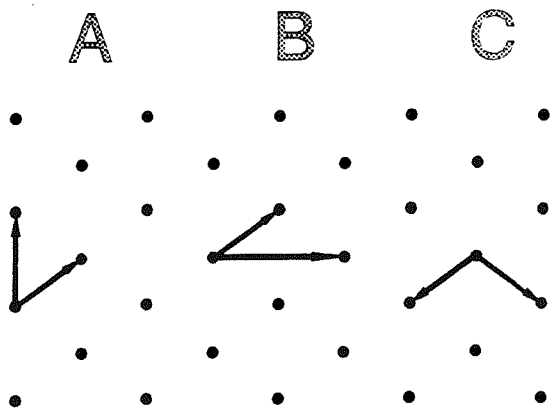

Fig. 5.2. Reciprocal lattice and three possible sets of basis vectors for designating overlayer structures on Fe(110).

Segregated and absorbed carbon and nitrogen are characterised by similar, complex patterns, conveniently referred to as "rings".[7-11] Bozso *et al.*[10] have interpreted the nitrogen ring pattern as a superposition of patterns from two incommensurate structures, which approach the structure of Fe_4N. Sulphur, from the absorption of H_2S at 420 K, has shown p(2x2) and c(3x1) patterns (designated using basis *A* and *B*, respectively, in fig. 5.2) which are assigned to simple overlayers.[12] The c(3x1) pattern was also observed after segregation of sulphur from the bulk.[7] Oxygen, in the early stages of uptake, showed c(2x2) and c(3x1) patterns (designated using basis *C* and *B*, respectively) which are attributed to chemisorbed oxygen, and a (1x1) pattern, which corresponds to the formation of an oxide.[13]

In the present study, the sample temperature was generally kept below 700 K during experiments or surface preparation (see Sect. 2.1.7) to reduce segregation or subsurface enrichment by the expected contaminants sulphur, carbon, nitrogen and oxygen (especially sulphur, where segregation only becomes important at temperatures above 970 K[14]). Carbon segregation, as indicated by the carbon ring pattern (Fig. 5.3), was frequently observed

during surface cleaning (the element could be identified by coadsorbing oxygen and checking for CO desorption). The segregation of carbon could be suppressed by periodic oxygen treatments (typically 10^{-7} torr O_2 for 1 hour at 710 K) to reduce levels of the contaminant in the subsurface region. It is possible, although it was never confirmed, that the observed ring patterns were occasionally caused by segregated nitrogen. The presence of sulphur in the subsurface region was clearly indicated by the observation of a c(3x1) pattern after annealing the sample to 900 K for a few hours. Occasionally, faint c(2x2) and c(3x1) patterns were observed during routine cleaning procedures, showing perhaps the segregation of oxygen. The importance of oxygen segregation was later confirmed by other workers[15] in an AES study using the same Fe(110) crystal, although it only became a significant problem at temperatures of about 850 K and above.

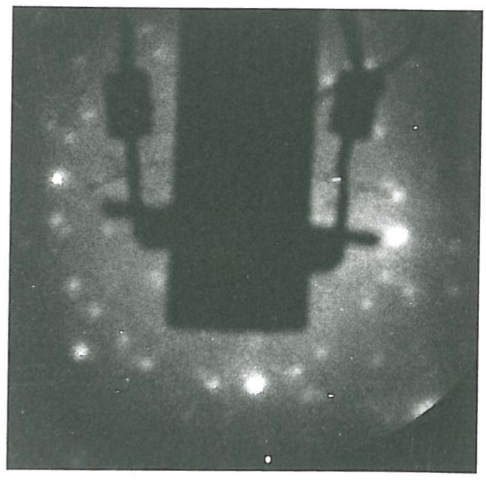

Fig. 5.3. Carbon ring LEED pattern (E = 187 eV), see text for explanation.

In the present study, the observation of a sharp p(1x1) pattern on a background of low intensity was taken to indicate a clean, well-ordered Fe(110) surface. The clean surface was further characterised in a TPD study of H_2.

5.1.2. Characterisation by thermal desorption of H_2

The clean surface of Fe(110) was also characterised by a set of reproducible and well-behaved H_2 temperature programmed desorption (TPD) spectra. Fig. 5.4 shows typical curves after exposures of between 0.2 and 1000 L at a sample temperature of 170 K.

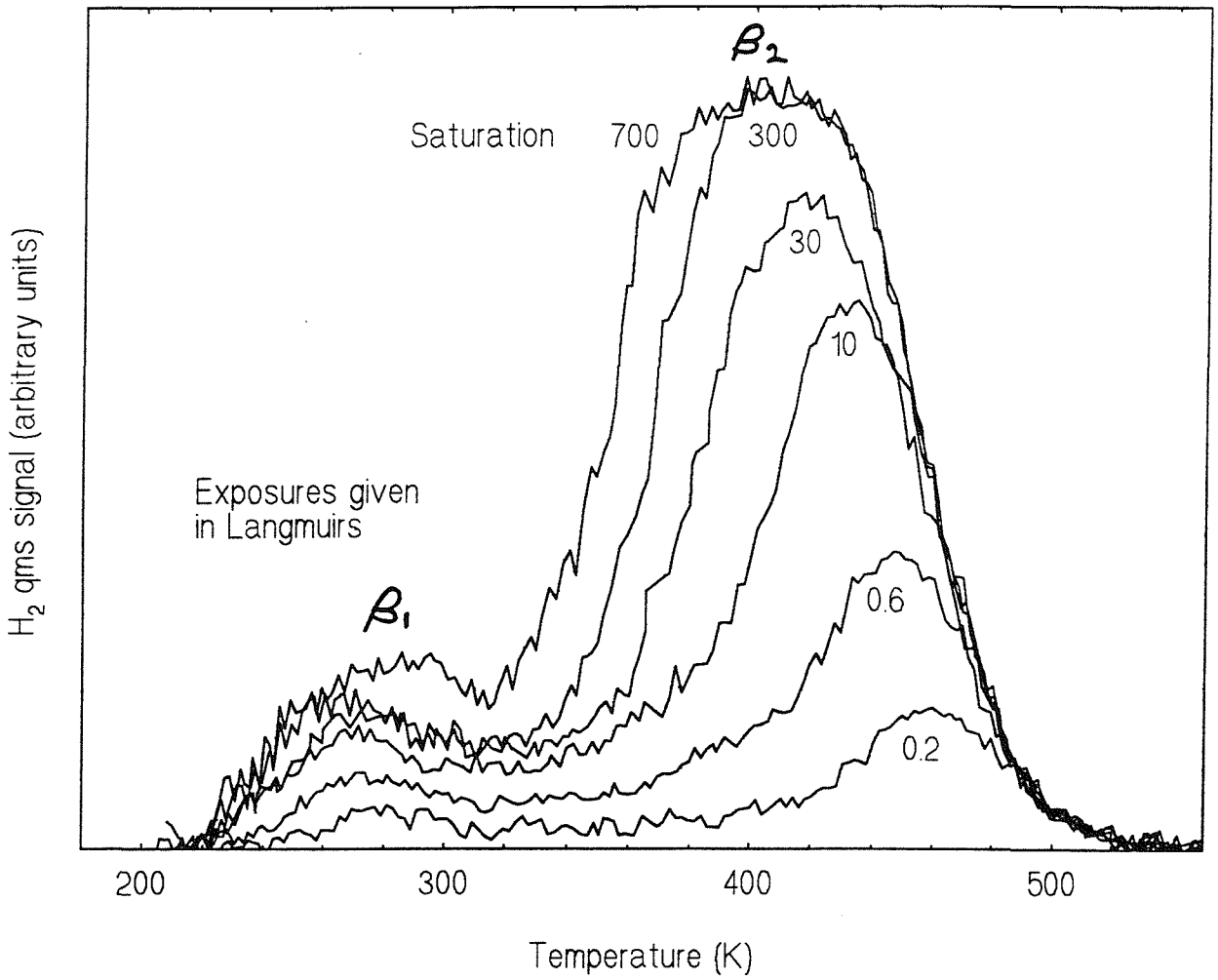

Fig. 5.4. *TPD spectra for recombinative desorption of H_2 from Fe(110), as a function of H_2 exposure. Heat rate 2.3 K s^{-1}.*

At all exposures studied, the spectra show a low temperature peak, assigned[16] as β_1, and a higher temperature peak, assigned as β_2, in which most of the H_2 desorbs. The high temperature β_2 peak, located at about 460 K after an exposure of 0.2 L, shifts to lower temperature with increasing exposure, indicating second-order desorption kinetics. The much smaller β_1 peak, centred at about 270 K at 0.2 L, does not shift significantly with exposure. Together, the peaks approach saturation after exposures of about 300 L. A third, lower temperature, peak reported by Berger and Rendulic[17] was not observed in the present study. The spectra were not analyzed to determine desorption energy because of overlap between the two peaks.

The observed development of the two peaks is in good agreement with previous studies.[15-18] Hydrogen has been shown[16] to completely dissociate on Fe(110) at temperatures as low as 140 K. Bozso *et al.*[16] have assigned the β_2 peak to a second-order recombinative desorption reaction, and the β_1 peak to recombinative desorption influenced by repulsive interactions among hydrogen adatoms in ordered overlayers. Several LEED studies have shown the formation of a series of ordered overlayers on unreconstructed Fe(110), ranging from a c(2x2) structure (basis *C* in fig. 5.2), which saturates at 0.5 monolayers (ML), to a (1x1) structure,[11,16,19] which saturates at 1 ML. We were unable to detect extra LEED spots during H_2 adsorption, presumably because hydrogen is such a weak scatterer.

The curve of hydrogen uptake *versus* H_2 exposure given in fig. 5.5 has been derived from the relative areas of TPD spectra by assuming that saturation coverage (θ_{sat}) at 170 K equals 1 ML, as indicated by the LEED results of Bozso *et al.*[16] (it should be noted, however, that Berger and Rendulic[17] determined θ_{sat} at 300 K to be 0.48 ML in a molecular beam study). Error in coverage in fig. 5.5 is at worst about $\pm$ 5%, arising from uncertainty in the position of the base line during measurement of the areas.

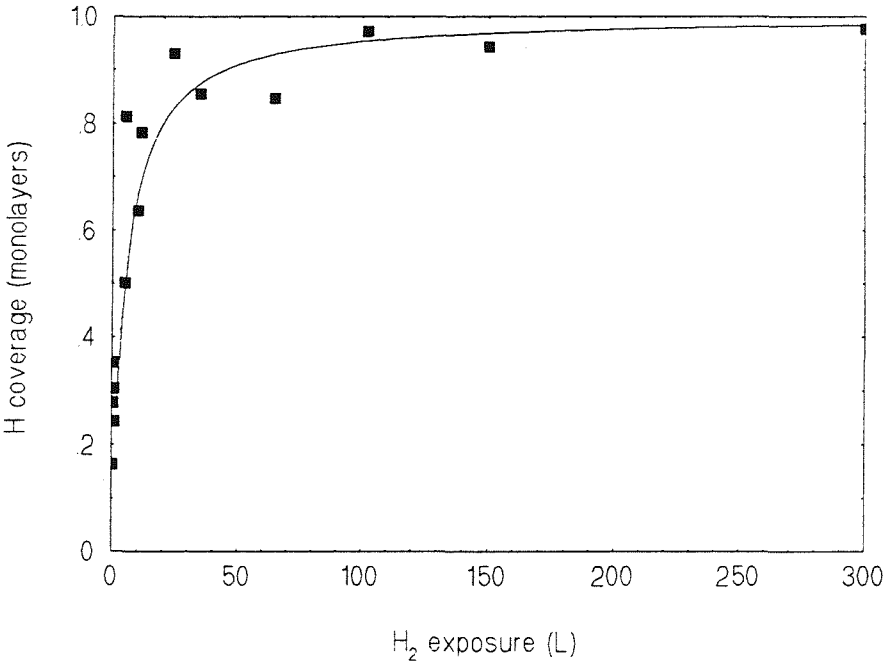

Fig. 5.5. Hydrogen coverage as a function of H_2 exposure for adsorption at 170 K. Theoretical curve (solid line) given by eq. (5.1) where S_0 = 0.10.

A theoretical fit to the uptake curve was found using

$$\theta = \frac{S_0}{S_0 + (1/L)} \tag{5.1}$$

where θ is the hydrogen coverage, S_0 is the initial sticking coefficient and L is the H_2 exposure This is the approach used by Benziger and Madix,[20] and applied to the D_2 on Fe(100) results in Sect. 4.1.3. The equation is derived by assuming a simple Langmuir type dissociative adsorption, where S_θ (the sticking coefficient at coverage θ) varies with coverage as $S_\theta(1 - \theta)^2$.

A reasonable fit is obtained with the initial sticking coefficient $S_0 = 0.10$. This compares well with the literature where S_0 has been determined as: 0.16 from uptake measurements[16] at 140 K; 0.18 in He atom reflectivity experiments[18] at 300 K; and, 0.12 in molecular beam experiments[17] at 300 K. Nevertheless, the method used to determine S_0 in the present work makes too many assumptions and approximations for the value to be considered accurate. However, the success of the theoretical fit does indicate that a simple dissociative adsorption model for H_2 on Fe(110) is valid, at least at higher coverages, as has been reported before[16,18] (although a recent study[15] suggests that the dependence is more likely somewhere between $(1 - \theta)$ and $(1 - \theta)^2$).

Reproducibility in the data and the good theoretical fit indicates that the desorption behaviour observed in the present study is characteristic of clean Fe(110). Anomalous spectra typically showed less H_2 desorption than expected for the exposure used. Such deviations were presumed to indicate surface contamination or poor surface ordering. We have used these adsorption/desorption characteristics, as a complement to LEED experiments, for checking surface cleanliness. However, Hodgson *et al.*[15] have recently suggested that H_2/Fe(110) TPD spectra are rather insensitive to surface contamination. They were unable to detect anomalies in their TPD spectra even though helium beam scattering measurements indicated that the surface was slightly contaminated (no indication of the coverages involved was given). In practise, LEED was used in the present study for routine inspection of surface cleanliness while TPD experiments were used as a check during sample preparation or when unexpected results were found.

5.2. LEED study of the interaction of phosphine (PH_3) with Fe(110) at 160 and 540 K

5.2.1. Introduction

In this section we report a LEED structural investigation of the interaction of PH_3 with Fe(110), to our knowledge the first time this system has been studied. Although it was originally intended that this study should complement the work on PH_3/Fe(100), reported in Sect. 4.2, the investigation has focused entirely on the structural chemistry of low coverages of phosphorus atoms on Fe(110). The relevant and rather scant literature has been reviewed in Sect. 4.2.

5.2.2. Results

The interaction of PH_3 with Fe(110), at pressures in the range 1 x 10^{-8} to 1 x 10^{-6} torr PH_3 and sample temperatures of 170 and 540 K, was investigated with LEED and thermal desorption spectroscopy. Results of PH_3 experiments on Fe(100) referred to in this section can be found in Sect. 4.2.2.

(i). Adsorption at 170 K

H_2 was the only desorbent detected in thermal desorption experiments, indicating that PH_3 is completely and irreversibly dissociated on Fe(110) at 170 K. A series of TPD spectra for the desorption of H_2 from dissociated PH_3 on Fe(110), at different PH_3 exposures, are shown in fig. 5.6. Although there was much outgassing from the sample mount after high PH_3 exposures, background subtraction was not the problem it had been in analysing the PH_3/Fe(100) data. Consequently, PH_3 uptake can be followed all the way to saturation at about 50 L.

Two peaks, assigned as β_1^P and β_2^P, can be identified in the development of the spectra in fig. 5.6. After very low PH_3 exposures in the range 0.1 to 0.4 L, H_2 desorbs in a single feature - the β_2^P peak - which is centred at about 430 K after an exposure of 0.1 L. The β_2^P peak shifts to lower temperatures with increasing exposure indicating second-order desorption

kinetics. A similar feature (the β_2 peak) was detected for H_2 on the clean surface, as shown in fig. 5.4. However, in contrast, the β_2^P peak appears at lower temperatures (by about 40 K) and the drop in peak temperature with increasing hydrogen uptake is noticeably larger (for example, the β_2^P drops by 60 K between 0.1 and 0.4 L, while the β_2 peak on the clean surface decreases by a similar amount over the range 0.2 L to saturation). No feature corresponding to the low temperature β_1 peak on the clean surface was detected in the spectra of H_2 from the phosphorus covered surface. Clearly, phosphorus has a strong effect on the H_2 desorption kinetics and energetics. These observations compare well with the results of Hedge and White[21] in their study of PH_3 adsorption on polycrystalline iron at 100 K. They reported a single feature at low phosphorus coverage which quickly shifted to lower temperatures with increasing exposure.

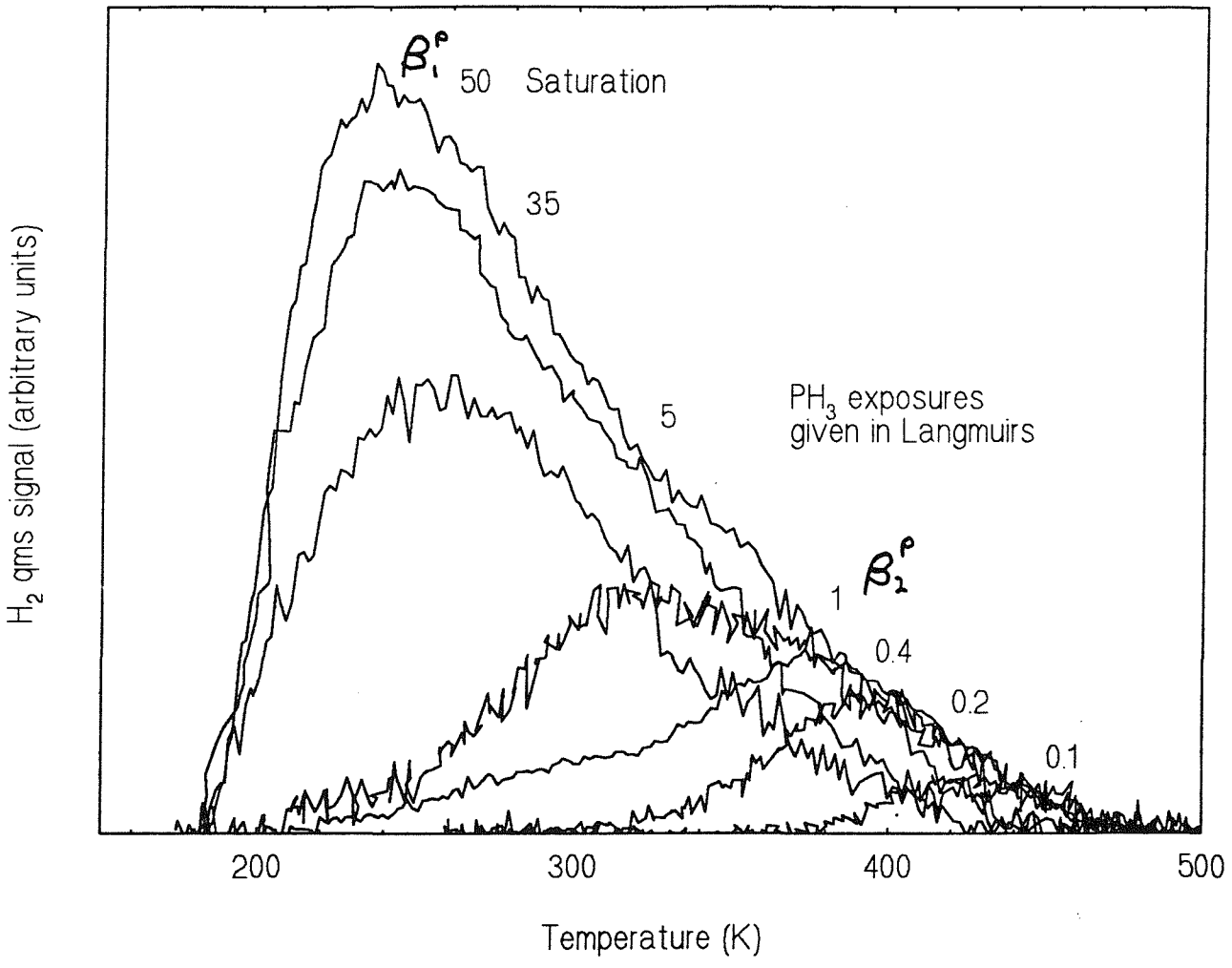

Fig. 5.6. *TPD spectra for recombinative desorption of H_2 from dissociated PH_3 on Fe(100), as a function of PH_3 exposure. Heat rate 2.3 K s^{-1}.*

At higher PH_3 exposures (from 5 L to saturation at 50 L), hydrogen desorbs in a broad, low temperature peak, centred about 270 K. It appears to be a new peak, distinct from the higher temperature β_2^P feature, and can be labelled β_1^P. This strongly contrasts with H_2 desorption from clean Fe(110) where at saturation nearly all of the hydrogen desorbs in a high temperature peak at about 400 K (fig. 5.4). It was not possible to detect clearly the emergence of the β_1^P peak at low phosphorus coverages, and there is some uncertainty that the β_1^P and β_2^P states coexist on the surface. For example, at 5 L PH_3 there is no evidence of desorption in the higher temperature β_2^P peak (although the β_1^P peak is quite broad), while at saturation desorption does extend to high temperatures and the TPD trace could be interpreted as a superposition of the two states.

It is clear that coadsorbed phosphorus has a strong influence on the H_2 desorption kinetics and energetics, even at low coverages (down to at least 0.1 monolayers, according to the uptake versus exposure curve reported, below, in fig. 5.8). The broad β_1^P peak can be assigned to a recombinative desorption reaction promoted by strongly repulsive lateral interactions between adsorbed phosphorus and desorbing hydrogen adatoms. As described in the previous chapter (Sect. 4.2.2), an analogous low temperature feature was seen for H_2 from PH_3 on Fe(100).

Structures formed during adsorption at 170 K were poorly ordered as indicated by LEED. The p(1x1)-Fe(110) pattern quickly deteriorated on exposing the clean surface to PH_3. With increasing exposure, the spots weakened, became more diffuse and the background intensity increased. After exposures of about 1 or 2 L, new features were just visible at fractional order positions and remained so up to saturation, although they were faint and diffuse. On flashing the surfaces to 400 or 500 K (desorbing all the hydrogen), the LEED features sharpened into a clear p(1x4) pattern, as shown in fig. 5.7 (structure designated using basis *B* in fig. 5.2).

The p(1x4) pattern can be interpreted as representing a simple phosphorus overlayer on unreconstructed Fe(110), with a saturation coverage (θ_{sat}) of 0.25 ML. Alternatively, as discussed below, it may represent a reconstruction, although size constraints probably mean that there is still only one phosphorus atom *per* p(1x4) unit mesh.

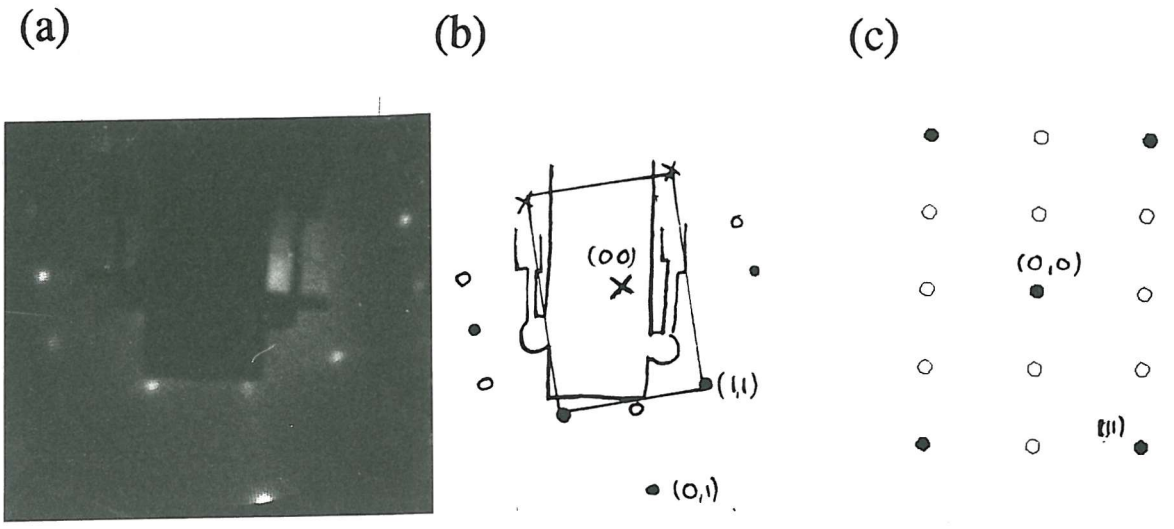

Fig. 5.7. (a) LEED pattern of p(1x4)P structure (E = 162 eV) formed by flashing surface to 400 K after PH_3 adsorption at 170 K , (b) diagrammatic representation of photograph and (c) schematic representation of p(1x4) pattern - in both cases showing first-order Fe(110) spots as filled circles and fractional-order p(1x4) spots as open circles.

The areas of the H_2 desorption spectra in fig. 5.6 can be calibrated, assuming that θ_{sat} = 0.25 ML, to give the curve of phosphorus coverage versus PH_3 exposure shown in fig. 5.8 (error in coverage is about ± 5%). The solid curve is a very approximate best fit, drawn by hand and intended as a guideline.

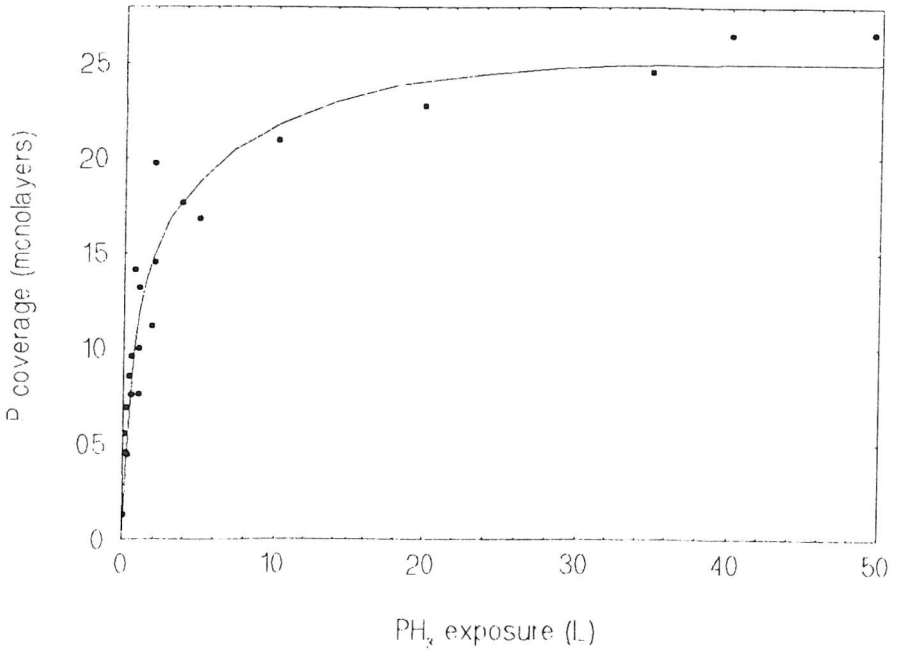

Fig. 5.8. Phosphorus coverage as a function of PH_3 exposure for adsorption at 170 K. Solid curve is given as a guide line.

The uptake curve is initially linear indicating a constant sticking coefficient, which may suggest that adsorption occurs through a mobile precursor state.

According to this curve, ordered structures are first observed after a coverage of about 0.13 ML. It also suggests that the β_1^P peak in the desorption spectra of H_2 from dissociated PH_3 (fig. 5.6) is first seen in the coverage range 0.05 to 0.2 ML.

(ii). Adsorption at 540 K

The structural chemistry of the early stages of the interaction of PH_3 with Fe(110) was investigated at the temperature 540 K, where all of the hydrogen from the dissociated molecule desorbed during the exposure. LEED observations were made after cooling the sample to 170 K.

Three overlayer LEED patterns were detected during PH_3 adsorption at 540 K. On a few occasions, a faint p(2x2) pattern was the first change detected in the LEED, after very low PH_3 exposures of between 0.4 and 1.0 L. The p(2x2) LEED pattern was not photographed but is shown schematically in fig. 5.9 (it is designated with the same basis - (*B* in fig. 5.2) - used for the p(1x4) pattern). The p(2x2) structure was apparently unstable at room temperature, rearranging to a p(1x4) overlayer after 20 minutes, although the transformation may possibly be induced by the electron beam of the LEED experiment. Either way, this instability probably explains the failed attempts to reproduce it. As will be discussed below, the structure can be interpreted as a simple phosphorus overlayer with a saturation coverage of 0.25 ML, equal to that of the p(1x4) structure.

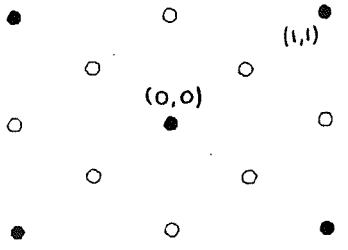

Fig. 5.9. *Schematic representation of the LEED pattern of the p(2x2)P structure, showing first-order Fe(110) spots as filled circles and fractional-order spots as open circles.*

However, the first change detected was generally the appearance of a p(1x4) pattern, after accumulated or single PH_3 exposures of 1.0 L or more. There was no evidence of a different pattern preceding the p(1x4) structure, despite careful observation. With increasing exposure, the p(1x4) spots became more diffuse and the background more intense, indicating increased structural disorder. After very high PH_3 exposures (from 60 to 2000 L), the LEED pattern was diffuse and no features were visible, indicating long range disorder. The disordered layer transformed into a p(1x4) structure on annealing for a few minutes at 900 K.

A third, low coverage structure with a complicated LEED pattern shown in fig. 5.10, was detected during adsorption at 540 K, and also at 300 K in one experiment. On several occasions this pattern was the first change observed in the LEED, after PH_3 exposures in the range 0.6 to 1.5 L, and subsequently transformed to a p(1x4) pattern with increasing exposure. The appearance of this structure may depend on surface preparation: it was observed in experiments where the surface had been annealed at 670 K after Ar^+ bombardment, rather than at the more frequently used temperature of 870 K. It may be that a high concentration of surface defects (present on the 670 K surface) is important for the formation of this structure.

(a)

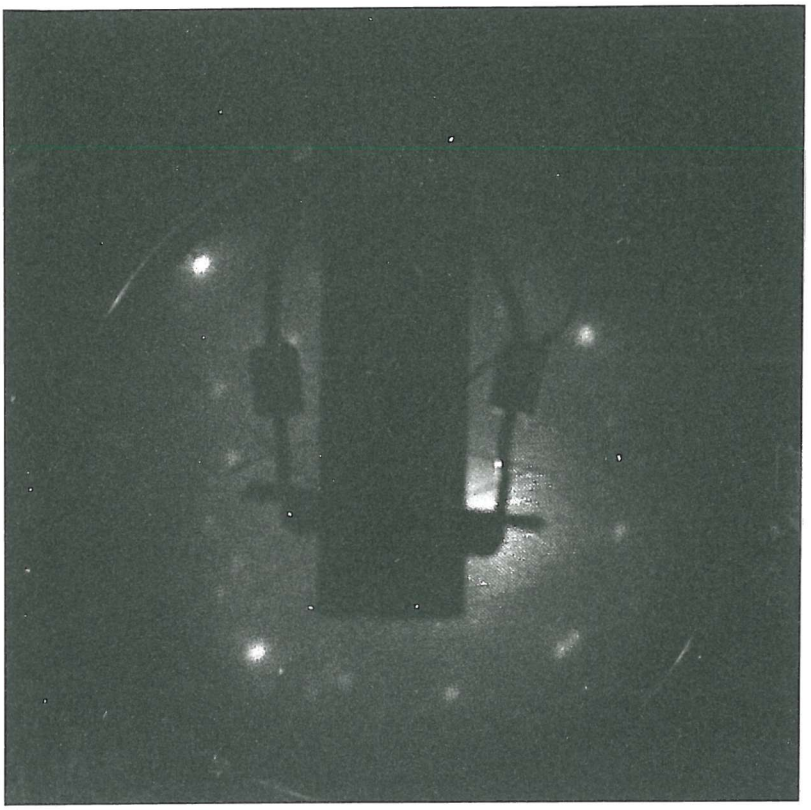

(b)

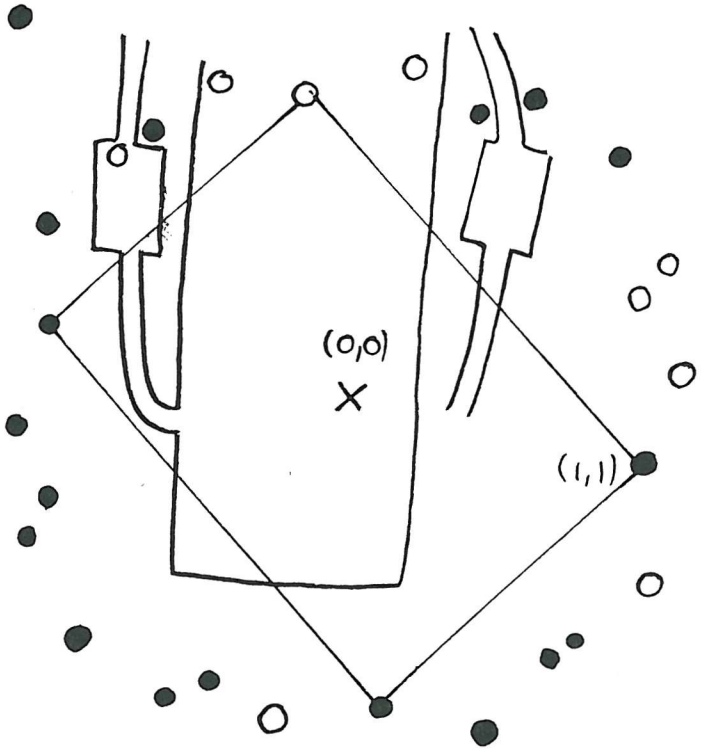

Fig. 5.10. *(a) LEED pattern of unidentified low phosphorus coverage structure (E = 110 eV) and (b) diagrammatic representation of photograph with visible spots shown as filled circles and the position of symmetrically related spots shown as open circles (for clarity, the reciprocal lattice centred-rectangle unit mesh, centred on zeroth order spot, is also shown).*

(iii). Reconstruction at high temperatures (800-900 K)

The thermal stability of phosphorus structures formed in adsorption experiments at 170 and 540 K was investigated using LEED. Observations were made after cooling the sample to 170 K.

Low coverage p(1x4) overlayers, formed by PH_3 exposures in the range 1 to 1.5 L at both temperatures (170 and 540 K), transformed to the complex, unidentified structure shown above in fig. 5.10, after annealing the surface at 850 K for 5 minutes. This reconstructed surface was stable to further periods of annealing (up to 1 hour) at temperatures up to 800 K. Higher coverage p(1x4) surfaces (up to saturation), formed at both adsorption temperatures, were more stable to high temperature annealing. After a few minutes of annealing at 850 or 900 K, the p(1x4) pattern was sharper, brighter and of stronger contrast, indicating improved structural ordering. With prolonged periods of high temperature annealing (1 or 2 hours), the p(1x4) pattern showed streaking in the $<\bar{1}10>$ and $<001>$ directions (indicating disorder within domains in these directions) and spot-splitting (indicating changes in the size of domains). Two new reconstructions were detected on annealing saturated phosphorus overlayers formed at 170 K. The patterns, which are shown in fig. 5.11, could not be reproduced in subsequent experiments, and the factors that led to their formation were not determined.

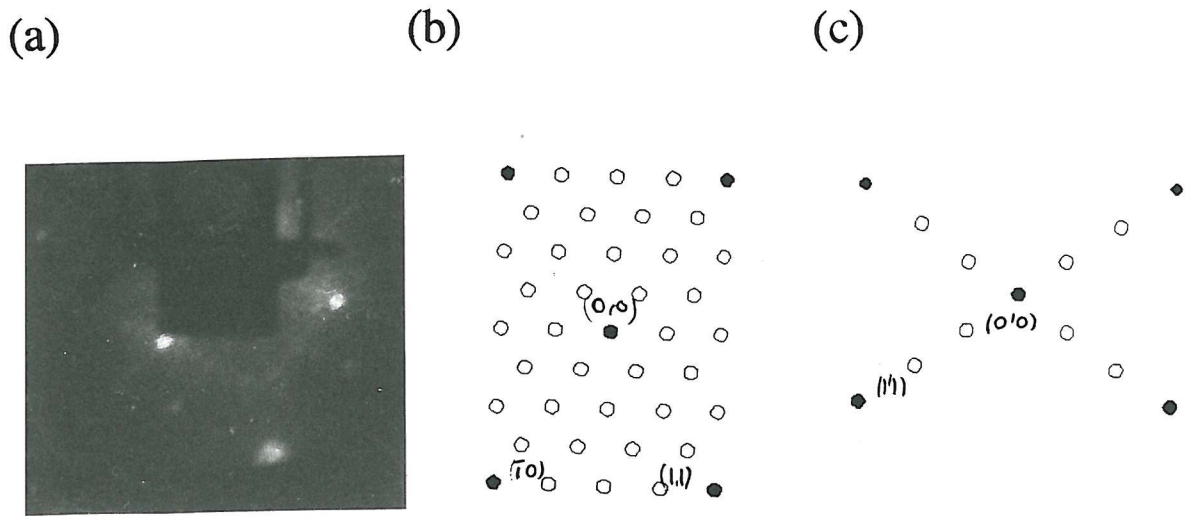

Fig. 5.11. *(a) LEED patterns of high temperature reconstruction and (b) schematic representation showing first order Fe(110) spots as open circles. (c) Schematic representation of second high temperature reconstruction showing first order Fe(110) spots as filled circles.*

5.2.3. Discussion

(i). Adsorption at 170 K

Results of experiments at 170 K can be explained by a straightforward dissociative chemisorption process. The absence of PH_3 desorption and the appearance of the H_2 desorption spectra, which was characteristic of a recombination reaction, show that PH_3 completely and irreversibly dissociates into phosphorus and hydrogen atoms. LEED indicates that phosphorus forms a poorly ordered structure. On flashing to 500 K, the surface reconstructs to a well-ordered p(1x4) structure.

Fig. 5.12 shows the relationship of the p(1x4) real-space unit mesh to the Fe(110) surface. It is likely that the unit mesh contains a single atom, bearing in mind the large size of phosphorus (the Van der Waals radius is 1.9 Å). A possible interpretation of the p(1x4) structure as a simple overlayer is given in fig. 5.12, where phosphorus atoms are tentatively located at the long bridge site.

In this structure, phosphorus atoms form up into rows in the $[\bar{1}10]$ direction, where they are separated by the distance 4.04 Å - the same as that found between phosphorus atoms in the c(2x2) overlayer on Fe(100). This arrangement with its preference for one direction is somewhat unlikely. Since the structure requires high temperatures to form, it appears to be activated. Together, these observations indicate that the structure is a reconstruction. In this case, the structural model in fig. 5.12 represents the array of surface net points that describes the reconstructed surface.

The comparatively small size of the unit mesh suggests that it probably contains only one phosphorus atom. Such a reconstruction may involve the rearrangement of iron atoms about phosphorus. A similar process was suggested in the previous chapter as a possible step in the growth of iron phosphide. A p(1x4) structure has been previously reported on the Fe(110) surface for the molecular and dissociative adsorption of CO at 340 L, although not as the lowest coverage structure.[11]

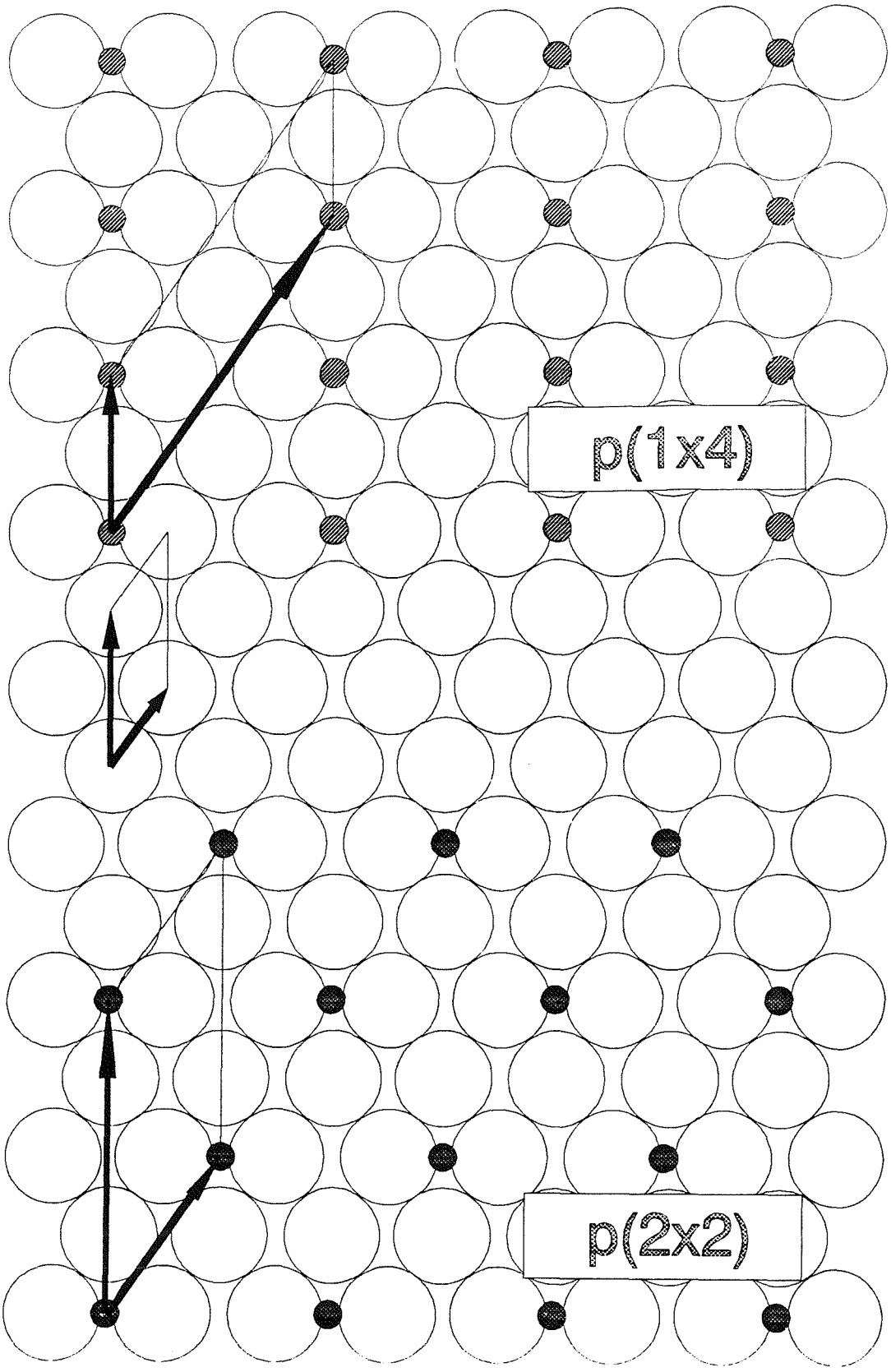

Fig. 5.12. Possible structural models for the p(1x4) and p(2x2) phosphorus overlayers where filled circles represent lattice points.

The desorption spectra of H_2 from dissociated PH_3 (fig. 5.6) clearly show the effect of coadsorbed phosphorus, even at coverages of less than 0.05 ML (according to fig. 5.8). The β_2^P peak is attributed to a second order recombination reaction, related to that on the clean surface, but showing the effect of strongly repulsive lateral interactions between hydrogen and phosphorus atoms. The observation of this feature at very low coverages (< 0.05 L) may indicate that in the initial stages of uptake the sites occupied by phosphorus are randomly spaced. Preferential adsorption at surface defects could promote such an effect. Consistent with this, the p(1x1) pattern of the clean surface immediately deteriorates on exposure to PH_3. The rate of uptake is high and almost linear in this stage (fig. 5.8).

The emergence of the β_1^P peak corresponds with the first indication of structural ordering in the phosphorus overlayer, at coverages of greater than 0.13 ML (1.0-2.0 L PH_3). At this stage, adsorption sites for PH_3 become blocked to the extent that the rate of uptake (fig. 5.8), and therefore sticking coefficient, begins to drop rapidly. The β_1^P peak probably arises from recombination reactions where hydrogen atoms are adsorbed at sites, very unlike those on the clean surface, of low binding energy induced by coadsorbed phosphorus. This may be related to hydrogen adsorption in regions between, or even within, domains of phosphorus in the p(1x4) structure. Indeed, the feature may be related to adsorption at sites on the proposed reconstructed surface, which may form during the TPD scan.

(i). Adsorption at 540 K

At 540 K, all hydrogen desorbs during the course of the PH_3 exposure, and the resulting phosphorus structures are well-ordered. Generally a p(1x4) structure is the only ordered structure detected during adsorption at 540 K. However, occasionally we have also observed a p(2x2) overlayer or a complex, unidentified structure (fig. 5.10), both of which transform to the p(1x4) structure with increasing exposure at high temperature. They can also transform without further phosphorus uptake: the p(2x2) structure converts to p(1x4) when left to stand at room temperature, while the complex structure reconstructs to the p(1x4) after annealing at high temperatures.

The results of LEED experiments are summarised schematically in fig. 5.13, where the exposure ranges for the different structures are plotted very approximately against phosphorus

coverage. The 170 K uptake curve in fig. 5.8 has been used to derive phosphorus uptake, assuming that the PH_3 sticking coefficient does not vary much between 170 and 540 K.

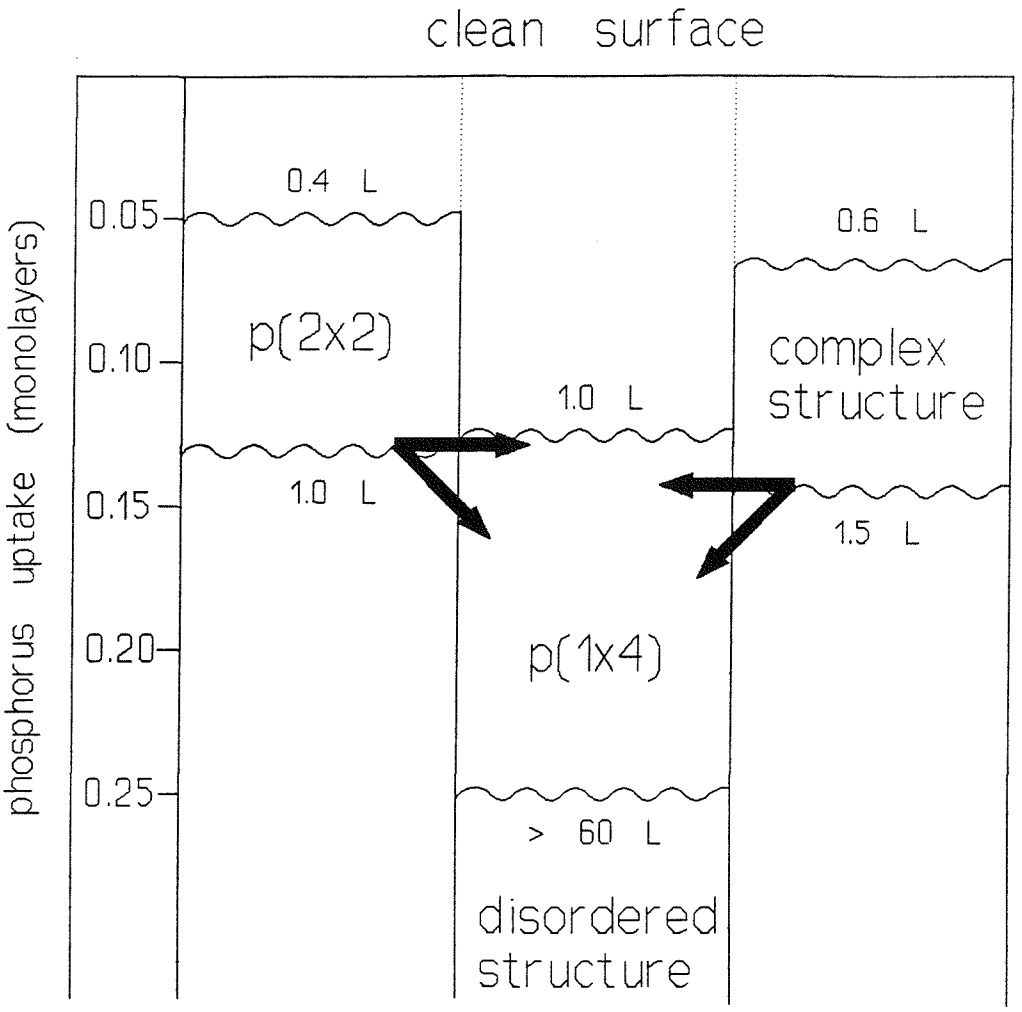

Fig. 5.13. Schematic representation of the structural results of adsorption at 540 K.

The p(1x4) structure at 540 K, like that at 170 K, can be attributed to a phosphorus chemisorption overlayer or a reconstruction, both of which saturate at a coverage of 0.25 ML (fig. 5.12). The low exposures involved, which compare well with those at 170 K, are consistent with this coverage interpretation (and also indicate that the sticking coefficient does not vary much between 170 and 540 K).

Saturation uptake at 170 K is associated with the formation of a poorly ordered structure which reconstructs, on annealing, to a p(1x4) structure. When the surface is initially exposed to PH_3 at 540 K, the p(1x4) structures are well ordered, showing bright, sharp LEED

patterns. However, after large exposures (60-2000 L) all LEED features have disappeared indicating structural disorder. There is no way to determine at what stage uptake saturates at 540 K, but this observation of a completely disordered phase, following the formation of the p(1x4) structure, may well indicate that phosphorus uptake passes beyond 0.25 ML. In the study of the interaction of PH_3 with Fe(100), described in the previous chapter, we showed that thin, disordered films, identified as iron phosphide, are formed at elevated temperatures (at 525 K, for example, ellipsometric results indicate that a film about 80 Å thick has formed). It is quite possible that similar films are formed on Fe(110). The disordered phase detected in the experiments at 540 K may be attributable to the formation of a thin film of iron phosphide.

A p(2x2) overlayer has been reported as the lowest coverage structure on Fe(110) for the adsorption of O_2,[13] C_2H_2,[11] C_2H_4,[11] and NH_3[11] at room temperature, and the adsorption of H_2S at 420 K.[12] A possible interpretation of the p(2x2) structure is given in fig. 5.12, where phosphorus atoms are tentatively located at the long bridging sites. As for p(1x4), it is likely, because of the large size of the atom, that there is only a single phosphorus in the unit mesh.

The room temperature transformation from the p(2x2) to the p(1x4) structure indicates that the p(2x2) arrangement is the thermodynamically less stable of the two. In the p(1x4) structure, phosphorus atoms are arranged into rows in the [001] direction separated by a distance of 4.04 Å, which is much smaller than the shortest approach distance between phosphorus atoms in the p(2x2) structure (4.95 Å in the $[\bar{1}11]$ direction). Perhaps unreasonably, this would indicate that some kind of attractive and stabilising interaction between phosphorus atoms in the [001] direction. Alternatively, the p(1x4) structure is interpreted as a stabilising surface reconstruction with a low activation barrier.

The complex structure with the pattern given in fig. 5.10 does not show any resemblance to any previously reported structures on Fe(110). This structure is associated with low coverages of phosphorus, and is formed by adsorption at 300 K and above, or by annealing low coverage p(1x4) structures at temperatures of 850 K. As noted above, the appearance of this structure may be associated with the pretreatment of the surface. Interpretation of the pattern has proved difficult. There are no simple relationships between the overlayer and Fe(110) surface meshes. The new pattern does not appear to possess a coincidence mesh, as there is no evidence of the expected features inside the first-order Fe(110) spots.

However, the pattern is consistent with the formation of an incommensurate layer, presumably of phosphorus atoms. The pattern is then a superposition of one or perhaps more incommensurate structures, each with two symmetrically equivalent domain orientations related by the mirror plane along the [001] direction. The size of the unit mesh (or meshes) must be small to explain why no features are detected inside the first order (1,0) and (1,1) spots of the Fe(110) pattern.

5.3. Conclusions

At 170 K, PH_3 completely dissociates on the Fe(110) surface, and phosphorus saturates in a poorly ordered structure. On annealing, phosphorus orders into a p(1x4) structure which may represent a surface reconstruction. Desorption spectra of hydrogen from the dissociated PH_3 clearly show the effects of sizeable repulsive lateral interactions between phosphorus and hydrogen atoms on the surface. Two peaks are detected in these spectra, both of which can be assigned to recombinative desorption reactions of hydrogen with a binding energy reduced by phosphorus. The lower temperature peak may be related to the proposed reconstruction.

A p(1x4) structure is also formed during adsorption at 540 K, where the hydrogen from dissociated PH_3 desorbs during dosing. This is occasionally preceded at low coverages by a p(2x2) structure or an unidentified structure with a complex LEED pattern. The p(2x2) structure can be interpreted as a simple chemisorption overlayer, with a saturation coverage of 0.25 monolayers. It is unstable and difficult to reproduce, and readily transforms (perhaps because of LEED electron beam effects) to a p(1x4) structure. The complex has not been interpreted but may be associated with the formation of coalesced phosphorus structures. The appearance of this structure may depend on the surface pretreatment. It is typically observed when the surface is annealed at comparatively low temperatures.

The appearance of structural disorder at high PH_3 exposures may be related to increased uptake beyond saturation of the p(1x4) structure. By analogy with results for PH_3 on Fe(100), this may correspond with the formation of very thin iron phosphide films. In this case, the p(1x4) reconstruction may be related to the initiation of iron phosphide growth. Several reconstructions, which correspond to changes in the unit mesh size of the chemisorbed phosphorus, are detected on annealing at high temperatures (800 to 990 K).

5.4. Future work

This is, to the best of our knowledge, the first time that PH_3 adsorption on Fe(110) has been studied, and consequently there is much to learn about the chemistry. Of particular interest would be an ellipsometric study of the interaction, complementing that of PH_3 on Fe(100) reported in Chapter 4. It is likely that films similar to those found on Fe(100) are formed on Fe(110) at high temperatures, and it would be interesting to compare results. Improved observations of the complex LEED pattern shown in fig. 5.10 may help to identify the structure.

5.5. References

1. A.J. Pignoccio and G.E.Pellissier, *Surf. Sci.* 7 (1967) 261.

2. S. Kato and H. Kobayashi, *Surf. Sci.* 27 (1971) 625.

3. C. Leygraf and S. Ekelund, *Surf. Sci.* 40 (1973) 609.

4. R. Feder and G. Gafner, *Surf. Sci.* 57 (1976) 45.

5. H.D. Shih, F. Jona, D.W. Jepsen and P.M. Marcus, *Bull. Am. Phys. Soc.* 22 (1977) 357.

6. E.A. Wood, *J. Appl. Phys.* 35 (1964) 1306.

7. G. Gafner and R. Feder, *Surf. Sci.* 57 (1976) 37.

8. G. Brodén, G. Gafner and H. P. Bonzel, *Appl. Phys.* 13 (1977) 333.

9. H.J. Grabke, *Mat. Sci. Engineering* 42 (1980) 91.

10. F. Bozso, G. Ertl and M. Weiss, *J. Catalysis* 50 (1977) 519.

11. K. Yoshida and G.A. Somorjai, *Surf. Sci.* 75 (1978) 46.

12. S.R. Kelemen and A. Kaldor, *J. Chem. Phys.* 75 (1981) 1530.

13. V.S. Smentkowski and J.T. Yates Jr, *Surf. Sci.* 232 (1990) 113.

14. M. Grunze, G. Strasser and O. Elshazly, *J. Vac. Sci. Technol.* A4 (1986) 2396.

15. A. Hodgson, A. Wight, G. Worthy, D. Butler and B.E. Hayden, *Faraday Dicuss.* 96 (1994) 161.

16. F. Bozso, G. Ertl and M. Weiss, *Appl. Surf. Sci.* 1 (1977) 103.

17. H.F. Berger and K.D. Rendulic, *Surf. Sci.* 251/252 (1991) 882.

18. E.A. Kurz and J.B. Hudson, *Surf. Sci.* 195 (1988) 31.

19. R. Imbihl, R.J. Behm, K. Christmann, G. Ertl and T. Matsushima, *Surf. Sci.* 117 (1982) 257.

20. J. Benziger and R.J. Madix, *Surf. Sci.* 94 (1980) 119.

21. R.I. Hedge and J.M. White, *J. Phys. Chem.* 90 (1986) 2159.

6. EXAFS STUDY OF THE LOCAL STRUCTURE OF PHOSPHORUS, SULPHUR AND ZINC IN ANTIWEAR FILMS

6.1. Introduction

Recent studies[1-4] of wear debris have provided the first direct evidence of the structure of the antiwear films of zinc dialkyl dithiophosphate (ZDDP). Wear debris has been shown to consist of microscopic particles of crystalline iron sulphide embedded in a structureless matrix, believed to be a phosphate glass containing zinc and iron cations. This work is reviewed below, but first the theory of phosphate glass structure is briefly described.

In the present study, we have used Extended X-ray Absorption Fine Structure (EXAFS) spectroscopy, a technique particularly suitable for studying amorphous materials,[5] to investigate the local structural environment of phosphorus, sulphur and zinc in antiwear films of ZDDP and related additives.

(i). Structure of phosphate glasses

Phosphate glasses are used in a range of technological applications.[6] Their rheological, optical, electrical and heat absorbing properties can be chosen by varying the composition, in particular the type and proportion of counter ions. Phosphate glasses have been prepared with various cations over a wide range of composition,[7] although the properties of simple phosphate glasses containing alkali metal cations (such as sodium) have been studied in most detail. The structures of phosphate glasses have recently been reviewed by Martin.[8]

The structurally analogous glasses of phosphate, silicate, germanate and borate (among others) have traditionally been classified together as the oxide glasses (so-called because they can be formed by P_2O_5, SiO_2, GeO_2, B_2O_3, *etc.*). The classic theory of glass structure was formulated by Zachariasen,[9] who first recognised that oxide glasses are based on random networks of covalently linked polyhedra of, for example, SiO_4 in silicates, GeO_4 and GeO_6 in germanates, or PO_4 in phosphates. In discussing the structures of oxide glasses, component elements are conventionally divided into the following three classes:

1. *Network formers* such as phosphorus or silicon which together with oxygen form the covalent skeleton of the structure (the network);
2. *Network modifiers* such as the alkali metals, which are present as cations and are typically located at interstitial sites in the network. They disrupt the structure of the covalent skeleton

and have a profound effect on the properties of the glass, such as viscosity and conductivity; and,

3. *Intermediates* such as transition metals, which are present as cations and are considered to have a structural role in between that of the glass formers and glass modifiers, sometimes forming the network and sometimes present interstitially depending on coordination sites.

Oxide glasses are typically formed by cooling molten mixtures of the oxides of the glass former, glass modifier and intermediate elements. Oxide glass composition is usually expressed as the proportions of the different component oxides. As mentioned above, phosphate glasses have been prepared over a wide range of compositions. For example, sodium phosphate glasses have been prepared in the compositional range P_2O_5 to $5Na_2O3P_3O_5$, although it is difficult to prepare glasses with less than 30% Na_2O because of their volatility.[8]

The basic structural unit of all phosphates is the PO_4 tetrahedron. In condensed phosphates, PO_4 units are joined together through shared corner oxygens (a maximum of three to each phosphorus atom) forming various chain, ring and three-dimensional network structures. In the crystalline state, the PO_4 units in condensed phosphates are systematically related and long range order is established (the structures of crystalline phosphates have been comprehensively reviewed by Corbridge[10]). In phosphate glasses, however, P-O-P bond angles and dihedral angle distributions are random and the PO_4 networks are disordered. In general, the structural disorder found in glasses is similar to that found in the liquid phase. In glass, however, freedom of movement on the atomic scale is drastically reduced and viscosity becomes so high that glass shows a rigidity comparable to crystalline solids.

From the perspective of hybridisation theory, the structure of the PO_4 tetrahedron is explained by the involvement of sp^3 hybrid orbitals on the phosphorus in the formation of four P-O σ bonds. In addition, *d* electrons on the phosphorus are involved in the formation of a π bond which can be delocalised, as described below. It has also been suggested[6] that P-O bonds to terminal oxygen in phosphates and phosphorus oxides have some dative character, involving the donation of lone pairs from the oxygen to the phosphorus (this would explain why such bonds are comparatively short).

In discussing the structures of phosphate glasses, it is useful to distinguish between bridging and non-bridging oxygens in the PO_4 unit. Bridging oxygens (BO) are those involved in P-O-P linkages between phosphates while non-bridging oxygen (NBO) are those formally considered to be either doubly bonded to phosphorus (P=O) or coordinated to cations (P-O-M). In condensed phosphates, a PO_4 unit can have one, two or three bridging oxygens and therefore participate in condensed phosphate structures as an end group, a middle group or a branching point, respectively, as fig. 6.1. shows.

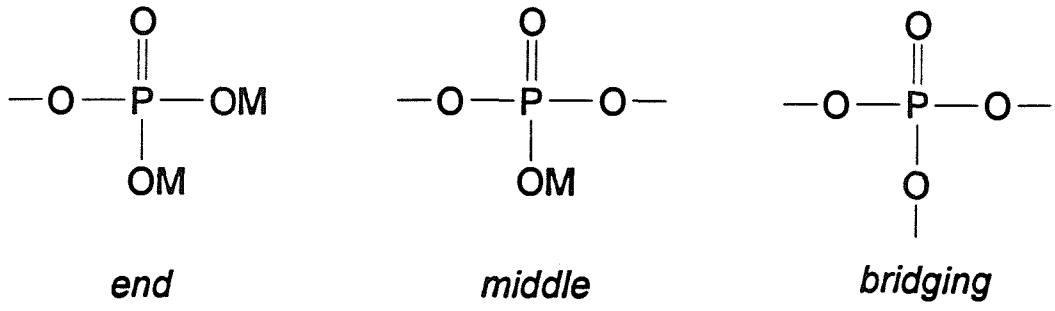

Fig. 6.1. Structural units in condensed phosphates (M = metal cation).

Spectroscopic evidence (reviewed by Martin[8]) shows that the π electrons in a PO_4 unit, which in fig. 6.1 are formally allocated to a single P=O double bond, are delocalised across non-bridging oxygens. This delocalisation can be represented by resonance structures like those for a middle group, shown in fig. 6.2. Delocalisation reduces the energy and increases the stability of a structural unit. The branching point, where the π bond is localised on one non-bridging oxygen only, is the least stable of the structural units. As noted in the "antibranching rule" of van Waser,[11] the branching unit is especially open to chemical attack (by water, for example), and three-dimensional network structures are relatively unstable.

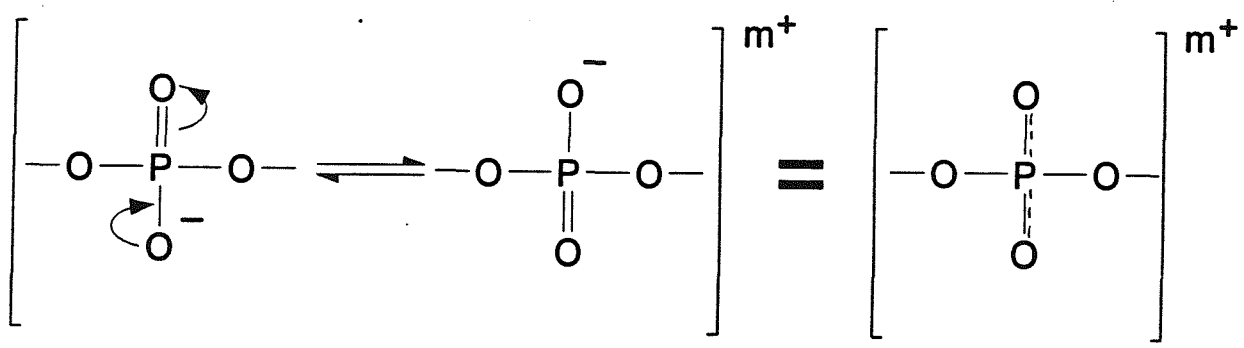

Fig. 6.2. Resonance structures for a middle group.

Increasing the proportion of modifier and intermediate cations in a phosphate glass increases the ratio of NBO to BO and, consequently, more P-O-P linkages are broken. In this way, the structure of a phosphate glass varies with composition. In the Zachariasen model of oxide glass structure,[9] the random network of glass forming polyhedra is considered to be continuous and the addition of more cations opens up the three-dimensional network. On the basis of experimental observations, van Waser developed a similar theory of phosphate glass structure and its dependence on composition. Van Waser[7] proposed that the phosphate network does not remain continuous as more cations are added, but breaks down into discrete, condensed phosphate chains. Using the theory of random reorganisation, van Waser predicted that the distribution of chain lengths depends on the ratio of cations-to-phosphate units.

Fig. 6.3 (after van Waser[7]) illustrates this dependence for a phosphate glass with alkali oxide modifier by showing how the structure depends on the mole ratio $R = M_2O/P_2O_5$ (this diagram also introduces the nomenclature of phosphates).

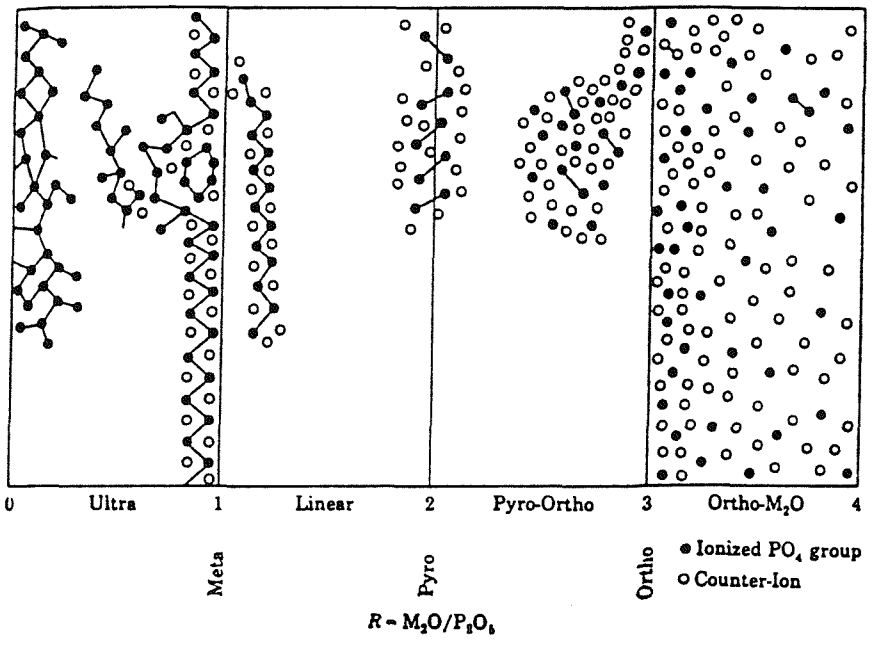

Fig. 6.3. Schematic showing variation of structure with composition for a phosphate glass.

At the limit of composition $R = 0$, it is expected that each PO_4 is a bridging unit so that the P_2O_5 glass is a three-dimensional network of branched PO_4 chains. This is analogous to the continuous network model of Zachariasen.[9] Results of the few structural studies of P_2O_5 glass are consistent with this model.[8] When cations are present in very small concentrations the

three dimensional network in a phosphate glass presumably survives, but as the concentration increases, the three-dimensional network begins to break-up into long chains. The highly branched condensed phosphates in the composition range $0 < R < 1$ are known as ultraphosphates.

At the composition of $R = 1$, the glass has the metaphosphate composition where effectively all the PO_4 units are middle groups. Breakdown of the three-dimensional network is complete and metaphosphates consist of infinitely long chains $[(PO_3)_n]^{n-}$ or ring structures.

As cation concentration is increased beyond the metaphosphate composition, the length of the phosphate chains become shorter, on average. Linear chain polyphosphates $[P_nO_{3n+1}]^{(n+2)-}$, whose average length depends on the relative proportions of end and middle groups, are found across the composition range $1 < R < 3$. When $R = 2$, all PO_4 units are end groups and the glass consists of diphosphate (pyrophosphate) $[P_2O_7]^{2-}$. As the cation concentration approaches the orthophosphate composition ($R = 3$), there are increasing numbers of discrete PO_4 units. This model is confirmed by paper chromatographic studies,[8] where a range of different-size linear polyphosphates have been detected with an average chain length that varies with the cation-to-phosphate ratio R.

When cation concentration reaches, and passes beyond, the orthophosphate composition ($R = 3$), the phosphate glass is then composed, almost entirely, of discrete PO_4 units.

(ii). Literature review: structure of ZDDP antiwear films

The first indication of the structure of zinc dialkyl dithiophosphate (ZDDP) antiwear films has come from a series of studies[1-4] of wear debris formed in wear tests lubricated with the simple formulation di-isopropyl ZDDP in *n*-dodecane.

Martin *et al.*[1] characterised the morphology of wear debris particles prepared in these studies, using electron microscopy. The particles, generated under mild boundary lubrication conditions, were foil-like and a few microns across. They consisted of small crystallites (5 to 10 nm wide) containing sulphur, iron, zinc and oxygen, embedded in an amorphous matrix composed of zinc, phosphorus and oxygen, which is probably the zinc phosphate indicated

in numerous previous studies (reviewed in Chapter 1). Watkins[12] had previously hypothesised that zinc phosphate formed in the contact zone would be a low melting-point fluid glass.

Subsequently, Martin *et al.*[2] used EXAFS to explore the local structural environment of iron and zinc in ZDDP wear debris. Fourier transforms of the K-edge EXAFS of both zinc and iron in the wear debris showed a single peak, indicating that there was no long range order about these elements. In contrast, when wear tests were run with additive-free base oil, iron in the wear particles was found in a crystalline (long range order) environment. A comparison with data for model compounds suggested that both iron and zinc in the wear debris were coordinated to oxygen. They were able to fit the data for iron in ZDDP wear debris with a single shell of 5.9 oxygen atoms at 1.89 Å, but no analysis of the results for zinc was made. It was concluded that the amorphous phase was an oxide glass where phosphorus and possibly sulphur were the network forming elements and zinc and iron cations were network modifiers. They hypothesised that structural amorphisation was induced by friction, through the generation of high temperatures or by mechanical action or a combination of these.

Belin *et al.*[3] then studied the near-edge structure of the K-edge of iron in ZDDP wear particles. By comparison with data for model compounds, they argued that the iron was in a high oxidation state (Fe^{3+} or more) and located in sites with distorted octahedral symmetry. The Fourier transform of the EXAFS of iron in the ZDDP wear debris showed, along with the large peak detected in the previous investigation, evidence of minor peaks at larger distances which they suggested were characteristic of iron in crystallites present in the matrix.

Most recently, Hallouis *et al.*[4] have made a careful study of wear debris, and in particular the small crystallites embedded in the particles, using electron microscopy and electron spectroscopy. Analysis of the amorphous matrix showed that it contained only iron, zinc, oxygen and phosphorus, which was present as a phosphate. The crystallites, in which all the sulphur was located, were characterised using composition analysis and diffraction techniques as non-stoichiometric iron (II) sulphide $Fe_{1-x}S$ with the hexagonal pyrrhotite structure. The sulphur-to-phosphorus ratio, which was correlated with the proportion of crystalline sulphide in the matrix, increased with increasing contact pressure.

6.2. Preparation of antiwear films

6.2.1. The wear test experiment

Antiwear film samples were prepared on a Cameron-Plint reciprocating wear test rig at the Thornton Research Centre (TRC), Shell UK Ltd. The rig (which is used in routine lubricant testing) operates under the relatively mild conditions of the mixed lubrication regime, where both the oil film and boundary lubricant layers are important in determining the extent of friction and wear. A diagram of the arrangement of the sliding contact is shown in fig. 6.4. In operation, a load-bearing steel slider attached to a reciprocating arm is pressed against a fixed steel foil, submersed in test lubricant to about 7 mm deep.

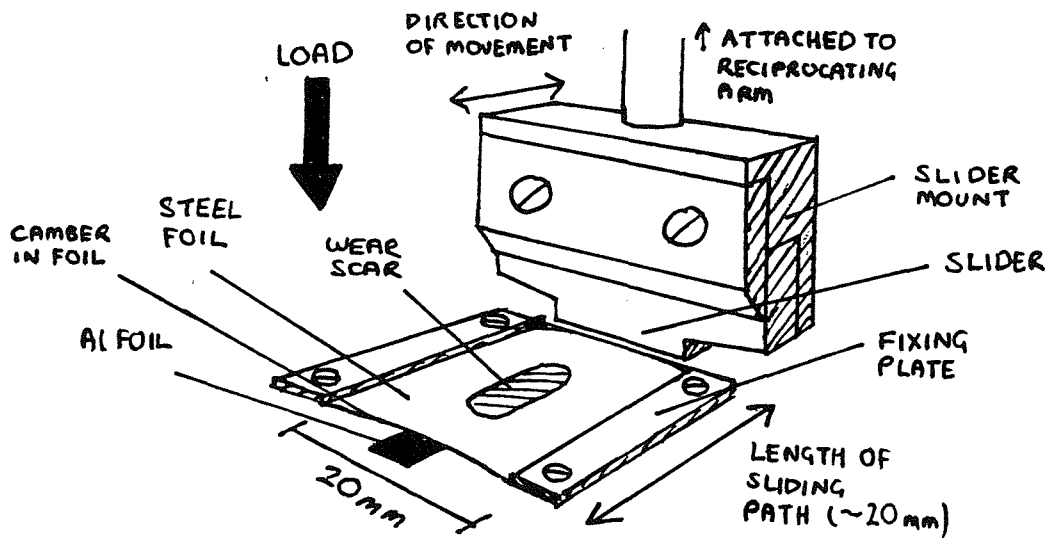

Fig. 6.4. Diagram of the load bearing contact in the wear test rig.

Before each wear test experiment, the foil specimen and the components of the rig in contact with the test lubricant were degreased with 1,1,1 trichloroethane, washed in an ultrasonic bath with an aqueous detergent solution and then rinsed with distilled water and dried. The foil was screwed-down on to a thin strip of aluminium foil (3 mm wide), running along the centre of the slider path, which is used to introduce a gentle camber to the surface (see fig. 6.4). The procedure for preparing antiwear films was then as follows. After the test lubricant had reached a constant temperature of 165 °C, the contact was run-in for a few minutes at a load of 1 kg and a reciprocating frequency that was gradually increased to a

constant value of 20 Hz. After run-in, the contact load was increased to 2 kg and the rig was left running for 4 hours. Relative changes in the frictional force could be monitored during the experiment. Successful wear test runs, where an antiwear film was formed, were characterised by a smooth decrease in frictional force to a steady state value within the first 15 minutes.

6.2.2. Additives and test lubricants

Test lubricants were prepared with pure, highly-refined base oils, as used in routine lubricant testing at TRC. The four additive formulations listed below (with details of their preparation) successfully reduced wear by forming antiwear films. The concentrations of the antiwear additives are given as percentage by weight: 1 wt% is the usual concentration for ZDDP in use while the concentrations for DPDS and TPP were found by trial and error.

1. *Di-isopropyl ZDDP, 1 wt%*

Di-isopropyl ZDDP was synthesised at the University of Southampton following procedures given in the literature.[13,14] Zinc oxide (6 g, 0.75 mol) was carefully added to an impure solution of di-isopropyl dithiophosphoric acid (a viscous brown-black liquid prepared by the reaction of phosphorus pentasulphide (16 g, 0.7 mol) with propan-2-ol (19.3 g, 0.3 mol) under nitrogen) producing a white slurry, in an exothermic reaction. Purification, by recrystallisation from hot propan-2-ol, yielded white crystals of pure di-isopropyl ZDDP (7 g, 30%) with a melting point of 142 °C (literature value[15] 141.5-142 °C). The infrared spectrum was in good agreement with the literature.[15] Di-isopropyl ZDDP was blended with the base oil by stirring and heating to 70 °C.

2. *Commercial ZDDP, 1 wt%*

This formulation was provided by TRC, ready blended. Unfortunately, the additive was not well characterised, although it was known to be composed of ZDDPs with secondary alkyl chains. (Generally, commercially prepared ZDDPs are only about 75% pure and contain a mixture of different types of ZDDP with different alkyl groups, along with contaminants such as basic ZDDP, left over from the manufacturing process.)

3. *Commercial ZDDP, 1 wt%*
Polyisobutane succinimide (a dispersant)
Calcium salicylate (a detergent)

These dispersant and detergent additives are known to be surface active in automobile engines, interfering with the formation of the ZDDP antiwear film.[16] They were included in this study to see if any structural effects could be detected by EXAFS. Again, the formulation was provided, ready-made, by TRC and was poorly characterised, although the ZDDP was characterised as a mixture of secondary alkyl ZDDPs. The concentrations of the dispersant and detergent additives were not given, although polyisobutane succinimide (the dispersant) was known to be present at relatively high levels compared to typical concentrations in commercial engine oils.

4. *Tripropyl phosphate (TPP), 7 wt%*
Dipropyl disulphide (DPDS), 2 wt%

TPP - $(CH_3CH_2CH_2O)_3PO$ - and DPDS - $(CH_3CH_2CH_2O)_2S_2$ - were chosen as models of typical phosphorus and sulphur-based antiwear additives. They are also closely related to decomposition products of ZDDP which may be involved in antiwear film formation. Both compounds were obtained, with a purity greater than 96%, from Aldrich Chemical Co. TPP dissolved in the base oil with gentle heating (50 °C) and stirring, while DPDS, a liquid, was miscible with the base oil.

6.2.3. Additive performance in wear tests

When the wear test rig was run with base oil but no additive, the foil specimen showed a deeply scarred wear track, as wide as the slider (10 mm) and as long as the path of the slider (8 mm), indicating that the camber of the surface had been worn down. Clearly, under test conditions the base oil gave inadequate wear protection.

In contrast, the four listed additive formulations reduced wear, when compared to the additive-free control, and showed visible evidence of film formation at the wear scar. In all specimens, the wear scar was much thinner (about 3 mm wide), was localised down the centre of the slider path, and showed a rounded entry and exit zone. There was very little damage where the edge of the slider ran, showing that the surface camber had not been worn

away. The antiwear films of the ZDDP additives were clearly visible as a dark blue-grey colour.[17-19] There was also a faint blue-brown coloration on the wear scar in the presence of the DPDS-TPP additive mixture.

Some indication of the relative performance of the additives could be gained from a qualitative assessment of the wear damage (the friction measurements used to monitor the wear tests could not be compared between experiments). The commercial additives gave the smallest, smoothest wear scars indicating that they gave the best antiwear performance. Di-isopropyl ZDDP produced a wear scar that was comparable in size but showed more indications of damage: in particular, there were deep scratch marks in the direction of sliding. The DPDS-TPP mixture gave the poorest antiwear performance as indicated by a more extensive and more severely scratched wear scar.

The specimen foils were stored under air, with a coating of oil residue left on the surface.

6.3. EXAFS data acquisition and analysis

X-ray absorption spectra of phosphorus, sulphur and zinc in the antiwear films were recorded at the Daresbury Synchrotron Radiation Source, about one week after the films had been prepared at TRC. Measurements of phosphorus and sulphur K-edges were made on the soft X-ray beam line 3.4, while the K-edge zinc spectra were recorded on beam line 9.2. The spectra of phosphorus, sulphur and zinc in antiwear films, and phosphorus and sulphur in various model compounds were recorded in fluorescence mode (preferred to transmission experiments because of the low concentrations of elements in the antiwear films and the high absorption coefficient of matter for soft X-rays). Spectra of zinc in model compounds were measured in transmission mode. Generally, the spectra presented here are the average of three measurements. The EXAFS oscillations $\chi(k)$ were extracted from the experimental data using standard techniques described above (Sect. 2.2).

k^3 weighted EXAFS spectra were analyzed using the EXCURV92 program on the Daresbury mainframe computer. Starting from structural models, theoretical curves were calculated using the curved wave method.[20] The fit to experimental data was optimised by varying various structural parameters using a least squares refinement method. Phase shifts were calculated within EXCURV92 using a Hartree-Fock muffin-tin method and $X\alpha$ potentials for calculating the atomic wave functions. Where possible, the phase shifts were verified by analysing the EXAFS of model compounds of known structure - acceptable errors were $\pm$ 0.02 Å for interatomic distances and $\pm$ 20% for coordination numbers.

The following model compounds were used to verify calculated phase shifts and provide chemical information from relative absorption edge positions (the materials are research grade chemicals unless otherwise stated):

1. Zinc orthophosphate, $Zn_3(PO_4)_2$;
2. Zinc phosphate glass, uncharacterised (provided by TRC);
3. Di-isopropyl ZDDP (prepared as described above);
4. Solid decomposition product of di-isopropyl ZDDP (made by heating ZDDP to 160°C);
5. Iron (II) sulphide, FeS;
6. Iron (II) sulphate heptahydrate, $FeSO_4 7H_2O$;
7. Zinc oxide, ZnO; and,
8. Zinc sulphide, ZnS.

6.4. Results

6.4.1. Phosphorus in antiwear films

X-ray absorption spectra were recorded before and after rinsing the antiwear film samples, which were coated with a film of oil from the wear test, with either hexane or methanol. No significant changes were detected after such treatments.

The K-edge absorption spectra of phosphorus in the different antiwear films are effectively identical (fig. 6.5). There are no significant differences in the edge position, near-edge structure and EXAFS oscillations recorded for the films of di-isopropyl ZDDP, commercial ZDDP - both with and without detergent and dispersant - and the DPDS-TPP mixture. Clearly, the oxidation state and local structural environment of phosphorus do not vary among the different films.

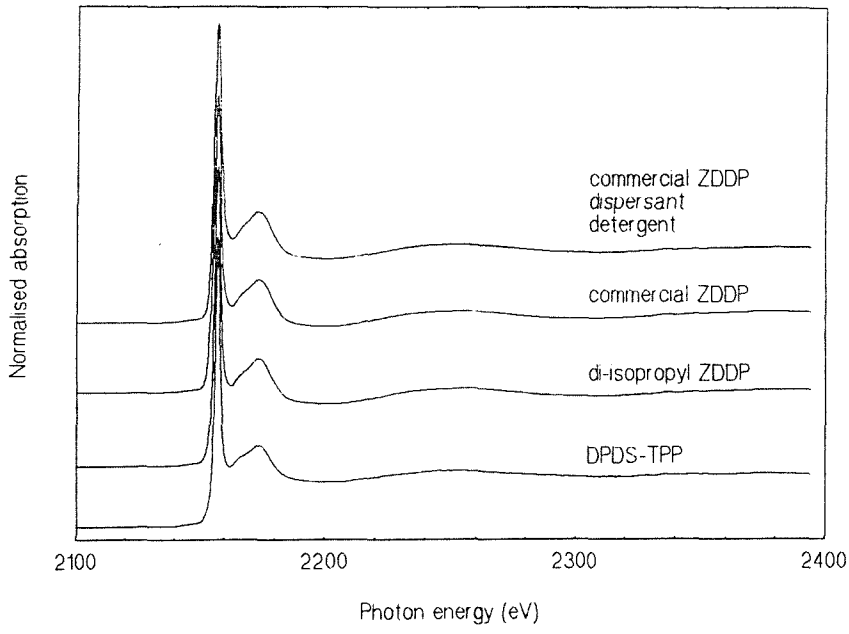

Fig. 6.5. Absorption spectra of phosphorus K-edge in antiwear films.

In fig. 6.6, the edge position and near-edge structure of phosphorus in a representative antiwear film are compared with similar data for the following model compounds: crystalline zinc phosphate $Zn_3(PO_4)_2$, glassy zinc phosphate (uncharacterised), di-isopropyl ZDDP and the decomposition product of di-isopropyl ZDDP. In the following discussion, the peak position is defined as the energy at the half height of the edge jump. A suitable standard

reference compound, such as elemental phosphorus, was unavailable to calibrate the photon energy in these spectra.

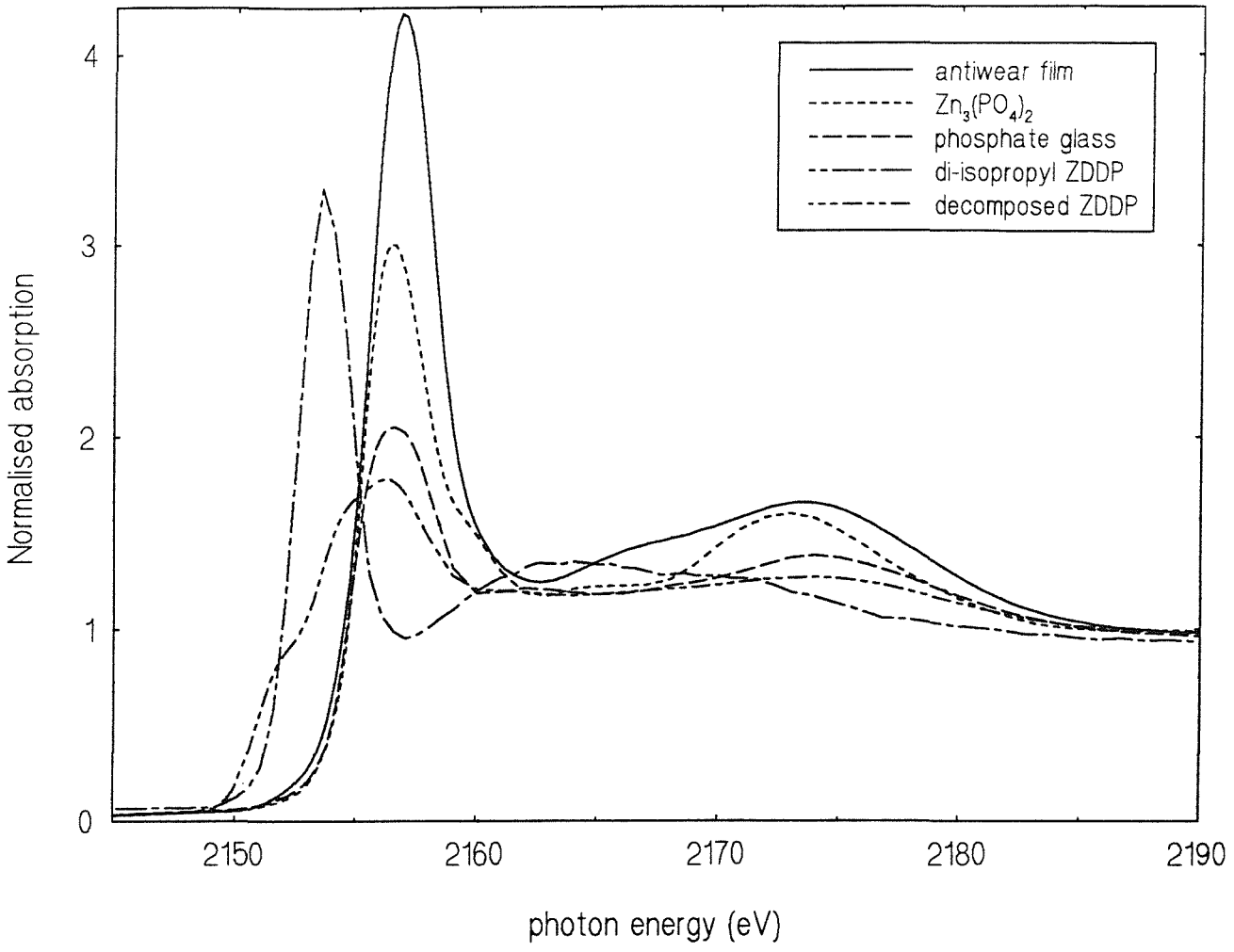

Fig. 6.6. *Comparison of phosphorus K-edges in an antiwear film and model compounds.*

The edge position of the antiwear film, at 2159.2 eV, is shifted to higher energy compared to di-isopropyl ZDDP or its decomposition product (a shift of 3.0 ± 0.3 and 3.5 ± 0.3 eV, respectively). The chemical environment of phosphorus in the ZDDP antiwear films is clearly distinct from that of the original additive. There is no chemical shift between the antiwear film and crystalline or glassy zinc phosphate indicating that phosphorus in the antiwear films is present as a phosphate, as expected from the literature (Chapter 1).

The chemical shift between the antiwear films (phosphate) and di-isopropyl ZDDP (thiophosphate) can be explained by considering the different chemical environments of phosphorus in the two cases. Oxygen is more electronegative than sulphur and consequently the electron density on phosphorus in the antiwear film (phosphorus coordinated to four oxygen) is reduced to a greater extent than in ZDDP (phosphorus coordinated to two oxygen and two sulphur). Because screening of nuclear charge becomes less effective as electron density is reduced, the 1*s* level is more tightly bound to the phosphorus in the antiwear film and the absorption edge appears at higher energy.

The near-edge structure of the solid thermal decomposition product of ZDDP can be interpreted as a superposition of features due to phosphorus fully coordinated to oxygen (phosphate) and phosphorus bonded to some sulphur as well as oxygen (thiophosphate). This is consistent with the literature (see Chapter 1) where the raw decomposition product has been characterised as a complex mixture of condensed phosphates (containing some thiophosphate units) and monomeric thiophosphates.

As noted above, there is no significant variation in the EXAFS recorded for phosphorus in the four different antiwear films. The EXAFS spectrum, k^3 weighted and phase shift corrected for oxygen, of a representative antiwear film (di-isopropyl ZDDP) is given in fig. 6.7. Absorption by sulphur, restricts the measurable range of the post-edge spectrum of phosphorus in the films to about 300 eV. This is not a significant problem, however, because the EXAFS oscillations do not extend far beyond the edge, as expected for a local structural environment of weakly scattering oxygen atoms.

The Fourier transform (fig. 6.7) clearly shows that the EXAFS is dominated by contributions from a single shell, indeed, there is no evidence of ordered structure beyond the first P-O coordination shell. This can be compared with the EXAFS and Fourier transform of crystalline $Zn_3(PO_4)_2$, given in fig. 6.8, where there is clearly the contribution from a second shell. Qualitatively, the EXAFS results are consistent with the idea that phosphorus in ZDDP antiwear films is present in a glassy phosphate, characterised only by very short range order.

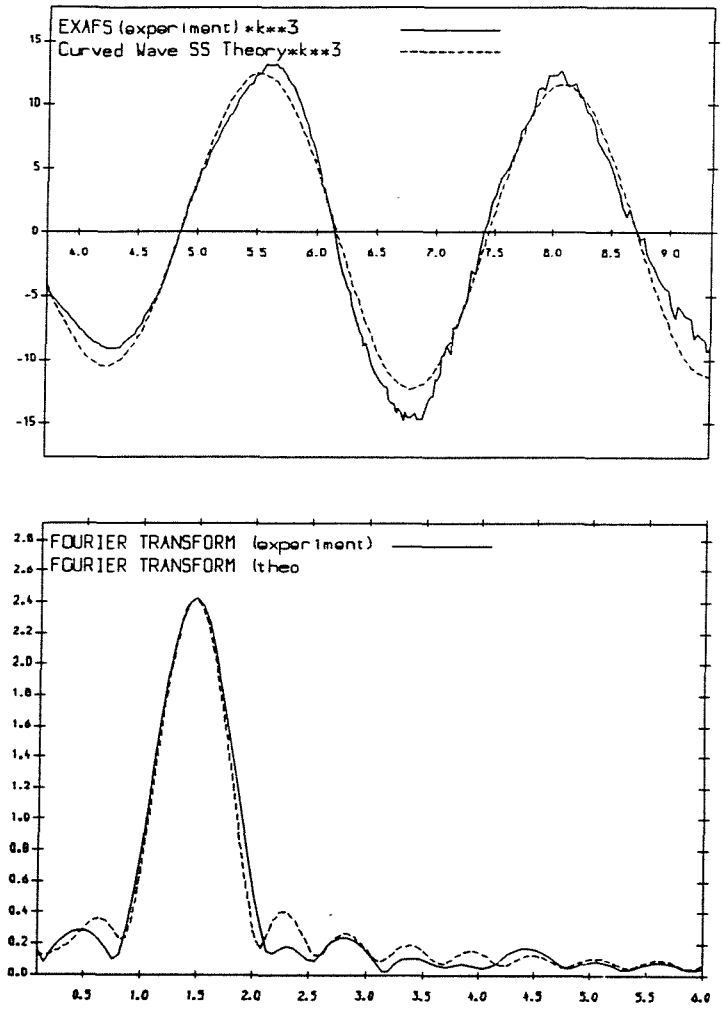

Fig. 6.7. P K-edge EXAFS and Fourier transform, phase shift corrected for oxygen, of the antiwear film of di-isopropyl ZDDP.

Phase shifts calculated by EXCURV92 for phosphorus and oxygen (and zinc) were verified by analysing the EXAFS of $Zn_3(PO_4)_2$. The data was fitted using a single scattering, two shell model of oxygen and zinc. In the fit, the number of atoms in the shell N, the shell radius R, Debye-Waller factor $2\sigma^2$ and photoelectron threshold energy E_0 were varied. N and R had to be varied separately because they were strongly correlated (with a correlation coefficient of

greater than 0.8). The results of the analysis are presented in table 6.1, and the theoretical and experimental spectra are compared in fig. 6.8.

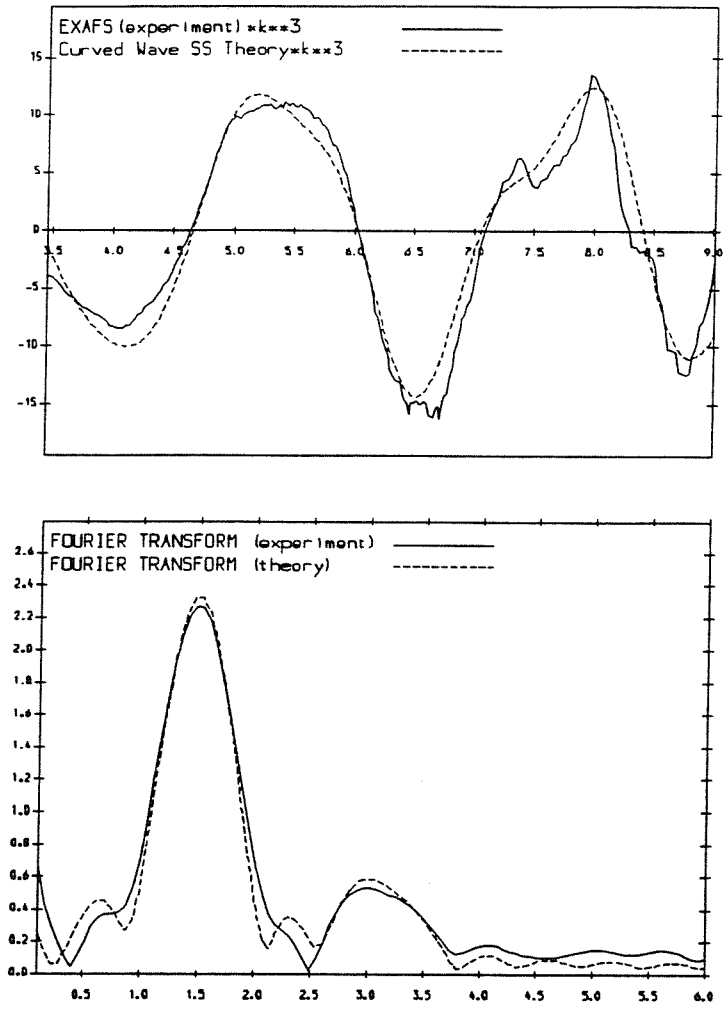

Fig. 6.8. P K-edge EXAFS and Fourier transform, phase shift corrected for oxygen, of $Zn_3(PO_4)_2$.

Analysis of the first (oxygen) coordination shell produced a coordination number of 4.1 and an interatomic distance of 1.55 Å. This is in fair agreement with X-ray diffraction results[21] where phosphorus is shown to be located in a slightly distorted tetrahedron of oxygen with bond lengths varying from 1.52 to 1.58 Å (average value of 1.53 Å ± 0.02 Å). Consequently, phase transferability was confirmed and errors of ± 0.02 Å in bond length and 20% in coordination number were shown to be realistic. Unfortunately, because of poor and insufficient data it was not possible to extract structural information for phosphorus in the zinc phosphate glass.

The EXAFS of the antiwear films was analyzed using a single scattering, single shell of oxygen model where N was set to 4.0 to represent the expected PO_4 phosphate unit and R, $2\sigma^2$, and E_0 were varied. The results of curve fitting for the antiwear film of di-isopropyl ZDDP are summarised in Table 6.1 and the theoretical and experimental EXAFS oscillations are compared in fig. 6.7. EXAFS of phosphorus in the other antiwear films gave identical results (within the limits of error).

Table 6.1. *P K-edge EXAFS derived structural parameters.*

Antiwear film of di-isopropyl ZDDP, R = 14.8%, E_0 = 19.0 eV, VPI = -4.2 eV, AFAC = 0.85.

$Zn_3(PO_4)_2$, R = 20.4%, E_0 = 10.69, VPI = -4.00, AFAC = 0.85.

Phosphorus in:	Shell	N	R (Å)	$2\sigma^2$ (Å^2)
Antiwear film	O	4.0	1.502	0.002
$Zn_3(PO_4)_2$	O	4.1	1.548	0.003
	Zn	3.9	3.076	0.020

EXAFS analysis yielded a first shell radius, and therefore P-O bond length, of 1.50 $\pm$ 0.02 Å for all the antiwear films. As will be discussed below, this is comparable to P-O bond lengths reported for other phosphate glasses. The Debye-Waller factors $2\sigma^2$ determined in the EXAFS analysis of the different antiwear films were in the range 0.001 to 0.002 Å^2. These comparatively low values indicate that there is little static disorder in the arrangement of the first shell of oxygen about the phosphorus in the phosphate unit.

It was not possible to resolve the EXAFS into the separate distances expected for P-O bonds to bridging and non-bridging oxygen because of strong correlations between R and $2\sigma^2$ (both within and between the two hypothetical shells).

6.4.2. Sulphur in antiwear films

Solvent washing (hexane and methanol) had no significant effect on the X-ray absorption spectra of sulphur in the films.

The K-edges of sulphur in the different antiwear films are shown in fig. 6.9. There is no chemical shift among the three different ZDDP films, which appear at 2471.7 ± 0.3 eV (energies were not calibrated with respect to a standard reference compound). However, their near-edge structure does show some significant differences. The absorption edge of the dipropyl disulphide and tripropyl phosphate (DPDS-TPP) film is distinct, showing a large chemical shift of about +8 eV compared to the other films.

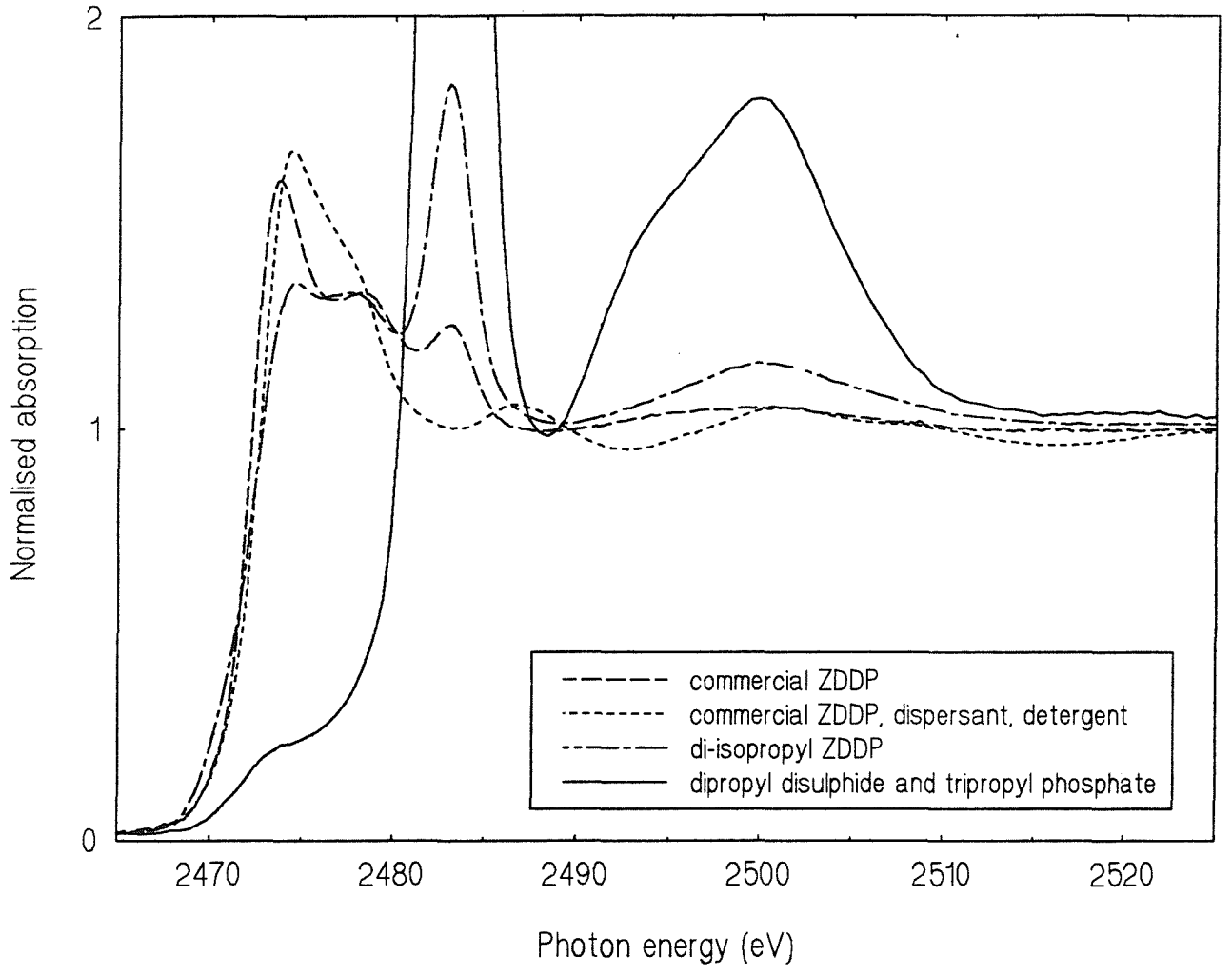

***Fig. 6.9.** Sulphur K-edges in the antiwear films.*

Fig. 6.10 shows the K-edge of sulphur in the model compounds di-isopropyl ZDDP (where sulphur is coordinated to two zinc and two oxygen atoms), ZnS (four zinc), FeS (six iron), and $FeSO_4{\cdot}7H_2O$ (four oxygen). The three model compounds where metal is coordinated to sulphur appear at similar energies (within 2.3 eV of each other) while the sulphate is shifted to higher energy because of the strongly electronegative environment of four oxygens.

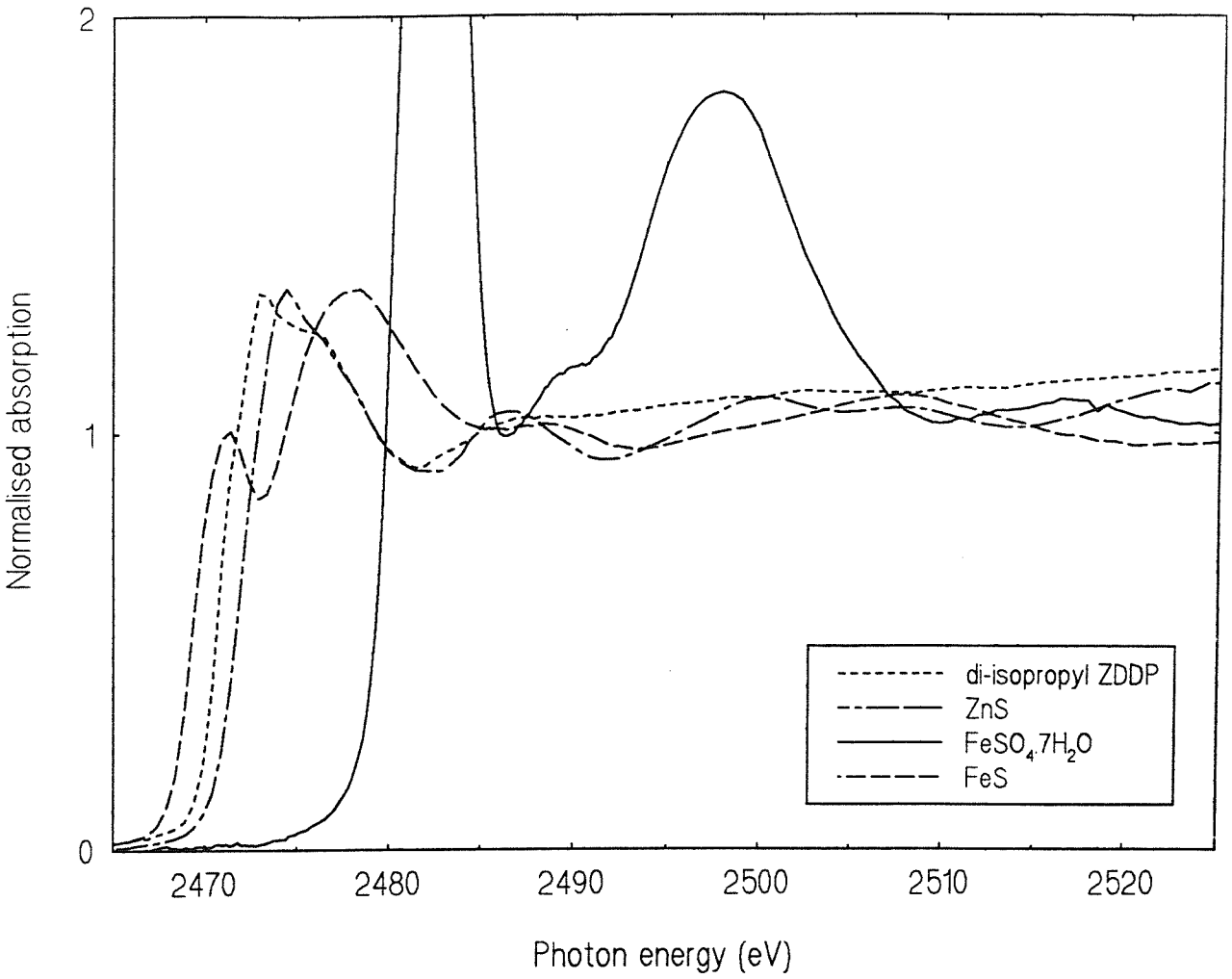

Fig. 6.10. *Sulphur K-edges in model compounds.*

Similarities between the edge positions of the ZDDP wear films and those of the model compounds FeS, ZnS and ZDDP clearly indicate that sulphur is predominantly coordinated to metal in these films. The antiwear film is unshifted relative to ZnS, and shifted by 1.0 ± 0.3 eV relative to ZDDP and 2.0 ± 0.3 eV relative to FeS. Results for phosphorus, described in the previous section, show that ZDDP completely reacts during film formation. Therefore, despite similarities in the appearance and position of the edge, the absorption cannot be attributed to unreacted ZDDP (in the oil coating or even absorbed on the surface).

The edge position and near-edge structure of sulphur in the antiwear film more closely resembles that of the model compound ZnS than FeS. However, EXAFS analysis of zinc in the commercial ZDDP film (see Sect. 6.4.3) has indicated that there is no Zn-S bonding, so, for one case at least, the formation of zinc sulphide can be discounted. (It should be noted that, as will be described below, there is good evidence for more than one chemical environment for sulphur in the antiwear films and, consequently, comparisons of their line structure with model compounds may be hindered by overlapping absorption edges.)

These results are consistent with previous studies (reviewed in Chapter 1) which have shown that sulphur in ZDDP forms iron sulphide in antiwear films. In a study of wear debris from a di-isopropyl ZDDP antiwear film, Hallouis *et al.*[4] found that all sulphur was located in a non-stoichiometric iron (II) sulphide with a hexagonal pyrrhotite structure. Pyrrhotites have a distorted NiAs structure, which at different compositions shows variations in superstructure.[23-28] There are three slightly different structural environments for sulphur in pyrrhotites, although in each case sulphur is coordinated to six iron atoms. The stoichiometric FeS model compound used in the present study has the closely related troilite structure (which also resembles a distorted NiAs structure).

The absorption edges of the DPDS-TPP antiwear film and the sulphate $FeSO_4{\cdot}7H_2O$ are effectively unshifted with respect to each other and their line structure is very similar. Both show a large edge feature, or "white line", characteristic of coordination to electronegative atoms.[22] This clearly indicates that sulphur in the DPDS-TPP film is coordinated to four oxygens in a sulphate. Absorption by unreacted DPDS in the oil can be discounted because, firstly, DPDS should absorb at a significantly lower energy (since each sulphur atom is coordinated to the comparatively electropositive environment of another sulphur and one oxygen) and, secondly, the removal of residual oil by solvent washing did not effect the absorption spectrum. Consequently, it appears that DPDS has reacted to form a film.

A sharp peak in the near-edge spectrum of the di-isopropyl ZDDP film and a small feature for the commercial ZDDP spectrum - but not apparently in the presence of other additives - appear at an energy coincidental with the white line in the spectrum of $FeSO_4{\cdot}7H_2O$ (or the DPDS-TPP film). There is also a peak in the di-isopropyl spectrum at the same position as the broad feature at about 2500 eV in the iron sulphate spectrum. This strongly suggests that some of the sulphur in the ZDDP antiwear films (but not, perhaps, when dispersant and

detergent are present) is located in a sulphate. There is also a small pre-edge peak in the absorption spectrum of the DPDS-TPP film which is not seen for $FeSO_4 7H_2O$. This feature coincides with the edge position of sulphur in the other antiwear films and therefore can be assigned to absorption by comparatively small amounts of sulphur coordinated to metal. It appears that there is more than one chemical environment for sulphur in these antiwear films.

The k^3 weighted EXAFS spectrum of sulphur in the DPDS-TPP film is given in fig. 6.11, phase shift corrected for oxygen. The Fourier transform (also given in fig. 6.11) shows that the EXAFS is dominated by contributions from a single shell, a characteristic of a short range order situation.

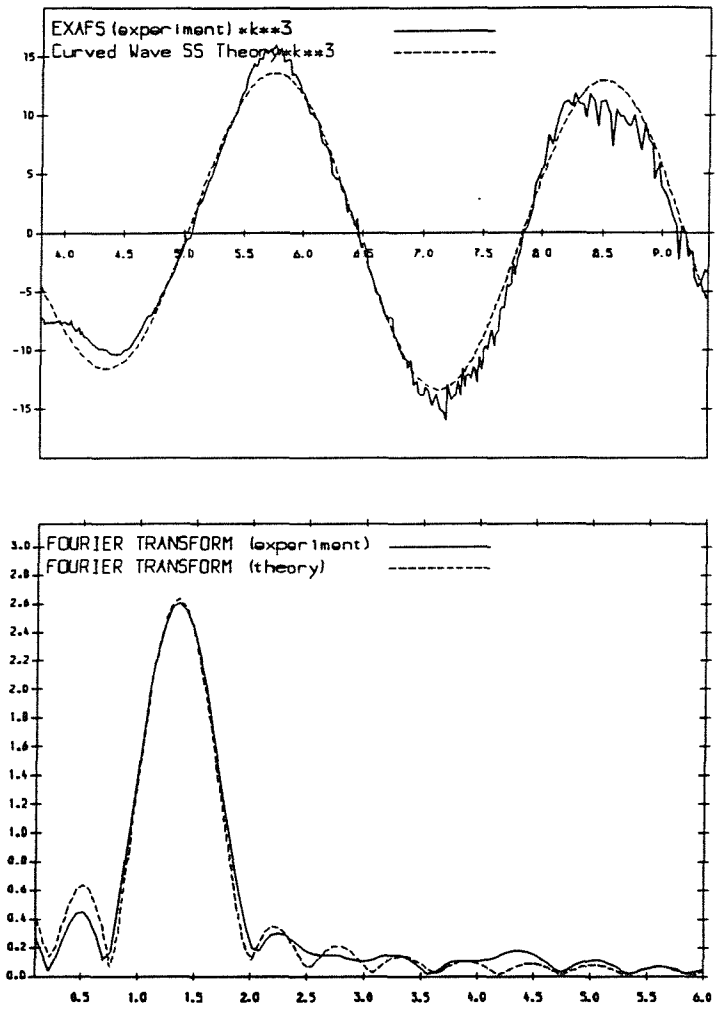

Fig. 6.11. S K-edge EXAFS and Fourier transform, phase shift corrected for oxygen, of the antiwear film of the DPDS-TPP mixture.

There is no evidence of ordered structure beyond the first coordination shell. The EXAFS (and absorption edge) of sulphur in the DPDS-TPP film strongly resembles that of phosphorus in the antiwear films (fig. 6.7), indicating structural similarities. It was not possible to test the transferability of the EXCURV92-calculated phase shifts for sulphur and oxygen (the absorption spectrum of the iron sulphate model compound was not recorded over a sufficiently large energy range). Nevertheless, the results of an EXAFS analysis are presented below.The EXAFS was successfully fitted with a single scattering, single shell of oxygen model. In the fit, the number of oxygens (N) in the coordination shell was set to 4.0, as expected for a sulphate, and R, $2\sigma^2$ and E_0 were varied. The results of the curve fitting are presented in Table 6.2 and the theoretical and experimental EXAFS oscillations are compared in fig. 6.11.

Table 6.2. *S K-edge EXAFS derived structural parameters for the antiwear film of the DPDS-TPP mixture. R = 12.9%, E_0 = 22.8 eV, VPI = -7.4 eV, AFAC = 0.94.*

Sulphur in:	Shell	N	R (Å)	$2\sigma^2$ (Å^2)
antiwear film of DPDS-TPP mixture	S	4.0	1.418	0.002

The EXAFS analysis implies a S-O bond length of 1.42 $\pm$ 0.02 Å. This is slightly shorter than any of the four S-O bond lengths reported[23] for the distorted tetrahedron SO_4 in $FeSO_4{\cdot}7H_2O$, which vary from 1.462 to 1.488 Å. The comparatively low value of the Debye-Waller factor $2\sigma^2$ indicates that there is little static disorder in the arrangement of the first shell of oxygen about the sulphur in the antiwear film.

The extraction of EXAFS from the spectra of ZDDP antiwear films proved difficult. Because of low sulphur content, the absorption spectra suffered from a poor signal-to-noise ratio, which became a problem at higher k values. Consequently, background subtraction was hindered.

The EXAFS spectra of the ZDDP antiwear films are presented in fig. 6.12, along with their Fourier transforms. The spectra are phase shift corrected for iron, assuming that iron sulphide has formed as expected from previous results (in particular, the wear debris study of Hallouis *et al.*[4], but also the wider ZDDP literature, reviewed in Chapter 1).

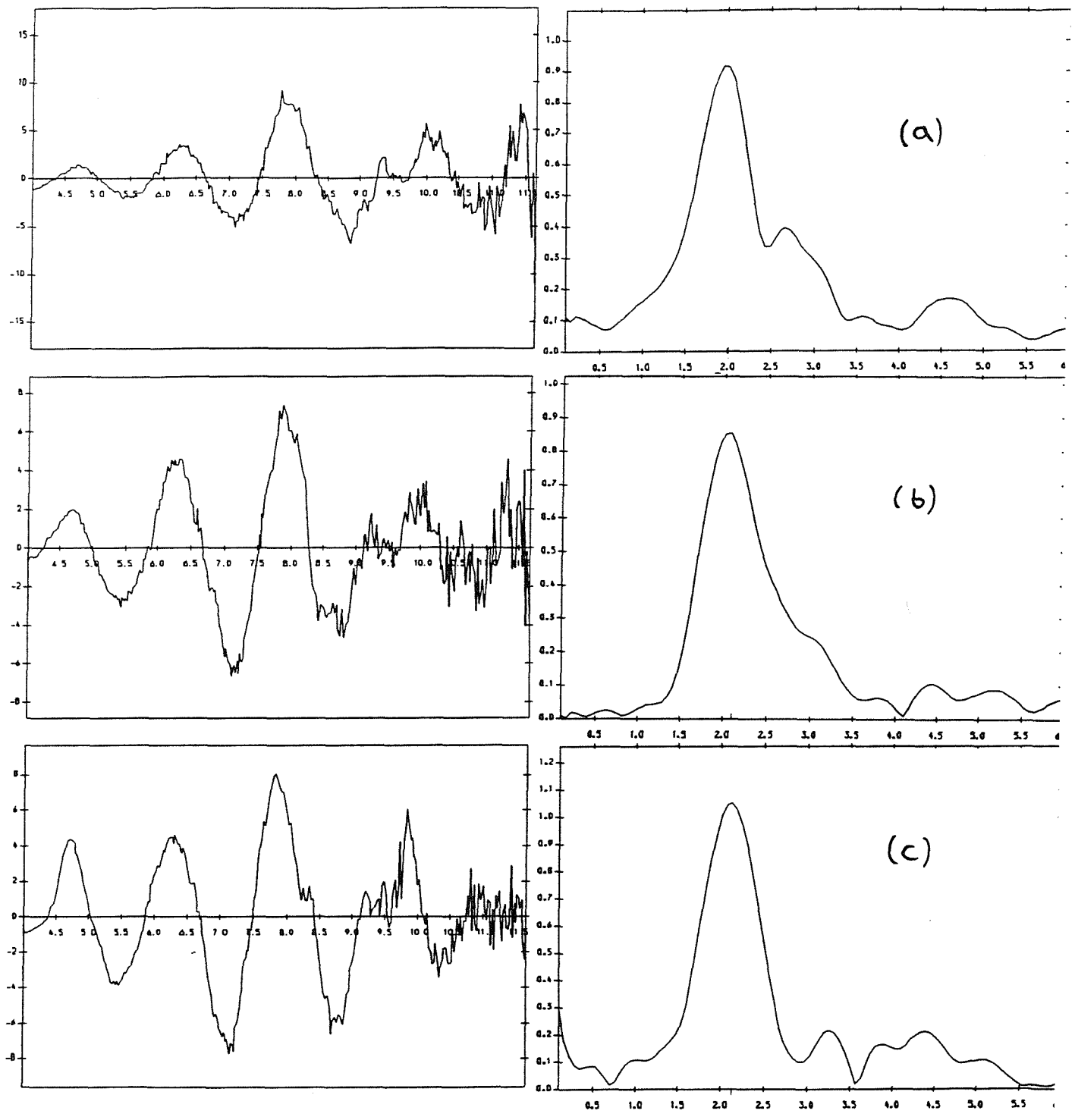

Fig. 6.12. *EXAFS spectra, phase shift corrected for iron, and Fourier transforms of sulphur in the antiwear films of (a) di-isopropyl ZDDP, (b) commercial ZDDP and (c) commercial ZDDP with dispersant and detergent.*

Unfortunately, we have been unable to find a meaningful fit to the data. In part, this arises from problems of poor background subtraction. The complexity of the sulphur environment is also expected to hinder analysis. As noted above, there is clear evidence that sulphur is located in more than one structural environment. Furthermore, iron sulphides are structurally complex. For example, in hexagonal pyrrhotite (the sulphide identified in wear debris by Hallouis *et al.*[4]) sulphur is coordinated to six iron atoms, in three slightly different environments, with Fe-S bond lengths that vary from 2.219 Å to 2.658 Å.[23]

Qualitatively, the EXAFS results for the ZDDP antiwear films are fairly consistent with the formation of iron sulphide. The major contribution to the EXAFS comes from coordination shells located at about 2.0 Å in the di-isopropyl ZDDP films and 2.1 Å in the two commercial ZDDP films. These are acceptably close to the Fe-S bond lengths in pyrrhotite (reported above) considering that the parameter E_0, which defines the start of the EXAFS ($k = 0$), has not been refined (this process effects the position of the peak).

There is also some evidence of contributions from other shells, although poor background subtraction makes it difficult to be certain. For example, the films of di-isopropyl ZDDP and commercial ZDDP with detergent and dispersant apparently show a coordination shell at 4.5 Å, which is consistent with a crystalline environment.

6.4.3. Zinc in antiwear films

The unavailability of beam time meant that it was only possible to characterise the zinc K-edge absorption spectrum for one of the samples: the antiwear film of the commercial ZDDP. Even though measurements were made in fluorescence mode, the EXAFS oscillations were comparatively small in amplitude and suffered from a poor signal-to-noise ratio.

Fig. 6.13 shows a comparison of the zinc K-edges of the antiwear film and the model compounds, commercial ZDDP, ZnS, ZnO, $Zn_3(PO_4)_2$ and zinc phosphate glass.

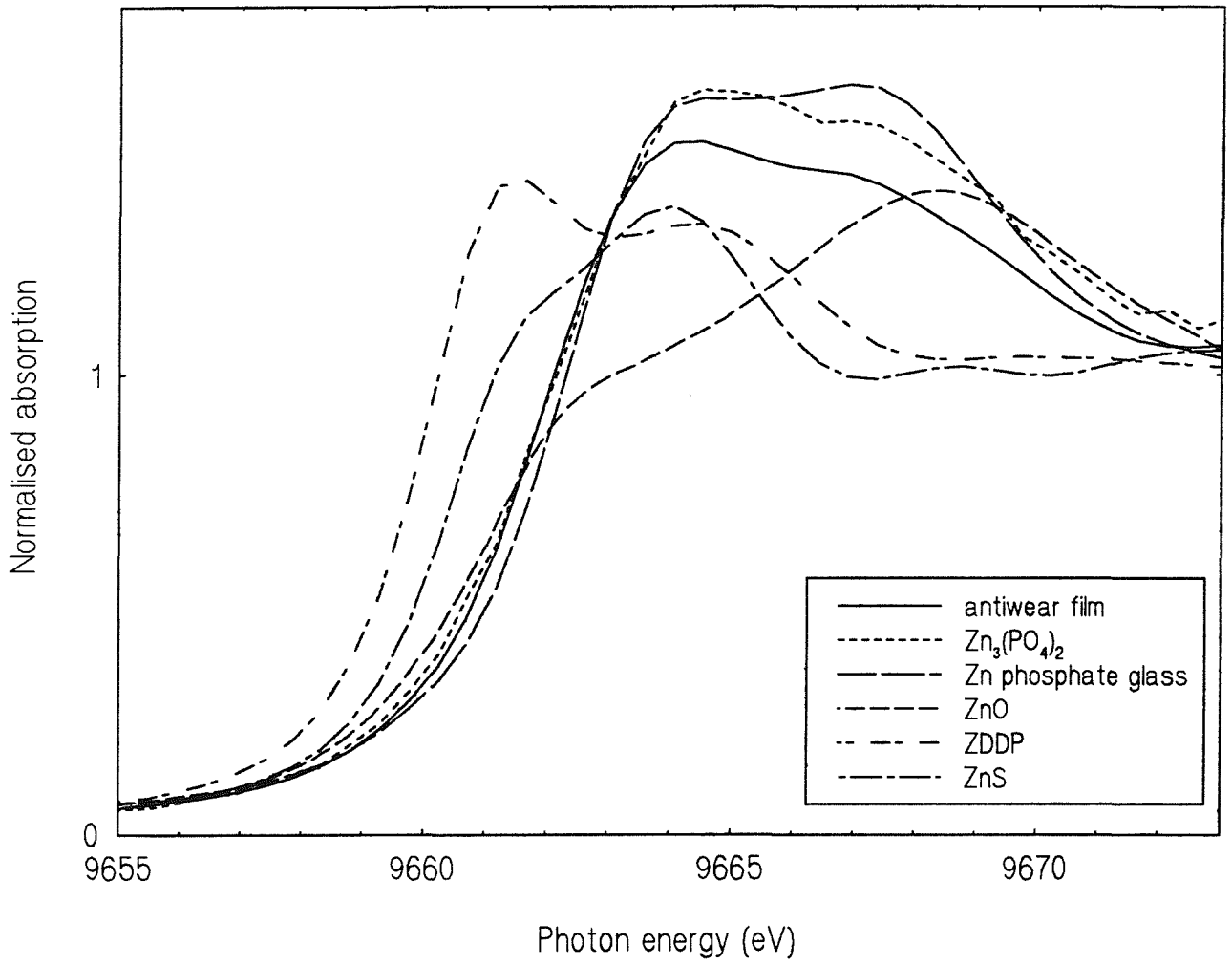

Fig. 6.13. *Zinc K-edges in the antiwear film of commercial ZDDP and model compounds.*

Remarkably, the edge position and near-edge structure of zinc in the antiwear film, at 9660.8 $\pm$ 0.3 eV, is very similar to that of zinc in the crystalline or glassy zinc phosphate (their edge energies are within 0.5 eV of that of the film). Zinc in ZnO appears at a similar

absorption energy but has a somewhat different near-edge structure. The absorption edge of the antiwear film has clearly shifted to higher energy with respect to ZDDP or ZnS (by about 1.5 and 1.0 eV, respectively). In agreement with Martin *et al.*,[2] these results indicate that zinc is coordinated to oxygen only. The close similarity in the near-edge structure of the antiwear film and $Zn_3(PO_4)_2$ presumably indicates a similar coordination symmetry, in which case zinc in the antiwear film is tetrahedrally coordinated to oxygen.

Phase shifts for zinc and oxygen, calculated by EXCURV92, were verified by analysing the EXAFS of the model compound ZnO (fig. 6.14).

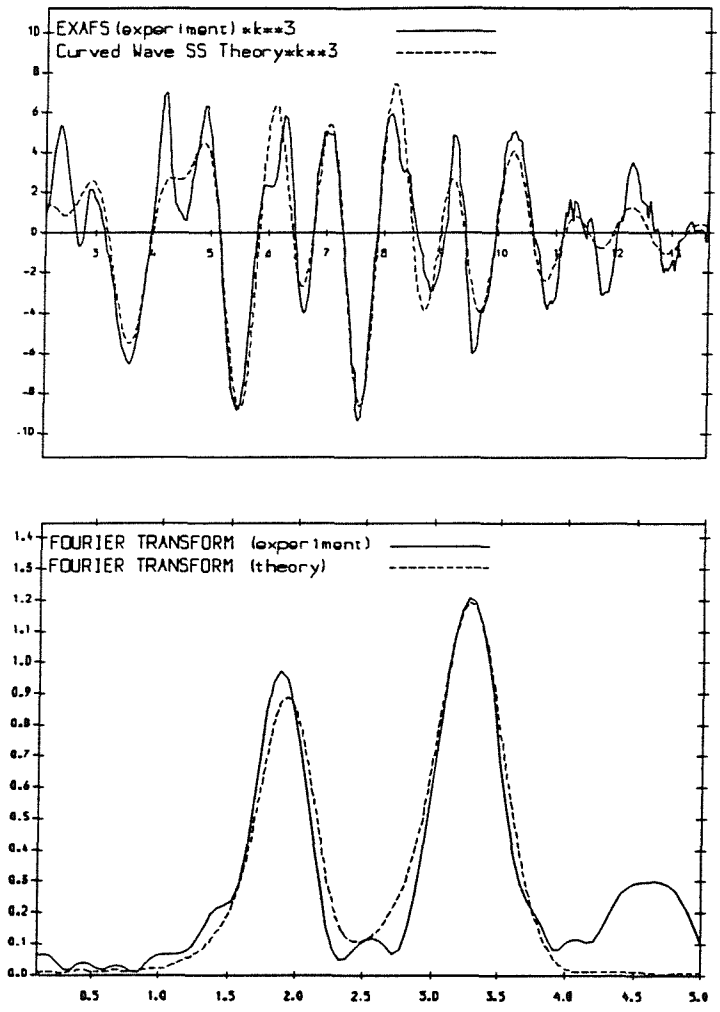

Fig. 6.14. Zn K-edge and Fourier transform, phase shift corrected for oxygen, of ZnO.

The Fourier transform of the EXAFS, also given in fig. 6.14, shows contributions from a number of shells. The first and second shells are attributable to oxygen and zinc respectively, and were fitted by setting the coordination numbers to their known values of 4 and 12 and varying R, $2\sigma^2$ and E_0 (for convenience, no attempt was made to fit the more distant shells, like the one at 4.5 Å in fig. 6.14, for example). Results of the analysis are presented in Table 6.3 and the theoretical and experimental spectra are compared in fig. 6.14.

Table 6.3. *Zn K-edge EXAFS derived structural parameters for ZnO*

R = 39.7%, E_0 = 13.9 eV, VPI = -3.0 eV, AFAC = 0.72.

Zinc in	Shell	N	R (Å)	$2\sigma^2$ (Å^2)
ZnO	O	4.0	1.964	0.015
	Zn	12.0	3.179	0.026

The overall fit was comparatively poor (R = 39.7%), but this was acceptable because no attempt had been made to resolve and account for the contribution of shells beyond the first and second. The EXAFS derived bond length for the first, oxygen-coordinated shell at 1.964 Å was in good agreement with the literature value (an average) of 1.978 Å.[30] Hence, transferability is confirmed for this set of phase shifts, and errors of ± 0.02 Å in bond length and 20% in coordination number are expected for the antiwear film data.

The EXAFS spectrum of the antiwear film (phase shift corrected and k^3 weighted) is shown, along with the Fourier transform, in fig. 6.15. The Fourier transform shows that the EXAFS is dominated by contributions from a single shell. It is possible, however, that high noise levels in the Fourier transform conceal shells at higher radius. As fig. 6.16 shows, such contributions can be seen in the Fourier transform of the EXAFS of $Zn_3(PO_4)_2$ and the zinc phosphate glass.

Initially, the EXAFS of the antiwear film was fitted with a single scattering, single shell of oxygen model by varying N, R, $2\sigma^2$ and E_0 (N and R were varied separately because of correlations). Results of the curve fitting analysis are summarised in Table 6.4 and the theoretical and experimental EXAFS oscillations are compared in fig. 6.15. The fit has an especially large R factor (54.5%) primarily because of poor signal-to-noise.

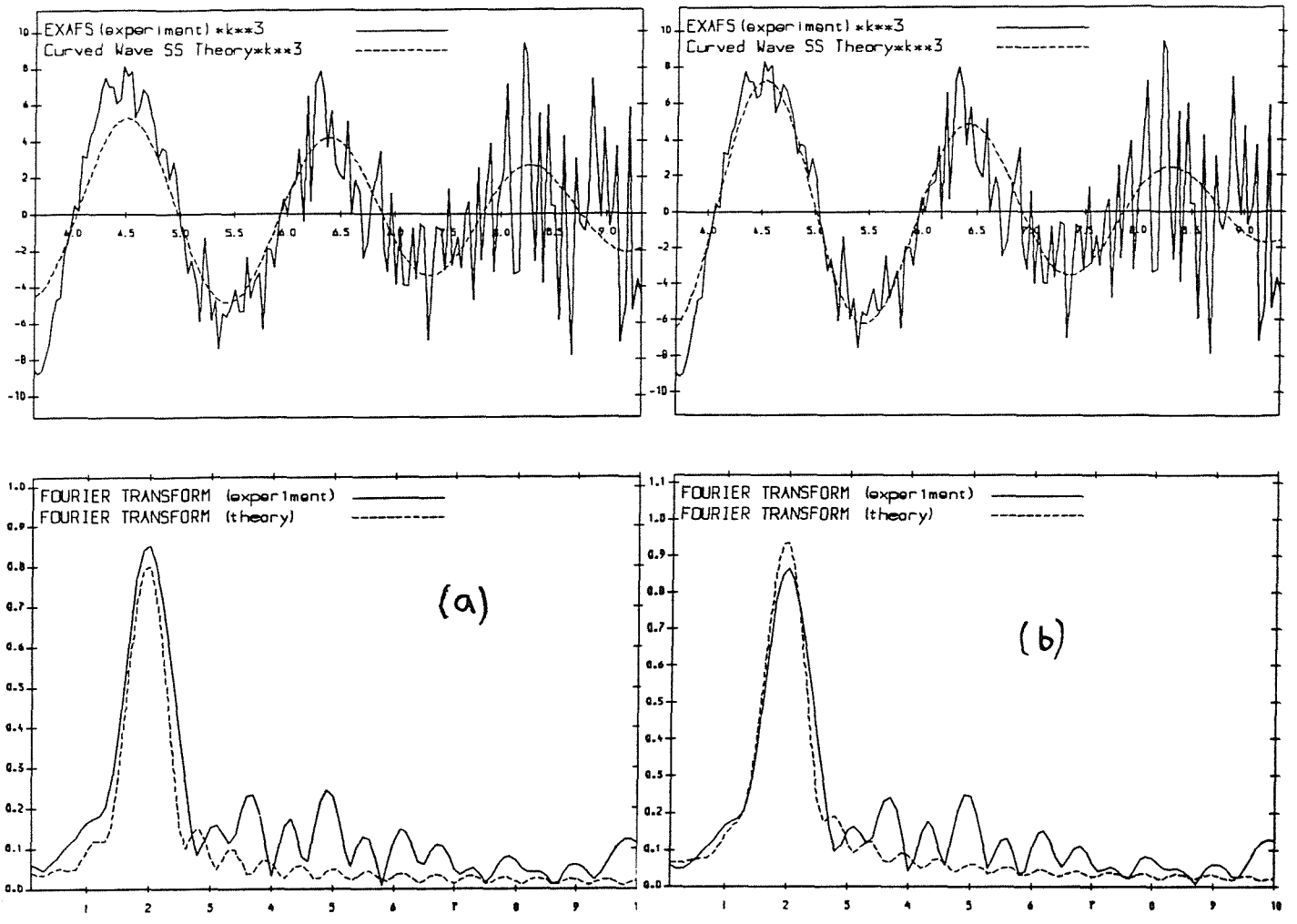

Fig. 6.15. Zn K-edge EXAFS and Fourier transforms, phase shift corrected for oxygen, of the antiwear film of commercial ZDDP showing fits where (a) coordination number was varied and (b) coordination number was fixed at N = 4.

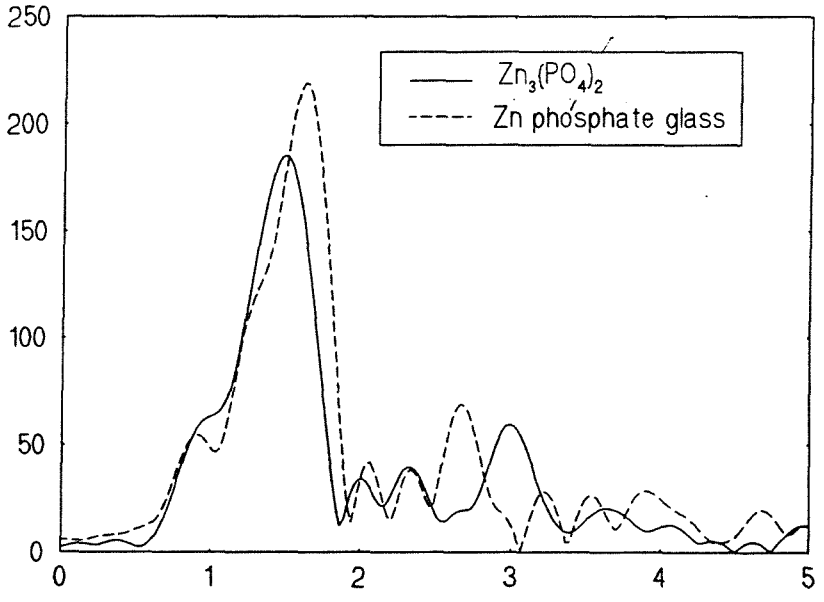

Fig. 6.16. Fourier transform of EXAFS of zinc in $Zn_3(PO_4)_2$ and zinc phosphate glass, not phase shift corrected for oxygen.

That analysis yielded a coordination number of 6.4 $\pm$ 1.3. As will be discussed below, there is some evidence in the literature for the 6-fold coordination of zinc to oxygen in zinc phosphate glasses. However, zinc is usually reported to be 4-fold coordinated in oxide glasses,[31-33] and Martin *et al.*[2] reported 4-fold coordination about zinc in the wear debris of di-isopropyl ZDDP. For this reason, the data was also fitted by setting N to 4.0 and varying R, $2\sigma^2$ and E_0. The results of this analysis are presented in table 6.4 and fig. 6.15, where it can be seen that this model led to a slight worsening of the fit (R = 60.58%).

The EXAFS was then Fourier filtered using square windows with the range 0.7 to 2.3 Å to separate the first shell from the noisy background. The isolated peak was fitted by varying N, R, $2\sigma^2$ and E_0. The curve fitting parameters are given in table 6.4, and the theoretical and experimental curves are compared in fig. 6.17.

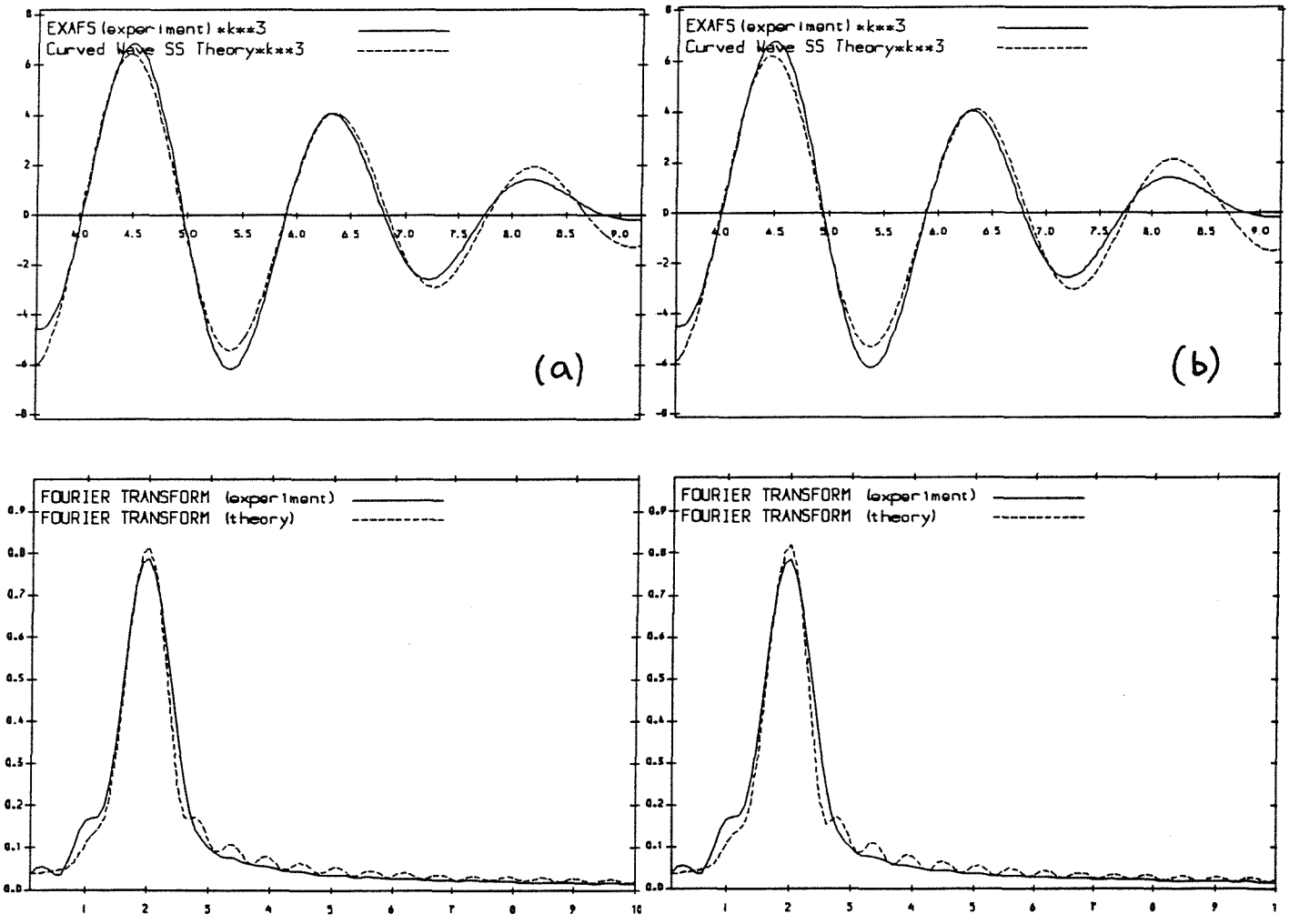

Fig. 6.17. *Fourier filtered data (window 0.7 to 2.3 Å) for zinc in the antiwear film of commercial ZDDP showing fits where (a) coordination number was varied, and (b) coordination number was fixed at N = 4.*

The best fit was found with a bond length of 2.00 ± 0.02 Å (a negligible increase over the value determined from the raw data) and a coordination number of 6.2 ± 1.3. Again, the Fourier filtered EXAFS was also fitted by setting the coordination number to 4.0 (fig. 6.17, Table 6.4). The comparable success of this fit suggests that the data is too poor for it to be possible to distinguish between 4-fold and 6-fold coordination.

Table 6.4. *Zn K-edge EXAFS derived structural parameters for antiwear film commercial ZDDP.*

Raw data, N varied, R = 54.5%, E_0 = 19.7 eV, VPI = -2.0 eV, AFAC = 0.72.

Raw data, N fixed, R = 60.7%, E_0 = 18.2 eV, VPI = -2.0 eV, AFAC = 0.72.

Fourier filtered (1), R = 18.4%, E_0 = 16.5 eV, VPI = -2.0 eV, AFAC = 0.72.

Fourier filtered (2), R = 15.8%, E_0 = 16.9 eV, VPI = -2.0 eV, AFAC = 0.72.

Zinc in:	Shell	*N*	*R* (Å)	$2\sigma^2$ (Å^2)
Antiwear film				
Raw data, N varied	O	6.4	1.979	0.022
Raw data, N fixed	O	4.0	1.989	0.014
Fourier filtered (1)	O	6.2	2.000	0.025
Fourier filtered (2)	O	4.0	2.000	0.021

The EXAFS determined first shell radius of 1.99 ± 0.02 Å (an average of the values from the different fits) is in fair agreement with the value of 1.96 ± 0.02 Å, reported by Martin *et al.*,[3] for zinc in the wear debris of di-isopropyl ZDDP antiwear films, and matches Zn-O bond distances found in other oxide glasses,[31] as will be discussed below.

6.5. Discussion

(i). Solvent washing

In previous studies, ZDDP antiwear film samples have often been washed with solvents - such as petroleum spirit,[34] alcohol,[35] acetone and toluene[36] or acetone-white spirit mixture[37] - to remove residual oil before measurements are made. In the structural studies described in Sect. 6.1,[1-4] the wear debris particles were pretreated with hexane. Surprisingly, no systematic study of the effect of solvent washing has been made, despite observations that part of the film can be removed by solvent rinsing.[12,36]

In the present work, rinsing the samples with methanol or hexane does not appear to cause any significant change in the absorption spectra. Absorption spectra recorded before rinsing did not show any evidence of unreacted additive. This suggests that any phosphorus, sulphur or zinc left in the oil was in very low concentrations.

(ii). Phosphorus in antiwear films

To the best of our knowledge, the present study represents the first time that the structural environment of phosphorus in ZDDP antiwear films has been characterised. This is somewhat surprising considering that, firstly, the structure of antiwear films may well be related to their function and performance and, secondly, this information is readily extracted using EXAFS.

Remarkably, the results for phosphorus in the four different antiwear films are effectively identical. They can be summarised as follows: Chemical shift information, and comparisons of near-edge structure, show that phosphorus is present as a phosphate. The EXAFS contains the contribution of only one coordination shell, indicating that there is no long range order in the phosphate beyond the first coordination shell of oxygen. Curve fitting analysis indicates that phosphorus is bonded to four oxygen atoms in a shell at a well-defined distance of 1.50 ± 0.02 Å. This value can be considered to be an average P-O bond length for the four oxygens. These results are entirely consistent with the indirect evidence provided by the wear debris studies[1-4] described in Sect. 6.1 that phosphorus is present as a glassy phosphate.

There is no indication of phosphorus in any other chemical environment in these films. The edge data recorded for model compounds show that it should be possible to differentiate between the coordination of sulphur and oxygen to phosphorus. In this way, the absence of thiophosphate is shown (although the level of detection of the measurement is not known).

The local structural environment of phosphorus in the antiwear film does not depend on the purity of the additive (there is no difference between commercial ZDDP and pure di-isopropyl ZDDP). It is unaffected by the presence of other surface active additives (dispersant and detergent). There is also no difference in the local environment of phosphorus in the antiwear films of ZDDP and the phosphate ester additive (therefore the local order is not affected by the presence of zinc).

The EXAFS derived average bond length of 1.50 $\pm$ 0.02 Å can be compared with other reported values for phosphate glasses, typically derived with X-ray or neutron diffraction methods (Table 6.5). Bond length data is only available for phosphate glasses at, or near, the metaphosphate composition (50% M_2O, 50% P_2O_5), and with two exceptions (described below) they are average values where no distinction can be made between separate distances within the PO_4 unit. It can be seen that the average P-O bond length determined for the antiwear film in the present study is significantly smaller than the reported values for metaphosphate glasses.

Suzuki and Ueno,[43] alone, were able to distinguish between P-O bonds to bridging (BO) and non-bridging oxygens (NBO) in their data for a sodium metaphosphate glass. In a study of silver metaphosphate glass, Dalba *et al.*[38] found that EXAFS contained the contribution of only one coordination shell, as expected for a long range disorder situation. However, they attempted to resolve this shell to obtain bond lengths to BO and NBO, by assuming that for each of the subshells the coordination number equalled two and the Debye-Waller factor equalled that of the crystalline compound. In the present work, the single shell contribution in the EXAFS of the antiwear films could not be fitted to separate subshells of BO and NBO because, as expected, correlations between the various structural parameters were too high and the ratio of NBO to BO was not known, beforehand.

Table 6.5. Some reported P-O bond lengths in phosphate glasses of different composition. XRD = X-Ray Diffraction, PND = Powder Neutron Diffraction. BO and NBO = bridging and non-bridging oxygens. Composition given as mole% of modifier oxide with P_2O_5.

Modifier	Mole% modifier	P-O bond length (Å)	Technique	Ref.
ZnO	45-55	1.53	XRD	38
"	50	1.54	PND	39
PbO, Fe_2O_3	50	1.55 - 1.58	XRD	40
Ag_2O	50	1.52	PND	41
"	50	1.55 *suggested to be* 1.48 (NBO) 1.62 (BO)	EXAFS	42
Na_2O	50	1.50 (NBO) 1.64 (BO)	PND	43
MgO	50	1.53	PND	39

The average P-O bond length determined in the present study (1.50 ± 0.02 Å) can also be compared with bond lengths found in crystalline phosphates, where, in general, clear distinctions can be made between bonding to BO and NBO. Table 6.6 gives such data for zinc and iron phosphate, since Martin *et al.*[2] have shown that both zinc and iron cations are present in the amorphous matrix of wear debris, although it is generally found that the type of counter ion does not have a strong effect on P-O bond length.[7,10] The shortest P-O bond lengths are found in the P-O-P linkages that hold together the ring of four PO_4 units in the tetrametaphosphate. Ortho-, pyro- and tripolyphosphates form a homologous series of chain polyphosphates with one, two, and three PO_4 units, respectively. In all cases, P-O bond lengths to non-bridging oxygen (NBO) - that is, terminal P=O double bonds and P-O-Zn bonds - are considerably smaller than bond lengths for bridging bonds (P-O-P). As data in Table 6.6 shows, P-O bonds in zinc and iron phosphates are comparable in length. In general P-O bond lengths increase in the order ring < terminal < chain.

Table 6.6. Some reported ranges of P-O bond lengths in crystalline zinc and iron phosphates, determined by X-Ray Diffraction. Bond types are NBO - bonds to non-bridging oxygen, BO - bonds to bridging oxygen in chain structures, and ring BO - bonds to bridging oxygen in ring structures.

Compound	Bond type	P-O bond length range (Å)	Ref.
α Zn orthophosphate	NBO	1.50 - 1.58	21
α Zn pyrophosphate (diphosphate)	NBO BO	1.489 - 1.531 1.567 - 1.600	44
Zn tripolyphosphate heptahydrate	NBO BO	1.49 - 1.52 1.59 - 1.63	45
Zn tetrametaphosphate octahydrate	ring BO NBO	1.472 - 1.488 1.597 - 1.600	46
Fe^{II} orthophosphate ($Fe_3(PO_4)_2$)	NBO	1.52 - 1.54	47
Fe^{III} orthophosphate ($Fe(PO_4)$)	NBO	1.524 - 1.529	48

The average P-O bond length found in the antiwear films compares well with distances found in crystalline phosphates for shorter P-O bonds to non-bridging oxygen.

The EXAFS derived antiwear film P-O bond length is expected to be some kind of weighted average reflecting the relative proportions of bridging and non-bridging oxygens in the phosphate. The shortness of the bond compared to values for the metaphosphate glasses (in Table 6.5) may indicate a comparatively higher ratio of non-bridging (NBO) to bridging (BO) oxygens. The NBO-to-BO ratio is expected to be approximately 1:1 in metaphosphate glasses (it would be exactly 1:1 for ring phosphates, it is slightly higher in long chain metaphosphates where end units are present). As the ratio increases, chain lengths decrease and presumably so does the average bond length as perceived by EXAFS.

The observation of the comparatively short bond length in the antiwear phosphate is consistent, for example, with the compositional studies discussed in Chapter 1 which identify the antiwear film as a pyrophosphate (NBO-to-BO ratio = 3:1). Generally, a range of chain lengths is present in a phosphate glass at given composition, so that a glass with an apparent pyrophosphate composition may also contain high concentrations of orthophosphate (PO_4 monomers). Onyiriuka[49] has shown that a high concentration of zinc in phosphate glass (33 mol% ZnO) is associated with high levels of orthophosphate.

Interestingly, there is no significant difference between the structural environments of phosphorus in the zinc-iron phosphate of the ZDDP films or the (presumably) iron phosphate of the TPP film. Iron and zinc might be expected to distort the PO_4 tetrahedron to different *measurable* extents (it appears that they do in crystalline orthophosphate, as shown in table 6.6, and the significant effect of different cations on bond length in metaphosphate glasses is clear in table 6.5). The absence of such an effect when comparing the ZDDP and TPP antiwear films may indicate that levels of cation are low, in which case the phosphate chains should be long. Alternatively, it may suggest that levels of iron are much higher than zinc in the ZDDP antiwear films, so that the effect of zinc on EXAFS-measured bond lengths is negligible. The systematic investigation of the role of iron and zinc will be an important next-step in the characterisation of the structure of ZDDP antiwear films.

(iii). Zinc in antiwear films

The structural environment of zinc in the commercial ZDDP antiwear film has also been characterised in the present study. Chemical shift information indicates that zinc is coordinated to oxygen, only, while EXAFS analysis reveals the contribution of an oxygen shell at a Zn-O separation of 1.99 $\pm$ 0.02 Å. There does not appear to be any contribution from more distant shells, indicating that there is no long range order about zinc.

Results of curve fitting analysis are ambiguous as to the coordination number of oxygen in the first shell. Noise in the spectra means that it is not possible to clearly distinguish between coordination numbers of 4 and 6, both of which have been reported for zinc in phosphate glasses (see below). However, these results compare well with the EXAFS study of zinc in wear particles from a di-isopropyl ZDDP antiwear film, reported by Martin *et al.*[2] They

found that zinc is coordinated to oxygen in a short-range order environment characterised by a Zn-O bond length of 1.96 Å, but did not derive a coordination number for oxygen. The results of the two studies indicate that zinc is not in a crystalline environment, but is scattered throughout the glassy phosphate network.

Generally, the physical properties of a phosphate glass containing a divalent modifier change monotonically with composition. Zinc phosphate, however, shows anomalous behaviour in such properties as refractive index and density[50] and elastic modulus and Vickers hardness[51] near the metaphosphate composition (mole ratio $ZnO/P_2O_5 = 1$). Following Kordes *et al.*,[50] this transition has often been attributed to a change of zinc-oxygen coordination from 6 - which is termed "normal" and is expected for a metallic ion of similar size to oxygen - to an "abnormal" value of 4 in the zinc phosphates showing the anomalous properties. Studies of the structure of zinc in phosphate glasses have concentrated on investigating this hypothetical transition. In general, however, zinc cations in oxide glasses are usually reported to be four-coordinated to oxygen, and are considered to act as modifiers.[31-33]

Bogomolova *et al.*,[52] using electron spin resonance spectroscopy, considered the coordination number to be a mixture of 4 and 6 in "abnormal" zinc phosphate glasses. Similarly, Musinu *et al.*[53] using XRD found a Zn-O bond length of 2.06 Å near the metaphosphate composition, which they considered to be intermediate between the distances expected for 4- and 6-fold coordination. At lower zinc concentrations, the Zn-O bond length of 1.94 Å was considered typical of 4-fold coordination. In another XRD study, Matsubara *et al.*[54] reported similar Zn-O bond lengths of 1.98, 1.95 and 1.97 Å, and a coordination number of 4, across the composition range 45 to 55% ZnO. They failed to detect an abrupt change in coordination number.

The Zn-O bond length of 1.99 ± 0.02 Å determined in the present study compares well with the shorter values reported for zinc phosphate glasses, indicating that the coordination of zinc in the antiwear films is 4. It is unfortunate that more and better quality results for the different additives were not obtained in the present study. Uncovering the role of modifying and intermediate cations in the phosphate matrix could well be important in understanding the properties of the antiwear film.

(iv). Sulphur in antiwear films

Although little quantitative information has been extracted from the EXAFS of sulphur in the antiwear films, some interesting qualitative observations can been made.

Results indicate that the DPDS additive has reacted to form a film. Chemical shift data shows that sulphur is almost entirely present as a sulphate. EXAFS analysis reveals an average S-O bond length of 1.42 $\pm$ 0.02 Å (which is slightly shorter than that found in iron sulphate heptahydrate[23]) and clearly shows that the sulphate is disordered beyond the first coordination shell. Similarly, phosphorus is also present in the DPDS-TPP film as a phosphate with no order beyond the first coordination shell. Apparently, sulphur and phosphorus are present as glass network formers in the DPDS-TPP film. In that case, it is likely that the two elements are intimately mixed together in the glass network.

A qualitative analysis of edge structure indicates that there may also be a small amount of metal-to-sulphur bonding in the DPDS film. This may well be present as iron sulphide, a compound which is generally believed to give the films of sulphur-based EP additives their beneficial EP performance (see Chapter 1). It can be speculated that levels of iron sulphide were low in this film because the wear test rig was run under the relatively mild conditions of the antiwear regime.

Sulphur in the antiwear films of ZDDP is found as both a crystalline iron sulphide and a (possibly amorphous) sulphate. The relative proportion of the two states varies with additive composition.

Chemical shift information shows that metal-to-sulphur bonding predominates in the ZDDP antiwear films. Zinc edge data, reported above, discounts the possibility of zinc-to-sulphur bonding (ZDDP or zinc sulphide), and so the compound is readily identified as iron sulphide. Peaks in the Fourier transforms of the unrefined experimental EXAFS give a reasonably consistent Fe-S bond length for an iron sulphide of about 2.1 Å. Hallouis *et al.*,[4] in a study of wear debris from a di-isopropyl ZDDP antiwear film, located sulphur in microscopic crystallites of the non-stoichiometric iron sulphide Fe_7S_8 with the pyrrhotite structure.[23-28] This material is a phase of FeS which forms at temperatures of 140 °C and above at atmospheric pressure (the temperature drops as pressure increases).[29] It is quite possible that

the iron sulphide postulated in the present study as a component of the ZDDP antiwear films is also located in similar crystallites of pyrrhotite.

It appears that sulphur is also present as a sulphate in the antiwear films of di-isopropyl and commercial ZDDP, but not, apparently, in the presence of the surface-active detergent and dispersant additives. As discussed in Chapter 1, sulphur in the antiwear films of ZDDP is generally believed to be located in an iron sulphide, although sulphate has occasionally been postulated. The data presented in this study gives clear evidence of the existence of this alternative chemical environment. It can be speculated that, as for the DPP-TPP film, the sulphate in the ZDDP films is present as a network former mixed intimately with the phosphate network.

Interestingly, the qualitative assessment of the antiwear performance of the additives may well correlate with the relative concentrations of sulphur in the two different environments of the film. In DPDS-TPP, which gave the worst performance, nearly all of the sulphur is present as a sulphate. The di-isopropyl ZDDP film, which gave the poorest performance of the ZDDP additives, also contains a comparatively high sulphate concentration (as indicated by relative peak heights). However, it is not possible to distinguish between the AW performance of the two commercial ZDDP mixtures.

6.6. Conclusions

Using EXAFS, we have characterised the local structural environments of phosphorus, sulphur and zinc in the antiwear films of di-isopropyl ZDDP, commercial ZDDP - both with and without detergent and dispersant - and DPDS-TPP mixture.

In all cases, phosphorus is only found in an amorphous phosphate whose structural parameters do not vary among the different additives. Bond length arguments support the suggestion, often made in the literature, that the antiwear films predominantly contain short chain phosphates. The absence of any differences in P-O bond lengths between the ZDDP antiwear films and the zinc-free DPDS-TPP film may indicate that iron is the principal counter ion in the phosphate matrix.

In the commercial ZDDP film, zinc is only found coordinated to oxygen in an environment of long range disorder. Similar conclusions were made in a previous study[2] of antiwear debris from a di-isopropyl ZDDP film. By comparison with the literature, zinc in the antiwear films of ZDDP can be considered to act as a modifier cation in the phosphate glass network.

The structural role of sulphur in these films is more complex. In the ZDDP antiwear films, sulphur is primarily coordinated to iron in a crystalline iron sulphide. In the DPDS-TPP additive film, sulphur is located almost entirely in an amorphous sulphate, although a small amount of iron sulphide may also be present. In the films of di-isopropyl ZDDP and commercial ZDDP, a relatively small proportion of sulphur is also found in an amorphous sulphate, alongside the crystalline sulphide.

The sulphate in the DPDS-TPP and ZDDP films is probably located in the phosphate glass network, in which case sulphur is considered to act as a network forming element. Antiwear performance may correlate with the relative levels of sulphate and sulphide in the film.

6.7. Future work

The present study has indicated that it is comparatively easy to get good structural information from the EXAFS of additive elements in antiwear films. It is quite possible that antiwear/extreme pressure (AW/EP) performance correlates with the structural characteristics of the film (there is evidence of this in the present work). Therefore, an important next step would be a systematic investigation of the effect of varying the additive type and composition on the EXAFS structural parameters of different elements, *correlated with AW/EP performance*. Further useful characterisation may come from comparing EXAFS derived structural information for antiwear films with that for zinc/iron phosphate glasses of different composition.

More immediately, attempts should be made to record better EXAFS spectra of sulphur in antiwear films so that structural information can be extracted.

An XPS line shape analysis of oxygen in the antiwear film phosphate may provide information about relative concentrations of bridging and non-bridging oxygen in the films, which would give some idea of the average phosphate chain lengths in antiwear films. The possibility of using chromatographic methods to separate different phosphate chain lengths in antiwear films, or their wear debris, could be considered, although the levels of phosphates may be too low for such an analysis.

Eventually, it could prove very worthwhile to extend the EXAFS analysis to a wider range of phosphorus- and sulphur-based additive films.

6.8. References

1. J.M. Martin, J.L. Mansot, I. Berbezier and H. Dexpert, *Wear* 93 (1984) 117.

2. J.M. Martin, M. Belin and J.L. Mansot, *ASLE Trans.* 29 (1986) 523.

3. M. Belin, J.M. Martin and J.L. Mansot, *ASLE Trans.* 32 (1989) 410.

4. M. Hallouis, M. Belin and J.M. Martin, *Lubr. Sci.* 2 (1989) 337.

5. G.N. Greaves, *"EXAFS and Near-Edge Structure III"*, Ed. K.O. Hodgson (Springer-Verlag, Berlin, 1982) p. 248.

6. A.E.R. Westman, *Topics in Phosphorus Chemistry* 9 (1977) 231.

7. J. van Waser, *"Phosphorus and its Compounds"*, Vol. I (Interscience Publishers, New York, 1951).

8. S.W. Martin, *Eur. J. Solid State Inorg. Chem.* 28 (1991) 163.

9. W.H. Zachariasen, *J. Am. Chem. Soc.* 54 (1932) 3841.

10. D.E.C. Corbridge, *Topics in Phosphorus Chemistry* 3 (1966) 527.

11. J. van Waser, *J. Am. Chem. Soc.* 72 (1950) 644.

12. R.C. Watkins, *Tribology Int.* 30 (1982) 1.

13. V.P. Wystrach, E.O. Hook and G.L.M. Christopher, *J. Org. Chem.* 21 (1956) 705.

14. D.E. Goldberg, W.C. Fernelius and M. Shamma, *Inorg. Syn.* 6 (1960) 142.

15. N.E. Gallopoulos, *Am. Chem. Soc., Div. Petr. Cem. Prepr.* 11 (1966) 21.

16. H.A. Spikes, *Lubr. Sci.* 2 (1989) 3.

17. R.J. Bird, R.C. Coy and J.F. Hutton, *ASLE Trans.* 23 (1980) 121.

18. J.M. Georges, *Tribol. Ser.* 7 (1982) 729.

19. P.M. Cann, H.A. Spikes and A. Cameron, *ASLE Trans.* 26 (1983) 48.

20. P.A. Lee and J.B. Pendry, *Phys. Rev. B* 11 (1975) 143.

21. C. Calvo, *Canad. J. Chem.* 43 (1965) 436.

22. P. Fragnaud, E. Prouzet, J.L. Mansot, J. Wery, G. Ouvrard and R. Brec *J. Non-Cryst. Solids* 162 (1993) 158.

23. W.H. Baur, *Acta Cryst.* 17 (1964) 1167.

24. M.E. Fleet, *Acta Cryst.* B27 (1971) 1864.

25. M. Tokonami, K. Nishiguchi and N. Morimoto, *Am. Mineral.* 57 (1972) 1066.

26. A. Nakano, M. Tokonami and N. Morimoto, *Acta Cryst.* B35 (1979) 722.

27. K. Koto and M. Kitamura, *Acta Cryst.* A37 (1981) 301

28. A. Yamamoto and H. Nakazawa, *Acta Cryst.* A38 (1982) 79.

29. H.E. King Jr and C.T. Prewhitt, *Acta Cryst.* B38 (1982) 1877.

30. S.C. Abrahams and J.L. Bernstein, *Acta Cryst.* B25 (1969) 1233.

31. S.J. Gurman and R.F. Pettifer, *Phil. Mag.* B40 (1979) 345.

32. A.B. Rosenthal and S.H. Garofalini, *J. Non-Cryst. Solids* 87 (1986) 254.

33. G. Ennas, A. Musinu, G. Piccaluga, A. Montenero and G. Gnappi, *J. Non-Cryst. Solids* 125 (1990) 181.

34. M.R. Phillips, M. Dewey, T.F.J. Quinn and H.N. Southworth, *Vacuum* 26 (1976) 451.

35. I.N.A. Sieber, K. Meyer, H. Kloss and A. Schopke, *Wear* 85 (1983) 43.

36. G. Johnston, P.M.E. Cann and H. Spikes, 5th Int. Colloq. Esslingen *"Additives and Lubricants for Operational Fluids"*, (1986) Paper 3.12.

37. H.J. Mathieu, D. Landolt and R. Schumacher, *Surf. Int. Anal.* 9 (1986) 477.

38. E. Matsubara, Y. Waseda, M. Ashizuka and E. Ishida, *J. Non-Cryst. Solids* 103 (1988) 124.

39. W. Matz, D. Stachel and E.A. Goremychkin, *J. Non-Cryst. Solids* 101 (1988) 80.

40. A. Musinu, G. Piccaluga and G. Pina, *J. Non-Cryst. Solids* 122 (1990) 52.

41. M. Tachez, R. Mercier, J.P. Malaguni and P. Chieux, *Solid State Ionics* 25 (1987) 263.

42. G. Dalba, P. Fornasini, F. Rocca, P. Largarde and G. Vlaic, *J. Non-Cryst. Solids* 106 (1988) 181.

43. K. Suzuki and M. Ueno, *J. de Physique* C8 (1985) 261.

44. B.E. Robertson and C. Calvo, *J. Solid State Chem.* 1 (1970) 120.

45. M.T. Averbuch-Pouchot, A. Durif and J.C. Guitel, *Acta Cryst.* B31 (1975) 2482.

46. M.T. Averbuch-Pouchot, *Z. Anorg. Chem.* 503 (1983) 231.

47. E. Kostiner and J.R. Rea, *Inorg. Chem.* 13 (1974) 2876.

48. Hok Nam Ng and C. Calvo, *Canad. J. Chem.* 53 (1975) 2064.

49. E.C. Onyiriuka, *J. Non-Cryst. Solids* 163 (1993) 268.

50. E. Kordes, W. Vogel and R. Feterowscky, *Z. Electrochem.* 57 (1953) 282.

51. M. Ashizuka, T. Sakai and A. Iwata, *Yogyo-Kyokai-Shi* 91 (1983) 87 and 176.

52. L.D. Bogomolova, V.A. Jachkin, V.N. Lazukin, T.K. Pavlushkina and V.A. Shmuckler, *J. Non-Cryst. Solids* 28 (1978) 375.

53. A. Musinu, G. Piccaluga, G. Pina, G. Vlaic, D. Narducci and S. Pizzini, *J. Non-Cryst. Solids* 136 (1991) 198.

54. E. Matsubara, Y. Waseda, M. Ashizuka and E. Ishida, *J. Non-Cryst. Solids* 103 (1988) 117.